SPRING 2025

GEMS & GEMOLOGY

VOLUME LXI

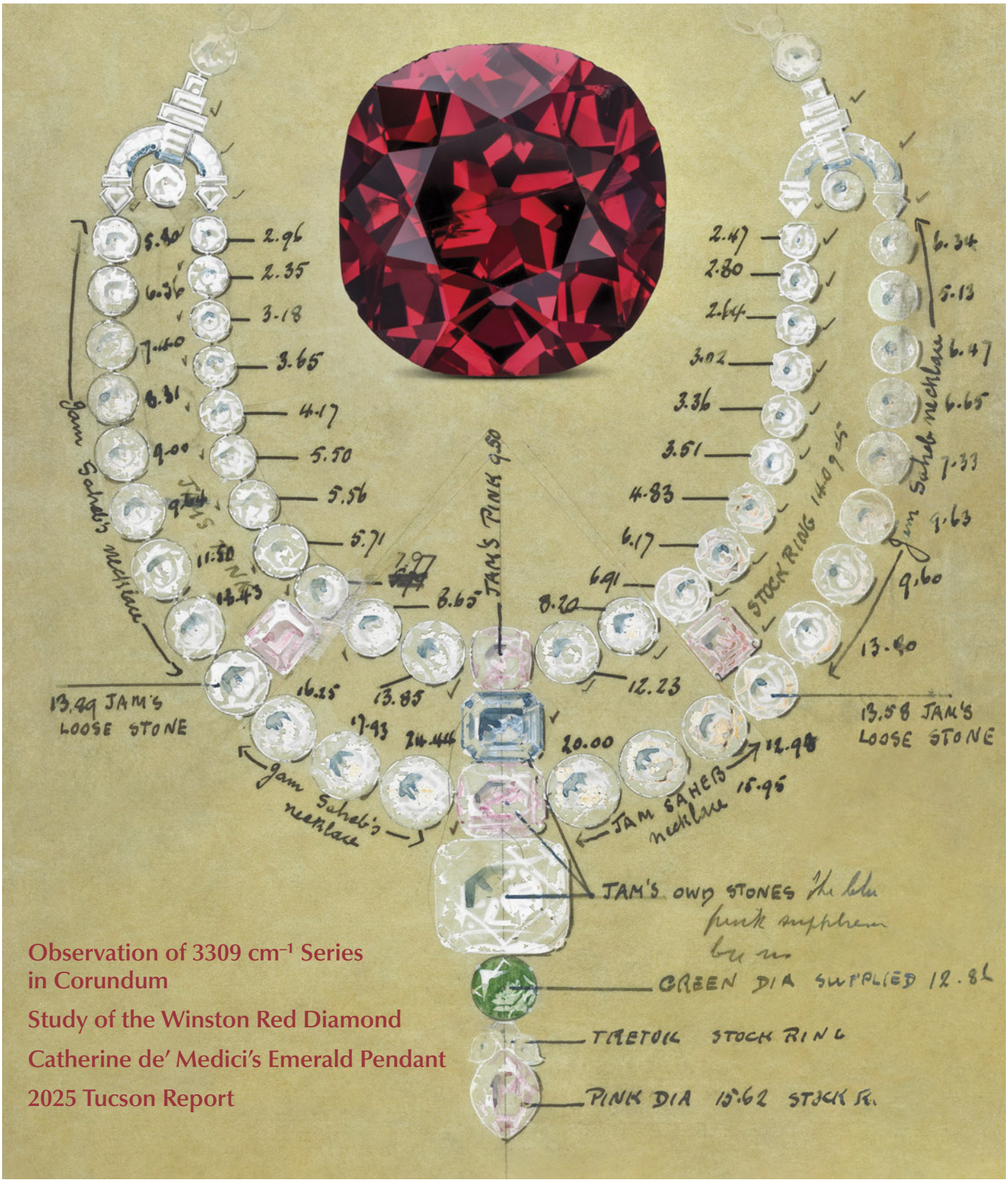

Observation of 3309 cm^{-1} Series in Corundum

Study of the Winston Red Diamond

Catherine de' Medici's Emerald Pendant

2025 Tucson Report

THE QUARTERLY JOURNAL OF THE GEMOLOGICAL INSTITUTE OF AMERICA

GEMS & GEMOLOGY®
Spring 2025
VOLUME 61, No. 1

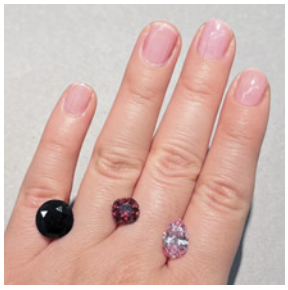
p. 19


p. 45

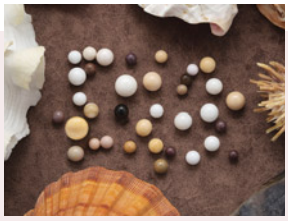
p. 67

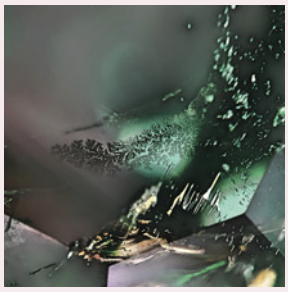
p. 75


p. 86

Editorial

Feature Articles

Regular Features

GEMS & GEMOLOGY®

gia.edu/gems-gemology

Customer Service
(760) 603-4200
gandg@gia.edu

Subscriptions
Copies of the current issue may be purchased for $29.95 plus shipping. Subscriptions are $79.99 for one year (4 issues) in the U.S. and $99.99 elsewhere. Canadian subscribers should add GST. Discounts are available for renewals, group subscriptions, GIA alumni, and current GIA students. To purchase print subscriptions, visit store.gia.edu or contact Customer Service. For institutional rates, contact Customer Service.

Database Coverage
Gems & Gemology's impact factor is 1.6, according to the 2023 Journal Citation Reports by Clarivate Analytics (issued June 2024). *G&G* is abstracted in Thomson Reuters products (Current Contents: Physical, Chemical & Earth Sciences and Science Citation Index—Expanded, including the Web of Knowledge) and other databases. For a complete list of sources abstracting *G&G*, go to gia.edu/gems-gemology, and click on "Publication Information."

Manuscript Submissions
Gems & Gemology, a peer-reviewed journal, welcomes the submission of articles on all aspects of the field. Please see the Author Guidelines at gia.edu/gems-gemology or contact the editors (gandgeditorial@gia.edu). Letters on articles published in *G&G* are also welcome. Please note that Field Reports, Lab Notes, Gem News International, Micro-World, Colored Stones Unearthed, Diamond Reflections, Charts, and In the Spotlight are not peer-reviewed sections but do undergo technical and editorial review.

Gems & Gemology is published quarterly by the Gemological Institute of America, a nonprofit educational organization for the gem and jewelry industry.

Postmaster: Return undeliverable copies of *Gems & Gemology* to GIA, The Robert Mouawad Campus, 5345 Armada Drive, Carlsbad, CA 92008.

Our Canadian goods and service registration number is 126142892RT.

Any opinions expressed in signed articles are understood to be opinions of the authors and not of the publisher.

About the Cover

This issue features a study of the 2.33 ct Winston Red diamond, now on public display at the Smithsonian National Museum of Natural History. The old mine brilliant-cut Fancy red diamond was once set in the Ceremonial Necklace of Nawanagar. We show it superimposed on the 1931 sketch of the original necklace without the red diamond, designed by Cartier London. Photo of the Winston Red by Robert Weldon; courtesy of Ronald Winston. Sketch courtesy of Archives Cartier London © Cartier.

Printing is by L+L Printers, Carlsbad, CA.

GIA World Headquarters The Robert Mouawad Campus 5345 Armada Drive Carlsbad, CA 92008 USA

Heated Corundum, the Remarkable Winston Red, and an Extraordinary Renaissance Jewel

You're in for a delectable treat with our Spring 2025 issue of *Gems & Gemology*! We cover detecting heated corundum, the rare and remarkable Winston Red diamond, and an extraordinary Renaissance jewel containing emeralds from a surprising source.

Our first paper by Dr. Wasura Soonthorntantikul and Dr. Aaron Palke presents criteria for accurate identification of three hydrogen-related peaks in the infrared spectra of certain rubies and sapphires—especially Mozambique ruby and Madagascar pink sapphire—that are diagnostic of heat treatment.

"...a characterization of one of the Smithsonian's rarest treasures: the 2.33 ct Winston Red diamond."

Next, lead author Dr. Gabriela Farfan and fellow colleagues offer a characterization of one of the Smithsonian's rarest treasures: the 2.33 ct Winston Red diamond. The group uses observation and advanced gemological testing to delve into the gem's origin of color, demonstrating that its uniquely rare, pure crimson hue is a balance of absorption related to plastic deformation and nitrogen-related defects.

In our final article, a team of researchers led by Dr. Gérard Panczer delivers a gemological investigation of a sixteenth-century pendant linked to Catherine de' Medici, Queen of France, and François Dujardin, goldsmith to King Charles IX. This new study indicates that the two principal green gems are emeralds from Pakistan, not Colombia as previously claimed, delivering striking evidence of the sophisticated trade routes between Asia and Europe at this time.

Our regular features have much to offer as well. *Lab Notes* presents interesting reports from GIA's global laboratories. *Micro-World* provides a glimpse at the inner beauty of gemstones, highlighting intriguing inclusions that catch our contributors' eyes. As this is our Spring issue, the *Gem News International* section reports on the 2025 Tucson gem shows and covers trends, noteworthy designs, and interesting finds.

Evaluate your knowledge of our 2024 feature articles in the annual *G&G* Challenge and learn which of those articles earned a Dr. Edward J. Gübelin Most Valuable Article Award.

Finally, I'd like to acknowledge Stuart Overlin and Faizah Bhatti—two wonderful colleagues—both of whom have left our journal after nearly three decades with GIA. Between them, as managing editor and creative director, respectively, they brought great flair to our words and graphics. We wish them every success and satisfaction in their future endeavors.

Duncan Pay | Editor-in-Chief | dpay@gia.edu

The 3309 cm^{-1} Series in Sapphire and Ruby: A Focus on FTIR Peak Position Variation

Wasura Soonthorntantikul and Aaron C. Palke

Heat treatment of some ruby and sapphire can be identified by detection of the 3309 cm^{-1} series in their infrared spectra. The 3309 cm^{-1} series consists of three peaks at 3309, 3232, and 3185 cm^{-1}, with two additional weak peaks at 3367 and 3295 cm^{-1}. Observation of this series in a ruby or sapphire has significantly different implications than the identification of a single peak at 3309 cm^{-1}. This series represents a specific form of hydrogen incorporation in the corundum structure that is a diagnostic indicator of heat treatment for certain types of ruby and sapphire, particularly ruby from Mozambique and pink sapphire from Madagascar. However, identification of this series can be challenging because other peaks can occur in the same region as the 3309 cm^{-1} series. This article presents criteria for accurate identification of the three main peaks in the 3309 cm^{-1} series by measuring their possible peak position ranges, allowing for separation from other possible unrelated peaks in this region. Measurements were made on heated and unheated natural and laboratory-grown blue sapphire and ruby from various origins. With increasing iron and/or chromium content, the positions of these three main peaks shifted narrowly, about 1.7 to 3.6 cm^{-1}, from minimum positions at 3308.9, 3231.2, and 3183.7 cm^{-1}. A positive linear relationship was observed between the positions of three main peaks in the 3309 cm^{-1} series and concentrations of iron for blue sapphire or the sum of iron and chromium for ruby. These relationships are useful to determine whether peaks in this region actually represent the 3309 cm^{-1} series or some other hydrogen-related species in the corundum structure. Additionally, peak widths in the 3309 cm^{-1} series also broaden with increasing iron or the sum of iron and chromium concentrations.

Fourier-transform infrared (FTIR) absorption spectroscopy is often useful for detecting heat treatment in corundum or, in some cases, for demonstrating the absence of any heat treatment process (e.g., Sripoonjan et al., 2016). The relevant infrared region is approximately 3000–3600 cm^{-1}, which is generally related to the stretching frequency of hydroxyl groups bound in the corundum (α-Al_2O_3) structure as well as hydroxyl group–related mineral inclusions in the corundum host (e.g., Moon and Phillips, 1991; Smith, 1995; Beran and Rossman, 2006).

Of particular interest for gemologists is a series of three main sharp peaks at approximately 3309, 3232, and 3185 cm^{-1} and two additional weak peaks at 3367 and 3295 cm^{-1}, together known as the 3309 cm^{-1} series. This series is related to the stretching vibrations of hydroxyl groups locally associated with titanium ions in the corundum structure (Moon and Phillips, 1991) and is commonly observed in natural blue sapphire from basalt-related deposits that are transported to the earth's surface by hot molten rock, or magma, producing natural thermal annealing. Most importantly, this series can also be introduced or removed from corundum by artificial heat treatment (Emmett et al., 2003). The presence of at least two peaks at approximately 3309 and 3232 cm^{-1} in the series has been considered diagnostic evidence of post-growth artificial heat treatment for metamorphic blue sapphire (e.g., Hughes and Perkins, 2019), ruby from some deposits (e.g., Smith, 1995; Krzemnicki, 2018; Vertriest and Saeseaw, 2019), and pink sapphire from Madagascar (e.g., Saeseaw et al., 2020). This can be especially helpful for identifying low-temperature heat

See end of article for About the Authors and Acknowledgments.
Gems & Gemology, Vol. 61, No. 1, pp. 2–15,
http://dx.doi.org/10.5741/GEMS.61.1.2

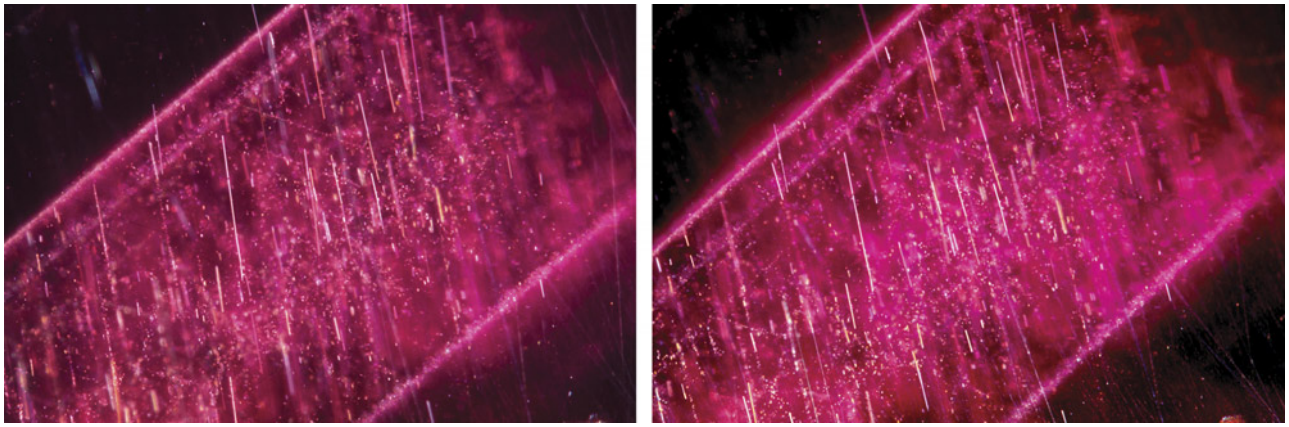

Figure 1. This Mozambique ruby contains needles and bands of particles before heating (left). The inclusions did not show any signs of alteration after heating at 900°C for 5 hours in air (right). However, the development of the 3309 cm^{-1} series in the FTIR spectrum was detected in this stone after heating, providing evidence of low-temperature heat treatment. Photomicrographs by Suwasan Wongchacree; field of view 1.75 mm.

treatment, which often does not affect inclusions and leaves no microscopic clues (figure 1).

The concentration of hydroxyl groups in natural corundum is generally 0.5 ppmw or lower (Beran and Rossman, 2006). Previous work has reported various hydroxyl group stretching absorption features in FTIR spectra of natural and laboratory-grown corundum (Müller and Günthard, 1966; Belt, 1967; Eigenmann et al., 1972; Volynets et al., 1972; Engstrom et al., 1980; Beran, 1991; Moon and Phillips, 1991, 1994; Ramírez et al., 1997, 2004; Kronenberg et al., 2000; Beran and Rossman, 2006; Smith and van der Bogert, 2006). In addition to the 3309 cm^{-1} series, other hydroxyl group–related absorption features with unknown origin have been documented in a similar region for both untreated and treated corundum, such as a peak at about 3220 cm^{-1} and the acceptor-dominated 3000 cm^{-1} series in untreated Montana sapphire (Palke et al., 2023), or several broad bands between 3050–3200 cm^{-1} in sapphire treated with both heat and pressure (Soonthorntantikul et al., 2021). Incorporation of different trace elements in the corundum structure can produce variability in the position and width of some hydroxyl group–related absorption bands. For example, Beran (1991) reported FTIR peaks for variously colored laboratory-grown sapphires, including three narrow hydroxyl group bands at 3310, 3230, and 3185 cm^{-1}, with an additional narrow band at 3290 cm^{-1} for some vanadium-, chromium-, iron-, and titanium-doped sapphires (color-change laboratory-grown sapphires) and a weak narrow band at 3280 cm^{-1} for colorless sapphire. Volynets et al. (1972) reported broad hydroxyl group–related absorption bands at approximately 3000 cm^{-1} for laboratory-grown sapphire doped with magnesium, also seen in laboratory-grown sapphire with cobalt and nickel as reported by Müller and Günthard (1966) and Eigenmann et al. (1972). Post-growth treatments of laboratory-grown materials, such as heat treatment (Moon and Phillips, 1991, 1994), hydrothermal treatment (Kronenberg et al., 2000), and electric field application with annealing (Ramírez et al., 2004), can alter the distribution of existing hydroxyl group band intensities or induce new hydroxyl group–related absorption features. Balan (2020) also performed density functional theory modeling and predicted the positions of various hydrogen-related species in the corundum structure. Additionally, in the gemological

In Brief

- The 3309 cm^{-1} series in FTIR spectra can be observed in unheated basalt-related blue sapphire, heated metamorphic blue sapphire and ruby, and laboratory-grown blue sapphire.
- Comparing the peak intensities between 3309 and 3232 cm^{-1} in natural unheated and heated blue sapphire, the more intense peak is more commonly found at 3309 cm^{-1} (3309 > 3232). In addition, the ratio of the peak intensities of the 3232 and 3185 cm^{-1} absorption coefficient is generally around 3.
- The positions of the three main peaks in the 3309 cm^{-1} series had a positive linear relationship with concentrations of iron and chromium. The widths of the peaks also slightly increase at higher iron and chromium concentrations.

laboratory, FTIR spectra are collected on a multitude of sapphires and rubies every year, and often peaks are observed that have not been described before in the literature, leaving their ultimate origin or meaning unknown.

All of this together could present a problem when determining whether a set of peaks in an FTIR spectrum of an unknown sapphire or ruby actually corresponds to the 3309 cm^{-1} series in order to identify potential heat treatment. A further complication comes from the work of Phan (2015), who reported that the 3309 cm^{-1} peak can shift position and identified a positive linear correlation between the position of the 3309 cm^{-1} peak and iron concentrations. This raises the question of when a peak in the vicinity of the 3232 cm^{-1} peak can be used as evidence of the presence of the 3309 cm^{-1} series.

This article elaborates on the correlations between positions of the peaks in the 3309 cm^{-1} series with trace element concentrations for ruby, metamorphic and basalt-related blue sapphire, and laboratory-grown sapphire. The aim of the work is to clarify when an FTIR feature can be considered evidence of the presence of the 3309 cm^{-1} series.

MATERIALS AND METHODS

Samples. A total of 659 samples of various types of blue sapphire and ruby were studied to cover a wide range of iron and chromium concentrations. This study set consisted of 395 untreated blue sapphires from basalt-related deposits, 52 untreated metamorphic blue sapphires, 63 laboratory-grown blue sapphires, 75 unheated rubies, and 74 heated rubies. The untreated blue sapphires from basalt-related and metamorphic deposits were selected from GIA's colored stone reference collection: 103 from Australia, 59 from Cambodia, 11 from Cameroon, 68 from Ethiopia, 74 from Nigeria, 29 from Thailand, and 51 from Vietnam for basalt-related deposits; and 9 from Myanmar (Burma), 21 from Madagascar, 12 from Sri Lanka, and 10 from Tanzania for metamorphic deposits. The rough samples were fabricated into wafers with a set of parallel polished surfaces that were either oriented (122 samples) or unoriented (325 samples) relative to the *c*-axis. The data for the laboratory-grown blue sapphires and unheated and heated rubies were extracted from the GIA database that analyzed these corundum samples from client submissions in faceted form. In the study, all selected samples showed at least one peak at 3309 cm^{-1} by itself or a set of peaks at 3309, 3232, and/or 3185 cm^{-1}.

Fourier-Transform Infrared (FTIR) Absorption Spectroscopy. Unpolarized FTIR spectra were taken on all samples at room temperature using a Thermo Nicolet 6700 or iS50 FTIR spectrometer equipped with an XT-KBr beamsplitter and a cryogenic MCT detector operating with a 4× beam condenser accessory. Resolution was set at 2 or 4 cm^{-1}. Polarized spectra were recorded with an iS50 FTIR spectrometer, which included a motorized zinc selenide wire grid polarizer accessory. The intensities, positions, and widths of the absorption peaks were determined by fitting the spectra with Thermo Scientific's GRAMS/AI spectroscopy software using a multipoint linear baseline correction together with the combined Gaussian (*G*)-Lorentzian (*L*) function [expressed as $(1–M)^* G + M^*L$, where *M* is mixture (%Lorentzian)]. In terms of peak intensity, the spectra were converted to absorption coefficient (α, cm^{-1}) using $\alpha = 2.303A/d$, where *A* is absorbance and *d* is path length in centimeters.

Laser Ablation–Inductively Coupled Plasma–Mass Spectrometry (LA-ICP-MS). Trace element chemistry was determined for all samples by LA-ICP-MS with a Thermo Fisher Scientific iCAP Q ICP-MS coupled with a Q-switched Nd:YAG laser ablation device operating at a wavelength of 213 nm. The laser conditions were set up with 55 μm diameter laser spots with fluence of approximately 10 J/cm^2 and a repetition rate of either 10 or 20 Hz. The dwell time was 40 seconds for each spot; the forward power was set at 1350 W, and the typical nebulizer gas flow was approximately 0.80 L/min. A special set of corundum reference standards was used for quantitative analysis of beryllium, magnesium, titanium, vanadium, chromium, iron, and gallium (Stone-Sundberg et al., 2017). NIST Standard Reference Materials 610 and 612 glasses were used for quantitative analysis of other elements. All elemental measurements were normalized on ^{27}Al as an internal elemental standard set at 529,250 ppmw with the following isotopes measured: ^{9}Be, ^{24}Mg, ^{47}Ti, ^{51}V, ^{53}Cr, ^{57}Fe, and ^{69}Ga. Detection limits of measurable trace elements in corundum were 0.03–0.9 ppma magnesium, 0.3–1.5 ppma titanium, 0.01–0.2 ppma vanadium, 0.1–1.2 ppma chromium, 1–12 ppma iron, and 0.01–0.09 ppma gallium.

RESULTS AND DISCUSSION

Relative Intensity of Peaks at 3309, 3232, and 3185 cm^{-1}. Focusing on the three main peaks at 3309, 3232,

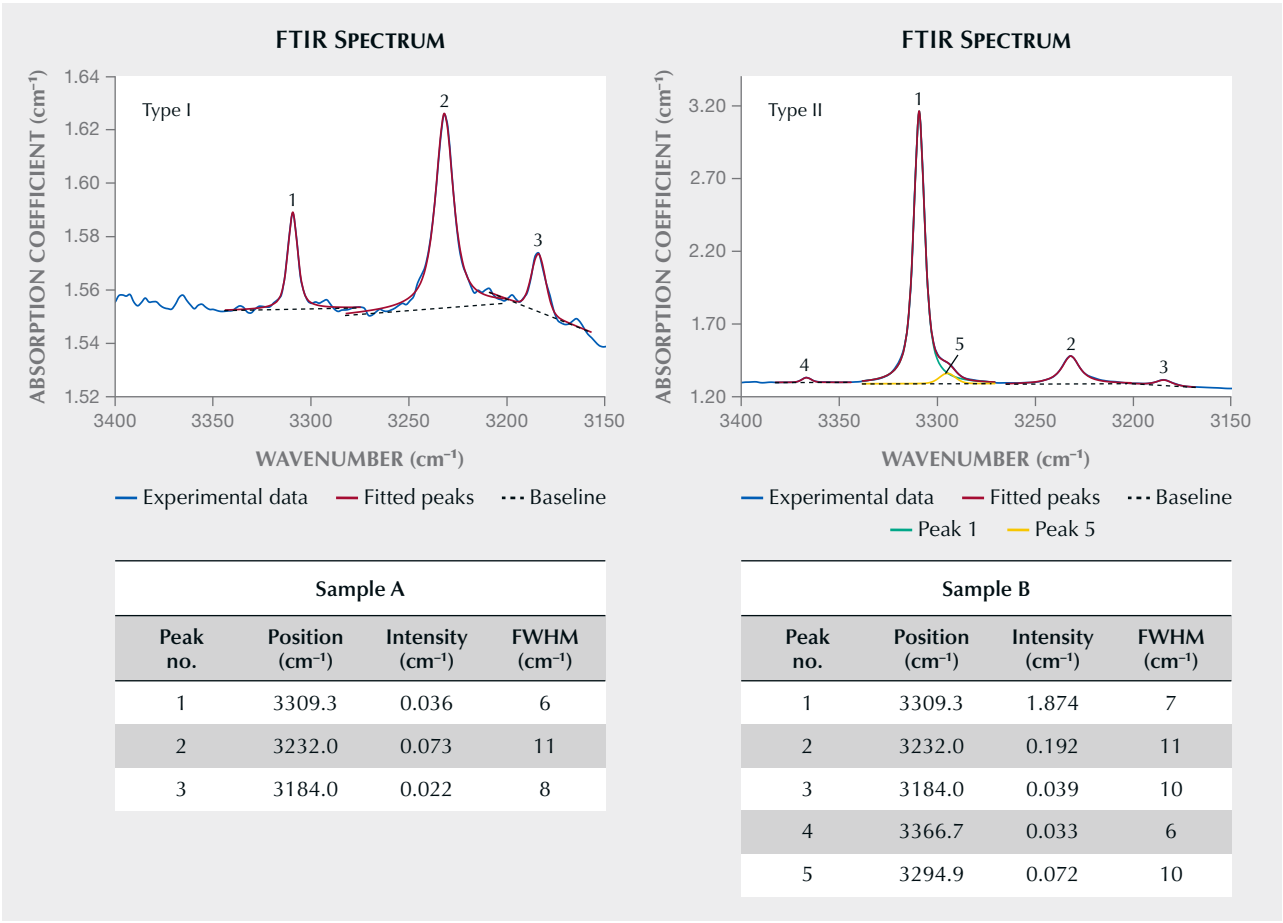

Sample A			
Peak no.	Position (cm^{-1})	Intensity (cm^{-1})	FWHM (cm^{-1})
1	3309.3	0.036	6
2	3232.0	0.073	11
3	3184.0	0.022	8

Sample B			
Peak no.	Position (cm^{-1})	Intensity (cm^{-1})	FWHM (cm^{-1})
1	3309.3	1.874	7
2	3232.0	0.192	11
3	3184.0	0.039	10
4	3366.7	0.033	6
5	3294.9	0.072	10

Figure 2. Examples of unpolarized FTIR spectra of the studied samples showing the 3309 cm^{-1} series for type I (left) and type II (right) according to Beran (1991). Sample A: Nigerian blue sapphire, wafer plane perpendicular to the c*-axis, thickness 1.114 mm. Sample B: Cambodian blue sapphire, wafer plane parallel to the* c*-axis, thickness 1.036 mm. The peak fitting of the 3309 cm^{-1} series is also illustrated using a multipoint linear baseline correction together with the combination of Gaussian and Lorentzian functions to fit peaks for measuring the positions, intensities, and full width at half maximum (FWHM). In the type II spectrum, a deconvolution of peak 5 that appears as a shoulder of peak 1 was also performed.*

and 3185 cm^{-1} (excluding the peaks at 3367 and 3295 cm^{-1}), the majority of untreated basalt-related blue sapphires in this study (~85%) revealed this set of three main peaks at 3309, 3232, and/or 3185 cm^{-1}, and the remaining samples showed only a single peak at 3309 cm^{-1}. The crystalline defect producing the 3309 cm^{-1} peak is attributed to hydroxyl groups associated with an aluminum vacancy and two tetravalent titanium ions (Ti^{4+}), whereas the defect producing the 3232 and 3185 cm^{-1} peaks is related to hydroxyl groups with an aluminum vacancy and a single Ti^{4+} in different configurations (Moon and Phillips, 1991, 1994). The peaks in the 3309 cm^{-1} series are strongly polarized, with maximum absorption intensity when the electric field of incoming light is perpendicular to the *c*-axis (Beran, 1991; Moon and Phillips, 1991; Phan, 2015). According to Beran (1991), there are two types of patterns for the 3309 cm^{-1} series based on the relative intensity (I) of the peaks at 3309 and 3232 cm^{-1}. Type I corundum has stronger absorption at 3232 cm^{-1}, while type II has stronger absorption at 3309 cm^{-1}. While Beran (1991) developed these types based on laboratory-grown sapphire, both types of the 3309 cm^{-1} series can also be found in natural corundum (Phan, 2015). The distribution of hydroxyl group peak intensities at 3309, 3232, and 3185 cm^{-1} depends on the final equilibrium temperature and thermal history of the sapphires (Moon and Phillips, 1991, 1994; Ramírez et al., 2004).

In this study, FTIR spectra of basalt-related blue sapphire samples displayed both type I and type II spectra (figure 2). Although the intensities of the three

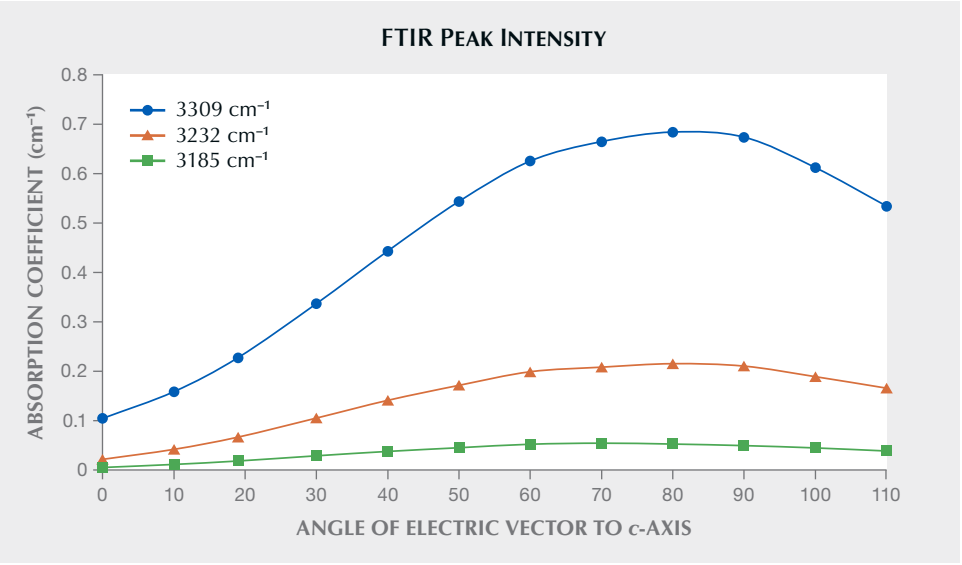

Figure 3. Absorption coefficients (cm⁻¹) at various electric vector angles relative to the c-axis for 3309, 3232, and 3185 cm⁻¹ peaks in the 3309 cm⁻¹ series. Sample: Nigerian blue sapphire, wafer plane parallel to the c-axis, thickness 3.388 mm.

main peaks varied with angles between the electric vector and the *c*-axis, the change in their peak intensities follows the same trends and their relative intensities remain the same, as shown in figure 3 and references therein. Unpolarized FTIR spectra of the studied samples can be used for further discussion on spectrum type/relative peak intensities for the 3309 cm⁻¹ series. In unheated basalt-related blue sapphire, type II (spectra with the intensity of the 3309 cm⁻¹ peak greater than the 3232 cm⁻¹ peak; 3309 > 3232) is more commonly found (>80%), whereas type I (spectra with intensity of the 3309 cm⁻¹ peak smaller than the 3232 cm⁻¹ peak; 3309 < 3232) and intermediate type (comparable intensities between 3309 and 3232) can be occasionally observed in material from Cambodia, Ethiopia, Nigeria, and Vietnam (figure 4). For other corundum types in the study, all of the laboratory-grown blue sapphires and a majority of the heated rubies (>90%) exhibit type II spectra for the 3309 cm⁻¹ series, whereas the remaining samples of heat-treated rubies show the 3309 cm⁻¹ series with intermediate type. The unheated natural metamorphic blue sapphires and unheated natural rubies show only a single peak at 3309 cm⁻¹.

With heat treatment, the intensity of the 3309 cm⁻¹ peak changes in the opposite direction to that of the 3232 and 3185 cm⁻¹ peaks (e.g., Moon and Phillips, 1991; Soonthorntantikul et al., 2019; Vertriest and

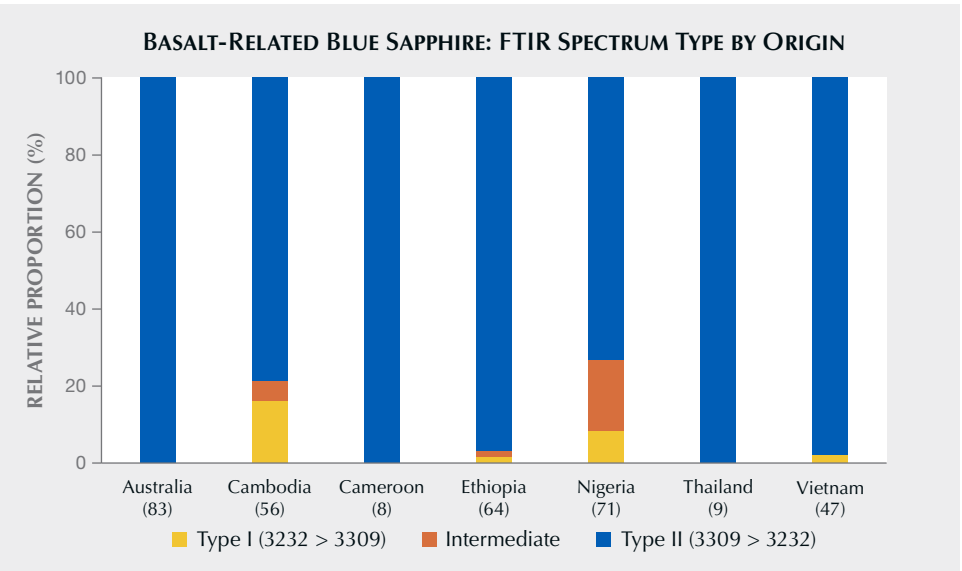

Figure 4. The distribution of the unpolarized FTIR spectra of the 3309 cm⁻¹ series observed in unheated blue sapphires from various basalt-related deposits in this study. The numbers in parentheses represent the number of samples from each deposit.

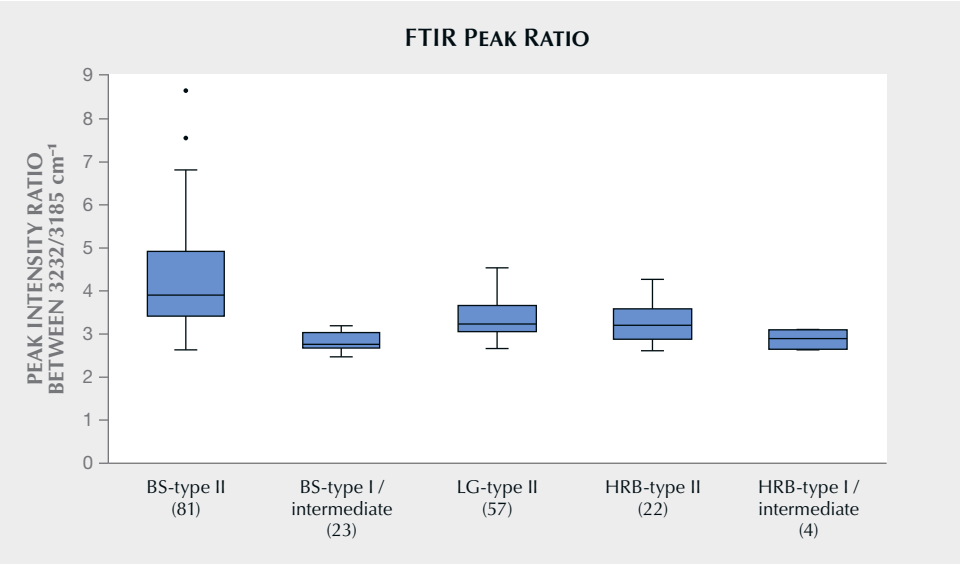

Figure 5. The distribution of peak intensity ratio between 3232 and 3185 cm^{-1} in different sample groups (extracted from unpolarized FTIR spectra): basalt-related blue sapphire (BS) with type II spectra, basalt-related blue sapphire with type I and intermediate spectra, laboratory-grown blue sapphire (LG) with type II spectra, heated ruby (HRB) with type II spectra, and heated ruby with type I and intermediate spectra. The numbers in parentheses represent the number of samples.

Saeseaw, 2019; Saeseaw et al., 2020). Usually the 3309 cm^{-1} peak decreases in intensity while the 3232 and 3185 cm^{-1} peaks increase, although some rare exceptions have been noted. Heating temperatures and cooling rates can alter the relative intensity of the 3309 and 3232 cm^{-1} peaks and may change the spectrum type (type I, type II, or intermediate) (e.g., Moon and Phillips, 1991; Kronenberg et al., 2000; Ramírez et al., 2004). In all corundum, the 3232 cm^{-1} peak is more intense than the 3185 cm^{-1} peak ($I_{3232} > I_{3185}$) (figure 5). Basalt-related blue sapphire with type I or intermediate spectra, laboratory-grown blue sapphire, and heated ruby all show a peak intensity ratio of approximately 3 for I_{3232}/I_{3185}, in agreement with laboratory-grown sapphire at thermal equilibrium from both Beran (1991) and Moon and Phillips (1991). The 3:1 intensity ratio for the 3232 and 3185 cm^{-1} bands comes from the structural arrangement of defect clusters with three available titanium sites for the defect species related to the 3232 cm^{-1} band and one site for the 3185 cm^{-1} band (Moon and Phillips, 1991). A slight deviation from the ratio of 3 is due to measurement errors for the weak 3185 cm^{-1} band. Basalt-related blue sapphire with type II spectra shows a great variability of the ratio I_{3232}/I_{3185}, ranging between 3 and 9. This may be caused by complexities in the defect structure and growth conditions for hydrogen incorporation in natural samples, in addition to inaccuracy in measuring the weak 3185 cm^{-1} band.

Relationship Between Peak Width and Position for the 3309, 3232, and 3185 cm^{-1} Bands and Trace Element Concentrations. IR peak positions and peak width of structural hydroxyl groups in corundum can be affected by the incorporation of different trace elements in the corundum lattice (e.g., Eigenmann et al., 1972; Volynets et al., 1972; Moon and Phillips, 1994; Phan, 2015). FTIR data collected with 4 cm^{-1} resolution were used here for peak width consideration. The main triplet of peaks at 3309, 3232, and 3185 cm^{-1} in the series are sharp peaks with full width at half maximum (FWHM) of less than 18 cm^{-1} for basalt-related blue sapphire, 11 cm^{-1} for laboratory-grown blue sapphire, and 19 cm^{-1} for unheated and heated ruby (figure 6). The narrow width of these hydroxyl group stretching bands is associated with intramolecular hydroxyl group bonds (Moon and Phillips, 1991). As seen in figure 6, the FWHM of the 3309 cm^{-1} peak is the narrowest among the three, and the width of the 3232 cm^{-1} peak is slightly larger than that of the 3185 cm^{-1} peak at similar iron concentrations. Laboratory-grown blue sapphires, which generally have much lower iron concentrations (<280 ppma), showed smaller widths of hydroxyl group peaks compared to those of natural blue sapphires from basalt-related deposits with relatively high iron (>750 ppma). As seen in figure 6, all the peaks in the 3309 cm^{-1} series for blue sapphires became wider with increasing iron concentrations (figure 6A) but show no relation to chromium due to their low chromium concentrations (figure 6C). On the other hand, rubies contain significant concentrations of not only chromium but also iron, and a broadening of peak widths in the series can be noticeably influenced by both chromium (figure 6D) and iron (figure 6B). Therefore, the trend of peak widths in the 3309 cm^{-1} series for individual rubies could be estimated from the plot based on total concentrations of iron and chromium (figure 6F).

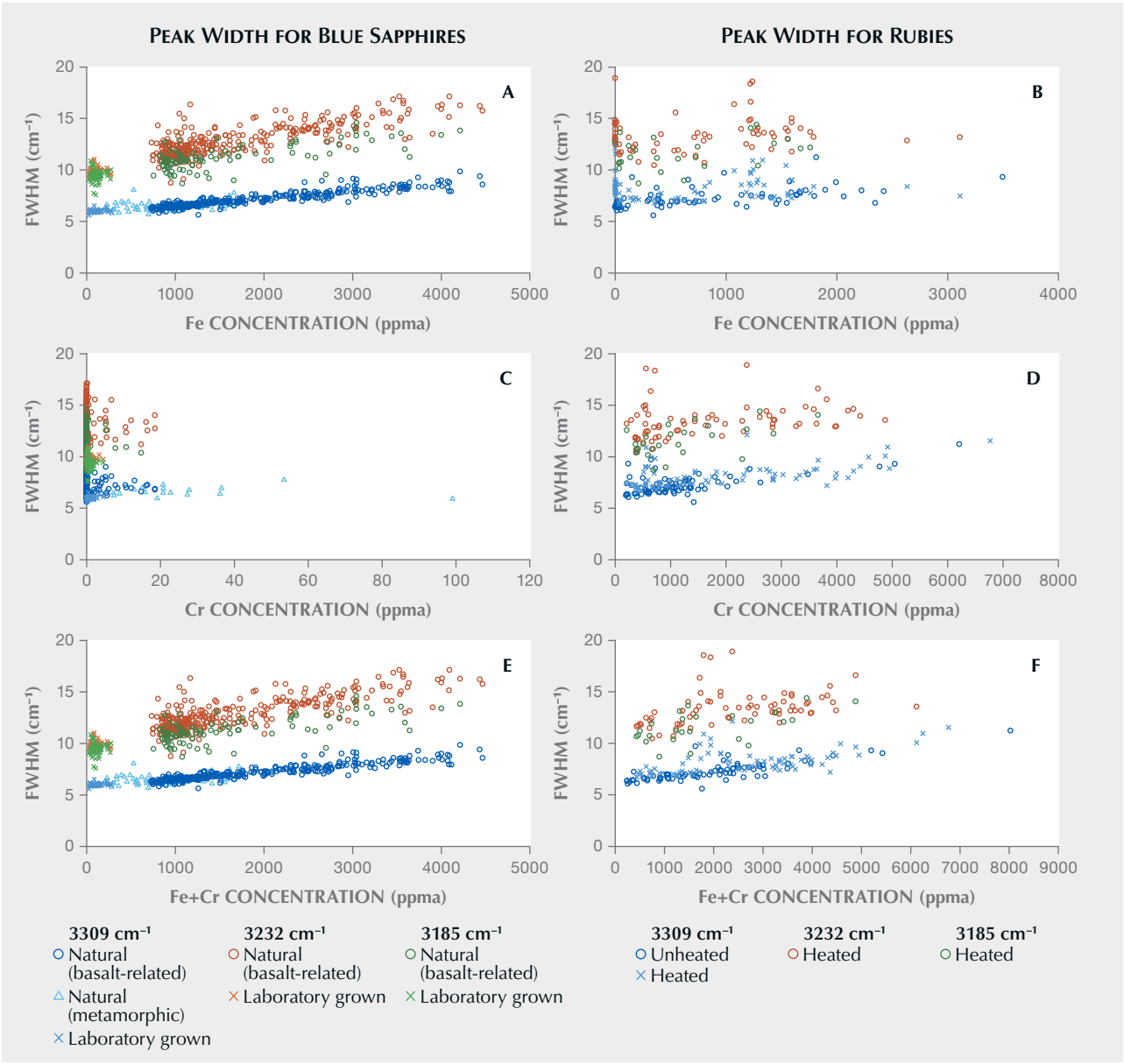

Figure 6. The correlation of FWHM of the peaks at 3309, 3232, and 3185 cm^{-1} with concentrations of iron (A and B), chromium (C and D), and the sum of iron and chromium (E and F) for blue sapphires (from metamorphic and basalt-related deposits as well as laboratory-grown material) and rubies. Resolution is 4 cm^{-1} for all data presented here. See supplementary tables S1 and S2 at https://www.gia.edu/gems-gemology/spring-2025-ftir-3309-series-corundum.

According to Phan (2015), variously colored natural sapphires from different localities revealed a peak at 3309 cm^{-1} or a group of peaks including 3309 cm^{-1}, and a positive linear relationship was observed between peak position at 3310 cm^{-1} (ranging from 3309 cm^{-1} to 3311 cm^{-1}) and iron concentration (0.4 to 1.78 wt.% Fe_2O_3, or at approximately 1000 to 4500 ppma iron) in those sapphires. In this study, the samples were expanded to broader iron concentrations, ranging from 204 to 4465 ppma in natural sapphires and 22 to 275 ppma in laboratory-grown blue sapphires. Although IR peak intensities of the 3309 cm^{-1} series change with polarization (Beran, 1991; Moon and Phillips, 1991), peak positions do not shift with polarization (standard deviation of ±0.01, ±0.1, and ±0.1 cm^{-1} for 3309, 3232, and 3185 cm^{-1}, respectively, at various polarization angles).

Figure 7 shows the correlation between the measured positions of the peaks in the 3309 cm^{-1} series (3309, 3232, and 3185 cm^{-1}) and iron concentrations

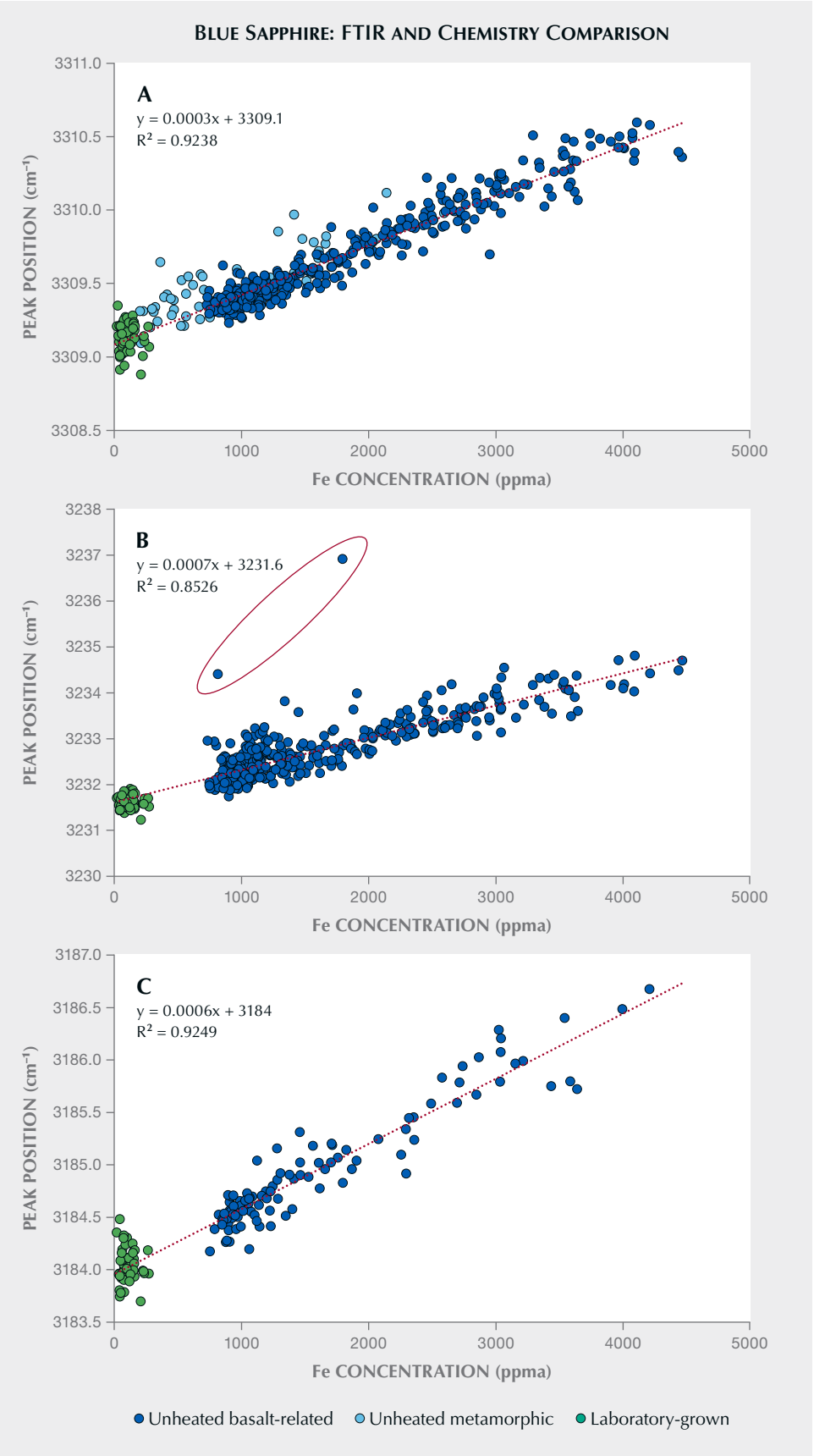

Figure 7. The linear relationship (red dotted lines) between FTIR peak positions at 3309 (A), 3232 (B), and 3185 cm^{-1} (C) in the 3309 cm^{-1} series and iron concentrations for blue sapphires. In plot B, two outliers are contained in the red oval. See supplementary table S3 at https://www.gia.edu/gems-gemology/spring-2025-ftir-3309-series-corundum.

in the natural and laboratory-grown blue sapphires. Laboratory-grown blue sapphire typically contains relatively low iron concentrations, as reflected in the study samples where iron was <280 ppma, and the measured peak position at 3309 cm^{-1} of this group ranged between 3308.9 and 3309.3 cm^{-1}. There is no observable correlation between the peak position of the 3309 cm^{-1} peak and iron concentration for laboratory-grown sapphires. This is due to the small range of iron concentration for these stones. For natural blue sapphires from metamorphic and basalt-related deposits in the study, the 3309 cm^{-1} peak was observed between 3309.1 and 3310.6 cm^{-1} for the samples with iron concentrations ranging from 204 to 4465 ppma. Although only the laboratory-grown sapphire data did not show any clear trend, the results acquired from natural and laboratory-grown sapphire groups align with each other. They showed a linear correlation of peak position at 3309 cm^{-1} over a wide range of iron concentrations (figure 7A and table 1), which is consistent with Phan (2015).

In addition to the 3309 cm^{-1} peak, the other two peaks at 3232 and 3185 cm^{-1} showed similar correlation of peak positions over a wide range of iron concentrations for natural and laboratory-grown blue sapphires (figures 7B and 7C and table 1). The peak at 3232 cm^{-1} varied from 3231.2 to 3234.8 cm^{-1} (excluding two outliers in the plots at 3234.4 and 3236.9 cm^{-1}), while the peak at 3185 cm^{-1} ranged between 3183.7 and 3186.7 cm^{-1}.

FTIR spectra of two outlier samples in the 3232 cm^{-1} plot are shown in figure 8. In both cases, a cursory

TABLE 1. Parameters of linear regression function of individual hydroxyl group stretching peaks for sapphire and ruby data in figures 7 and 9, respectively.

	3309 cm^{-1}	3232 cm^{-1}[a]	3185 cm^{-1}
	Blue sapphire		
Samples	510	397	161
R^2	0.92	0.85	0.92
Standard error	0.10	0.29	0.18
Intercept	3309.1	3231.6	3184.0
Slope	3.4×10^{-4}	7.0×10^{-4}	6.2×10^{-4}
Observed peak frequencies	3308.9–3310.6	3231.2–3234.8	3183.7–3186.7
Iron concentration (in ppma)	22–4465	22–4465	22–4465
	Ruby		
Samples	149	70	25
R^2	0.84	0.75	0.84
Standard error	0.17	0.32	0.25
Intercept	3309.1	3231.9	3184.4
Slope	2.8×10^{-4}	4.3×10^{-4}	4.5×10^{-4}
Observed peak frequencies	3308.9–3311.5	3231.8–3234.4	3184.4–3186.7
Sum of iron and chromium concentrations (in ppma)	240–8025	240–8025	240–8025

[a]*Two outliers in figure 7 are omitted.*

inspection of the spectra might lead one to use the peaks at 3234.4 or 3236.9 cm^{-1} as evidence of the 3309 cm^{-1} series and therefore an indicator of heat treatment. However, the significant deviations of their positions should give cause for caution in this interpretation. In fact, in one sample, the peak is far outside the observed range for the 3232 cm^{-1} peak of 3231.2 to 3234.8 cm^{-1}. For the other sample, the peak is in the known range for the 3232 cm^{-1} peak, but this peak position would only be observed at much higher iron concentrations than measured in this sample. (The standard deviation of 12 data points in this sample is less than 9% for iron concentration with measurements on both sides of the sample.) Both samples have similar FTIR patterns (figure 8): a doublet of peaks at 3379 and 3394 cm^{-1} and a peak at 3309.7 cm^{-1} for sample A and at 3309.3 cm^{-1} for sample B. Of importance, with iron concentrations of 1795 ppma for sample A and 815 ppma for sample B, the positions of the peaks at 3309 cm^{-1} align with the linear correlation shown in figure 7A. Finally, there is no observable peak at 3185 cm^{-1}. These observations indicate that the 3236.9 cm^{-1} or 3234.4 cm^{-1} peaks in both samples are not related to the 3309 cm^{-1} series, especially considering that the 3236.9 cm^{-1} peak is outside the possible range of 3231.2–3234.8 cm^{-1} seen in figure 7B. Similar spectra have been seen in other stones submitted to the GIA laboratory, with a doublet at 3379/3394 cm^{-1} as well as a smaller peak around 3235 cm^{-1}. It is possible that the peaks at 3234.4 and 3236.9 cm^{-1} in these samples are part of another unidentified series together with the 3379/3394 cm^{-1} doublet. Importantly, there is no evidence of a 3309 cm^{-1} series in the FTIR spectra in figure 8.

Unlike for iron, in blue sapphire there is no correlation between peak positions for the 3309 cm^{-1} series and other measurable trace elements, including titanium, vanadium, chromium, and gallium. This may be because these other trace elements are present at relatively low concentrations in blue sapphire. FTIR spectra of the basalt-related blue sapphires in this study also show other narrow peaks together with the 3309 cm^{-1} series peaks, such as doublet peaks at approximately 3379 and 3394 cm^{-1} (16% of the studied samples), a weak 3265 cm^{-1} peak (5%), a weak 3210 cm^{-1} peak (5%), a weak 3278 cm^{-1} peak (2%), and a weak 3165 cm^{-1} peak (less than 1%). Among these additional peaks, it is notable that the weak

Figure 8. FTIR spectra of two blue sapphires with the peak at approximately 3232 cm^{-1} falling significantly outside a linear trend between peak frequency and iron concentrations in figure 7B. It is possible that the peaks at 3237 and 3234 cm^{-1} in both spectra are not related bands in the 3309 cm^{-1} series. The peaks at 3379 and 3394 cm^{-1} with unknown defect origins are also present in both spectra. Sample A: Nigerian blue sapphire, unoriented, thickness 2.89 mm (left). Sample B: Cameroon blue sapphire, wafer plane parallel to the c*-axis, thickness 3.923 mm (right).*

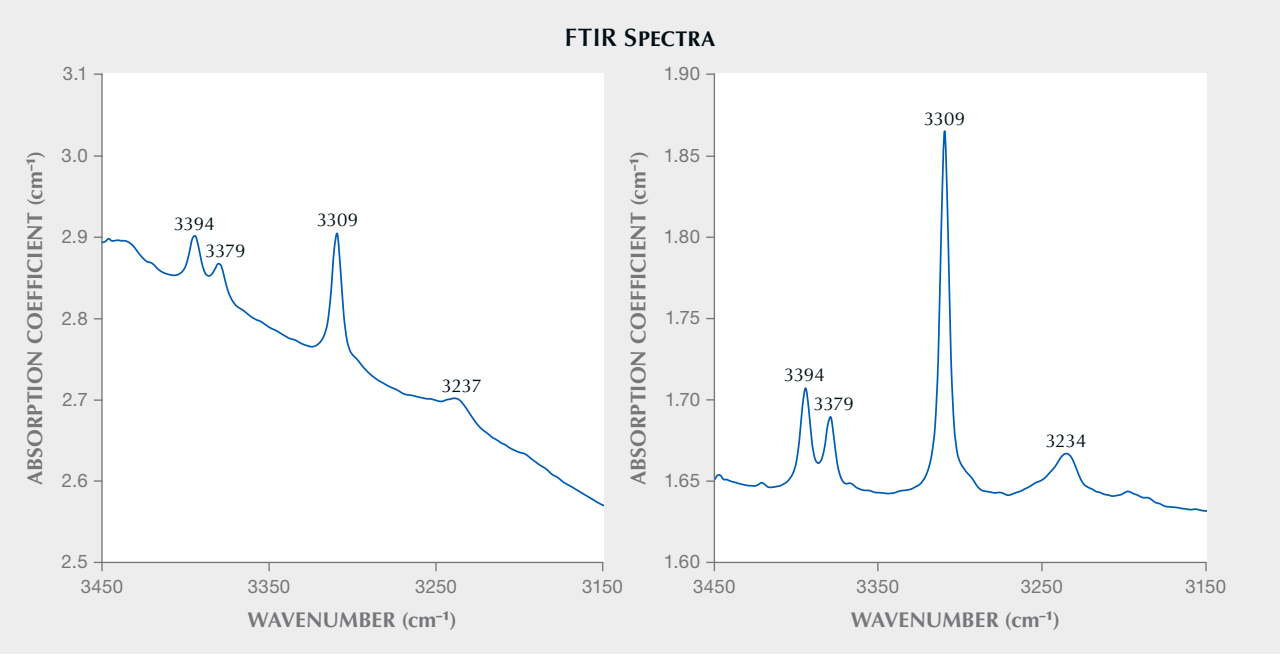

3210 cm^{-1} peak is usually found in type I and type II spectra with relatively strong 3232 cm^{-1} peak intensity (>25% of the 3309 cm^{-1} intensity).

Blue sapphires typically contain low chromium concentrations, and the peak position shift within the 3309 cm^{-1} series correlates solely with iron concentrations. In rubies, chromium is present at relatively high concentrations in addition to iron, which can vary from very low to high concentrations. Therefore, it is likely that both iron and chromium can have an impact on a peak position variation for the 3309 cm^{-1} series in rubies when they are present at significant concentrations.

FTIR spectra and trace element chemistry of the natural rubies were measured to determine the relationship between peak positions in the 3309 cm^{-1} series and concentrations of iron and chromium. The studied ruby samples, either untreated or heated, contain a wide range of iron and chromium concentrations: 195–6765 ppma chromium, 0–3497 ppma iron, and 240–8025 ppma for the sum of chromium and iron. The shift of peak position toward higher wavenumbers was observed at higher chromium or iron concentrations with a certain degree of linear correlation, for example, R^2 of 0.56 and 0.16 for the plots of the 3309 cm^{-1} peak against concentrations of chromium and iron, respectively. Unlike blue sapphires, unheated and heated rubies showed a linear correlation between the positions of the peaks in the 3309 cm^{-1} series and the sum of chromium and iron concentrations, with $R^2 > 0.75$ for three peaks in the series (figure 9, opposite page and table 1). The relationship between peak positions at approximately 3309, 3232, or 3185 cm^{-1} and the sum of chromium and iron concentrations in natural rubies (figure 9 and table 1) follow the same trend as those in blue sapphires at various iron concentrations (figure 7 and table 1). The data plotted in figures 6, 7, and 9 are available in the supplementary data sheet at https://www.gia.edu/gems-gemology/spring-2025-ftir-3309-series-corundum.

As demonstrated above, high concentrations of either iron or chromium can produce a small shift of peak positions at 3309, 3232, and 3185 cm^{-1} toward higher wavenumbers and also a slight broadening of the widths of these peaks. This may be caused by the larger ionic radius of Fe^{3+} and Cr^{3+} than Al^{3+} [0.645 Å for Fe^{3+}, 0.615 Å for Cr^{3+}, and 0.535 Å for Al^{3+} in an octahedral site (Shannon, 1976)]. In comparison with Al-O bond lengths [1.86 and 1.97 Å in α-Al_2O_3 (Wyckoff, 1963)], longer bond distances for Fe-O [1.90 and 2.05 Å in α-Al_2O_3: Fe^{3+} (Gaudry et al., 2003)] and Cr-O [1.92 and 2.01 Å in α-Al_2O_3: Cr^{3+} (Gaudry et al., 2003)] result in weaker cation-oxygen interactions from surrounding environments of hydroxyl groups, and therefore, intramolecular OH stretching strengthens and shifts toward higher frequencies.

Identification of the 3309 cm^{-1} Series for the Stones with Unknown Treatment. Several important conclusions can be made regarding the identification of the 3309 cm^{-1} series when looking for evidence of heat treatment in ruby and sapphire:

- The peaks in the 3309 cm^{-1} series do shift position but over a relatively narrow range.
- Peaks identified near the 3309, 3232, and 3185 cm^{-1} peaks but outside the ranges prescribed here cannot be considered evidence of the 3309 cm^{-1} series, and thus those peaks should not be used as evidence of heat treatment.
- The 3185 cm^{-1} peak is observed only when there is also a 3232 cm^{-1} peak that is at least three times more intense than the 3185 cm^{-1} peak. A peak in the vicinity of the 3185 cm^{-1} peak without a 3232 cm^{-1} peak is not part of the 3309 cm^{-1} series and should not be used as evidence of heat treatment.
- If trace element measurements are available, they can be used along with the relationships outlined here to determine if certain peaks may be part of the 3309 cm^{-1} series.

Figure 10 provides an excellent example of these concepts, showing the FTIR spectrum of a ruby sub-

Figure 10. FTIR spectrum of a ruby submitted to the GIA laboratory. The presence of a peak at 3180 cm^{-1} was not considered evidence of heat treatment in this case because it is outside the range of possible positions for the 3185 cm^{-1} peak. The absence of a 3232 cm^{-1} peak also rules out the presence of the 3309 cm^{-1} series.

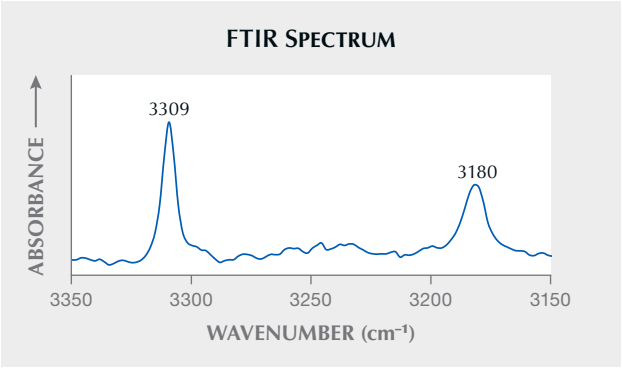

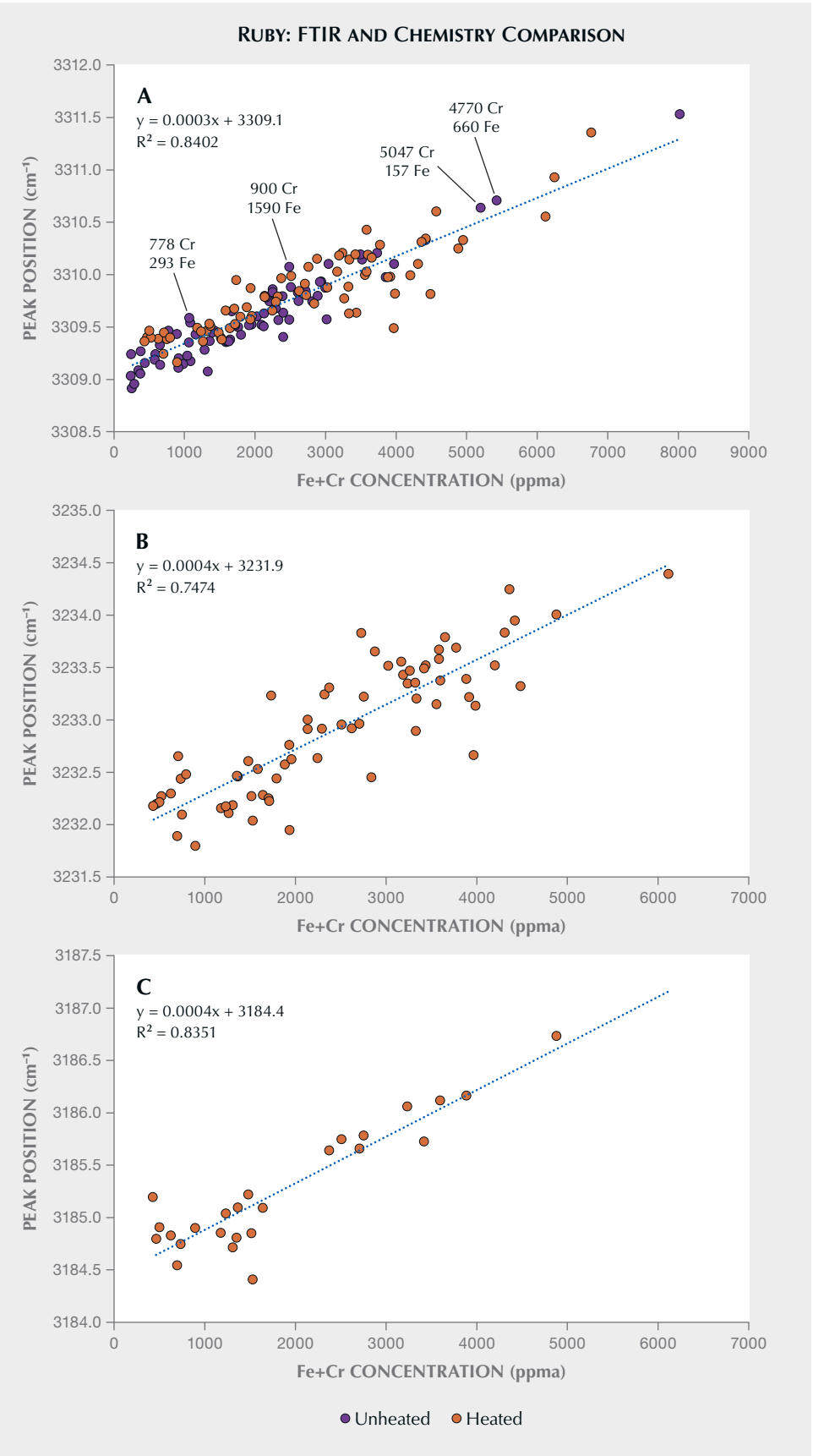

Figure 9. The linear relationship (blue dotted lines) of FTIR peak positions at 3309 (A), 3232 (B), and 3185 cm^{-1} (C) and the sum of iron and chromium concentrations for rubies. In plot A, some points are noted to show that in some cases the chromium and iron concentrations separately are not linearly correlated with the 3309 cm^{-1} peak position. The combination of iron and chromium can affect the peak frequency shift in rubies. See supplementary table S4 at https://www.gia.edu/gems-gemology/spring-2025-ftir-3309-series-corundum.

mitted to the GIA laboratory for an identification report. This spectrum shows a 3309 cm^{-1} peak as well as a peak at 3180 cm^{-1}. The second is near where one may expect to see a 3185 cm^{-1} peak, but it is out of range for that peak, especially considering that this feature only shifts up in position and would never shift down. Additionally, the absence of a peak at 3232 cm^{-1} demonstrates that this peak at 3180 cm^{-1} cannot be used as evidence of heat treatment.

CONCLUSIONS

The 3309 cm^{-1} series in FTIR, consisting of three main peaks at approximately 3309, 3232, and 3185 cm^{-1}, is associated with hydroxyl group stretching in titanium-bearing corundum. FTIR spectral parameters including relative intensity, peak width, and peak position were studied for different types of blue sapphire and ruby with a wide variety of trace element chemical compositions (figure 11). Considering the relative peak intensities of the 3309 cm^{-1} series within the FTIR spectra of untreated natural blue sapphires, we found that the strongest peak is more commonly found at 3309 cm^{-1} than at 3232 cm^{-1}. All of the samples in this study exhibited a 3232 cm^{-1} peak of greater intensity than the peak at 3185 cm^{-1}. The ratio of the peak intensities of the 3232 and 3185 cm^{-1} absorption coefficients in basalt-related blue sapphires with type I and intermediate spectra, laboratory-grown blue sapphires, and heated rubies was determined to be approximately 3, whereas basalt-related blue sapphires with type II spectra had a broader range of ratio values (3 to 9). The peak widths of the three main peaks in the 3309 cm^{-1} series broadened with increasing concentrations of iron in blue sapphires and total chromium plus iron in rubies. A slight variation of peak positions at approximately 3309, 3232, and 3185 cm^{-1} was observed at different concentrations of major trace elements in sapphire and ruby. These peaks shifted linearly toward higher wavenumbers from the minimum positions at 3308.9, 3231.2, and 3183.7 cm^{-1} with increasing iron concentrations for blue sapphires, and increasing sum of chromium and iron concentrations for rubies. A correlation between triplet peaks in the 3309 cm^{-1} series and iron (in blue sapphires) or the sum of iron and chromium (in rubies) can be useful to determine whether the 3309 cm^{-1} series is present in an FTIR spectrum.

Figure 11. Various types of corundum (ranging from 1.16 to 33.16 ct) that can present the 3309 cm^{-1} series in FTIR spectra: unheated basalt-related blue sapphire (two stones in the bottom row), heated metamorphic blue sapphire (two stones in the top row), and pink sapphire and ruby. Photos by Robert Weldon, Orasa Weldon, Vincent Pardieu, Emily Lane, and Tino Hammid; stones courtesy of B&B Fine Gems, Kenneth Kin Ming Siu, and Joao Jose Ip Lau Tchun.

ABOUT THE AUTHORS
Dr. Wasura Soonthorntantikul is a research scientist at GIA in Bangkok. Dr. Aaron Palke is senior manager of research at GIA in Carlsbad, California.

ACKNOWLEDGMENTS
The authors thank many GIA colleagues for their valuable assistance with sample preparation and FTIR and LA-ICP-MS data collection, as well as Sudarat Saeseaw and Wim Vertriest for providing helpful comments and suggestions on an early version of the manuscript. We also thank the peer reviewers for their constructive feedback.

REFERENCES

Balan E. (2020) Theoretical infrared spectra of OH defects in corundum (α-Al_2O_3). *European Journal of Mineralogy*, Vol. 32, No. 5, pp. 457–467, http://dx.doi.org/10.5194/ejm-32-457-2020

Belt R.F. (1967) Hydrothermal ruby: Infrared spectra and X-ray topography. *Journal of Applied Physics*, Vol. 38, No. 6, pp. 2688–2689, http://dx.doi.org/10.1063/1.1709972

Beran A. (1991) Trace hydrogen in Verneuil-grown corundum and its colour varieties—an IR spectroscopic study. *European Journal of Mineralogy*, Vol. 3, No. 6, pp. 971–976.

Beran A., Rossman G.R. (2006) OH in naturally occurring corundum. *European Journal of Mineralogy*, Vol. 18, No. 4, pp. 441–447, http://dx.doi.org/10.1127/0935-1221/2006/0018-0441

Eigenmann K., Kurtz K., Günthard Hs. H. (1972) Solid state reactions and defects in doped Verneuil sapphire. III. Systems α-Al_2O_3: Fe, α-Al_2O_3: Ti and α-Al_2O_3: (Fe, Ti). *Helvetica Physica Acta*, Vol. 45, pp. 452–480.

Emmett J.L., Scarratt K., McClure S.F., Moses T., Douthit T.R., Hughes R., Novak S., Shigley J.E., Wang W., Bordelon O., Kane R.E. (2003) Beryllium diffusion of ruby and sapphire. *G&G*, Vol. 39, No. 2, pp. 84–135.

Engstrom H., Bates J.B., Wang J.C., Abraham M.M. (1980) Infrared spectra of hydrogen isotopes in α-Al_2O_3. *Physical Review B*, Vol. 21, No. 4, pp. 1520–1526, http://dx.doi.org/10.1103/PhysRevB.21.1520

Gaudry E., Kiratisin A., Sainctavit P., Brouder C., Mauri F., Ramos A., Rogalev A., Goulon J. (2003) Structural and electronic relaxations around substitutional Cr^{3+} and Fe^{3+} ions in corundum. *Physical Review B*, Vol. 67, pp. 094108-1–094108-10, http://dx.doi.org/10.1103/PhysRevB.67.094108

Hughes E.B., Perkins R. (2019) Madagascar sapphire: Low-temperature heat treatment experiments. *G&G*, Vol. 55, No. 2, pp. 184–197, http://dx.doi.org/10.5741/GEMS.55.2.184

Krzemnicki M.S. (2018) New research by SSEF studies methods for detecting low-temperature heated rubies from Mozambique. Swiss Gemmological Institute, https://www.ssef.ch/wp-content/uploads/2018/09/SSEF-PRESS-RELEASE-New-research-by-SSEF-studies-methods-for-detecting-low-temperature-heated-rubies.pdf

Kronenberg A.K., Castaing J., Mitchell T.E., Kirby S.H. (2000) Hydrogen defects in α-Al_2O_3 and water weakening of sapphire and alumina ceramics between 600 and 1000°C: I. Infrared characterization of defects. *Acta Materialia*, Vol. 48, No. 7, pp. 1481–1494, http://dx.doi.org/10.1016/S1359-6454(99)00448-6

Moon A.R., Phillips M.R. (1991) Defect clustering in H,Ti: α-Al_2O_3. *Journal of Physics and Chemistry of Solids*, Vol. 52, No. 9, pp. 1087–1099, http://dx.doi.org/10.1016/0022-3697(91)90042-X

——— (1994) Defect clustering and color in Fe,Ti: α-Al_2O_3. *Journal of the American Ceramic Society*, Vol. 77, No. 2, pp. 356–367, http://dx.doi.org/10.1111/j.1151-2916.1994.tb07003.x

Müller R., Günthard Hs. H. (1966) Spectroscopic study of the reduction of nickel and cobalt ions in sapphire. *Journal of Chemical Physics*, Vol. 44, No. 1, pp. 365–373, http://dx.doi.org/10.1063/1.1726471

Palke A.C., Renfro N.D., Hapeman J.R., Berg R.B. (2023) Gemological characterization of Montana sapphire from the secondary deposits at Rock Creek, Missouri River, and Dry Cottonwood Creek. *G&G*, Vol. 59, No. 1, pp. 2–45, http://dx.doi.org/10.5741/GEMS.59.1.2

Phan D.T.M. (2015) Internal characteristics, chemical compounds and spectroscopy of sapphire as single crystals. Doctoral dissertation, University of Johannes Gutenburg Mainz, https://d-nb.info/1075170532/34

Ramírez R., González R., Colera I., Vila R. (1997) Protons and deuterons in magnesium-doped sapphire crystals. *Journal of the American Ceramic Society*, Vol. 80, No. 4, pp. 847–850, http://dx.doi.org/10.1111/j.1151-2916.1997.tb02913.x

Ramírez R., Colera I., González R., Chen Y., Kokta M.R. (2004) Hydrogen-isotope transport induced by an electric field in α-Al_2O_3 single crystals. *Physical Review B*, Vol. 69, article no. 041302, http://dx.doi.org/10.1103/PhysRevB.69.014302

Saeseaw S., Khowpong C., Vertriest W. (2020) Low-temperature heat treatment of pink sapphires from Ilakaka, Madagascar. *G&G*, Vol. 56, No. 4, pp. 448–457, http://dx.doi.org/10.5741/GEMS.56.4.448

Shannon R.D. (1976) Revised effective ionic radii and systematic studies of interatomic distances in halides and chalcogenides. *Acta Crystallographica*, Vol. A32, pp. 751–767, http://dx.doi.org/10.1107/S0567739476001551

Smith C.P. (1995) A contribution to understanding the infrared spectra of rubies from Mong Hsu, Myanmar. *Journal of Gemmology*, Vol. 24, No. 5, pp. 321–335.

Smith C.P., van der Bogert C. (2006) Infrared spectra of gem corundum. *G&G*, Vol. 42, No. 3, pp. 92–93.

Soonthorntantikul W., Saeseaw S., Palke A., McClure S. (2021) Gem News Internationl: FTIR observation on sapphires treated with heat and pressure. *G&G*, Vol. 57, No. 3, pp. 283–286.

Soonthorntantikul W., Khowpong C., Atikarnsakul U., Saeseaw S., Sangsawong S., Vertriest W., Palke A. (2019) Observations on the heat treatment of basalt-related blue sapphires. *GIA Research News*, May 1, https://www.gia.edu/gia-news-research/observations-heat-treatment-of-basalt-related-blue-sapphires

Sripoonjan T., Wanthanachaisaeng B., Leelawatanasuk T. (2016) Phase transformation of epigenetic iron staining: Indication of low-temperature heat treatment in Mozambique ruby. *Journal of Gemmology*, Vol. 35, No. 2, pp. 156–161.

Stone-Sundberg J., Thomas T., Sun Z., Guan Y., Cole Z., Equall R., Emmett J.L. (2017) Accurate reporting of key trace elements in ruby and sapphire using matrix-matched standards. *G&G*, Vol. 53, No. 4, pp. 438–451, http://dx.doi.org/10.5741/GEMS.53.4.438

Vertriest W., Saeseaw S. (2019) A decade of ruby from Mozambique: A review. *G&G*, Vol. 55, No. 2, pp. 162–183, http://dx.doi.org/10.5741/GEMS.55.2.162

Volynets F.K., Sidorova E.A., Stsepuro N.A. (1972) OH groups in corundum crystals which were grown with the Verneuil technique. *Journal of Applied Spectroscopy*, Vol. 17, pp. 1626–1628.

Wyckoff R.W.G. (1963) *Crystal Structures*, Vol. 1, 2nd ed. John Wiley and Sons, New York, p. 7.

A Study of the Winston Red: The Smithsonian's New Fancy Red Diamond

Gabriela A. Farfan, Ulrika F.S. D'Haenens-Johansson, Stephanie Persaud, Eloïse Gaillou, Russell C. Feather II, W. Henry Towbin, and Daniel C. Jones

Red diamonds are among the rarest gems on Earth, especially Fancy red diamonds that are pure red and unmodified by brown, orange, or purple. At 2.33 ct, the Winston Red diamond is the fifth-largest Fancy red diamond known to exist and the only Fancy red diamond on public exhibit. On April 1, 2025, it was unveiled in a new exhibit at the Smithsonian National Museum of Natural History in Washington, DC. This is the first scientific and historical study conducted on this noteworthy stone. Optical observation along with spectroscopic, cathodoluminescence, and photoluminescence analyses confirmed the presence of plastic deformation bands and dislocation network patterns that classify the Winston Red as a type IaAB (A<B) Group 1 "pink" diamond and indicate that it underwent significant pressure and temperature conditions. The Winston Red owes its pure crimson color to a careful balance of absorption features: the 550 nm band associated with plastic deformation as well as the nitrogen-related N3 (N_3V^0), H3 (N_2V^0), and H4 ($N_4V_2^0$) defects. To place it in a broader context, the Winston Red's characteristics were compared to those of all other Fancy red diamonds that have been submitted to GIA. The history of the Winston Red diamond can now be traced back to 1938, but its old mine brilliant cut suggests an even richer story. Based on its mineralogical characteristics and history, the likely geographic origin of the stone has been narrowed down to Venezuela or Brazil; however, its precise origin remains unknown.

The 2.33 ct Winston Red diamond (figure 1) is on the verge of becoming one of the most famous fancy-color diamonds in the world. Currently the largest pure red diamond on public display, it is the fifth-largest red diamond with the coveted Fancy red GIA color grade. As part of one of the most significant donations to the National Gem Collection in the last decade, this diamond is the "cherry on top" of a world-class collection of fancy-color diamonds that went on display in an exhibit titled "The Winston Red Diamond and the Winston Fancy Color Diamond Collection" at the Smithsonian National Museum of Natural History (NMNH) on April 1, 2025.

Formerly referred to as the "Raj Red," the Winston Red is an old mine brilliant-cut diamond measuring approximately 8 mm in diameter with a very large culet and an extremely thin bruted girdle (again, see figure 1). The red color distribution is described as even, and the clarity is graded I_2 due to a combination of inclusions, chips around the girdle, and a particularly large but shallow feather that runs perpendicular to the table, as illustrated in the natural colored diamond report issued by GIA in 2023 (figure 2). Yet the color makes the Winston Red truly remarkable and one of the most beautiful red diamonds in the world.

In this study, scientists from the Smithsonian NMNH Department of Mineral Sciences teamed up with GIA and the curator from the Paris School of Mines to examine this rare diamond. This provided a unique opportunity to showcase the science behind the beautiful red color, interrogate the geological nature of its uncommon occurrence, and reveal the rich history of the stone before going on display at the Smithsonian. This investigation also highlights the threefold mission of natural history museums: to display awe-inspiring specimens, preserve natural history for future generations, and uncover new knowledge through scientific examination. Every specimen is

See end of article for About the Authors and Acknowledgments.
Gems & Gemology, Vol. 61, No. 1, pp. 16–42,
http://dx.doi.org/10.5741/GEMS.61.1.16

Figure 1. The 2.33 ct Winston Red diamond, displaying a vibrant Fancy red color. The old mine brilliant-cut stone measures approximately 8 mm in diameter. Photo by Robert Weldon; courtesy of Ronald Winston.

useful for study—especially those that are extraordinary and historically valuable, such as the Winston Red diamond.

Comparison to Other Red Diamonds. Unmodified Fancy red diamonds are among the rarest objects of natural history on the planet; only 24 stones over one

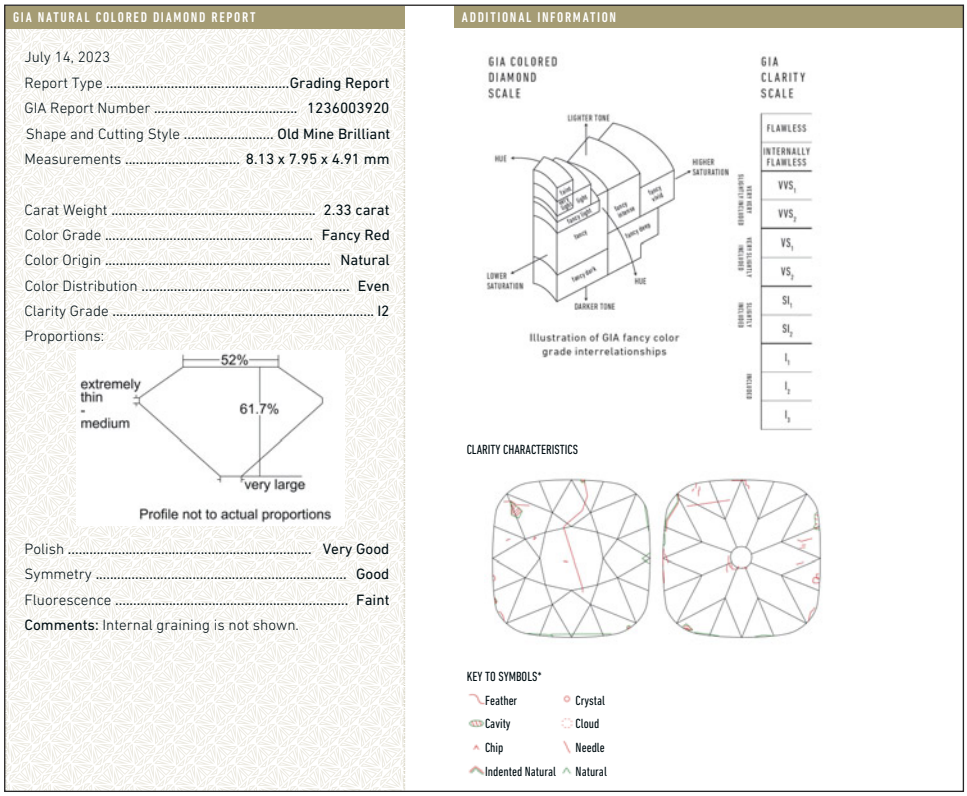

GIA NATURAL COLORED DIAMOND REPORT

July 14, 2023
Report Type ..... Grading Report
GIA Report Number 1236003920
Shape and Cutting Style ..... Old Mine Brilliant
Measurements ..... 8.13 x 7.95 x 4.91 mm

Carat Weight ..... 2.33 carat
Color Grade ..... Fancy Red
Color Origin ..... Natural
Color Distribution ..... Even
Clarity Grade I2
Proportions:

Profile not to actual proportions

Polish ..... Very Good
Symmetry ..... Good
Fluorescence ..... Faint
Comments: Internal graining is not shown.

ADDITIONAL INFORMATION

Illustration of GIA fancy color grade interrelationships

CLARITY CHARACTERISTICS

KEY TO SYMBOLS*

Feather, Crystal, Cavity, Cloud, Chip, Needle, Indented Natural, Natural

Figure 2. GIA Natural Colored Diamond Report for the Winston Red.

TABLE 1. Diamonds given a Fancy red (unmodified) color grade by GIA that are over one carat and reported in public records (e.g., auction and tender websites, publications), ranked by size.

Rank	Name	Weight (ct)	Cut or shape[a]	Clarity	Origin	References
1	Moussaieff Red	5.11	Trilliant	Unknown	Brazil, Minas Gerais, Rio Abaeté	King and Shigley, 2003; Wilson, 2014; Hoover et al., 2018
2	Winston Red	2.33	Old mine brilliant	I_2	Unknown	This study
3	Argyle Everglow	2.11	Cut-cornered rectangular modified brilliant	VS_2	Australia, Argyle	Argyle Tender, 2017
4	Unnamed	2.09	Heart brilliant	SI_2	Unknown	Christie's Hong Kong, 2014
5	Unnamed	1.92	Cut-cornered rectangular mixed cut	VS_2	Unknown	Phillips de Pury, New York, 2001; Sotheby's Hong Kong, 2011; Christie's Geneva, 2013
6	Argyle Enigma	1.75	Cut-cornered rectangular mixed cut	SI_2	Australia, Argyle	Argyle Tender, 2019
7	Noor Red	1.71	Heart brilliant	SI_2	Unknown	Sotheby's New York, 2020
8	Giacampos Red	1.57	"Oval"	Unknown	Brazil, Minas Gerais, Santo Inácio River	Svisero et al., 2017; Hoover et al., 2018
9	Argyle Phoenix	1.56	Round brilliant	I_2	Australia, Argyle	Argyle Tender, 2013; Phillips Geneva, 2024
10	Argyle Aurora	1.47	Oval modified brilliant	SI_2	Australia, Argyle	Argyle Tender, 2015
11	Unnamed	1.44	Cut-cornered rectangular mixed cut	I_2	Australia, Argyle	Sotheby's Geneva, 2022
12	Unnamed	1.38	Cushion modified brilliant	SI_2	Unknown	Sotheby's New York, 2019
13	Argyle Cardinal	1.21	Cut-cornered rectangular mixed cut	SI_2	Australia, Argyle	Argyle Tender, 2014
14	Red Miracle	1.21	Cut-cornered rectangular mixed cut	SI_2	Unknown	Phillips Geneva, 2024
15	Argyle Prima	1.20	Pear brilliant	SI_1	Australia, Argyle	Argyle Tender, 2015
16	Argyle Isla	1.14	Cut-cornered rectangular modified brilliant	I_1	Australia, Argyle	Argyle Tender, 2017
17	Argyle Mira	1.12	Cut-cornered rectangular modified brilliant	SI_2	Australia, Argyle	Argyle Tender, 2018
18	Argyle Scarlett	1.10	Oval brilliant	I_1	Australia, Argyle	Argyle Tender, 2009
19	Argyle Aria	1.09	Oval modified brilliant	I_1	Australia, Argyle	Argyle Tender, 2016
20	Argyle Avenoir	1.07	Oval modified brilliant	I_2	Australia, Argyle	Argyle Tender, 2019
21	Unnamed	1.06	Round-cornered rectangular modified brilliant	I_2	Unknown	Sotheby's Hong Kong, 2022
22	Unnamed	1.05	"Oval"	SI_2	Unknown	Christie's, 2002
23	Unnamed	1.03	Cut-cornered rectangular step cut	SI_1	Unknown	Sotheby's New York, 2021
24	Argyle Bohème	1.01	Cut-cornered rectangular modified brilliant	I_2	Australia, Argyle	Argyle Tender, 2021

[a]*Diamond shapes in quotation marks indicate cases in which cut details are unknown.*

In Brief

- At 2.33 ct, the Winston Red diamond, now on display at the Smithsonian National Museum of Natural History in Washington, DC, is the fifth-largest confirmed Fancy red diamond with a pure, unmodified red color.
- Fancy red diamonds are exceedingly rare, accounting for only approximately 0.04% of fancy-color diamonds submitted to GIA.
- The Winston Red's color is the result of a combination of absorption features: the 550 nm band associated with plastic deformation as well as the nitrogen-related N3 (N_3V^0), H3 (N_2V^0), and H4 ($N_4V_2^0$) defects.
- Investigation into its rich history and gemological properties suggest that the Winston Red most likely originates from Brazil or Venezuela.

carat exist in the public record, as identified in auction catalogs and news articles by this study (table 1). Beyond those listed in table 1, there are additional privately owned stones that have passed through GIA and other gemological laboratories but are excluded from these detailed tables as they are not public knowledge. The Winston Red is notable for being the fifth-largest unmodified Fancy red diamond among all the Fancy reds graded by GIA, and the second-largest Fancy red diamond that is in the public record, as listed in table 1. It is also the largest Fancy red diamond on public display now that it is officially part of the National Gem and Mineral Collection. The immense value of diamonds with the coveted Fancy red color grade is exemplified by the 2024 sale of the 1.56 ct, I_2 clarity Argyle Phoenix, which simultaneously commanded the highest price ($4.2 million) and price per carat ($2.7 million/ct) for a Fancy red diamond to date.

More than 20 years ago, the largest confirmed Fancy red diamond, the 5.11 ct Moussaieff Red, was on loan for the temporary "Splendor of Diamonds" exhibit at the Smithsonian NMNH in 2003 (King and Shigley, 2003). Since then, the only red-hued diamond exhibited at the Smithsonian has been the 5.03 ct DeYoung Red, with a darker, "red-brown" color (table 2; Shigley and Fritsch, 1993). Notably, in GIA's color grading system, a diamond is not considered a red diamond unless the final word in the color description is *red*. Hence some historically "red" diamonds listed in table 2 may include stones that were not predominantly red, such as the DeYoung Red. The stark differences in hue and saturation between the Winston Red and the DeYoung Red are visible when they are placed side by side (figure 3).

In 1987, GIA examined the Winston Red and issued a gem identification report describing it as a "brownish-orange-red" diamond. The fancy-color grading system has since been refined and standardized with controlled viewing and lighting environments, expanded terminology, and color comparators such as colored diamond master stones and Munsell color chips (King et al., 1994). King et al. (2002) highlight the particular challenge of color grading predominantly red diamonds. Their scarcity left few historic points of reference, resulting in a range of opinions regarding what a "red" diamond should look like. A Fancy red diamond has a unique appearance compared to other red gemstones. The GIA Natural Colored Diamond Report issued in 2023, with modern color grading, determined that the Winston Red is Fancy red (again, see figure 2).

Natural, untreated diamonds that have been described by GIA as having a predominantly red hue are exceedingly rare (e.g., Kane, 1987; King et al., 2002, 2014; King and Shigley, 2003; Eaton-Magaña et al., 2018). Analysis of more than a million natural fancy-color diamonds submitted to GIA for laboratory

Figure 3. The Winston Red diamond (center, 2.33 ct), alongside the much darker "red-brown" DeYoung Red (left, 5.03 ct) and the DeYoung Pink diamonds (right, 2.82 ct). All three stones are currently on public exhibit at the Smithsonian NMNH. Photo by Gabriela Farfan.

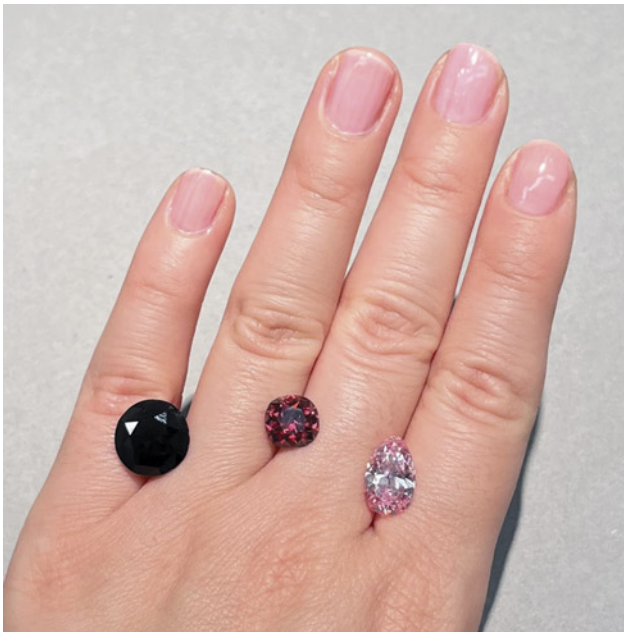

TABLE 2. Significant "red" diamonds described as reddish or red in the public domain of sizes larger than the 2.33 ct Winston Red diamond.

Rank[a]	Name	Weight (ct)	Shape	Color description or color grade[b]	Notes	References
Unconfirmed	Lichtenburg Red	18	Rough	"Red"	—	Wilson, 2014
Unconfirmed	Unnamed	10.26	Pear	"Chinese red"	—	Wilhelm, 1860, pp. 126–127; Shigley and Fritsch, 1993
Unconfirmed	Unnamed	8.00	Unknown	"Red"	—	Shigley and Fritsch, 1993; Kunz, 1926, p. 596
Unconfirmed	Unnamed	7.44	Round	"Garnet"	—	Wilhelm, 1860, pp. 108–109; Shigley and Fritsch, 1993
Unconfirmed	Unnamed	6.00	Cushion	"Red"	Reportedly from South Africa	Kunz, 1926, p. 596; Gill, 1978, p. 85; Shigley and Fritsch, 1993
Unconfirmed	Edcora Red	5.71	Pear	"Red-brown"	Called the "lost stone"; last seen in Hong Kong	—
1	Moussaieff Red	5.11	Triangular	Fancy red	Formerly "Red Shield"	King et al., 2002; King and Shigley, 2003
2	Kazanjian Red	5.05	Square	"Blood red"	Formerly "De Beers Red"; reportedly from Lichtenburg, South Africa	Drukker, 1971; Gaal, 1977, p. 241; Gill, 1978, p. 85; Shigley and Fritsch, 1993
3	DeYoung Red	5.03	Round	"Red-brown"	—	Shigley and Fritsch, 1993
4	Unnamed	5	Unknown	"Ruby red"	—	Shepherd, 1934; Monnickendam, 1955, p. 154; Shigley and Fritsch, 1993
5	Unnamed	5	Round	"Port wine red"	—	Gill, 1978, p. 86; Shigley and Fritsch, 1993
6	Unnamed	3.98	Round	"Brownish red"	—	Wilhelm, 1860, pp. 94–95; Shigley and Fritsch, 1993
7	Fancoldi Red	3.16	Round	Fancy Intense purplish red	—	Wilson, 2014; Hoover et al., 2018
8	Christmas Red	3.15	Round	Fancy reddish orange	—	Wilson, 2014
9	Unnamed	2.50	Round	"Port wine red"	—	Gill, 1978, p. 86; Shigley and Fritsch, 1993
10	Unnamed	2.50	Marquise	"Deep cherry red"	—	Gill, 1978, p. 86; Shigley and Fritsch, 1993
11	Unnamed	2.50	Round	"Red"	Reportedly from Brazil	Gill, 1978, p. 85; Shigley and Fritsch, 1993
12	Winston Red	2.33	Cushion[c]	Fancy red	Formerly "Raj Red"	—

[a]The first six are not ranked as their records cannot be confirmed.
[b]Color descriptions in quotation marks indicate cases in which formal fancy-color grades are not available.
[c]Shape refers to a cut diamond's outline; hence the old mine brilliant-cut Winston Red diamond has a cushion shape.

services (i.e., excluding D-to-Z color diamonds) reveals that predominantly red diamonds account for only approximately 0.07% of the stones. Among these red diamonds, those graded Fancy red account for 56.9% (i.e., 0.04% of all fancy-color diamonds), with the remainder modified by purple (39.5%), orange (2.0%), or brown (1.6%). King et al. (2002) describe and illustrate the differences between the Fancy Deep pink, Fancy Vivid pink, and Fancy red color grades, noting the distinctive tone and saturation associated with Fancy red diamonds. The narrow ranges of tone and saturation for diamonds described as red also mean that they can receive only one fancy grade: Fancy. The only other colors that warrant this approach are Fancy black and Fancy white diamonds.

The geological processes involved in creating red color in diamonds are extreme (discussed later) and may contribute to the small sizes and lower clarity grades that most red diamonds have received from GIA (see appendix 1 at https://www.gia.edu/gems-gemology/spring-2025-winston-red-diamond). The vast majority of Fancy red (i.e., unmodified) diamonds are small, with only 4% larger than two carats, the largest being the 5.11 ct Moussaieff Red. Over 75% of Fancy red diamonds have received clarity grades of SI_1 to I_2, and approximately 30% have I_1 or I_2 clarity grades. In order of incidence, the most common clarity features were feathers, crystal inclusions, and natural surfaces. For most buyers, lower clarity in Fancy red diamonds is of little concern compared to the coveted red color (King et al., 2014). Typically, the shapes and cutting styles for Fancy red diamonds were chosen to maximize weight and enhance face-up color, with less than 4% of diamonds being cut into round shapes. The three most common shapes were rectangular (50%), square (16%), and oval (12%). Popular cutting styles were modified brilliants, most notably the cut-cornered rectangular and square modified brilliants, referred to as "radiant cut" in the trade.

The Winston Red ranks 12th in size among the larger confirmed "red" diamonds of the world, according to public records (table 2). The largest confirmed historically "red" diamonds are the Moussaieff Red (5.11 ct trilliant cut), followed by the Kazanjian Red (5.05 ct square cut), and the DeYoung Red (5.03 ct round brilliant cut). Still, accounts of six even larger reddish diamonds (18, 10.26, 8.00, 7.44, 6.00, and 5.71 ct) have been listed in previous studies as recorded in the Gem Catalogue of the Duke of Brunswick-Luneburg in 1860 and others (Kunz, 1926; Gill, 1978; Shigley and Fritsch, 1993; Wilson, 2014). It is important to note that although table 2 encompasses diamonds historically regarded as red, most lack a formal color grade. Other than the Moussaieff Red and Winston Red, none of the significant red diamonds in table 2 have received the Fancy red color grade (indicating pure, unmodified red) that follows today's standards, and most are red with modifying colors (e.g., Fancy purplish red) or have not been graded by GIA. Some, such as the DeYoung Red, are described as red-brown and other colors that would not qualify as red today because the final word in the color description is not "red" (e.g., brownish red).

Categorizing Pink and Red Diamonds. It is well established that red diamonds acquire their color through the same mechanisms as pink diamonds (red is a more saturated pink color), relating to crystal deformation (King et al., 2002; Eaton-Magaña et al., 2018). In this article, we will discuss red and pink diamonds interchangeably. Here, we explore the literature on causes of color in pink and red diamonds to compare to the Winston Red and provide clues about its color origin, geological formation, and even geographic origin.

Although diamond is considered a hard, brittle material, it can deform plastically under applied pressures at high temperatures (Smith, 2023). Plastic deformation of diamond involves the generation of dislocations and their movement, generally resulting in slip along octahedral {111} planes in <110> directions (Evans and Wild, 1965). Diamond crystal distortion can also lead to an abrupt and localized change in the lattice orientation, resulting in mechanical twinning (Titkov et al., 2012). Following plastic deformation, natural annealing processes can also lead to dislocations reorganizing into lower-energy arrangements, notably the polygonized dislocation networks with cellular appearances observed in deformed low-nitrogen diamonds (e.g., Sumida and Lang, 1981; Kanda et al., 2005; Fisher, 2009; Laidlaw et al., 2021). Pink diamonds are often separated into groups that consider the nitrogen content as defined by the diamond type classification system (described by Breeding and Shigley, 2009), as well as the distribution of the pink color. This naming convention was originally developed by Gaillou et al. (2010, 2012) and expanded by Eaton-Magaña et al. (2020). Briefly, Group 1 pink diamonds are defined as those containing low concentrations of aggregated nitrogen, with B-centers (N_4V^0) dominating over A-centers (nitrogen pairs) (type IaA<B). Microscopic observations show pink color throughout the stones, with wavy lamellae or graining. Detailed analyses through luminescence

imaging techniques reveal cellular dislocation patterns, typical of plastically deformed diamonds with low nitrogen. In contrast, Group 2 pink diamonds are type IaA>B with higher nitrogen concentrations. Their pink color is restricted to straight, discrete pink lamellae attributed to mechanical microtwinning, with colorless regions between the lamellae. Glide planes coinciding with the lamellae can be observed by luminescence imaging. The relative concentrations of A- and B-centers are often used to separate Group 1 and Group 2 pink diamonds, frequently stated as Group 1 = IaA<B, Group 2 = IaA>B. However, expanded Fourier-transform infrared (FTIR) analysis of pink diamonds suggests that Group 1 diamonds are characterized by %IaB>35% (Howell et al., 2015). Finally, Group 3 diamonds are comparatively "nitrogen-free" type IIa diamonds (detected by FTIR absorption), with uniform pink color created by the same crystallographic defects responsible for the pink color in Group 1 and Group 2 diamonds. In this study, we exclude the rare (light) pink type IIa diamonds colored by $NV^{0/-}$ centers (e.g., Eaton-Magaña et al., 2020), also called "Golconda pink diamonds," as the Winston Red diamond does not fall into that category.

HISTORY OF THE WINSTON RED

When the Winston Red diamond—formerly referred to as the "Raj Red"—first arrived at the Smithsonian, we knew very little about its history. The stone's donor, Ronald Winston, noted that he had purchased the stone from the Maharaja of Jamnagar from India in the late 1980s (R. Winston, pers. comm., 2023). Yet the stone's old mine cut promised a much richer history. Currently, we have traced the Winston Red's history back to September 1938, when Jacques Cartier sold the stone to the Maharaja of Nawanagar, Digvijaysinhji (also known as "the Good Maharaja"). In the Cartier London archives is a November 1938 communication to the maharaja in which Jacques Cartier wrote that he could envision the diamond set in a ring or "put in your big necklace between the green diamond and the pink diamond pendeloque […]. The red diamond would take the place of the white triangular diamond." There is no record of the red diamond being set by Cartier, and it was apparently sent to India shortly after the letter was sent. Unfortunately, at this time, Cartier archivists have not been able to uncover when or where Cartier acquired the diamond before

Figure 4. The Ceremonial Necklace of Nawanagar created by Cartier London and worn by the maharaja (A); originally sketched by Cartier in 1931, without the red diamond (B); and reproduced by A.V. Shinde circa 1958 and in 2002, containing a 2.34 ct red diamond (C). Photos courtesy of Archives Cartier Paris © Joshi & Vara, Archives Cartier London © Cartier, and Keswani (2004), respectively.

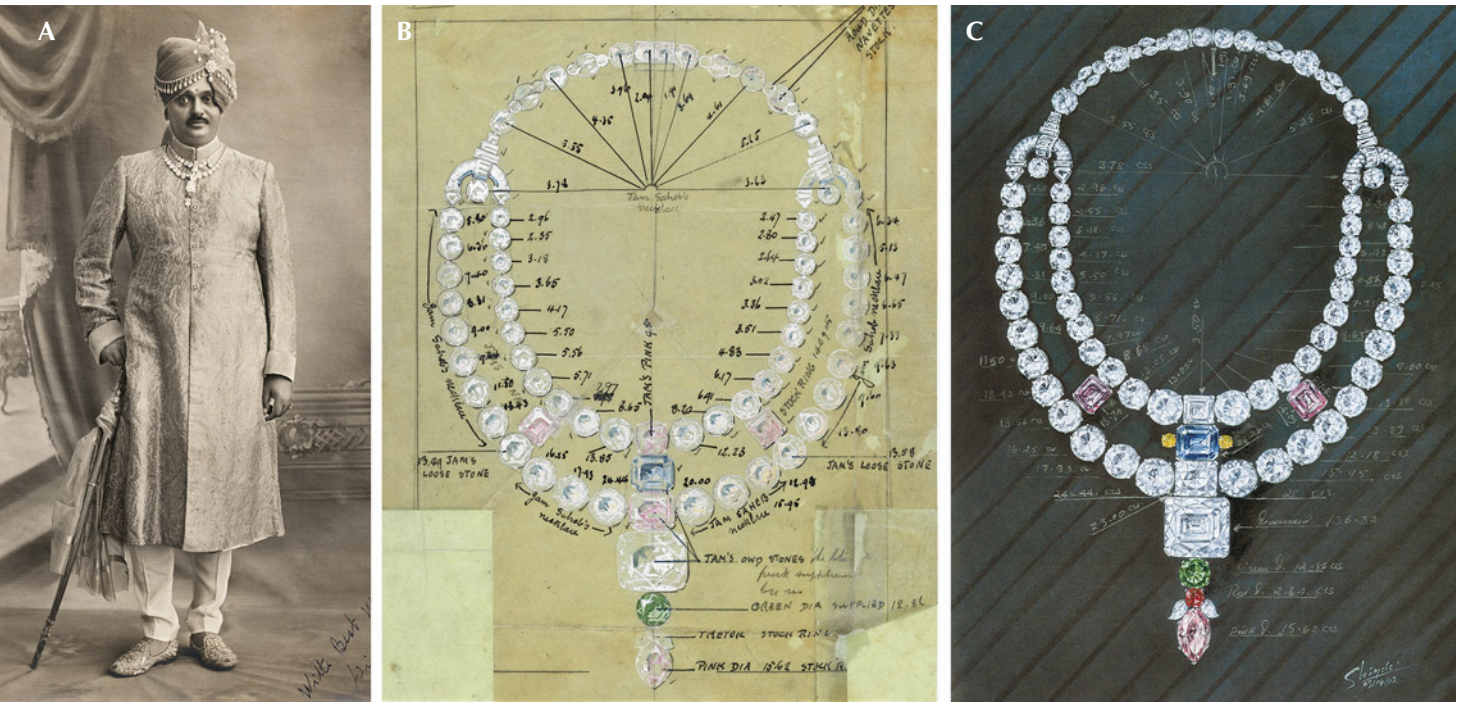

selling it to the maharaja. We are hopeful that more information will eventually provide additional clues about the stone's history and geographic origin.

The "big necklace" that Jacques Cartier referred to was the Ceremonial Necklace of Nawanagar, which Cartier assembled and considered one of his greatest works (figure 4, A and B, from the Cartier Archives; Spink, 2018; F. Cartier Brickell, pers. comm., 2024). This magnificent necklace contained over 600 carats of diamonds, including large pink, blue, and green stones highlighted by the 136.32 ct blue-white Ranjitsinhji diamond. It was commissioned in 1931 for the previous Maharaja of Nawanagar, Ranjitsinhji, who was Digvijaysinhji's uncle. In *The Biography of Colonel His Highness Shri Sir Ranjitsinhji Vibhaji* by Roland Wild, Jacques Cartier (1934) wrote a section in the appendix about the Nawanagar Jewels. He stated that the necklace was "the most extraordinary piece of the whole collection—a really superb realization of a connoisseur's dream." The version of the necklace with the red diamond added at the bottom was later re-sketched by A.V. Shinde circa 1958 and in 2002 (figure 4C).

In 1947, several newspapers showed evidence of the red diamond being set into the Ceremonial Necklace of Nawanagar, as Cartier originally suggested, in an image of the maharaja holding the necklace (figure 5). We currently do not know by whom or when it was set into the necklace. By the early 1960s, the necklace was being dismantled. Still, the Ceremonial Necklace of Nawanagar managed to maintain a certain level of fame beyond its lifetime. In 2018, it served as inspiration for the movie *Ocean's 8*, which features a copy of the necklace nicknamed the "Toussaint Necklace" after a former Cartier creative director, Jeanne Toussaint. Using only colorless diamonds (represented by cubic zirconia diamond imitations in the movie prop created by Cartier), the original design was modified to be smaller and worn by the actress Anne Hathaway.

In 1988, Ronald Winston, son of famous jeweler Harry Winston, acquired the red diamond from Digvijaysinhji's son Jam Saheb Sri Shatrusalyasinhji, who succeeded his father as the titular Maharaja of Nawanagar in 1966. The "Raj Red" diamond, as Winston called it at the time, was to be publicly unveiled at the November 1988 opening of the Harry Winston salon in Tokyo, but the festivities were postponed in deference to the failing health of Japan's Emperor Hirohito. Instead, the diamond debuted one year later at the anniversary of the Tokyo salon's opening, where actress Brooke Shields wore it mounted in a gold pinky ring (figure 6). She was also adorned in a white diamond necklace and a blue diamond ring, a trio that Winston touted as the "American Collection."

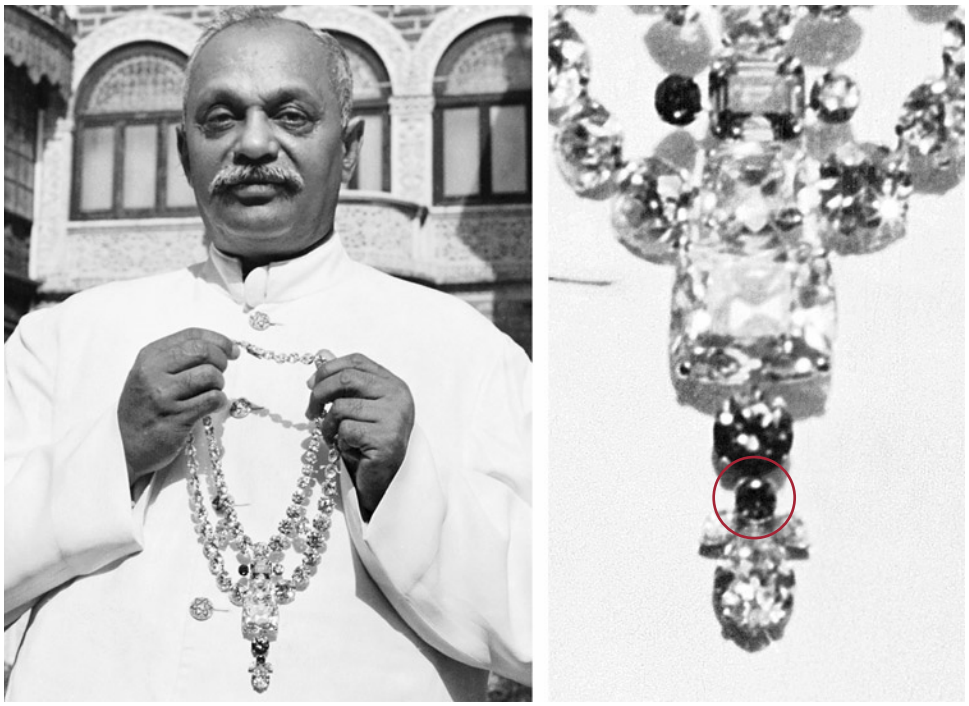

Figure 5. Left: The Ceremonial Necklace of Nawanagar held by the Maharaja Digvijaysinhji in 1947. Photo courtesy of Cartier Paris Documentation © Acme Photo. Right: Zoomed in on the red diamond, circled in red.

Figure 6. Brooke Shields wears the Winston Red diamond set in a pinky ring as part of the "American Collection" for a 1989 Harry Winston event in Tokyo. Photo by Itsuo Inouye; courtesy of Associated Press.

In December 2023, Ronald Winston officially gifted the diamond, now known as the Winston Red, to the National Gem Collection at the Smithsonian NMNH, where it resides in Washington, DC. The Winston Red is now on exhibit in the Winston Gallery as a neighbor to the Hope diamond, displayed alongside a subset of 40 stones from Winston's world-class collection of more than 100 other fancy-color diamonds.

METHODS

The Winston Red diamond was carefully studied using a range of spectroscopic and imaging techniques to gain a better understanding of the combination and distribution of point and extended defects responsible for its red color, providing insights into its formation and geological history. Combining forces, GIA scientists traveled to the NMNH with an instrument suite for diamond analysis and set up a temporary lab in the Department of Mineral Sciences to study the diamond using an expanded array of instruments from both organizations.

Optical Imaging. Photomicrographs were captured with a Nikon DS-Ri2 camera with a SMZ-2 microscope base with a 1× plan apo objective (1–11.25× magnification) under darkfield, brightfield, and fiber-optic illumination. Anomalous birefringence patterns, indicative of strain, were evaluated by placing the sample between cross-polarized filters under brightfield illumination.

FTIR Absorption Spectroscopy. A room-temperature FTIR absorption spectrum covering the 400–6000 cm^{-1} range with a 1 cm^{-1} resolution was collected using a Thermo Fisher Nicolet iS50 spectrometer equipped with a KBr and quartz beam splitters, a MCT-A detector, and a DRIFT (diffuse-reflectance infrared Fourier transform) accessory. The system and sample chamber were purged with dry air to minimize absorption features from atmospheric water. Unlike the other data of the Winston Red presented in this study, the FTIR spectrum used for defect concentration analysis was originally collected at GIA when it was submitted for grading in 2023.

Visible/Near-Infrared (Vis-NIR) Absorption Spectroscopy. An absorption spectrum spanning across the visible to near-infrared range (400–987 nm) was recorded with a custom-built GIA instrument using a fiber-coupled spectrometer (Ocean Optics QE Pro), a multicore reflection probe, and a tungsten-halogen light source (Avantes AvaLight-Hal-S-Mini). This high-resolution apparatus enabled the detection of very weak and sharp absorption features with the sample cooled to liquid nitrogen temperature (77 K).

Photoluminescence (PL) Spectroscopy. Photoluminescence spectroscopy analysis was carried out using three different instruments: two were non-confocal, collecting bulk emission spectra, whereas the third was a high-resolution confocal system used to map the distribution of luminescent defects. The first bulk-analysis instrument, designed and built by GIA, uses a 405 nm fiber-coupled laser (CNI FC-D-405-50mW) for excitation, with the room-temperature diamond placed on a small platform directly onto the output fiber. The PL signal was collected through a similarly positioned fiber and analyzed using a spectrometer with ~1.2 nm spectral resolution (Avantes Avaspec-Mini).

The second custom device allowed us to investigate the diamond's PL when cooled to 77 K using a wide selection of laser excitations. The sample was placed in a foam cup containing liquid nitrogen, and the excitation was delivered through direct contact with a bifurcated fiber coupled to a laser bank consisting of four Hübner Cobolt lasers: 457 nm (08-DPL 457 nm), 514.5 nm (06-MLD 514.5 nm), 633 nm (06-MLD 633 nm), and 830 nm (0.6-MLD 830 nm). The emission was collected and analyzed using a 550 mm Czerny-Turner spectrometer (Horiba iHR550) with a 600 l/mm grating and 90 µm slit width, leading to a spectral resolution of 0.13 nm using an EMCCD detector (Horiba Synapse EM).

Room-temperature PL maps were acquired using a Horiba Evolution Raman spectrometer equipped with 405 and 532 nm lasers, run with SwiftMode (set to 0.00001 sec/spot). Preliminary low spatial resolution maps over a selected pavilion facet were collected using a 5× objective (Olympus MPlan N, 0.1 NA) with the 405 nm laser (~5 mW) and a 300 l/mm grating over 412–522 nm. High spatial resolution maps (1× 1 µm steps and 0.25 × 0.25 µm steps) were then collected using a 50× long-distance objective (Olympus SLMPlan, 0.45 NA) and a 75 nm pinhole. Each map was collected with a 405 nm laser (~3 mW) to cover the 412–522 nm range and a 532 nm laser (~40 mW) to cover the 569–678 nm range. Where possible, PL maps were Raman normalized to account for slight sample tilt.

DiamondView Deep-UV Fluorescence Imaging. Fluorescence images under deep-UV illumination (<225 nm) were captured with a De Beers DiamondView system. Unlike standard short- and long-wave UV light sources, the above band-gap energy illumination provided by this device produces near-surface fluorescence from practically all diamonds. The resulting fluorescence images reveal clear patterns that can help decipher how a diamond grew and whether it was subjected to subsequent geological processes such as deformation (Welbourn et al., 1996; D'Haenens-Johansson et al., 2024). Different filters could be placed between the sample and the built-in camera; in addition to the standard filter that reduces signal contamination from the light source, colored filters were used to restrict the detected wavelengths: blue (390 nm band-pass), green (475 nm long-pass), orange (550 nm long-pass), and red (725 nm long-pass).

Scanning Electron Microscopy (SEM) and Cathodoluminescence (CL) Imaging. Cathodoluminescence and secondary electron images (SEI) were collected at the NMNH using a Thermo Fisher Quattro scanning electron microscope furnished with a retractable real color RGB CL detector (red, green, and blue channels). All analyses were collected using low vacuum mode at room temperature with 15 kV and 1.3 nA at a working distance of 10 mm. The Winston Red was uncoated for all of these measurements.

RESULTS AND DISCUSSION

Optical Microscopy. For orientation purposes, pavilion facet 1 (P1) is defined by a relatively large chip at the interface between P1 and the culet (figure 7A). The rest of the pavilion facets are labeled in clock-

Figure 7. Optical images of the Winston Red diamond. A: Chip between pavilion facet 1 (P1) and the culet. B: Labeled pavilion facets (P1–P8), as determined by the chip on P1. C: Graining viewed from P2. Photomicrographs by W. Henry Towbin.

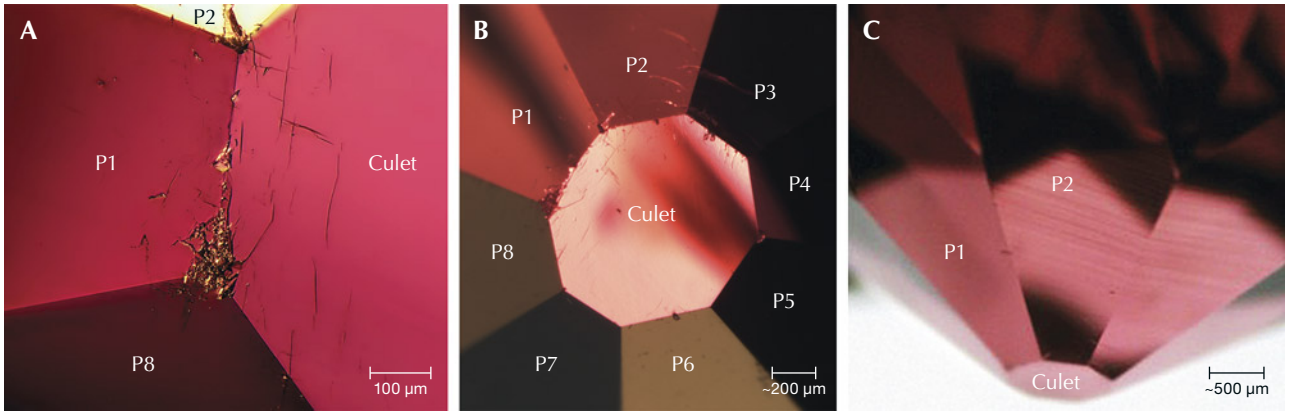

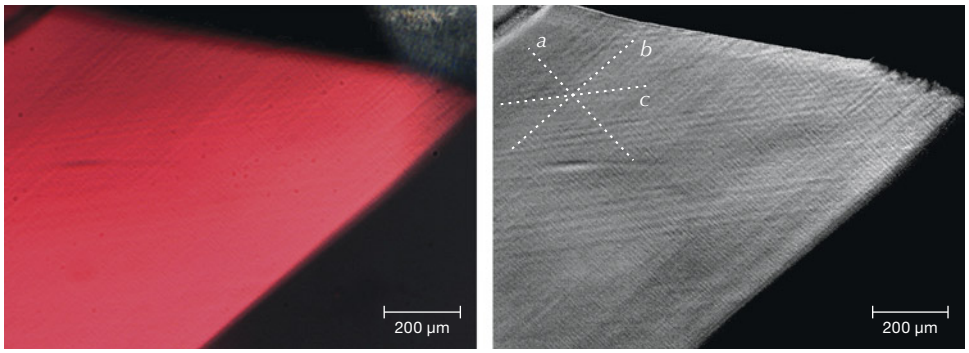

*Figure 8. Three directions of graining on a facet in true colors (left) and in black and white showing variations in hue (right). The three directions of graining (*a, b, *and* c*) are outlined in white dashed lines. Images by W. Henry Towbin.*

wise order (figure 7B). In this study, we focus on pavilion facet 2 (P2) for imaging and mapping techniques (figure 7C).

The face-up color of the stone appears homogeneous (again, see figure 1), but detailed optical microscopy revealed that the red color saturation is not homogeneous within the stone. This effect is most clearly observed when viewed through the pavilion facets, as seen in figure 7C. Three directions of red lamellae and thin bands, also known as graining, are visible. Colored graining and lamellae are associated with {111} oriented slip or glide bands. All three crystallographically equivalent directions of graining are visible in a plane-polarized view of a facet (figure 8, left), especially when the hues are represented in black and white (figure 8, right). Each direction of graining has a different periodicity, ranging from 9 to 13 µm along direction *a*, 15 to 23 µm along direction *b*, and 17 to 33 µm along direction *c* (figure 8, right). In at least one direction, the graining appears in bands with wavy textures, such as reported for Group 1 pink diamonds by Gaillou et al. (2012; see appendix 1 for more photos). Unlike Group 2 pink diamonds, in which the pink color is typically confined to the lamellae and surrounded by colorless layers in between, the Winston Red diamond is red throughout—but with deeper red saturation along the lamellae (figure 7C).

In at least one instance, two directions of the banding converge to create a hollow Rose channel that appears to be associated with an unidentified inclusion (figure 9, A and B). In pink diamonds, Rose channels are due to plastic deformation and are the consequence of the intersection of two directions of mechanical microtwinning (Schoor et al., 2016).

At first glance, the culet facet appears to have a chipped vertex (figure 7B), but microscopic observation reveals a box pattern similar to that of a coated diamond (Machado et al., 1985; Harris et al., 2022). We have interpreted this as the remnants of the rough diamond surface (figure 7A).

When viewed between cross-polarized filters, both mottled and wavy linear anomalous birefringence patterns could be observed, depending on the orientation (figure 9C). The dominant direction of linear anomalous birefringence features followed that of the lamellae and graining, but a pattern of finer linear features crossing through the primary direction could also be resolved. These observations have also been reported for Group 1 diamonds (Gaillou

Figure 9. A Rose channel with an inclusion in plane-polarized light (A) and cross-polarized light (B). Cross-polarized light showing two directions of graining and wavy patterns (C). Images by W. Henry Towbin.

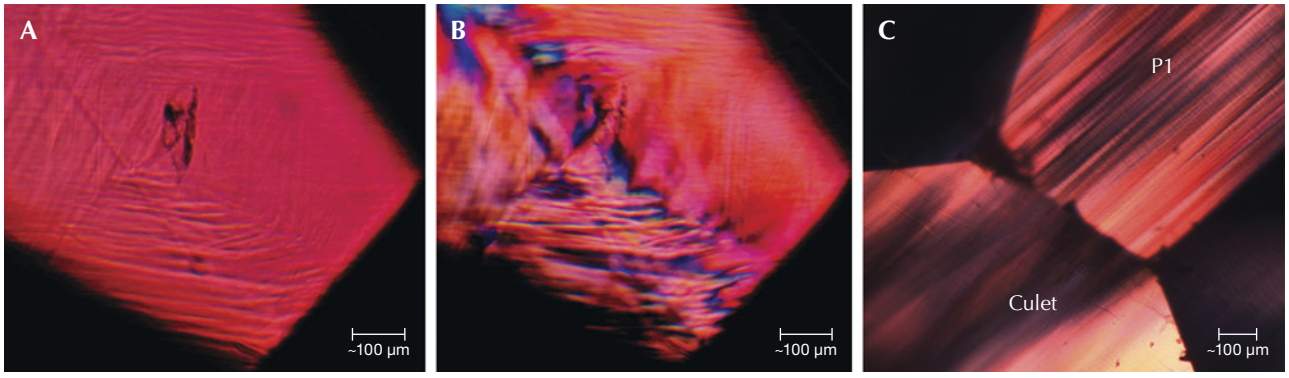

et al., 2012; Eaton-Magaña et al., 2020). High levels of strain were not restricted to discrete lamellae, unlike in Group 2 diamonds.

Characterization by FTIR and Vis-NIR Absorption Spectroscopy. *FTIR absorption spectroscopy.* FTIR spectroscopy was used to evaluate the presence of nitrogen-related defects in the Winston Red diamond. Aggregated nitrogen in both the A- and B-center forms were detected (nearest-neighbor nitrogen pairs and N_4V^0, respectively) in the resulting spectrum (figure 10, left), meaning that it can be classified as type IaAB (e.g., Breeding and Shigley, 2009). The most recognizable feature for A-centers is a broad peak at ~1282 cm^{-1}, whereas the B-centers are detected at ~1175 cm^{-1}. Concentrations were calculated with a Python script following the fitting methods of David Fisher's CAXBD97n Excel spreadsheet (De Beers Technologies, Maidenhead, UK), using the absorption coefficient relationships by Boyd et al. (1994, 1995) following spectral normalization based on the height of the two-phonon absorption in diamond (Palik, 1985). The total nitrogen concentration was determined to be 83 ± 8 ppm, with 76 ± 8 ppm B-centers and 7 ppm A-centers (i.e., 92% IaB). Additional absorption features include a sharp peak at 3107 cm^{-1} (N_3VH^0) (Goss et al., 2014) and broad bands around 4167 and 4839 cm^{-1} (most likely Amber Center 1; see Massi et al., 2005). Notably, the Amber Center 2 (4065 cm^{-1}) and the platelet peak, which can vary in position between 1358 and 1380 cm^{-1} (Woods, 1986; Speich et al., 2017), were not detected. Platelets are thin layers of carbon self-interstitial aggregates that form as A-centers convert to B-centers. Diamonds for which platelet concentrations are proportional to the B-center concentration are classified as "regular" according to Woods (1986). The absence of platelets for the Winston Red diamond would classify it as "irregular," which may suggest that they were broken apart by heating or significant deformation (Woods, 1986).

FTIR studies of pink diamonds by Gaillou et al. (2010) and Howell et al. (2015) suggest that Group 1 diamonds are type IaA<B with a relatively high aggregation state (%IaB>35%) and low total nitrogen concentrations that are generally below 200 ppm (but can extend up to ~800 ppm), as is similarly observed for the Winston Red diamond (figure 10, right, red diamond symbol). Meanwhile, Group 2 diamonds have a wider range of total nitrogen concentrations (150–1600 ppm) and relatively low aggregation (%IaB<35%). FTIR analysis of 399

Figure 10. Left: FTIR absorption spectrum of the Winston Red classifies it as a type IaAB diamond, with detectable concentrations of aggregated nitrogen as A-centers (nitrogen pairs, broad peak at ~1282 cm^{-1}) and B-centers (N_4V^0, ~1175 cm^{-1}). The weak broad bands around 3000 cm^{-1} are attributed to surface oil contamination. Right: Plot of the total nitrogen concentration vs. the nitrogen aggregation state (%IaB) for 399 Fancy red diamonds analyzed by FTIR at GIA, with the Winston Red diamond indicated with the red diamond symbol. Of this set, 156 of the diamonds originated from the Australian Argyle mine, whereas three were reportedly recovered in Minas Gerais, Brazil. The Winston Red diamond belongs to the Group 1 designation used for pink diamonds.

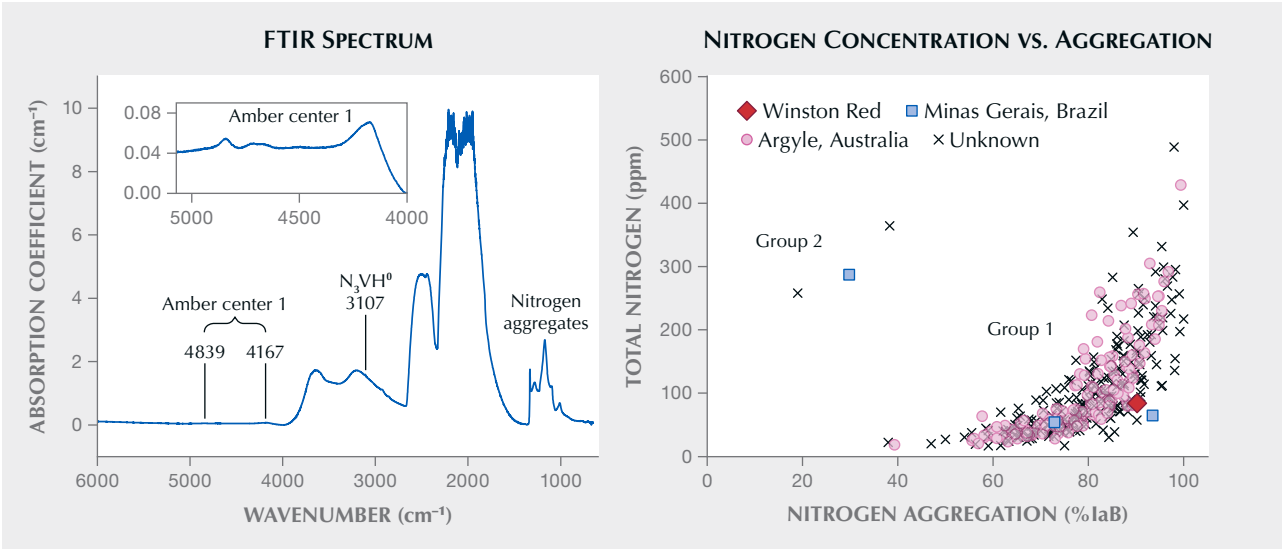

Fancy red diamonds submitted to GIA suggests that they overwhelmingly belong to Group 1, with only three samples (0.8%) showing total nitrogen concentration and aggregation states consistent with Group 2 diamonds (figure 10, right). For this sample set, 39.1% (156) of the diamonds are known to originate from Argyle, Australia, whereas 0.8% (3) were reportedly recovered in Minas Gerais, Brazil. The geographic origins of the remaining diamonds are unknown. These results may be biased by the high representation of type IaA<B pink to red diamonds from the prolific Argyle mine, and it is likely that the majority of the unknown samples share that origin (e.g., Rolandi et al., 2008; King et al., 2014; Eaton-Magaña et al., 2018). None of the red diamonds examined at GIA belong to Group 3 (type IIa, colored by 550 nm band), which encompasses 24% of natural pink diamonds (Eaton-Magaña et al., 2018, 2020). As with colorless diamonds, the larger pink diamonds are generally type IIa (S. Eaton-Magaña, pers. comm., 2024). It is possible that the saturated color associated with Fancy red diamonds cannot be achieved in type IIa diamonds. If so, this incompatibility may also explain the relatively modest sizes attained by red diamonds.

Vis-NIR Absorption Spectroscopy. Vis-NIR absorption spectroscopy collected at liquid nitrogen temperature was used to investigate the color centers responsible for the Winston Red diamond's Fancy red grade (figure 11; see also table 3). The dominant feature observed is a broad asymmetric absorption band centered at around 550 nm, along with nitrogen-related absorption from N3 (N_3V^0, zero phonon line, or ZPL, at 415 nm), H4 ($N_4V_2^0$, ZPL at 496 nm), and H3 (N_2V^0, ZPL at 503.2 nm) centers (e.g., Green et al., 2022). This gives rise to a transmission window in the red part of the visible spectrum, producing the diamond's characteristic color. The 550 nm absorption band is responsible for the pink color in over 99% of natural pink-hued diamonds, as well as all natural red diamonds that have been graded at GIA (Eaton-Magaña et al., 2018, 2020; also confirmed by the current authors). The absorption intensity of the 550 nm band, as well as the diamond's size and cut, determine the color saturation and whether it will be predominantly pink or red (King et al., 2002; Eaton-Magaña et al., 2018). The subtle balance of the 550 nm band and the N3, H4, and H3 absorption features are responsible for the Winston Red's pure unmodified red color. Although this 550 nm band has been associated with

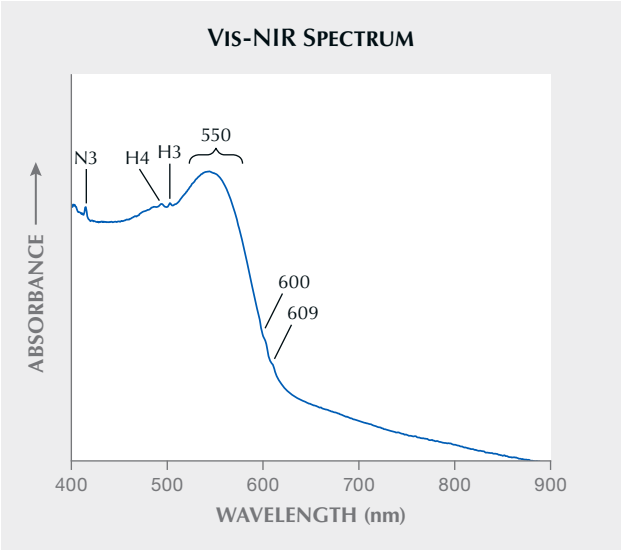

Figure 11. The Vis-NIR absorption spectrum of the Winston Red diamond is dominated by a strong 550 nm band, along with absorption by N3 (415 nm), H4 (496 nm), and H3 (503.2 nm) centers. Weak absorption from the "609 nm system" is also detected. Data was collected at 77 K with the sample in its equilibrium color state, prior to any significant ultraviolet light exposure that could induce photochromism.

plastic deformation, the defect structure has not yet been determined (e.g., Orlov, 1977; Collins, 1982; Gaillou et al., 2010; Howell et al., 2015; Eaton-Magaña et al., 2018, 2020). The band is observed in both pink type Ia (Groups 1 and 2) and type IIa (Group 3) diamonds, suggesting that nitrogen content is not directly linked to the pink color centers. However, this does not rule out that the presence of nitrogen may still be indirectly involved in pink color formation. In pink diamonds, the 550 nm band is typically observed along with a band at 390 nm (e.g., Eaton-Magaña et al., 2018); however, its presence could not be confirmed for the Winston Red diamond because the collected spectrum did not extend below 400 nm. Peaks at 609 and 600 nm, associated with the "609 nm system" first defined by Fritsch et al. (2007), are weakly observed, overlapping with the low energy tail of the broad 550 nm band. The 609 nm system, which presents as a series of oscillations spanning between ~550 and 609 nm, has been reported for pink diamonds colored by the 550 nm band, being most noticeable in low-nitrogen or type IIa pink diamonds (Shigley and Fritsch, 1993; Fritsch et al., 2007; Eaton-Magaña et al., 2018, 2020). This 609 nm emission system possibly mirrors the 550 nm absorption band and might be due to the same unknown defect (Eaton-Magaña et al., 2020). Due to

TABLE 3. Absorption and PL spectroscopy features in the Vis-NIR range for the Winston Red diamond.

Feature (nm)	Feature (eV)	Spectroscopic technique	Description
415.2	2.986	Absorption, PL	N_3V^0, known as N3
490.7	2.527	PL	Observed in plastically deformed diamond
494.5	2.507	PL	Unknown
496.2	2.499	Absorption, PL	$N_4V_2^0$, known as H4
503.2	2.464	Absorption, PL	N_2V^0, known as H3
535.8	2.314	PL	Possibly interstitial-related; commonly observed in diamonds with B-centers
550	2.254	Absorption	Broad band associated with pink color in natural diamonds; thought to arise from plastic deformation
552.7	2.243	PL	Unknown
576	2.152	PL	Unidentified defect that is not the NV^0 (575 nm) center
586.9	2.112	PL	Unknown
600.7	2.064	PL	Unknown
609 (600, 594, 586, 573)	2.036	Absorption	"609 system" seen in pink diamonds, with oscillations to lower wavelength; possibly linked to the 700 nm emission band (see Fritsch et al., 2007 and Eaton-Magaña et al., 2020)
616.5	2.011	PL	Unknown
626.1	1.980	PL	Unknown
646.8	1.917	PL	Unknown
654.9	1.893	PL	Unknown
660.8	1.876	PL	Commonly seen in pink diamonds
668.7	1.854	PL	Commonly seen in pink diamonds; possibly Ni-related
700	1.771	PL	"700 nm emission band," also referred to as the 600–750 nm emission band; includes oscillations to lower wavelength and possibly linked to the 609 nm system seen in absorption (Eaton-Magaña et al., 2020)
710	1.746	PL	Observed in some pink diamonds
731.4	1.769	PL	Possibly related to interstitial nitrogen
741	1.673	PL	V^0, known as GR1
890	1.393	PL	Unknown
900	1.378	PL	Unknown
915	1.355	PL	Unknown

their extreme rarity, few Fancy red diamond UV-Vis-NIR absorption spectra have been published (Shigley and Fritsch, 1993; Eaton-Magaña et al., 2018); these reports also show intense absorption in the 550 nm band, coupled with comparatively weak absorption from N3, H4, and H3 centers, consistent with the Winston Red diamond.

Luminescence Spectra and Imaging. *Photoluminescence Spectra.* Non-confocal photoluminescence measurements using various laser wavelengths (405, 457, 514, 633, and 830 nm) captured an array of luminescent features in the Winston Red diamond, as shown in figure 12 and detailed in table 3. The 405 nm–excited PL spectrum was collected at room temperature and the remaining data with the sample liquid nitrogen–cooled to 77 K. The spectrum collected with the 405 nm laser is dominated by the N3 defect, with weak H3, as would be expected based on their detection in the stone's Vis-NIR absorption spectrum (figure 12), combined with the weak concentration of luminescence-quenching A-centers detected by FTIR absorption (again, see figure 10) (Thomaz and Davies, 1978). Several of the PL features detected for the Winston Red are commonly observed in the luminescence spectra for pink diamonds colored by the 550 nm absorption band (e.g., Iakoubovskii and Adriaenssens, 2002; Gaillou et al., 2010; Eaton-Magaña et al., 2018, 2020). Notably, the 514 nm laser effectively excited an intense broad luminescence band that peaks at around 700 nm, dominating the 500–850 nm wavelength range (figure 12C). Eaton-Magaña et al. (2018, 2020) demonstrated that the intensity of this emission band correlates with the 550 nm absorption band, suggesting that it can be used as a proxy for this absorption. The "pink emission band" includes a series of characteristic oscillations that also possibly relate to the 609 nm system in absorption, seen in figure 11 (Eaton-Magaña et al., 2018, 2020). The 700 nm emission band, also referred to as the 600–750 nm emission band, has been shown to have consistent peak positions (Eaton-Magaña et al., 2020). The 490.7 nm, H4, H3, 576 nm, and 668.7 nm luminescence peaks observed for the Winston Red have previously been associated with Group I (type IaA<B) pink diamonds, being less common for those belonging to Group 2 (type IaA>B) (Eaton-Magaña et al., 2020). The 490.7 nm defect is thought to be nitrogen-related and a product of plastic deformation (Collins and Woods, 1982). Other notable features are the 535.8, 654.9, 660.8, and 710 nm peaks. The former is commonly seen in diamonds with B-centers and may be interstitial-related (Laidlaw et al., 2021), consistent with the Winston Red's diamond type. A weak strain-broadened GR1 (neutral vacancy, V^0, ZPL at 741 nm) is also detected (Iakoubovskii and Adriaenssens, 2002; Gaillou et al., 2010). The 830 nm laser excited unidentified broad bands centered at 890, 900, and 914 nm.

The authors are not aware of any published PL spectra for natural Fancy red diamonds, so this study presented an opportunity to explore data collected internally at GIA for 10 client-submitted diamonds using similar excitation wavelengths. Comparison of the spectra for the Winston Red and the Fancy red diamond suite reveals the clearest similarities when excited by the 633 nm laser. The 654.9, 660.8, and 668.2 nm peaks were always detected together, though their intensities do not correlate, suggesting that they do not share a common defect origin. The 660.8 nm peak appears to be a zero-phonon line with vibronic structure that results in a series of broad bands at higher wavelengths, with the most distinctive peaking at ~682, 691, and 703 nm, as determined by comparing the peak ratios for all samples they were detected in. The vibronic structure associated with the 660.8 nm peak fell below the detection limit of the spectrum collected for the Winston Red diamond and cannot be seen in figure 8, left. The 710 nm peak, which dominates the 633 nm excited PL for the Winston Red (figure 12D), was detected for 80% of the other Fancy red diamonds. Notably, the spectra for all the other Fancy red diamonds show a peak at 731.4 nm that was not observed for the Winston Red. The 731.4 nm peak has been attributed to a characteristic of interstitial nitrogen (Deljanin et al., 2008). GR1 was detected for all these samples. Spectra collected with the 514 nm laser show more variability, with only the spectrum for the Winston Red diamond displaying a clear 700 nm band—the others appear to include an additional overlapping band that rises steeply from ~500 nm and peaks at ~600 nm. However, we do note that all the samples showed an emission at 535.8 nm, with nearly all also showing emissions from H3, H4, and 576 nm peaks (typically one peak being absent). Finally, PL spectra collected with the 830 nm laser revealed that all the diamonds for which the 710 nm emission was detected also showed unidentified broad peaks at 890, 900, and 914 nm, with varying intensities. Although this sample set is limited, it was sufficient to demonstrate a range of peaks commonly observed for Fancy red diamonds, yet it did not unravel any distinctive trends between the peaks.

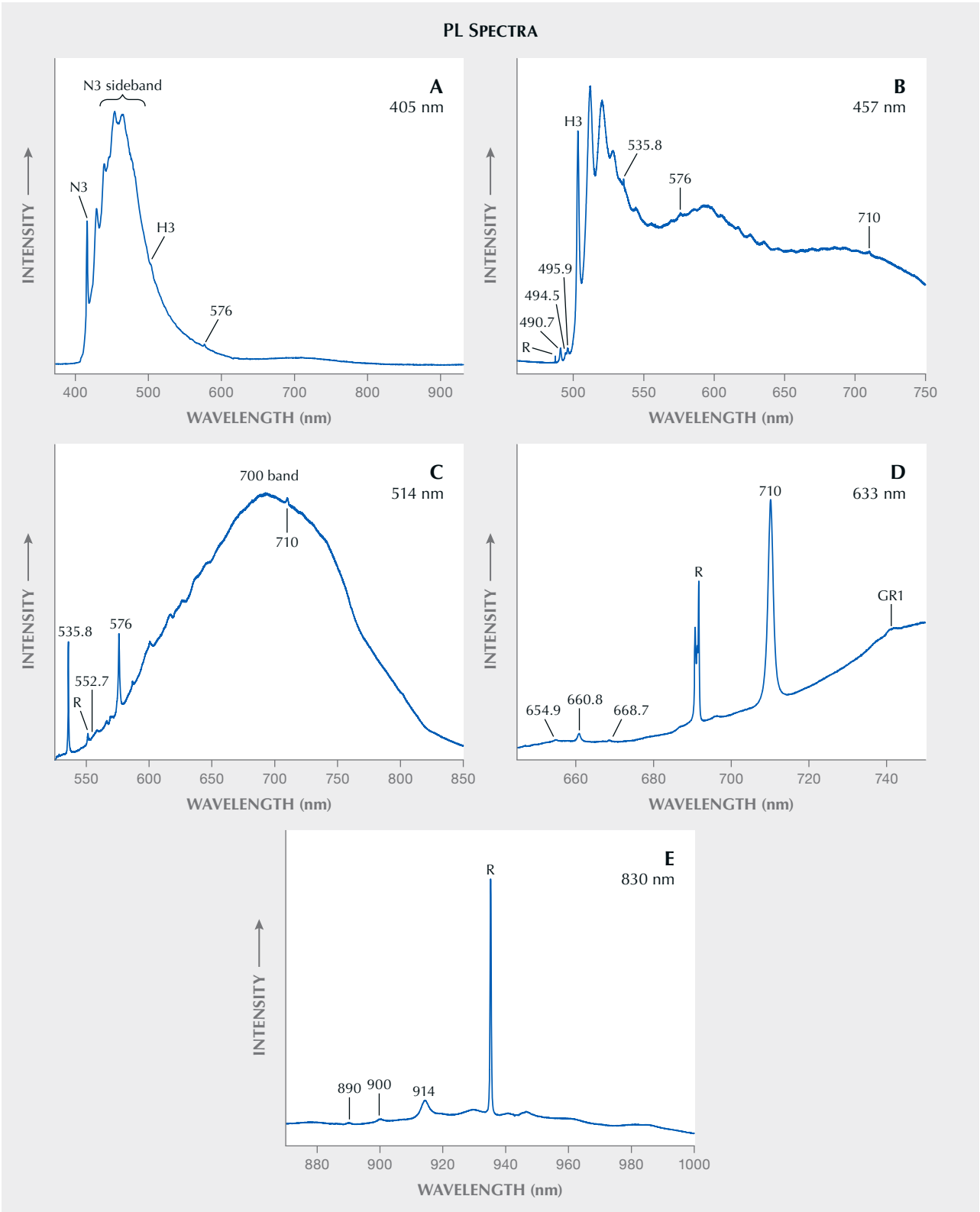

Figure 12. Photoluminescence spectra of the Winston Red diamond using 405 nm (A), 457 nm (B), 514 nm (C), 633 nm (D), and 830 nm (E) lasers. All spectra except for A were collected with the sample cooled to 77 K. Spectra B–D were Raman normalized to the integrated intensities of the diamond Raman peaks (R); the splitting of the Raman peak in D is a result of the excitation laser line shape.

Fluorescence Observations and DiamondView Imaging. The Winston Red diamond's fluorescence was first investigated during its grading at GIA in 2023 using long-wave UV (365 nm) illumination, an identifying characteristic described in its grading report as "faint" blue (again, see figure 2). This blue fluorescence arises from the N3 defect (also excited by the 405 nm laser in figure 12A) and has been detected in ~93% of the Fancy red diamonds graded at GIA.

Weak heterogeneous green fluorescence was observed for the Winston Red when illuminated with a color-neutral halogen light from a fiber-optic probe (SCHOTT KL 1500 HAL Fiber Optic Light Source Illuminator) during microscopic examination, with the emission following the stone's graining. This effect, commonly known as "green transmission," is caused by the emission of H3 centers and was also reported for the DeYoung Red (Shigley and Fritsch, 1993). The fiber-optic light source emits weakly below 415 nm and is more efficient at exciting fluorescence from H3 centers than from N3 centers (Luo and Breeding, 2013). Green transmission has been noted for ~60% of the Fancy red diamonds inspected at GIA.

When viewed under deep-UV (<225 nm) illumination from the DiamondView device, the Winston

Figure 13. DiamondView images of the Winston Red's table (A and B) and selected pavilion facets (C and D). The reference images on the left (A and C) and the fluorescence images on the right (B and D) were collected under white light and deep-UV illumination, respectively. The distribution of the blue N3 fluorescence reveals the diamond's intrinsic growth pattern. The inset of an area outlined in black lines in D shows the graining features as best observed using the red filter (725 nm long-pass). Comparison of the diamond's color for images A and C highlights its reversible photochromism, changing to a brown color following UV exposure. The white rectangle in D indicates a region that was further explored using photoluminescence mapping techniques. Images by Ulrika F.S. D'Haenens-Johansson.

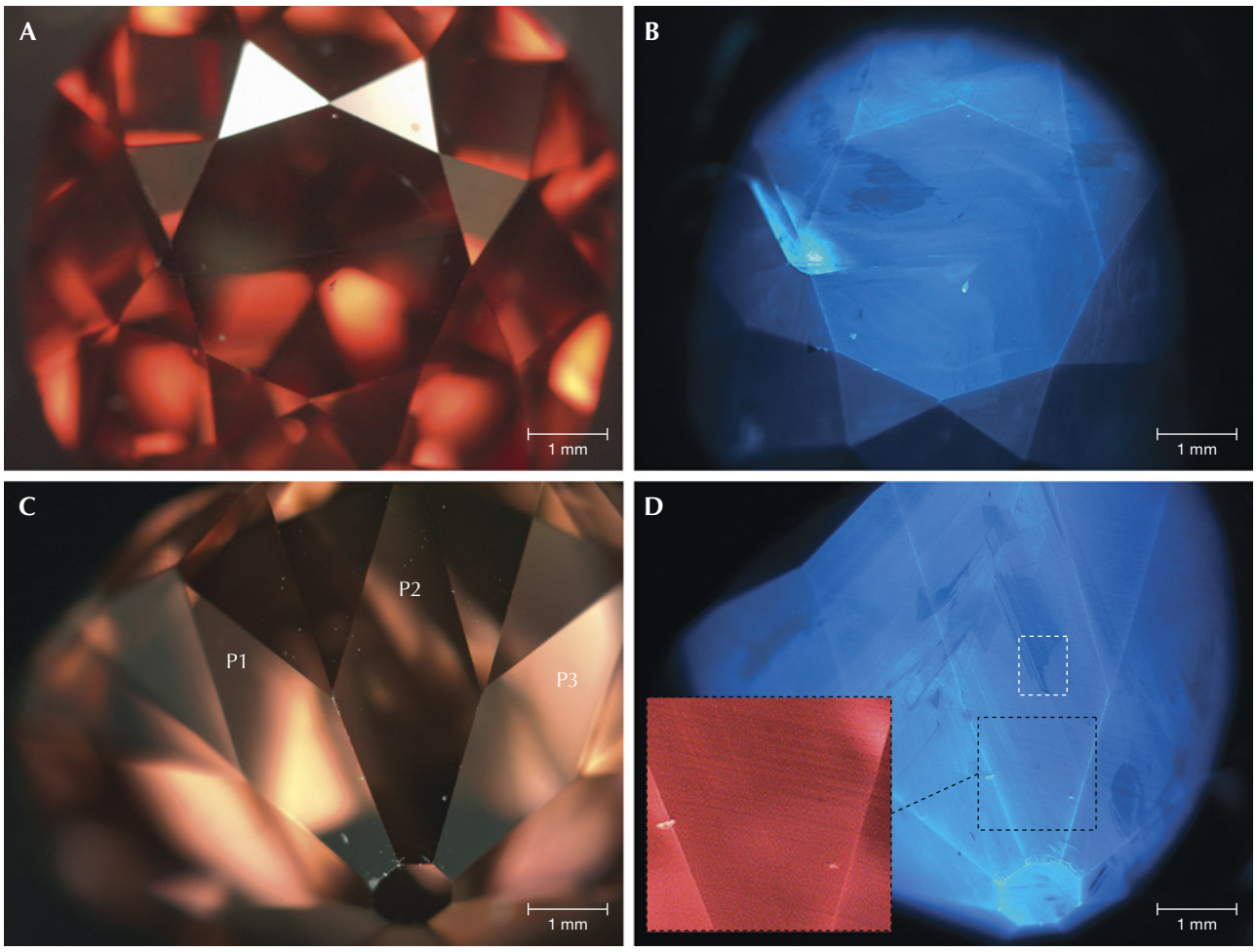

Red diamond displays blue fluorescence from N3 centers (figure 13), revealing a natural growth pattern. Along the pavilion facets, linear features that follow the lamellae (figures 7C and 13D) can be weakly resolved crossing through various growth zones—evidence of plastic deformation. The dominance of the N3 fluorescence under this excitation wavelength means that the colored filter detection accessories mainly transmit in its high wavelength "tail" (refer to the 405 nm–excited PL spectrum in figure 12A) and hence do not provide clear information on the identity and distribution of other fluorescing defects.

The Winston Red diamond—similar to pink and red diamonds colored by the 550 nm band—is photochromic. Illumination with ultraviolet light (long-wave, short-wave, or deep-UV from the DiamondView) results in a temporary color change, reducing the depth of color and imparting an orangy brown hue to the red stone. This can be clearly seen when comparing the color of the diamond in the white light images before and after deep-UV exposure (figure 13, A and C, respectively). Studies of the photochromism of the 550 nm absorption band sometimes refer to the color change following UV exposure as "bleaching," yet the effect varies, resulting in color changes toward yellow, brown, or orange hues, or a simple reduction in color saturation (e.g., Fisher et al., 2009; Byrne et al., 2012, 2014; Eaton-Magaña et al., 2018, 2020). The brown hue observed in the Winston Red diamond following UV exposure may be related to an underlying absorption continuum that relates to the Amber 1 centers detected by FTIR absorption (again, see figure 10). The color change is reversible, with exposure to longer wavelengths (>530 nm) or strong white light leading to color recovery. If kept in the dark, the "bleached" state may be maintained for an extended period of time. Though this was not tested for the Winston Red, Byrne et al. (2012) estimated that the color recovery of bleached pink diamonds that are kept in the dark at room temperature may take on the order of 100 days.

Hyperspectral Photoluminescence Imaging. The distribution of luminescing centers on the pavilion facet noted as P2 in figures 7 and 13 were investigated in more detail by photoluminescence mapping of N3, the 576 nm peak, and the 700 nm broad band (integrating over the spectral window 625–677 nm) emissions (figure 14). This facet was selected as it showed visible color graining, as well as growth and plastic deformation–related structures in the fluorescence images. N3 was excited using a 405 nm laser, whereas the remaining two centers were excited by a 532 nm laser. With the available excitation wavelengths, it was not possible to excite H4 or H3 without simultaneously exciting the significantly stronger N3; hence the distribution of these centers was not considered. N3, the 576 nm peak, and the 700 nm emission band show wavy linear distributions following two primary directions. The intensity variations are subtle for N3 and more pronounced for the 576 nm peak and 700 nm emission band. The N3 defect will strongly correlate to the initial growth of the diamond, incorporating different concentrations of nitrogen, which eventually form N3, creating

Figure 14. PL mapping of various spectroscopic features on the P2 facet defined in figure 7. On a small region near the facet junction on the right side of P2: peak area of the N3 ZPL at 415 nm normalized to the Raman peak area (A), peak area of the 576 nm ZPL (B), and emission area of the 625–677 nm region associated with the broad band centered at ~700 nm (C).

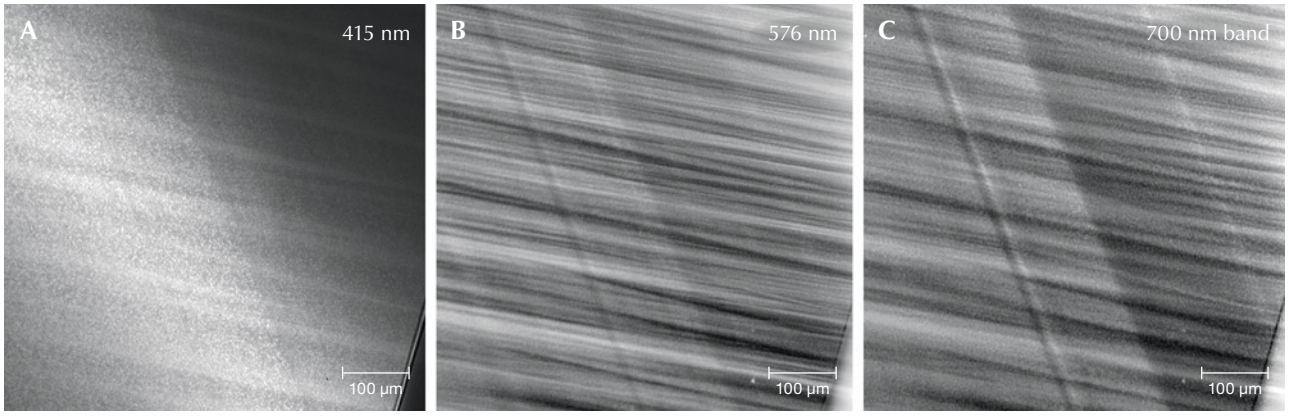

growth bands, while the 576 and 700 nm features are more directly related to plastic deformation. Although there are similarities between the luminescing defect distributions, they do not match exactly. Notably, they were not solely restricted to sharp, straight lamellae or slip planes. The approximately linear patterns cross uninterrupted through different growth zones, as seen in figure 15, indicating that they are the result of post-growth processes such as natural plastic deformation. A granular or "fish-scale" pattern can also be resolved (Gaillou et al., 2012), with the grains being bright with dark outlines, which is more pronounced in the PL maps for N3 and the 700 nm band.

Eaton-Magaña et al. (2020) explored the distribution of the 490.7 nm, H4, H3, and 576 nm peaks, as well as the 700 nm band, in pink Group 1 (type IaA<B) and Group 2 (type IaA>B) diamonds. For Group 1 pink diamonds, they found that luminescence intensities increased within the wavy pink lamellae, tracking with higher color concentrations, yet they noted detectable intensities between lamellae. This was considered consistent with pink coloration observed throughout the stone. The Group 2 pink diamonds did not show as many luminescent defects, and the discussion was restricted to the distribution of H3 and the 700 nm band. Emissions from these centers were segregated to the color-restricted straight lamellae. The distributions of luminescing features for the Winston Red diamond are similar to those reported for Group 1 pink diamonds.

Cathodoluminescence and Secondary Electron Imaging. Cathodoluminescence imaging of the Winston Red diamond corroborates many of the features that we observe with optical, fluorescence, and hyperspectral PL imaging (figure 16). The blue CL

Figure 15. Following similar analytical procedures, a region encompassing a distinctive growth zone as outlined in white in figure 13D is PL mapped for N3 (A), the 576 nm peak (B), and the 700 nm band (C). The yellow arrow in A shows an area at the edge of the growth zone that is devoid of N3. D–F: The same information shown in A–C is repeated for the region outlined in white in image A.

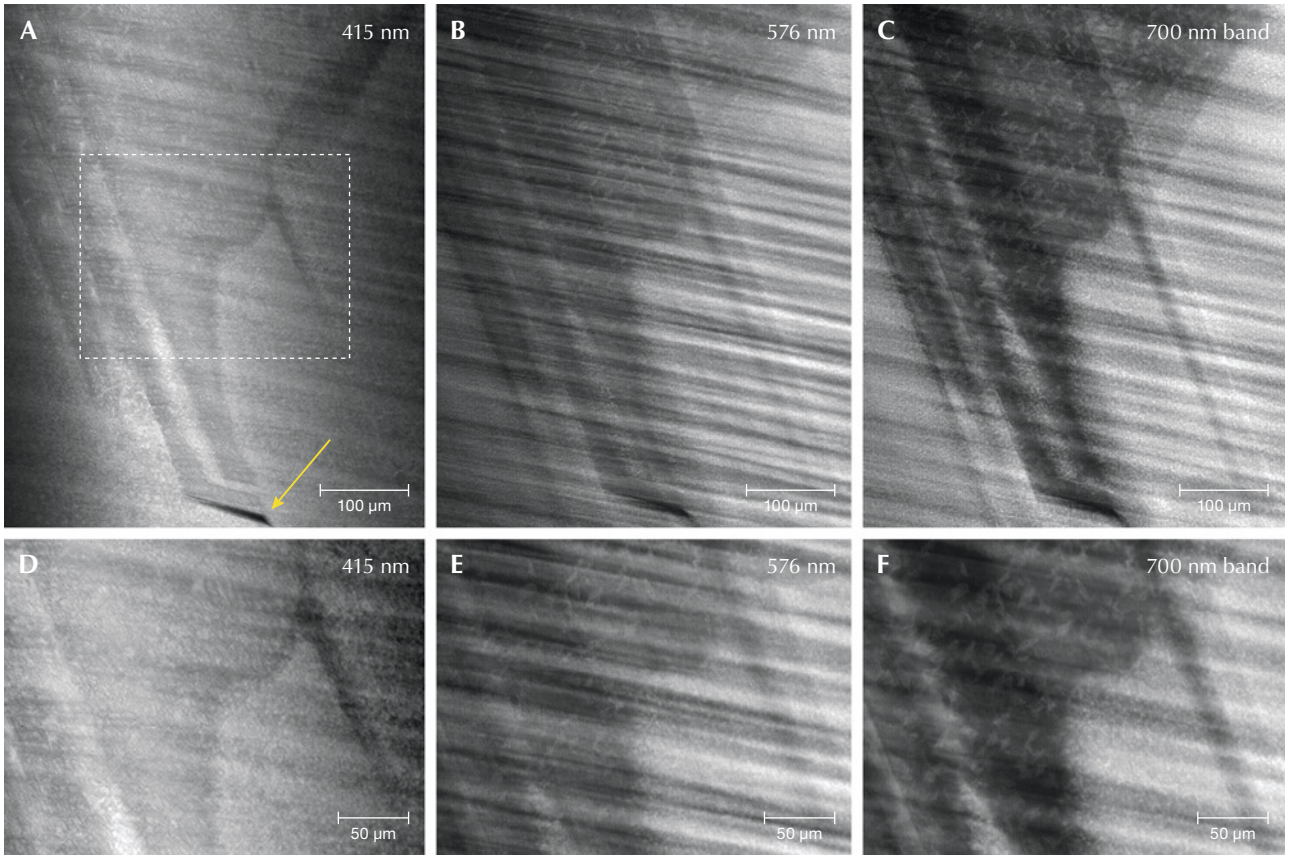

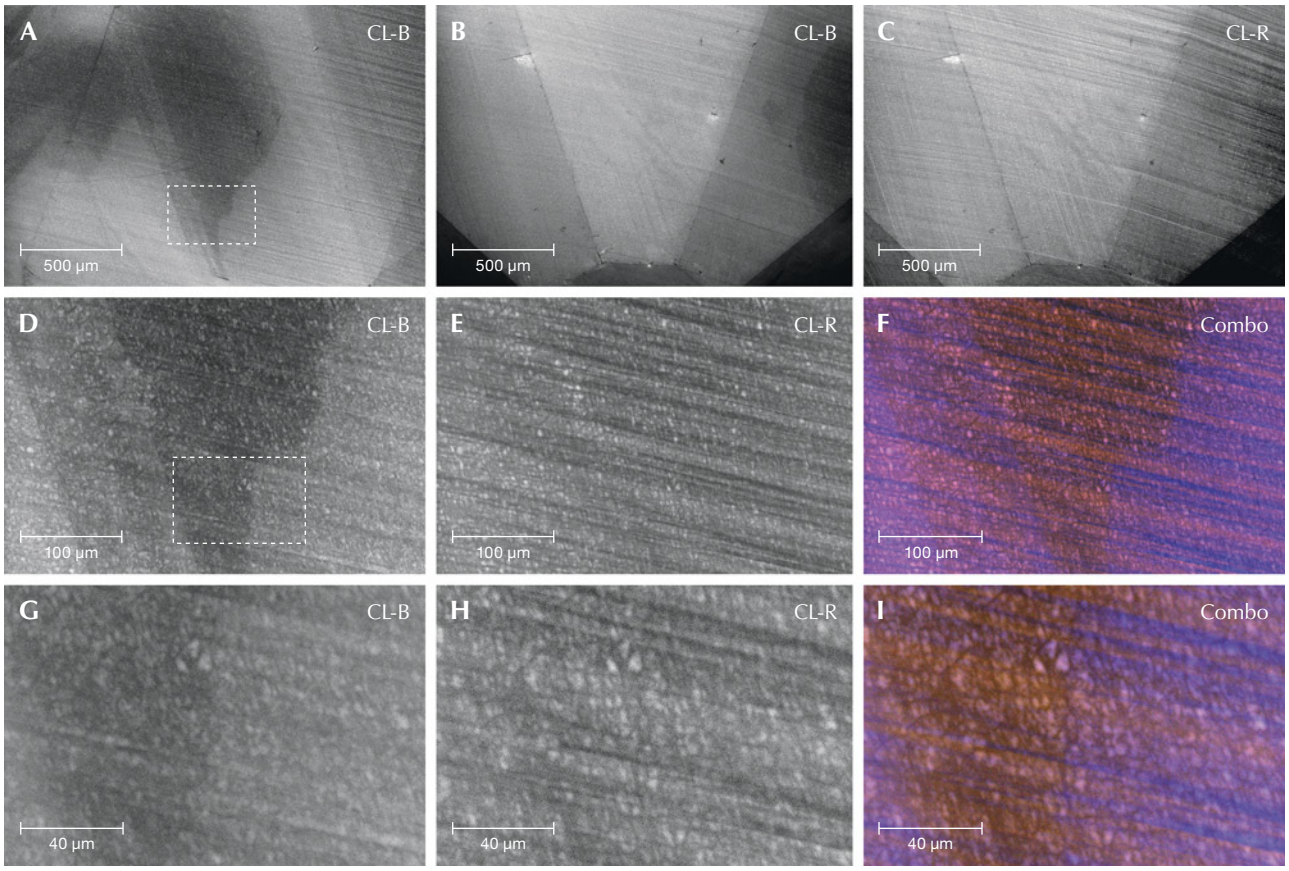

Figure 16. SEM-based cathodoluminescence imaging. A: Pavilion facet 2 (P2) is imaged with the blue CL channel in the center of P2 to show a growth feature, similar to what is seen in the DiamondView (figure 13D). The region near the culet of P2 is imaged with the blue CL channel (B) and the red CL channel (C; to better show the lamellae). At higher magnification in the region outlined in A, the blue CL channel (D) shows the growth pattern and begins to reveal fish-scale dislocation network patterns (granular textures), while E clearly shows the lamellae. F: A combined image of the red, green (not shown), and blue CL channels shows the growth feature, the lamellae, and the dislocation networks. G–I: Follow the same order of features as D–F, but at higher magnification for the region outlined in white lines in D.

channel, similar to the DiamondView blue filter, clearly reveals growth zones (figure 16, A and B), especially at higher magnifications (figure 16, D and G). Although it was not possible to confirm by CL spectroscopy, the intensity variations captured by this channel are primarily associated with the N3 defect, showing patterns consistent with the DiamondView fluorescence (figure 13, B and D) and hyperspectral PL images (e.g., figure 15A). Blue "Band A" emission (broad band ~400–500 nm) associated with unidentified defects located in the material adjacent to dislocations may also contribute to the signal (Dean, 1965; Ruan et al., 1992; Gaillou et al., 2012; Laidlaw et al., 2021). Slip bands associated with the graining are weakly detected. Images collected with the green channel did not reveal any significant differences, likely capturing the high-wavelength tail of the N3 emission (not shown) rather than weaker emissions by H4, H3, or 576 nm defects, consistent with green filtered DiamondView imaging observations.

The various directions of graining observed with optical and DiamondView imaging show up very clearly with the red CL channel (figure 16C). The red CL channel images fail to reveal the growth features shown by the blue CL channels (figure 16, E and H), possibly suggesting that the luminescence it captures is not directly related to the nitrogen uptake of the growth zone. Instead, they show a similar periodicity in lamellae as observed in the optical grayscale hue

image (figure 8, right). The combination of the blue and red channel signals showcases the complex growth and deformation-related features, such as the slip bands and dislocation networks, in the Winston Red diamond (figure 16, F and I).

An interesting discovery for the Winston Red diamond is the presence of cellular dislocation networks and subgrain boundaries that can be resolved by PL mapping and CL imaging (figure 14A; figure 15, A and D; and figure 16, D–I). The dislocations effectively quench the luminescence from the color centers (Laidlaw et al., 2021), resulting in a granular texture that extends across different growth zones and slip bands. At the magnifications employed in this study, the density of the granular texture did not noticeably change between the slip bands. Transmission electron microscopy imaging of cellular dislocation networks in plastically deformed brown type IIa diamonds shows that the boundaries between the grains or cells are composed of high concentrations of dislocations (Laidlaw et al., 2021). Laidlaw et al. also reported clear differences in the dislocation microstructure between brown and colorless regions of the same sample. Previous pink diamond studies have also observed the cellular dislocation networks in low-nitrogen type IaA<B diamonds, enveloping grains with yellowish green luminescence from H3 centers (Gaillou et al., 2010, 2012). These patterns are most commonly observed in Group 1 pink diamonds, such as those from Argyle (Australia), Santa Elena (Venezuela), and marine deposits in Namibia (Gaillou et al., 2010, 2012; Howell et al., 2015). Referred to as "fish-scale" patterns, they were attributed to interactions between two or more directions of strain. The Winston Red diamond has similarly experienced deformation along several directions, as evidenced by its cross-cutting lamellae and Rose channels in figures 8, 9, 14, and 15.

Surprisingly, these cellular dislocation networks seem to have influenced the topography of the Winston Red diamond's facets, as seen with SEI (figure 17). Faint linear features consistent with slip planes can also be resolved. This topography may have been produced by differences in the hardness of the regions with high concentrations of dislocations. Note that the surface features presented in figure 17 (right) are observed at higher magnification than the CL images shown in figure 16.

Origin of the Color in the Winston Red Diamond. The Winston Red diamond exhibits a saturated red color that is homogeneous to the unaided eye (again, see figure 2). However, it is heterogeneous under magnification, following the graining in thin alternating red bands along three different directions (again, see figure 8). In some areas, a wavy red pattern is also observed. Although the distribution is not uniform, the regions between these lamellae also show pink or red color. The observed color is primarily due to an intense broad absorption band at 550 nm, with contributions from nitrogen-related N3 (N_3V^0), H3 (N_2V^0), and H4 ($N_4V_2^0$) defects (e.g., Orlov, 1977; Collins, 1982; Gaillou et al., 2010; Howell et al., 2015; Eaton-Magaña et al., 2018). The wavy appearance of the color graining in the Winston Red diamond, coupled with its type IaA<B classification and

Figure 17. Left: Secondary electron imaging (SEI) showing how dislocation network patterns are expressed at the surface of the diamond in the same region as in figure 16G. The box shapes are from the electron beam having rested at those regions at higher magnifications. Right: Higher magnification imaging reveals further details for the dislocation network patterns and lamellae.

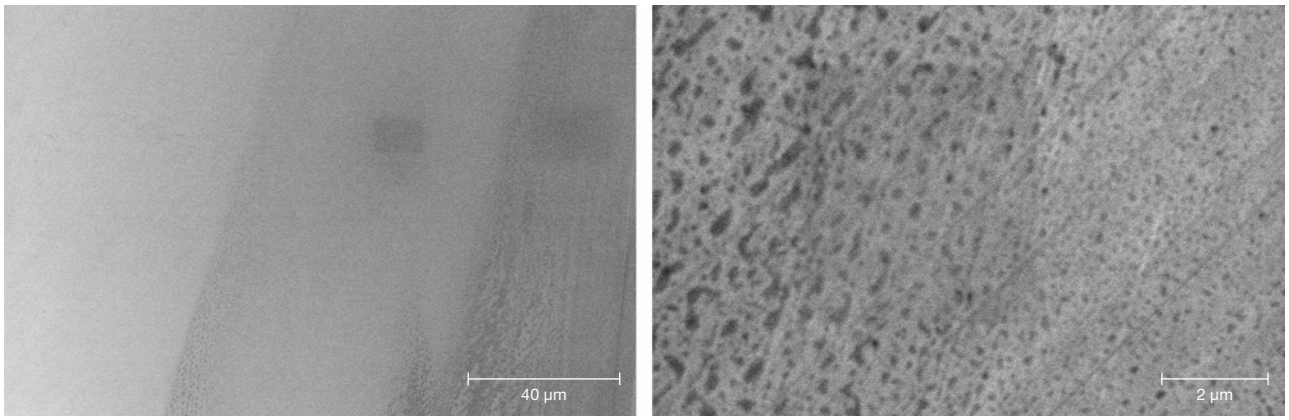

characteristic distribution of luminescing centers, show that it belongs to the pink diamond Group 1 designation, with the Fancy red color being a result of a high concentration of "pink" defects, coupled with the sample's size and cut.

The production of pink and brown colors in diamonds is closely associated with plastic deformation, and both hues frequently coexist (e.g., Eaton-Magaña et al., 2018). The timing and geological conditions that cause the shear stresses and temperatures necessary for plastic deformation resulting in pink and/or brown colors are still under debate (Smith, 2023). Diamond's explosive magmatic ascent may result in plastic deformation and the production of these defects (e.g., Fisher, 2009). Yet it is also possible that the deformation associated with these colors occurred earlier during mantle residency, where diamonds may have experienced temperatures between 900° and 1400°C (Stachel and Harris, 2008; Nimis, 2022). DeVries (1975) demonstrated that plastic deformation and microtwinning can occur at temperatures above 900°C, though deformation at temperatures as low as 770°C has also been reported (Brookes et al., 1999). After color is formed in the diamond, color preservation depends on the original defect concentrations, temperature, and time (Fisher, 2009; Fisher et al., 2009; Smith et al., 2010). Following or concurrent with deformation, exposure to high temperatures over many millions of years may also result in defects annealing out (Fisher, 2009; Fisher et al., 2009). Annealing experiments on natural brown type IIa diamonds have shown that the 550 nm band defect has a higher thermal stability than the vacancy clusters associated with the brown color, and that pink color can intensify as brown color anneals out (Fisher, 2009; Fisher et al., 2009). In summary, the Winston Red diamond likely required a perfect geological journey in order to produce and preserve such an intense red color.

Here we explore possible causes of pink and red color production and consider why Group 1 pink to red diamonds, like the Winston Red, often have colors that are more saturated and homogeneous than those reported for Group 2 diamonds (Gaillou et al., 2012; Eaton-Magaña et al., 2020). Notably, analysis of hundreds of Fancy red diamonds submitted to GIA emphasizes the prevalence of Group 1 diamonds and the extreme rarity of Group 2 diamonds (0.8%; 3 of 399 Fancy red diamonds) (figure 10, right). While the structure of the color center of the 550 nm absorption band primarily responsible for pink and red colors in diamond is still unknown, it is associated with plastic deformation. Plastic deformation can generate and move dislocations in diamond and/or create mechanical twins. However, neither dislocations nor microtwins themselves are responsible for (significant) color as they can also be observed in high concentrations in colorless diamond. Due to the frequent coexistence of brown and pink colors, the latter defect may have a similar structure to the vacancy clusters responsible for brown color (Fisher, 2009; Fujita et al., 2009; Jones, 2009; Mäki et al., 2009; Guagliardo et al., 2013). It is also possible that the movement of dislocations through plastic deformation may modify preexisting defects, creating new structures that produce pink color (Fisher et al., 2009; Laidlaw et al., 2021). The detection of the 550 nm absorption band for "nitrogen-free" type IIa diamonds (Group 3) suggests that the defect responsible may not necessarily include nitrogen, yet it is possible that the mechanism for its production is still affected by nitrogen.

Nitrogen content, preexisting dislocations, and other defects such as platelets are known to influence plastic deformation in diamonds (Evans and Wild, 1965, 1966; Wild et al., 1967; Brookes et al., 1999, 2000; Brookes and Daniel, 2001; Fisher et al., 2009). Nitrogen and platelets are thought to restrict the movement of dislocations during plastic deformation, which in natural type I diamonds are generally concentrated along {111} slip and glide planes (Evans and Wild, 1965, 1966; Wild et al., 1967). Both Group 1 and Group 2 pink diamonds are type Ia, yet those belonging to Group 1 are characterized by lower total nitrogen concentrations that are heavily aggregated, along with reduced platelet concentrations that would typically classify them as "irregular" (Woods, 1986; Gaillou et al., 2012; Howell et al., 2015). Their lower concentrations of total nitrogen and platelets may make them more ductile than Group 2 pink diamonds, facilitating plastic deformation.

It is also possible that Group 1 diamonds may have experienced more extreme deformation and natural annealing events than Group 2 diamonds (e.g., multiple events, higher temperatures, and/or prolonged time frames), resulting in their polygonized dislocation networks, higher nitrogen aggregation states, and relatively low (or absent) platelet concentrations (Sumida and Lang, 1981; Woods, 1986; Howell et al., 2015; Nimis, 2022). If the formation mechanism for the 550 nm absorption band defect involves the movement of dislocations, the

presence of polygonized dislocations between slip bands in Group 1 diamonds may be tied to the pink to red colors observed between lamellae (figure 7C) and the overall more even color compared to Group 2 diamonds.

In the case of Group 2 pink diamonds—which do not show polygonized dislocations—the pink color is concentrated around mechanical microtwins (pink lamellae) (Mineeva et al., 2007, 2009; Gaillou et al., 2010; Howell et al., 2015). Howell et al. (2015) suggested that microtwinning events are key to pink color production and speculated that the absence of direct evidence for microtwinning in Group 1 pink diamonds could be explained by "detwinning processes," possibly occurring during secondary deformation events. These hypotheses require future testing with diamonds of different nitrogen contents and aggregation states, under strain and temperature conditions similar to those in Earth's mantle. Additionally, studying more diamonds of known geographic origins would provide more concrete clues to tie pink diamond groups and colors to craton age and geological history.

In summary, the origin of the red color in the Winston Red diamond appears to be linked to two factors: relatively low nitrogen concentrations that facilitate plastic deformation, and exposure to high pressure and temperature conditions that led to significant dislocation generation and movement along several directions, resulting in the production of high concentrations of pink color–producing defects throughout the diamond. Additionally, the temperatures that the diamond experienced must have been insufficient to anneal and destroy the 550 nm band defect that produced the pink color (Fisher et al., 2009). This combination of features illustrates the unique crystallization, geological residence, and transportation history necessary for the Winston Red diamond's beautiful saturated red color.

The Geographic and Geologic Origin of the Winston Red Diamond. Historical records do not provide a geographic source for the Winston Red diamond, but the new data presented here offer some clues that unveil a likely origin. Unlike for some gem minerals, the geographic origin of gem-quality diamonds that formed deeper in Earth's relatively geochemically homogenous mantle cannot be determined based on the usual combination of inclusions, spectroscopic characteristics, and chemistry (e.g., Smith et al., 2022). Other gems are predominantly formed in the continental crust and bear characteristic signatures (e.g., inclusions) of their host rocks and geological environment. In diamonds, inclusions may give clues to paragenesis (e.g., peridotitic or eclogitic), age, and formation depth (>140 km). The Winston Red diamond contains only a few visible inclusions that are too deep inside it to identify with Raman spectroscopy (figures 2 and 9).

For pink and red diamonds, the story is slightly different. It has been demonstrated that two geological settings produce pink and red diamonds: Group 1 formed in Proterozoic (0.5–2.5 Ga) cratons, while Group 2 formed in Archean (2.5–4 Ga) cratons (Gaillou et al., 2012; Howell et al., 2015). No known primary deposits contain both Group 1 and Group 2 diamonds; however, the study of pink diamonds of known localities is limited. Information on Group 3 (type IIa colored by the 550 nm band) pink diamonds is even more rare (Eaton-Magaña et al., 2020). The current article presents FTIR data for nearly 400 Fancy red diamonds analyzed at GIA (figure 10, right), including 39.1% originating from Argyle, Australia, and 0.8% reportedly from the Minas Gerais region of Brazil.

As discussed above, the visual and spectral characteristics of the Winston Red are consistent with Group 1 diamonds. Group 1 pink diamonds with these characteristics have been reported from Argyle in Australia, Santa Elena in Venezuela, and the marine deposits in Namibia (e.g., Gaillou et al., 2010, 2012; Howell et al., 2015). Kaminsky et al. (2000) were the first to link diamonds from Venezuela (placers from the 730 Ma Guaniamo kimberlites) and Argyle (primary deposit in the 1180 Ma Argyle lamproite), as they had similar mineralogical features and geological environments. Diamonds from these deposits have a high proportion of inclusions associated with an eclogitic paragenesis and are mostly type IaA<B with low nitrogen concentrations. They formed at the bases of Proterozoic cratons that may contain a significant proportion of eclogites, formed by subduction of the continental crust. Both underwent strong tectonothermal events, with intrusions of magma and/or rifting, which are different from the more ancient Archean cratons.

As mentioned earlier, we can now trace the history of the Winston Red diamond to 1938 and suspect that, based on the old mine cut, the stone was discovered even earlier. Since we have determined that the Winston Red is a Group 1 stone, sources of Group 2 pink and possible red diamonds can be excluded, such as South Africa, Russia, Tanzania, and Canada (Gaillou et al., 2012), with the

latter two additionally having been discovered too recently. As far as we are aware, no red diamonds have been reported from India, an important historic source of diamonds. Indian pink diamonds tend to be faint to light pink type IIa colored by NV centers or the 550 nm band (Group 3) (Eaton-Magaña et al., 2018, 2020). Thus, this locality may be excluded as well. Considering Group 1 diamonds, the most commonly prolific source of pink and red diamonds is the Argyle mine. FTIR analysis of 156 Fancy red diamonds from Argyle submitted to GIA indicates that they, too, belong to Group 1. However, Argyle diamonds were first discovered in 1979 (e.g., Shigley et al., 2001); thus, this origin can be ruled out for the Winston Red. Diamonds in marine sediments from Namibia were first reported as early as the end of the nineteenth century (Schneider, 2020). A few diamonds were recovered in 1910 on Possession Island, but the operation was shut down the same year due to economic pressures. Further prospecting of the Namibian seashore began in 1958, with production beginning in the 1960s (Schneider, 2020). As for Venezuelan diamonds, several alluvial sources in the state of Roraima have been reported as early as 1890 (Harlow, 1998). Thus, Venezuela is a potential source.

Brazil is another well-known historic locality for producing pink and red diamonds, including the famous 5.11 ct Moussaieff Red diamond cut from a 13.90 ct crystal recovered from an alluvial deposit in Noroeste de Minas, Minas Gerais, Brazil, in the mid-1990s (e.g., King et al., 2002; King and Shigley, 2003; Svisero et al., 2017; Hoover et al., 2018). Unfortunately, limited information is available for this diamond, though it is noted as type Ia (no nitrogen content or aggregation state reported). Brazilian pink diamonds have been reported from the Alto Paranaíba province in the state of Minas Gerais; however, the diamonds in alluvial deposits in both Brazil and Venezuela may come from several sources (e.g., Svisero, 1995; Newman et al., 2009; Svisero et al., 2017; Hoover et al., 2018). To the best of our knowledge, only a few diamonds from Brazil have associated published data. Three Brazilian diamonds studied by Kane in 1987 (a 0.54 ct Fancy reddish purple, a 0.59 ct Fancy purple-pink, and a 0.95 ct Fancy purplish red) exhibited "closely spaced red and pink graining and color zonings" and "tatami" features. The photo in that article does not give a clear answer regarding the graining type (wavy band versus discrete lamellae), but the red color appears to be dense, like the Winston Red diamond (again, see figures 7 and 8). Unfortunately, the diamond types were not reported, but the "almost total absorption below 410 nm" suggests they were type Ia. A photo of a "Fancy Red diamond from Brazil" (no carat weight mentioned) in Shigley and Breeding (2013) shows lamellae with a relief effect, such as those from Group 2 diamonds. The current study presents FTIR data for three diamonds reportedly from Minas Gerais, suggesting that alluvial (secondary) deposits in Brazil may produce both Group 1 and Group 2 diamonds. To conclude, narrowing down our geographic origin based on dates of mining operations of Group 1 diamonds suggests that Venezuela or Brazil is the most likely origin of the Winston Red diamond; however, the true origin is still unknown.

CONCLUSIONS

The Winston Red is a magnificent unmodified Fancy red diamond recently gifted to the National Gem and

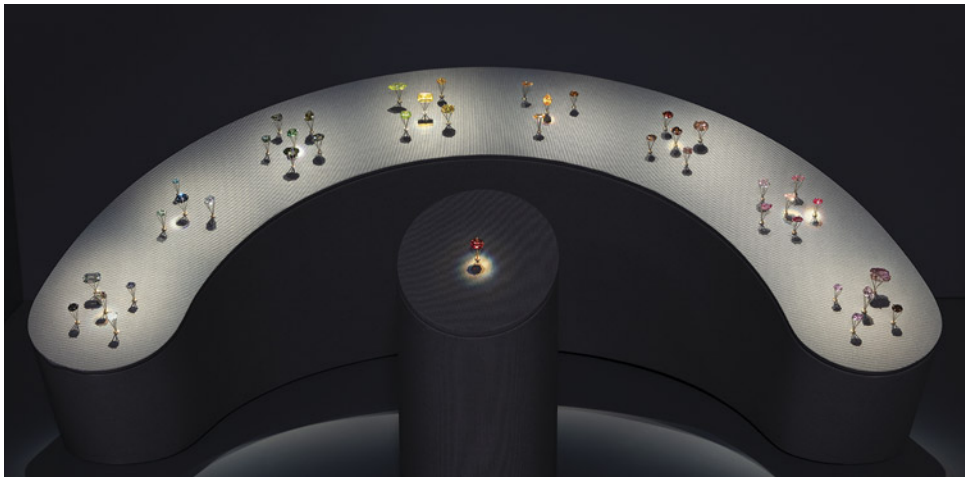

Figure 18. The Winston Red on exhibit with the Winston Fancy Color Diamond Collection in the Winston Gallery of the NMNH. Photo by James Tiller; courtesy of the Smithsonian Institution.

Mineral Collection and has been on public display at the Smithsonian NMNH since April 1, 2025 (figure 18). This first study of the gemstone reveals that the Winston Red diamond is type IaAB, with a low concentration of aggregated nitrogen defects (~7 ppm A-centers and ~76 ppm B-centers, i.e., 92% IaB). Exploring the cause of its iconic red color, a strong 550 nm absorption band is detected, along with absorption from N3 (N_3V^0), H3 (N_2V^0), and H4 ($N_4V_2^0$) centers, in agreement with previous studies of pink and red diamonds. In particular, its uniform red bodycolor is the result of a high density of pink lamellae or grain lines caused by plastic deformation, with intersecting {111}-oriented slip or glide planes aligned along at least three crystallographically equivalent directions. Colorless regions are not observed between lamellae. A cellular network of polygonized dislocations that resemble fish-scale patterns is also observed under CL and PL. Spectral and imaging analyses of the Winston Red suggest that it can be considered a particularly color-saturated example of a Group 1 "pink" diamond (e.g., Gaillou et al., 2010, 2012; Howell et al., 2015). To achieve its red color and dense dislocation networks, the Winston Red diamond likely experienced immense strain under mantle conditions.

To narrow down possible geographic origins of the Winston Red, we explored known Group 1 pink and red diamond deposits that match our historic timeline of the Winston Red diamond (pre-1938). Venezuela or Brazil is the most likely geographic origin; however, too few studies have been conducted on pink or red diamonds from these localities to support a conclusive determination. Hence, the geographic origin of the Winston Red diamond remains unknown.

ABOUT THE AUTHORS

Dr. Gabriela A. Farfan is the Coralyn W. Whitney curator of gems and minerals, and Russell C. Feather II is collection manager for the National Gem Collection, at the Smithsonian Institution, NMNH. Dr. Eloïse Gaillou is director and curator of the Mineralogy Museum of Mines Paris – PSL (Paris School of Mines). Dr. Ulrika F.S. D'Haenens-Johansson is senior manager of diamond research, Stephanie Persaud is a research associate, and Dr. W. Henry Towbin is a postdoctoral research associate, at GIA in New York. Dr. Daniel C. Jones is a research scientist at GIA in New Jersey.

ACKNOWLEDGMENTS

The authors would like to acknowledge Ronald Winston for generously gifting the Winston Red diamond to the National Gem Collection, as well as the many Smithsonian staff who helped facilitate this gift. Many thanks to Rob Wardell and Tim Rose for helping with SEM and CL analyses and to the Department of Mineral Sciences and NMNH staff for accommodating our temporary diamond lab at the NMNH. Wuyi Wang was instrumental in supporting the GIA researchers and making this project happen. Simon Lawson, R.J. Pisani, Mehdi Toosi, and Kevin DeLeon are thanked for developing the photoluminescence spectroscopy device used in this study and rapidly adapting it for mobility. Paola Martinez-Naranjo, Lilia Benjamin, and Paul Johnson are acknowledged for their assistance with the logistical plans for the instrument move. Jon Neal is acknowledged for his helpful insights into the GIA color grading system. Bonnie Zhangluo is thanked for help with the statistical analysis of diamond records at GIA. We also thank Sally Eaton-Magaña, Tom Moses, Simon Lawson, and Andrew Scott for feedback on the manuscript. We thank the archivists at Cartier (especially Libby Dale, Jenny Rourke, César Imbert, Gregory Bishop, and Violette Petit), archivists at Harry Winston, Inc. (especially Angela Hedges, Jennifer Grimes, and Levi Liu), and Francesca Cartier Brickell for their help in uncovering the history of the stone. Gabriela Farfan is supported by the Coralyn Whitney Curator Endowment, and the Department of Mineral Sciences Laboratories are supported by the Coralyn Whitney Laboratory Endowment. W. Henry Towbin is supported by the Richard T. Liddicoat Postdoctoral Research Associate Fellowship at GIA.

REFERENCES

Boyd S.R., Kiflawi I., Woods G.S. (1994) The relationship between infrared absorption and the A defect concentration in diamond. *Philosophical Magazine B*, Vol. 69, No. 6, pp. 1149–1153, http://dx.doi.org/10.1080/01418639408240185

—— (1995) Infrared absorption by the B nitrogen aggregation in diamond. *Philosophical Magazine B*, Vol. 72, No. 3, pp. 351–361, https://doi.org/10.1080/13642819508239089

Breeding C.M., Shigley J.E. (2009) The "type" classification system of diamonds and its importance in gemology. *G&G*, Vol. 45, No. 2, pp. 96–111, http://dx.doi.org/10.5741/GEMS.45.2.96

Brookes E.J., Daniel R.D. (2001) Influence of nitrogen content on the mechanical properties of diamond. In M.H. Nazaré and A.J. Neves, Eds., *Properties, Growth and Applications of Diamond*, Vol. 26, INSPEC, London, pp. 142–148.

Brookes E.J., Greenwood P., Xing G. (1999) The plastic deformation and strain-induced fracture of natural and synthetic diamond. *Diamond and Related Materials*, Vol. 8, No. 8-9, pp. 1536–1539, http://dx.doi.org/10.1016/S0925-9635(99)00080-1

Brookes E.J., Comins J.D., Daniel R.D., Erasmus R.M. (2000) A study of plastic deformation profiles of impressions in diamond. *Diamond and Related Materials*, Vol. 9, No. 3-6, pp. 1115–1119, http://dx.doi.org/10.1016/S0925-9635(99)00203-4

Byrne K.S., Anstie J.D., Chapman J.G., Luiten A.N. (2012) Optically reversible photochromism in natural pink diamond. *Diamond and Related Materials*, Vol. 30, pp. 31–36, http://dx.doi.org/10.1016/j.diamond.2012.09.005

Byrne K.S., Chapman J.G., Luiten A.N. (2014) Photochromic charge transfer processes in natural pink and brown diamonds.

Journal of Physics: Condensed Matter, Vol. 26, No. 3, article no. 035501, http://dx.doi.org/10.1088/0953-8984/26/3/035501
Cartier J. (1934) The Nawanagar Jewels. In R. Wild, *The Biography of Colonel His Highness Shri Sir Ranjitsinhji Vibhaji*. Rich & Cowan Limited, London, pp. 323–326.
Collins A.T. (1982) Colour centers in diamond. *Journal of Gemmology*, Vol. 18, pp. 37–75.
Collins A.T., Woods G.S. (1982) Cathodoluminescence from "giant" platelets, and of the 2•526 eV vibronic system, in type Ia diamonds. *Philosophical Magazine B*, Vol. 45, No. 4, pp. 385–397, http://dx.doi.org/10.1080/01418638208227446
Dean P.J. (1965) Bound excitons and donor-acceptor pairs in natural and synthetic diamond. *Physical Review*, Vol. 139, No. 2A, article no. A588, http://dx.doi.org/10.1103/PhysRev.139.A588
D'Haenens-Johansson U.F.S., Eaton-Magaña S., Towbin W.H., Myagkaya E. (2024) Glowing gems: Fluorescence and phosphorescence of diamonds, colored stones, and pearls. *G&G*, Vol. 60, No. 4, pp. 560–580, http://dx.doi.org/10.5741/GEMS.60.4.560
Deljanin B., Simic D., Zaitsev A., Chapman J., Dobrinets I., Widemann A., Del Re N., Middleton T., Deljanin E., De Stefano A. (2008) Characterization of pink diamonds of different origin: Natural (Argyle, non-Argyle), irradiated and annealed, treated with multi-process, coated and synthetic. *Diamond and Related Materials*, Vol. 17, No. 7-10, pp. 1169–1178, http://dx.doi.org/10.1016/j.diamond.2008.03.014
DeVries R.C. (1975) Plastic deformation and "work-hardening" of diamond. *Materials Research Bulletin*, Vol. 10, No. 11, pp. 1193–1199, http://dx.doi.org/10.1016/0025-5408(75)90026-4
Drukker M. (1971) The red diamond. In A.N. Wilson, Ed., *International Diamond Annual*, Vol. 1, Diamond Annual Ltd., Johannesburg, pp. 140–141.
Eaton-Magaña S., Ardon T., Smit K.V., Breeding C.M., Shigley J.E. (2018) Natural-color pink, purple, red, and brown diamonds: Band of many colors. *G&G*, Vol. 54, No. 4, pp. 352–377, http://dx.doi.org/10.5741/GEMS.54.2.352
Eaton-Magaña S., McElhenny G., Breeding C.M., Ardon T. (2020) Comparison of gemological and spectroscopic features in type IIa and Ia natural pink diamonds. *Diamond and Related Materials*, Vol. 105, article no. 107784, http://dx.doi.org/10.1016/j.diamond.2020.107784
Evans T., Wild R.K. (1965) Plastic bending of diamond plates. *The Philosophical Magazine: A Journal of Theoretical Experimental and Applied Physics*, Vol. 12, No. 117, pp. 479–489, http://dx.doi.org/10.1080/14786436508218894
—— (1966) Plastic deformation of diamond at temperatures below 1800°C. *The Philosophical Magazine: A Journal of Theoretical Experimental and Applied Physics*, Vol. 13, No. 121, pp. 209–210, http://dx.doi.org/10.1080/14786436608211997
Fisher D. (2009) Brown diamonds and high pressure high temperature treatment. *Lithos*, Vol. 112S, pp. 619–624, http://dx.doi.org/10.1016/j.lithos.2009.03.005
Fisher D., Sibley S.J., Kelly C.J. (2009) Brown colour in natural diamond and interaction between the brown related and other colour-inducing defects. *Journal of Physics: Condensed Matter*, Vol. 21, No. 36, article no. 364213, http://dx.doi.org/10.1088/0953-8984/21/36/364213
Fritsch E., Rondeau B., Hainschwang T., Quellier M.-H. (2007) A contribution to the understanding of pink color in diamond: The unique, historical "Grand Condé." *Diamond and Related Materials*, Vol. 16, No. 8. pp. 1471–1474, http://dx.doi.org/10.1016/j.diamond.2006.12.006
Fujita N., Jones R., Öberg S., Briddon P.R. (2009) Large spherical vacancy clusters in diamond – Origin of the brown coloration? *Diamond and Related Materials*, Vol. 18, No. 5-8, pp. 843–845, http://dx.doi.org/10.1016/j.diamond.2008.10.061
Gaal R.A.P. (1977) *The Diamond Dictionary*, 2nd edition, Gemological Institute of America, Santa Monica, CA, 342 pp.
Gaillou E., Post J.E., Bassim N.D., Zaitsev A.M., Rose T., Fries M.D., Stroud R.M., Steele A., Butler J.E. (2010) Spectroscopic and microscopic characterizations of color lamellae in natural pink diamonds. *Diamond and Related Materials*, Vol. 19, No. 10, pp. 1207–1220, http://dx.doi.org/10.1016/j.diamond.2010.06.015
Gaillou E., Post J.E., Rose T., Butler J.E. (2012) Cathodoluminescence of natural, plastically deformed pink diamonds. *Microscopy and Microanalysis*, Vol. 18, No. 6, pp. 1292–1302, http://dx.doi.org/10.1017/S1431927612013542
Gill J.O. (1978) A study of coloured diamonds. *Jewelers' Circular-Keystone*, Vol. 149, No. 6, pp. 83–86.
Green B.L., Collins A.T., Breeding C.M. (2022) Diamond spectroscopy, defect centers, color, and treatments. *Reviews in Mineralogy and Geochemistry*, Vol. 88, No. 1, pp. 637–688, http://dx.doi.org/10.2138/rmg.2022.88.12
Goss J.P., Briddon P.R., Hill V., Jones R., Rayson M.J. (2014) Identification of the structure of the 3107 cm^{-1} H-related defect in diamond. *Journal of Physics: Condensed Matter*, Vol. 26, No. 14, article no. 145801, http://dx.doi.org/10.1088/0953-8984/26/14/145801
Guagliardo P., Byrne K., Chapman J., Sudarshan K., Samarin S., Williams J. (2013) Positron annihilation and optical studies of natural brown type I diamonds. *Diamond and Related Materials*, Vol. 37, pp. 37–40, http://dx.doi.org/10.1016/j.diamond.2013.04.011
Harlow G.E. (1998) *The Nature of Diamonds*. Eds: American Museum of Natural History, George E. Harlow. Cambridge University Press, 278 pp.
Harris J.W., Smit K.V., Fedortchouk Y., Moore M. (2022) Morphology of monocrystalline diamond and its inclusions. *Reviews in Mineralogy and Geochemistry*, Vol. 88, No. 1, pp. 119–166, http://dx.doi.org/10.2138/rmg.2022.88.02
Hoover D.B., Karfunkel J., Walde D., Moraes R.A.V., Michelfelder G., Renger F.E., Ribeiro L.C.B., Krambrock K., Klock C.F. (2018) The Alto Paranaíba region, Brazil: A continuing source for pink diamonds? *Australian Gemmologist*, Vol. 26, No. 9-10, pp. 196–204.
Howell D., Fisher D., Piazolo S., Griffin W.L., Sibley S.J. (2015) Pink color in type I diamonds: Is deformation twinning the cause? *American Mineralogist*, Vol. 100, No. 7, pp. 1518–1527, http://dx.doi.org/10.2138/am-2015-5044
Iakoubovskii K., Adriaenssens G.J. (2002) Optical characterization of natural Argyle diamonds. *Diamond and Related Materials*, Vol. 11, No. 1, pp. 125–131, http://dx.doi.org/10.1016/S0925-9635(01)00533-7
Jones R. (2009) Dislocations, vacancies and the brown colour of CVD and natural diamond. *Diamond and Related Materials*, Vol. 18, No. 5-8, pp. 820–826, http://dx.doi.org/10.1016/j.diamond.2008.11.027
Kaminsky F.V., Zakharchenko O.D., Griffin W.L., Channer D.M. DeR., Khachatryan-Blinova G.K. (2000) Diamond from the Guaniamo area, Venezuela. *Canadian Mineralogist*, Vol. 38, No. 6, pp. 1347–1370, http://dx.doi.org/10.2113/gscanmin.38.6.1347
Kanda H., Ahmadjan A., Kitawaki H. (2005) Change in cathodoluminescence spectra and images of type II high-pressure synthetic diamond produced with high pressure and temperature treatment. *Diamond and Related Materials*, Vol. 14, No. 11–12, pp. 1928–1931, https://doi.org/10.1016/j.diamond.2005.08.015
Keswani R. (2004) *Shinde Jewels*. Assouline, New York.
King J.M., Moses T.M., Shigley J.E., Liu Y. (1994) Color grading of colored diamonds in the GIA Gem Trade Laboratory. *G&G*, Vol. 30, No. 4, pp. 220–242, http://dx.doi.org/10.5741/GEMS.30.4.220
King J.M., Shigley J.E., Guhin S.S., Gelb T.H., Hall M. (2002) Characterization and grading of natural-color pink diamonds. *G&G*, Vol. 38, No. 2, pp. 128–147, http://dx.doi.org/10.5741/GEMS.38.2.128
King J.M., Shigley J.E. (2003) An important exhibition of seven rare gem diamonds. *G&G*, Vol. 39, No. 2, pp. 136–143, http://dx.doi.org/10.5741/GEMS.39.2.136
King J.M., Shigley J.E., Jannucci C. (2014) Exceptional pink to red

diamonds: A celebration of the 30th Argyle Diamond Tender. *G&G*, Vol. 50, No. 4, pp. 268–279, http://dx.doi.org/10.5741/GEMS.50.4.268
Kane R.E. (1987) Three notable fancy-color diamonds: Purplish red, purple-pink, and reddish purple. *G&G*, Vol. 23, No. 2, pp. 90–95, http://dx.doi.org/10.5741/GEMS.23.2.90
Kunz G.F. (1926) Precious Stones. In G.A. Roush, Ed., *The Mineral Industry - Its Statistics, Technology, and Trade during 1925*. McGraw Hill, New York, NY, 906 pp.
Laidlaw F.H.J., Diggle P.L., Breeze B.G., Dale M.W., Fisher D., Beanland R. (2021) Spatial distribution of defects in a plastically deformed natural brown diamond. *Diamond and Related Materials*, Vol. 117, article no. 108465, http://dx.doi.org/10.1016/j.diamond.2021.108465
Luo Y., Breeding C.M. (2013) Fluorescence produced by optical defects in diamond: Measurement, characterization, and challenges. *G&G*, Vol. 49, No. 2, pp. 82–97, http://dx.doi.org/10.5741/GEMS.49.2.82
Machado W.G., Moore M., Woods G.S. (1985) On the dodecahedral growth of coated diamonds. *Journal of Crystal Growth*, Vol. 71, No. 3, pp. 718–727, http://dx.doi.org/10.1016/0022-0248(85)90382-3
Mäki J.-M., Tuomisto F., Kelly C.J., Fisher D., Martineau P.M. (2009) Properties of optically active vacancy clusters in type IIa diamond. *Journal of Physics: Condensed Matter*, Vol. 21, article number 364216, http://dx.doi.org/10.1088/0953-8984/21/36/364216
Massi L., Fritsch E., Collins A.T., Hainschwang T., Notari F. (2005) The "amber centres" and their relation to the brown colour in diamond. *Diamond and Related Materials*, Vol. 14, No. 10, pp. 1623–1629, http://dx.doi.org/10.1016/j.diamond.2005.05.003
Mineeva R.M., Speransky A.V., Titkov S.V., Zudin N.G. (2007) The ordered creation of paramagnetic defects at plastic deformation of natural diamonds. *Physics and Chemistry of Minerals*, Vol. 34, pp. 53–58, http://dx.doi.org/10.1007/s00269-006-0127-5
Mineeva R.M., Titkov, S.V., Speransky, A.V. (2009) Structural defects in natural plastically deformed diamonds: Evidence from EPR spectroscopy. *Geology of Ore Deposits*, Vol. 51, pp. 233–242, http://dx.doi.org/10.1134/S1075701509030052
Monnickendam A. (1955) *The Magic of Diamonds*. Hamond, Hamond and Company, London, 191 pp.
Newman J.A., de Newman Carvalho D.T., Gandini A.L., Gomes N.S., Rojas A.J. (2009) Caracterizacion mineralogica del diamante de los placeres aluvionales del Rio Icaburu, Santa Elena de Uairen, Estado Bolivar, Venezuela. *Revista de la Asociacion Geologica Argentina*, Vol. 64, No. 3, pp. 472–480.
Nimis P. (2022) Pressure and temperature data for diamonds. *Reviews in Mineralogy and Geochemistry*, Vol. 88, No. 1, pp. 533–565, http://dx.doi.org/10.2138/rmg.2022.88.10
Orlov Y.L. (1977) *The Mineralogy of the Diamond*. New York: Wiley & Sons, 248 pp.
Palik E.D. (1985) *Handbook of Optical Constants of Solids*. Academic Press, London.
Rolandi V., Brajkovic A., Adamo I., Fontana I. (2008) Argyle type Ia pink diamonds. Gemmological properties, FTIR, UV-Vis and CL features. *Australian Gemmologist*, Vol. 23, No. 5, pp. 194–203.
Ruan J., Kobashi K., Choyke W.J. (1992) On the "band-A" emission and boron related luminescence in diamond. *Applied Physics Letters*, Vol. 60, No. 25, pp. 3138–3140, http://dx.doi.org/10.1063/1.106748
Schneider G.I.C. (2020) Marine diamond mining in the Benguela Current Large Marine Ecosystem: The case of Namibia. *Environmental Development*, Vol. 36, article no. 100579, http://dx.doi.org/10.1016/j.envdev.2020.100579
Schoor M., Boulliard J.C., Gaillou E., Duparc O.H., Estève I., Baptiste B., Rondeau B., Fritsch E. (2016) Plastic deformation in natural diamonds: Rose channels associated to mechanical twinning. *Diamond and Related Materials*, Vol. 66, pp. 102–106, https://doi.org/10.1016/j.diamond.2016.04.004
Shepherd G.F. (1934) Largest ruby-red diamond. *G&G*, Vol. 1, No. 6, p. 172.
Shigley J.E., Fritsch E. (1993) A notable red-brown diamond. *Journal of Gemmology*, Vol. 23. No. 5, pp. 259–266.
Shigley J.E., Chapman J., Ellison R.K. (2001) Discovery and mining of the Argyle diamond deposit, Australia. *G&G*, Vol. 37, No. 1, pp. 26–41, http://dx.doi.org/10.5741/GEMS.37.1.26
Shigley J.E., Breeding C.M. (2013) Optical defects in diamond: A quick reference chart. *G&G*, Vol. 49, No. 2, pp. 107–111, http://dx.doi.org/10.5741/GEMS.49.2.107
Smith E.M., Helmstaedt H.H., Flemming R.L. (2010) Survival of the brown color in diamond during storage in the subcontinental lithospheric mantle. *Canadian Mineralogist*, Vol. 48, No. 3, pp. 571–582, http://dx.doi.org/10.3749/canmin.48.3.571
Smith E.M., Smit K.V., Shirey S.B. (2022) Methods and challenges of establishing the geographic origin of diamonds. *G&G*, Vol. 58, No. 3, pp. 270–288, http://dx.doi.org/10.5741/GEMS.58.3.270
Smith E.M. (2023) Plastic deformation: How and why are most diamonds slightly distorted? *G&G*, Vol. 59, No. 1, pp. 94–100.
Speich L., Kohn S.C., Wirth R., Bulanova G.P., Smith C.B. (2017) The relationship between platelet size and the B′ infrared peak of natural diamonds revisited. *Lithos*, Vol. 278-281, pp. 419–426, http://dx.doi.org/10.1016/j.lithos.2017.02.010
Spink M. (2018) Indian passion. In *The Cartier Collection: Jewelry, Vol. 1*, Flammarion, Paris, pp. 256–276.
Stachel T., Harris J.W. (2008) The origin of cratonic diamonds – Constraints from mineral inclusions. *Ore Geology Reviews*, Vol. 34, No. 1-2, pp. 5–32, http://dx.doi.org/10.1016/j.oregeorev.2007.05.002
Sumida N., Lang A.R. (1981) Cathodoluminescence evidence of dislocation interactions in diamond. *Philosophical Magazine A*, Vol. 43, No. 5, pp. 1277–1287, http://dx.doi.org/10.1080/01418618108236156
Svisero D.P. (1995) Distribution and origin of diamonds in Brazil: An overview. *Journal of Geodynamics*, Vol. 20, No. 4, pp. 493–514, http://dx.doi.org/10.1016/0264-3707(95)00017-4
Svisero D.P., Shigley J.E., Weldon R. (2017) Brazilian diamonds: A historical and recent perspective. *G&G*, Vol. 53, No. 1, pp. 2–33, http://dx.doi.org/10.5741/GEMS.53.1.2
Thomaz M.F., Davies G. (1978) The decay time of N3 luminescence in natural diamond. *Proceedings of the Royal Society of London, Series A*, Vol. 362, No. 1710, pp. 405–419, http://dx.doi.org/10.1098/rspa.1978.0141
Titkov S.V., Krivovichev S.V., Organova N.I. (2012) Plastic deformation of natural diamonds by twinning: Evidence from X-ray diffraction studies. *Mineralogical Magazine*, Vol. 76, No. 1, pp. 143–149, http://dx.doi.org/10.1180/minmag.2012.076.1.143
Welbourn C.M., Cooper M., Spear P.M. (1996) De Beers natural versus synthetic diamond verification instruments. *G&G*, Vol. 32, No. 3, pp. 156–169, http://dx.doi.org/10.5741/GEMS.32.3.156
Wild R.K., Evans T., Thomson J.J., Lang A.R. (1967) Birefringence, x-ray topography and electron microscope examination of the plastic deformation of diamond. *Philosophical Magazine*, Vol. 15, No. 134, pp. 267–279, http://dx.doi.org/10.1080/14786436708227700
Wilhelm K.F.A. (1860) *Catalogue de Brillants et Autres Pierres Precieuses de Son Altesse Monseigneur le duc Soverain de Brunswick-Lunebourg*. chez Chauvet, Bijoutier, Paris, 282 pp., https://archive.org/details/CatalogueDeBrillantsEtAutresPierresPrecieusesDeSonAltesseMonseigneur/mode/2up
Wilson W.E. (2014) Red diamond. *Mineralogical Record*, Vol. 45, No. 2, pp. 201–214.
Woods G.S. (1986) Platelets and the infrared absorption of type Ia diamonds. *Proceedings of the Royal Society of London, Series A*, Vol. 407, No. 1832, pp. 219–238, http://dx.doi.org/10.1098/rspa.1986.0094

Protect Your Customers and Your Business.

GIA®

The most effective defense against diamond deception.

In under two seconds, the easy-to-use **GIA iD100®** can identify a diamond as natural with 100% accuracy.

Speed, precision, and convenience – the ideal tool to add to your protocol.

Learn More

GIA.edu/iD100

Emeralds in Catherine de' Medici's Pendant: An Unexpected Geographic Origin

Gérard Panczer, Robin Fesquet, Lasha Moshi, Geoffray Riondet, Marie-Laure Cassius-Duranton, Lætitia Gilles-Guéry, Aurélien Delaunay, and Stefanos Karampelas

A sixteenth-century pendant on display at the Museum of the National Library of France in Paris has been linked to Catherine de' Medici, Queen of France from 1547 to 1559, and François Dujardin, goldsmith to King Charles IX beginning in 1570. The pendant is adorned with two emeralds that one historian claimed were Colombian without documentation or scientific proof. This study aims to confirm the nature of these emeralds and determine their geographic origin. The microscopic, spectroscopic, and chemical data collected in this study indicate that these two emeralds are from Pakistan. The presence of emeralds from Pakistan in this sixteenth-century European pendant provides strong evidence of the existence of trade routes between Asia and Europe during this period of time, or even before, and suggests such emeralds might be present in other royal jewels.

A pendant linked to Catherine de' Medici (figures 1 and 2) is part of the collections of the Museum of the National Library of France (Musée de la Bibliothèque nationale de France—BnF) in Paris. The museum includes the Cabinet of Coins, Medals and Antiques (Cabinet des monnaies, médailles et antiques), which was created to preserve collections of medals, coins, glyptic art, and jewels belonging to various kings of France. Established by King Charles IX, who reigned between 1560 and 1574, the Cabinet of Coins, Medals and Antiques was created as a distinct entity from the French crown jewels collection founded by King François I in 1530. As one of the oldest museums in France, it eventually opened to the public during the French Revolution in 1791.

DESCRIPTION, INTERPRETATION, AND HISTORICAL BACKGROUND

The pendant, typical of Renaissance jewelry, is made of enameled gold adorned with six gemstones in a closed-back setting that prohibits light from passing through. The symmetrical composition is organized around a large rectangular green gem. The upper part

Figure 1. The reverse side of Catherine de' Medici's pendant featuring cloisonné enamel of various colors (BnF collection no. 56.336). Photo by Serge Oboukhoff; courtesy of the Museum of the National Library of France.

See end of article for About the Authors and Acknowledgments.
Gems & Gemology, Vol. 61, No. 1, pp. 44–56,
http://dx.doi.org/10.5741/GEMS.61.1.44

Figure 2. Catherine de' Medici's sixteenth-century pendant, measuring approximately 5.5 × 4.0 × 1.4 cm and weighing 52.35 g, in enameled gold with emeralds and four colorless gems (BnF collection no. 56.336). Photo by Serge Oboukhoff; courtesy of the Museum of the National Library of France.

of the pendant is comprised of a mask and a motif forming the letter M, with a smaller triangular gem set in the center, and symmetrically flanked by four colorless step-cut gems, two trapezoidal and two square. Two winged putti frame the main gem, which is underlined by the *dextrarum iunctio* (joining right hands) motif. At the bottom of the pendant is a small wire loop from which a pearl may have been suspended, as was customary in sixteenth-century European jewelry. The gold frame is richly decorated with *ronde-bosse* enamel in a variety of bright colors. The reverse side of the pendant is entirely covered with cloisonné enamel of various colors, depicting a geometric design of button patterns, stylized flowers, six-rayed stars, and gold palm motifs (figure 1). There are no visible clasps, but

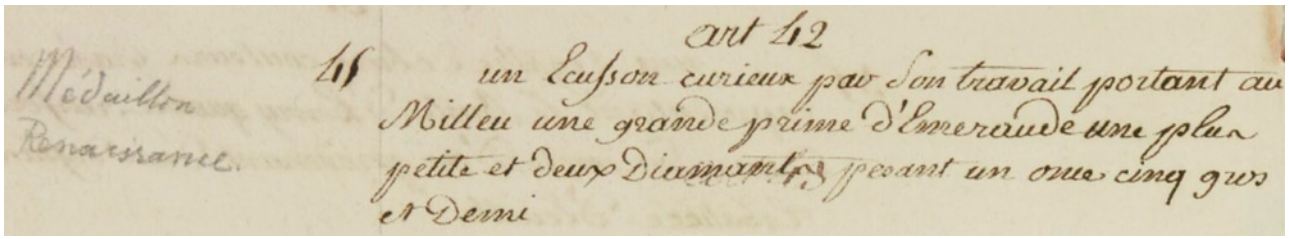

Figure 3. Description of the pendant by Pierre Bénézech in article 42 of Procès-verbal des objets envoyés par l'administration de la Monnaie au Muséum des Antiques de la Bibliothèque nationale *(December 21, 1796). For translation, see table 1.*

two small hooks on the side (upper right of figure 1) could have been used to sew the jewel onto a hat or hang it from a chain.

The first description associated with the pendant was written by Pierre Bénézech, Minister of the Interior during the Directoire, in 1796 (figure 3, translation in table 1). Interestingly, Bénézech described the main gem as "*une grande prime d'Emeraude*," which at the time meant the large green gem was not very transparent but more translucent to opaque. This description was published in *Procès-verbal des objets envoyés par l'administration de la Monnaie au Muséum des Antiques de la Bibliothèque nationale* (Report on items sent by the Mint to the National Library's Museum of Antiques) that later became the Cabinet of Coins, Medals and Antiques. In this report, the origins of some of the precious objects were written in the margins. Some of the objects came from the Garde-Meuble, where the royal collections were conserved. However, nothing is written in the margin next to the pendant, so the royal origin of such a jewel can only be a supposition based upon the current state of knowledge (figure 3; see again table 1). Other later descriptions are associated with the pendant. Among them is one by Théophile Marion Dumersan (1780–1849), curator at the Cabinet of Coins, Medals and Antiques of the Royal Library, which was uncovered during the present study (figure 4, translation in table 1).

TABLE 1. Historical descriptions of Catherine de' Medici's pendant.

Year	Author	Description (English translation from French)
1796	Pierre Bénézech, Minister of Interior during the Directoire from 1795 to 1797	"A curious escutcheon bearing in the middle 'a large emerald stone,' a smaller one and two diamonds weighing one ounce, five gros and a half." (Bénézech, 1796)
1838	Théophile Marion Dumersan, Curator at the Cabinet of Coins, Medals and Antiques of the Royal Library	"A very elegant enamel jewel, in which is set an emerald supported by two loves. At the top, a small frontal head. Below, two hands joined, a symbol of union. This jewel was probably made for a wedding: it dates from the fifteenth century" (Dumersan, 1838)
1858	Anatole Chabouillet, Curator at the Cabinet of Coins, Medals and Antiques of the Royal Library	"Jewel representing the altar of Concord. An emerald table in the shape of a long square represents the altar, which is characterized by two joined hands in enameled gold below. In the rich frame of this table are two loves which serve as supports. An emerald triangle is placed above the table. H: 55 mm; W: 40 mm. Good sixteenth-century work" (Chabouillet, 1858, quoted by Scordia, 2010)

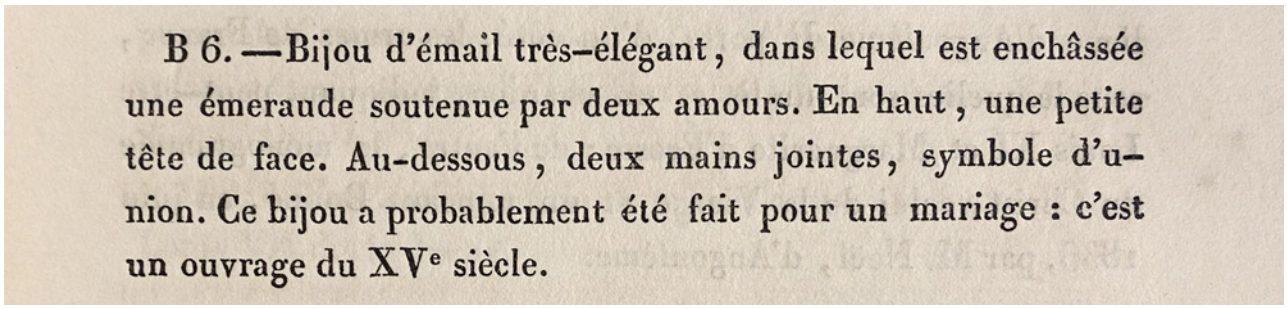
B 6. —Bijou d'émail très-élégant, dans lequel est enchâssée une émeraude soutenue par deux amours. En haut, une petite tête de face. Au-dessous, deux mains jointes, symbole d'union. Ce bijou a probablement été fait pour un mariage : c'est un ouvrage du XV^e siècle.

Figure 4. Description of the pendant by Théophile Marion Dumersan (1838), from author GR's private library. For translation, see table 1.

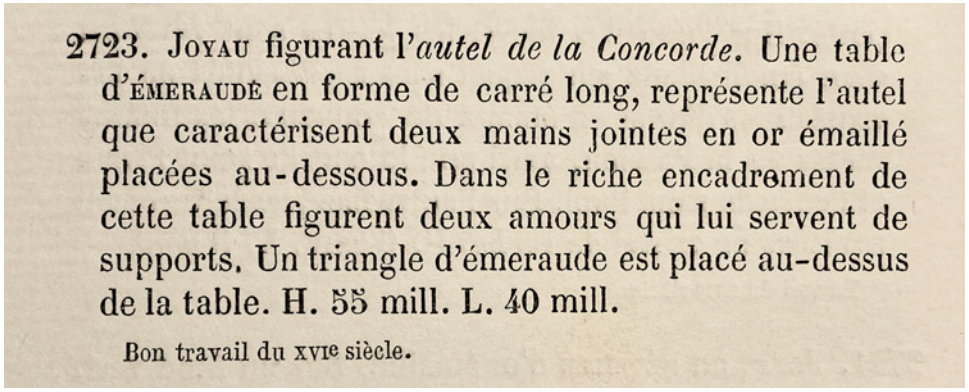
2723. Joyau figurant l'*autel de la Concorde*. Une table d'émeraude en forme de carré long, représente l'autel que caractérisent deux mains jointes en or émaillé placées au-dessous. Dans le riche encadrement de cette table figurent deux amours qui lui servent de supports. Un triangle d'émeraude est placé au-dessus de la table. H. 55 mill. L. 40 mill.

Bon travail du XVIe siècle.

Figure 5. Description of the pendant by Anatole Chabouillet (1858), from author GR's private library. For translation, see table 1.

Regarding its meaning, such a jewel can have different interpretations. The one proposed by Dumersan, who hypothesized a bridal jewel, is particularly convincing, even if the statement that the piece was made during the fifteenth century is most likely inaccurate. In 1858, Anatole Chabouillet (1814–1899), curator of the Cabinet of Coins, Medals and Antiques of the Royal Library from 1859 to 1890, qualified the pendant in his *Catalogue* as "good sixteenth-century work" and described it as "*l'autel de la Concorde*" (the altar of Concord) (figure 5; see table 1 for translation), traditionally associated with marriage since antiquity. The combination of the *dextrarum iunctio* motif with the emerald's symbolism related to faith, virginity, chastity, and love during the Renaissance was particularly meaningful in a bridal context (Cassius-Duranton, 2022, 2024). Regarding the pendant's provenance, however, none of the descriptions listed and translated in table 1 mention the commissioner or recipient of the jewel.

In Brief

- A sixteenth-century pendant, linked to Catherine de' Medici, is on display at the Museum of the National Library of France in Paris, and contains two emeralds previously believed to be of Colombian origin.
- Microscopic, spectroscopic, and chemical analyses confirm that the emeralds are from Pakistan, challenging the previous assumption.
- The presence of Pakistani emeralds in the pendant provides evidence of trade routes between Asia and Europe during the sixteenth century, or potentially even earlier if the emeralds of this jewelry piece are reused, and may suggest similar emeralds in other royal jewels.

The pendant's association with Catherine de' Medici (1519–1589) was suggested for the first time in 1966 by Yvonne Hackenbroch, curator at the Metropolitan Museum of Art in New York and recognized specialist of Renaissance jewelry. Catherine de' Medici (figure 6) was born in Florence and was Queen of France from 1547 to 1559 by marriage to King Henry II. She was the mother of three French kings who succeeded one another: François II (1559–1560), Charles IX (1560–1574), and Henry III (1574–1589).

Figure 6. Catherine de' Medici, Queen of France from 1547 to 1559. Oil painting on wood (23.9 × 19.1 cm) by François Clouet, ca. 1565. Courtesy of Carnavalet Museum – History of Paris.

The time of her sons' reigns has been called "the age of Catherine de' Medici" because she extensively influenced French politics with controversial results. In 1966, Hackenbroch discovered an exceptional document in the BnF manuscript department ("*Recueil de devises grecques...,*" 16th century): a letter of order dated November 16, 1571, written by Catherine de' Medici to French jeweler François Dujardin, commissioning an emerald jewel for Christmas (de Vielcastel, 1855) (figure 7).

Hackenbroch included this English translation in her 1966 publication:

> The emerald is a brittle stone which breaks easily, and there are two hands symbolizing faith which enclose the emerald; there must be a word saying that fides and friendship which are the desire of the one who presents this jewel are not like the stone, but like the two hands which are inseparable and the color of the enamel on the jewel which is yellow lasting without growing pale.
>
> Du Jardin [...] in order that there should be no mistake concerning my wish to receive at Christmas that I asked of you in a note written by my hand, I beg you to hurry executing and sending it to me for the already mentioned Christmas time, while I pray to God, Du Jardin, to protect you. Written at Duretal, November 16th 1571.

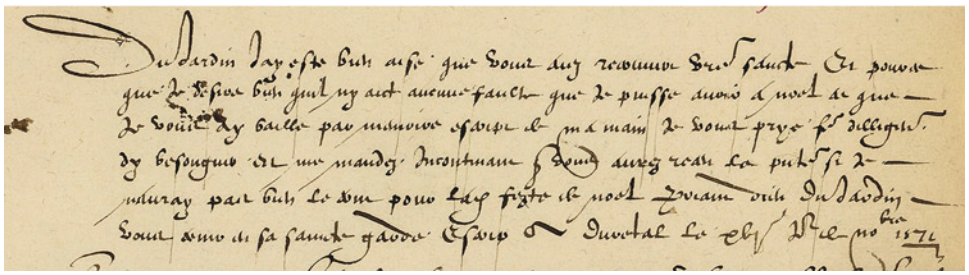

*Figure 7. Letter of order by Catherine de' Medici to jeweler François Dujardin commissioning an emerald jewel ("*Recueil de devises grecques...," *16th century).*

Although the above description does not exactly fit the jewel presented here, it is very similar. This document led Hackenbroch to associate the pendant with an important historic provenance, Catherine de' Medici, and Dujardin, a prestigious jeweler of the Renaissance and goldsmith to King Charles IX from 1570 to 1574. Based on her knowledge of the historic context, but without any documentary evidence, she suggested it was a jewel related to the French Wars of Religion (1562–1598), given by Catherine de' Medici as a Christmas gift to her son King Charles IX (1550–1574), who reigned from 1560 to 1574 (Hackenbroch, 1966). The political dimension does not contradict the bridal interpretation of the jewel, because, at the highest level of the state, marriage was used as a political weapon to create alliances. Conferring multiple meanings and different levels of interpretation (public, private, intimate) on a work of art was a common practice in the Renaissance (Scordia, 2010).

Further supporting Hackenbroch's hypothesis, we can connect the *dextrarum iunctio* motif to another work associated with Catherine de' Medici. This motif was also depicted on the binding of the *Horae ad usum Romanum* ("Roman hours for use"), called the *Book of Hours of Catherine de' Medici* and among the most important manuscripts of the French Renaissance. Initially ordered by King François I circa 1530, who gave it to Catherine after her marriage in 1533 to his son King Henry II (1519–1559) who reigned from 1547 to 1559 (*Horae ad usum Romanum*, 16th century), the book was transformed through time by Catherine de' Medici and later by its successive owners during the sixteenth and seventeenth centuries. During its restoration from 2019 to 2022, Maxence Hermant and Mathieu Deldicque determined that the precious binding in enameled gold was ordered in 1572 by Catherine de' Medici from her goldsmith, Mathurin Lussault. Interestingly, on the binding, inscribed on a ribbon surrounding the *dextrarum iunctio* motif, is the Latin motto *Firmus amor junctae adstringunt quem vincula dextrae* ("The enduring love whose clasped hands tighten the bonds"). The binding corners are covered with the Queen's monogram composed of two embracing Cs bearing an H, representing Catherine de' Medici and her late husband King Henry II's initials (Hermant and Deldicque, 2022) (figure 8).

Figure 8. Horae ad usum Romanum *(*Book of Hours of Catherine de' Medici*), 16th century (10.5 × 7.0 cm). BnF, MS NAL 82.*

Regarding the emeralds in the pendant, no document provides any information about their provenance or geographic origin. In 2010, medieval historian Lydwine Scordia published an article dedicated to the jewel. After reiterating Hackenbroch's point of view, she wondered about the origin of the emeralds set in the pendant and claimed the following:

> "The magnificent color of the emeralds in this pendant indicates that they were mined in South America. Until the voyages of Columbus, emeralds came from the Indian continent. The discoveries of the sixteenth century transformed the geography of their extraction. The emeralds in this jewel are said to have come from a gift from the Aztec emperor Montezuma II to Cortes, who in turn gave them to Charles Quint. The latter is said to have given them to the court on his election to the empire in 1519; unless they were given at the time of Philip II's marriage to Elisabeth de Valois, daughter of Henri II and Catherine de Médicis, in 1559."

However, Scordia gives no historic source to support these statements, and according to historians like Kris Lane, who studied the history of the Colombian emerald trade, they seem highly improbable because the arrival of Colombian emeralds on the European market occurred after 1519 (Lane, 2010). The only reliable way to determine a gem's geographic origin is based on gemological analysis, not on general knowledge and beliefs.

Therefore, the main goal of this paper is to present the first gemological, spectroscopic, and chemical study of the green gems of this historic pendant, presenting their characteristics and in parallel assessing their geographic origin. This study is in line with other scientific studies (e.g., Bosshart, 1989; Fritsch et al., 2007; Gaillou and Post, 2007; Farges et al., 2015; Karampelas et al., 2022) conducted on historical artifacts conserved in museums, in order to advance knowledge on such national treasures.

MATERIALS AND METHODS

Only the two green gems in Catherine de' Medici's pendant were examined in this study. Due to its historic importance, the pendant was analyzed in its conservation place, using strictly nondestructive mobile instruments belonging to the Université de Lyon and the Laboratoire Français de Gemmologie (LFG). The BnF Museum generously provided access to the piece, limited to two three-hour sessions for four people.

Observation was performed using a Zeiss Stemi 508 binocular microscope (magnification up to 80×) equipped with a fiber-optic light source and an incorporated camera to acquire photos. Luminescence was examined using a 6-watt ultraviolet lamp (Vilber Lourmat VL-6.LC) with long-wave (365 nm) and short-wave (254 nm) UV light.

Raman spectra were acquired with an Ocean Optics QE Vis-NIR mobile spectrometer with a 785 nm laser excitation. Raman spectra were recorded in the 200–2000 cm^{-1} range with an exposure time of 5 seconds and five accumulations, at a spectral resolution of 10 cm^{-1}. The spectrometer was calibrated using the 1331.8 cm^{-1} diamond band. Ultraviolet/visible/near-infrared (UV-Vis-NIR) spectra were collected with an Ocean Optics USB2000 mobile spectrometer coupled with optical fibers for light delivery to the sample and detection of the resulting signal, from 250 to 980 nm, with an acquisition time of 1.2 seconds (two cycles) and a spectral resolution of 1.5 nm. Energy-dispersive X-ray fluorescence (EDXRF) analyses were performed using a Thermo Scientific NITON XL3t 980 GOLDD+ XRF Analyzer (accelerating voltage 50 kV and beam current 40 μA) with a lateral resolution of 3 mm and an analysis time of 120 seconds. The preinstalled "ores" mode was calibrated using NIST SRM 610 and 612 glass standards.

RESULTS AND DISCUSSION

The two gems are of dark green color and both cut en cabochon; the larger is rectangular and the smaller triangular. The approximate dimensions of both emeralds (confirmed by Raman spectroscopy) were measured, with the larger being about 21.5 × 16.5 × 4.5 mm and the smaller about 9.5 × 6.5 × 3.5 mm. The emeralds' lengths and widths were measured directly with a Leveridge caliper because of the closed-back setting, but the stones' depths could only be measured indirectly. This was done using an optical microscope by precisely focusing on the samples' surfaces and bottoms and calculating the difference (apparent depth) using the microscope's vernier scale. The emeralds' depths were calculated by multiplying the apparent depths by the samples' refractive index (1.58 used here). The approximate calculated weights were 12.5 and 1.5 ct, respectively (Carmona, 1998). Both emeralds were inert under long-wave and short-wave UV light.

Figure 9 shows the Raman spectrum of the larger sample; the smaller emerald presents a very similar Raman spectrum. The Raman band at around 685 cm^{-1} is associated with Be-O stretching, and the vibrational band at around 1070 cm^{-1} is related to Si-O and/or Be-O stretching in beryl (Moroz et al., 2000;

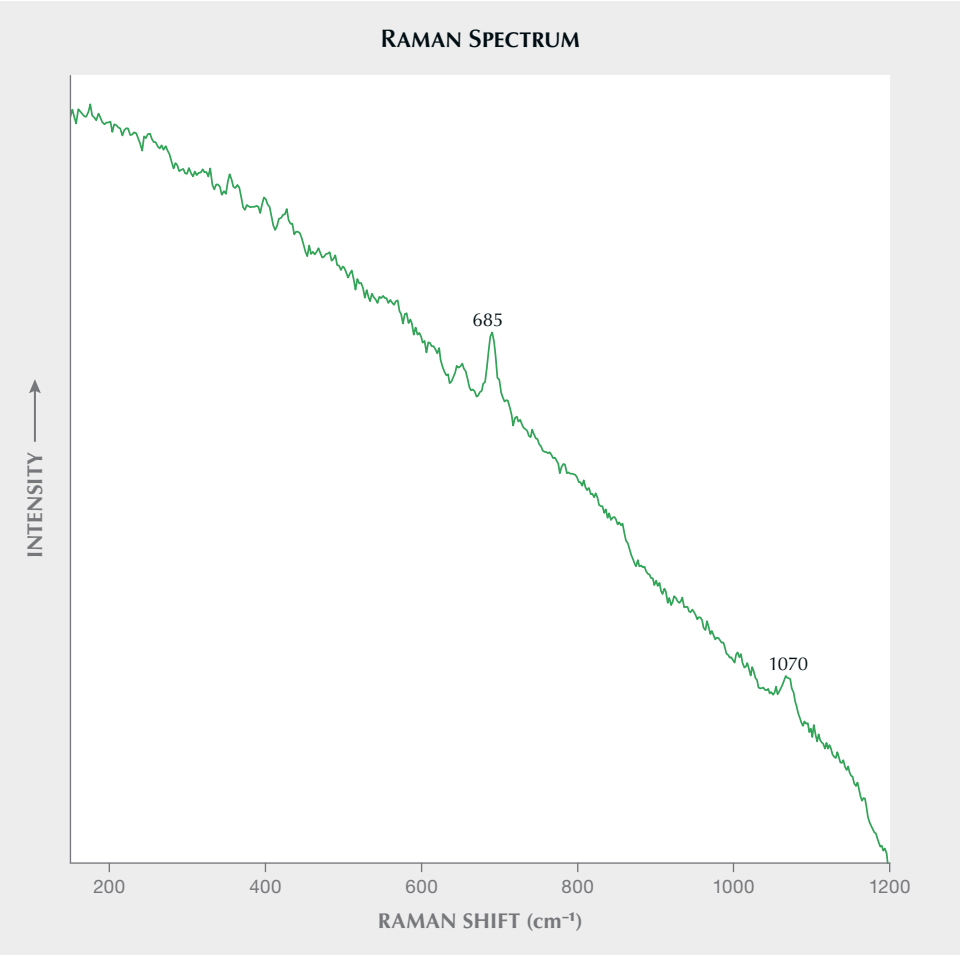

Figure 9. Raman spectrum of the large emerald with a laser excitation at 785 nm. The bands at approximately 685 and 1070 cm^{-1} are characteristic of beryl, while the more intense background signal toward the lower Raman shifts is due to strong luminescence in the red and near-infrared regions.

Bersani et al., 2014). A strong luminescence in the red and near-infrared regions created a background signal that is more intense in the lower Raman shift region.

Observing the emeralds under an optical microscope was difficult because of the mounting, but both gems were found to contain natural inclusions. The larger emerald displayed various fissures as well as roundish multiphase inclusions and a large number of closely clustered thin films (figure 10). The smaller emerald was more included, exhibiting mainly

Figure 10. Inclusions in the pendant's larger emerald: fissures (A), multiphase inclusions with roundish outlines (B), and thin films (C). Photomicrographs by Gérard Panczer (A) and Aurélien Delaunay (B and C); fields of view 3.0 mm (A) and 1.5 mm (B and C).

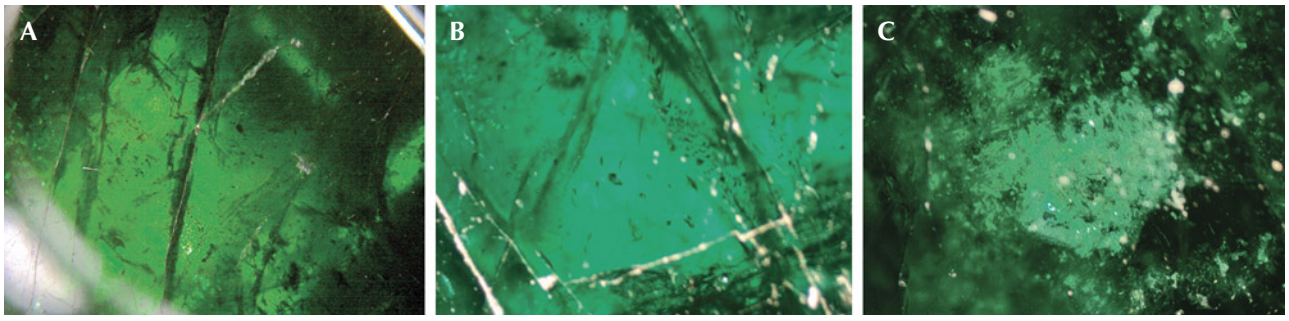

flakes/sheets, possibly micas (identified only under the microscope), as well as some small roundish multiphase inclusions (figure 11). These inclusions are not consistent with those observed in emeralds from Colombia; for example, multiphase inclusions with jagged outlines are usually present in emeralds from Colombia, and due to their geological formation, micas are completely absent (Bosshart, 1991; Saeseaw et al., 2014, 2019). No indications of treatment, such as clarity enhancement, were observed microscopically in either of these samples.

UV-Vis-NIR absorption spectra from 250 to 980 nm are shown in figure 12. Both emeralds present similar spectra, with intense absorptions at around 430 and 620 nm that are both linked to Cr^{3+} in the octahedral site, as well as two sharp bands (R-lines) of weak intensity at around 680 nm due to Cr^{3+} (Bosshart, 1991; Saeseaw et al., 2014, 2019; Schmetzer, 2014). Absorptions of low to medium intensity linked to iron at around 370 and 835 nm (Fe^{3+} and Fe^{2+}, respectively) are observed at the UV and NIR regions of the electromagnetic spectra, and a water-related band at around 965 nm was observed (Wood and Nassau, 1967; Saeseaw et al., 2014, 2019; Schmetzer, 2014). These spectra are different from those observed in the vast majority of emeralds from Colombia, as the latter rarely present iron-related absorptions of low to medium intensity in the UV and NIR regions of the spectra (Bosshart, 1991; Saeseaw et al., 2014, 2019; Karampelas et al., 2019). In some rare cases, iron-related absorptions might be present in Colombian emeralds (see figure 3 in Saeseaw et al., 2019), but these rarer Colombian emeralds still have inclusion scenes similar to all emeralds from Colombia, as well as very low concentrations of alkali metals (see text below for rubidium content).

EDXRF chemical analyses are presented in table 2. Both emeralds show relatively high concentrations of chromium and iron and low concentrations of vanadium. It is important to note that all measurements were made with a mobile instrument on a cabochon with no absolutely flat surface, a measurement not as precise or as accurate as a benchtop spectrometer (e.g., chromium content is extremely high for the large emerald). However, the relative intensities of the chromophore elements were Cr>Fe>>V. These chemical analyses are different from those observed in emeralds from Colombia, which have higher vanadium content and lower iron content: V≥Cr>Fe and in some cases Cr>V>Fe (Schwarz and Pardieu, 2009; Saeseaw et al., 2014, 2019; Karampelas et al., 2019; Alonso-Perez et al., 2024; and references therein). Moreover, both emeralds present detectable levels of scandium and rubidium, with cesium and gallium below the detection limit of the instrument. Emeralds from Colombia have rubidium levels below 10 ppmw and rarely have iron levels at or above 2000 ppmw (Saeseaw et al., 2014, 2019; Karampelas et al., 2019).

Taking into account the microscopic, spectroscopic, and chemical data presented above, the sup-

Figure 11. Flakes/sheets (possibly mica) and roundish multiphase inclusions in the pendant's smaller emerald. Photomicrographs by Aurélien Delaunay; fields of view approximately 0.8 mm (left) and 1.5 mm (right).

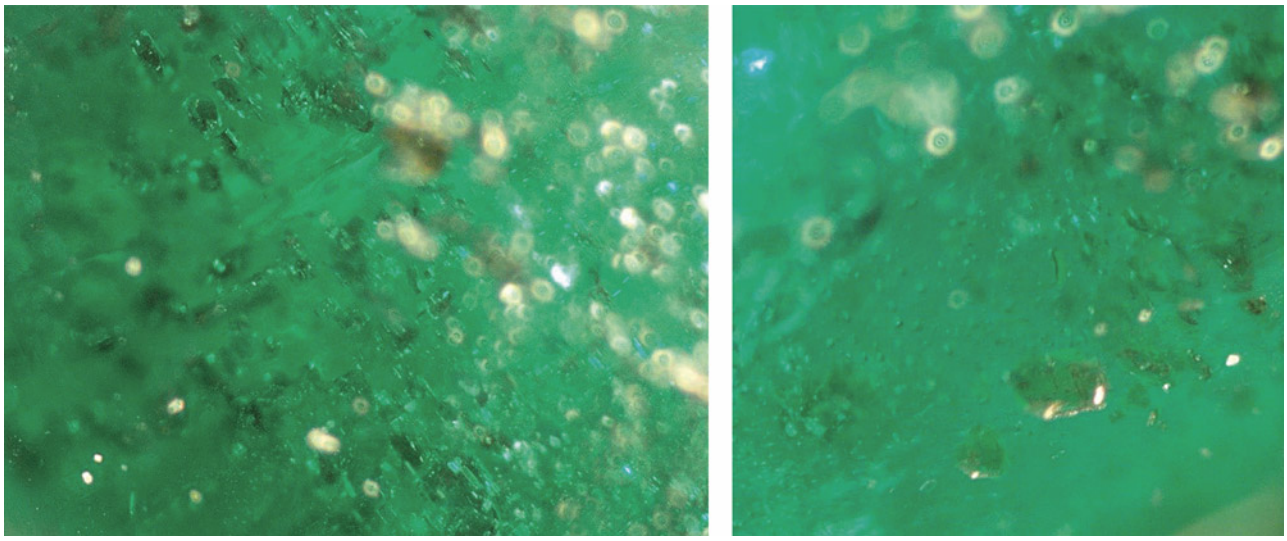

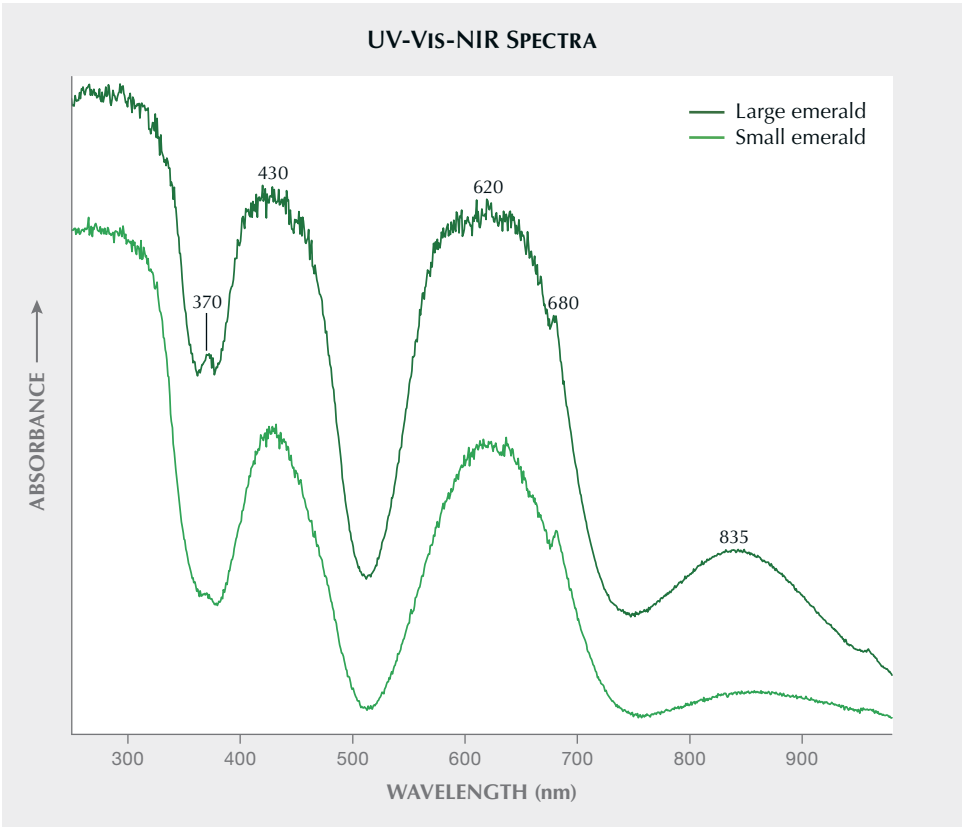

Figure 12. UV-Vis-NIR absorption spectra of the large and small emeralds. In both spectra, absorptions related to chromium (430 and 620 nm) and iron (370 and 835 nm) are observed. These spectra are different from those observed in the majority of emeralds from Colombia. The absorption band at around 965 nm is related to beryl's water absorption. Spectra are offset vertically for clarity.

posed Colombian origin of these emeralds can be eliminated. However, South American emeralds were mentioned in the literature; these include not only those from Colombia but also those from Brazil. Brazilian emeralds are not mentioned in the literature before the twentieth century; other American origins mentioned are Mexico and Peru, but it was found that those stones were actually from Colombia (Webster, 1955; Weldon et al., 2016).

TABLE 2. Trace element concentrations (in ppmw) measured by EDXRF.

	Large emerald	Small emerald	Detection limit (ppmw)
No. of measurements	4	2	
Cr	22151–22807	9992–10320	35
Fe	10475–11323	8214–8842	35
V	319–403	282–348	35
Sc	300–400	250–350	15
Rb	44–56	47–59	10

The characteristics of the studied emeralds match those observed in emeralds from Swat Valley in Pakistan. In particular, the relatively high iron and chromium, the relatively low vanadium, and the detectable rubidium measured with EDXRF, as well as the low to medium absorption features in the visible range due to iron, can be observed in emeralds from this region. The inclusions observed in the studied samples have been observed in those from Swat Valley (Guo et al., 2020; Cornuz, 2021). Emeralds from other historic sources, such as Egypt, Afghanistan, and Austria, present different microscopic and chemical characteristics (Saeseaw et al., 2014, 2019; Nikopoulou et al., 2023, 2025).

The Swat Valley emerald deposits are generally cited as having been discovered in 1958 (Gübelin, 1982). However, the emerald in a Gallo-Roman earring preserved in the National Museum of Natural History (Muséum National d'Histoire Naturelle) in Paris, discovered in Miribel, France, in 1997, was found to have an oxygen isotope composition corresponding to emeralds from Swat Valley (Giuliani et

al., 2000; Schwarz and Giuliani, 2002). Additionally, a thirteenth-century reliquary crown conserved in the Diocesan Museum in Namur (Belgium) appears to contain emeralds from Pakistan based solely on chemistry (Bruni et al., 2021). These results should be further confirmed using nondestructive methods similar to those employed in the present study.

Swat Valley emeralds are believed to have been mined since ancient times, thus long before 1958 as mentioned by Gübelin (1982). After the conquests of Alexander the Great (300 BCE), Pakistan, including Peshawar and Swat, became part of the Maurya Empire, and then later, of the Kingdom of Gandhara, whose valleys served as trade routes for silk and other products. Therefore, these emerald deposits, located on the Silk Road, were likely exploited at that time (Schwarz and Pardieu, 2009; Michelou et al., 2022). The emeralds currently mined in Pakistan are generally small, but larger samples can be found as well (Schwarz and Giuliani, 2002; Guo et al., 2020). This is consistent with historic sources described in some ancient texts.

Before the discovery of Colombian emerald deposits during the sixteenth century, Bactria, Egypt, and Scythia were recognized as the main emerald sources. These were mentioned by Pliny the Elder in his *Natural History*, written during the first century. Pliny was considered a major authority on naturalism, and his comments on gems were repeated in lapidaries—ancient treatises dedicated to gemstones—until the advent of modern science. Pliny's main source was Theophrastus, pupil of Aristotle, contemporary of Alexander the Great, and author of the first preserved lapidary book in Western history, *On Stones*, written at the end of the fourth century BCE. He wrote the first description of *smaragdos* (σμάραγδος), a bright green gemstone found only in Bactria, a historic region of Central Asia spanning parts of present-day Afghanistan, Tajikistan, Uzbekistan, and northwest Pakistan. Hence, Pakistan could be one of the first historic emerald sources. Egyptian emeralds were discovered later, during the Roman Empire, and supplied an important international trade as reported by Greek, Indian, Arab, and Persian lapidaries until the discovery of Colombian emeralds (Cassius-Duranton, 2024).

The mystery of Scythian emeralds has so far not been solved. According to the Greek historian Herodotus, the Scythian tribes covered a large territory between Europe and Asia, including the Ural region (Herodotus, 440 BCE). No Russian emeralds have been identified in jewelry from before the nineteenth century. An Austrian origin has been suggested of some historical emeralds (identified solely with oxygen isotopes; Giuliani et al., 2000), but Austria was not included in the area once called Scythia and is not mentioned in the lapidaries. Ancient scholars offered varying interpretations of Scythia's location. Herodotus also mentioned the Scythians from Asia, and the Roman Solinus (third to fourth centuries), inspired by Pliny the Elder, discussed different Scythias, including the "Asian Scythia" described as the country of the emeralds (Solinus, third century BCE).

Reportedly, when Hernán Cortés entered modern-day Mexico in 1519, he received emeralds from Montezuma as gifts, and the Spanish originally assumed Peru as the source, where emeralds were abundant among the Incas (see Weldon et al., 2016, and references therein). Spanish conquistador Gonzalo Jiménez de Quesada reached the Eastern Cordillera of the Andes in 1537 and founded Bogotá in 1538. Friar Pedro Simón chronicled Quesada's discovery of the first emerald source (see again Weldon et al., 2016, and references therein). But even if the emerald deposits of Chivor and Muzo in Colombia were discovered by the Spaniards during the sixteenth century and were used before by the native Chibcha and Muisca, the massive arrival of Colombian emeralds on the international market began no sooner than in the early seventeenth century (Lane, 2010). In the lapidaries, Anselmus Boetius de Boodt (1609) is among the first who wrote about emeralds from the New World, saying that they were less beautiful than "oriental" emeralds whose provenance were uncertain. Later, authors such as Robert de Berquen (1661) and Pouget Fils (1762) also mentioned "oriental" emeralds in their treatises, comparing them with the new ones found in the West. This might be the reason a Colombian emerald of medium quality was described as from Egypt in a museum collection (Karampelas et al., 2024).

The results of the gemological analyses presented here have demonstrated that emeralds from Pakistan were used during the sixteenth century, consistent with reports from the authors of the lapidaries. The present study also shows that knowing the geographical origins of gemstones adds important information to the history of jewelry pieces. This hypothesis invalidates a South American origin of the emeralds in the pendant and allows us to consider a supply route from South Asia to Europe during the sixteenth century (Putnam, 2023) or reuse of ancient gems.

CONCLUSIONS

A pendant linked to Catherine de' Medici, part of the collection of the BnF Museum, is considered one of the most extraordinary Renaissance jewels containing emeralds. Before the present study, its emeralds were believed to be of South American/Colombian origin. However, chemical (e.g., Cr>Fe>>V), spectroscopic (e.g., iron-related absorptions in the visible range), and microscopic analyses (presence of mica and roundish multiphase inclusions and absence of multiphase inclusions with jagged outlines) rule out this assumption; these characteristics are more consistent with those of emeralds from Pakistan (Swat Valley). This article confirms the benefits of interdisciplinary research projects between historians and gemologists and the importance of scientific studies of museum samples, as such research can help historians in their understanding of artworks and allow curators to better inform the public. Hopefully this study encourages more institutions to grant access to researchers, so they can share new information about specimens with the scientific community as well as the general public.

ABOUT THE AUTHORS

Dr. Gérard Panczer (gerard.panczer@univ-lyon1.fr) is a professor at the Institute of Light and Matter at Lyon 1 University in Villeurbanne, France, where Robin Fesquet and Lasha Moshi are gemology students. Geoffray Riondet is an expert in ancient jewels (Maison Riondet, Lyon, France). Marie-Laure Cassius-Duranton is a gemology and art history researcher, and Dr. Lætitia Gilles-Guéry is a gemologist, at L'ECOLE, School of Jewelry Arts (with the support of Van Cleef & Arpels) in Paris, France. Aurélien Delaunay is director at Laboratoire Français de Gemmologie (LFG) in Paris. Dr. Stefanos Karampelas (s.karampelas@lfg.paris or skarampelas@geo.auth.gr) is chief gemologist at LFG, as well as professor of mineralogy and gemology at the School of Geology of the Aristotle University of Thessaloniki (Greece).

ACKNOWLEDGMENTS

The authors warmly thank Mathilde Avisseau-Broustet, chief curator in the Department of Coins, Medals and Antiques, in charge of the collections of glyptic art, sculptures, bronzes, and decorative arts at the National Library (Paris) for having given them access to the studied pendant. The authors also thank the reviewers for their constructive comments that improved the quality of the manuscript.

REFERENCES

Alonso-Perez R., Day J.M.D., Pearson D.G., Luo Y., Palacios M.A., Sudhakar R., Palke A. (2024) Exploring emerald global geochemical provenance through fingerprinting and machine learning methods. *Artificial Intelligence in Geosciences*, Vol. 5, article no. 100085, http://dx.doi.org/10.1016/j.aiig.2024.100085

Bénézech P. (1796) Lettre du ministre de l'Intérieur aux conservateurs, annonçant l'envoi de l'état des objets choisis à la Monnaie, Paris, 29 frimaire an V. Acquisitions provenant de la Monnaie, du Garde-meuble. Archives du cabinet des médailles (1794-an IX), https://gallica.bnf.fr/ark:/12148/btv1b10466043p

Bersani D., Azzi G., Lambruschi E., Barone G., Mazzoleni P., Raneri S., Longobardo U., Lottici P.P. (2014) Characterization of emeralds by micro-Raman spectroscopy. *Journal of Raman Spectroscopy*, Vol. 45, No. 11–12, pp. 1293–1300, http://dx.doi.org/10.1002/jrs.4524

Boetius de Boodt A. (1609) *Le parfaict ioallier ou histoire des pierreries, French translation of Gemmarum et lapidum historia*, Antoine Huguetan, Lyon, 1644, Bibliothèque nationale de France, Paris.

Bosshart G. (1989) The Dresden Green. *Journal of Gemmology*, Vol. 21, No. 6, pp. 351–362.

——— (1991) Emeralds from Colombia (Part 2). *Journal of Gemmology*, Vol. 22, No. 7, pp. 409–425.

Bruni Y., Hatert F., George P., Cambier H., Strivay D. (2021) A gemmological study of the reliquary crown of Namur, Belgium. *European Journal of Mineralogy*, Vol. 33, No 2, pp. 221–232.

Carmona C.I. (1998) Estimating weights of mounted colored gemstones. *G&G*, Vol. 34, No. 3, pp. 202–211.

Cassius-Duranton M.-L. (2022) Le pendentif aux émeraudes du Cabinet des Médailles et des Antiques. Proposition d'interprétation. *Revue de l'Association Française de Gemmologie*, No. 217, pp. 26–27.

——— (2024) The many faces of the emerald in the western world: History, culture and symbols. *Garden of Emeralds. Discover the Gemstones*, L'ECOLE Van Cleef & Arpels Shanghai, exhibition catalogue, pp. 56–91.

Chabouillet A. (1858) Catalogue général et raisonné des camées et pierres gravées de la Bibliothèque impériale, suivi de la description des autres monuments exposés dans le Cabinet des médailles et antiques, Paris, No. 2723, p. 406.

Cornuz L. (2021) The relationship between the geological context and the inclusions found into the emeralds of the Mingora district (Swat Valley, Pakistan). Mémoire de DU de Gemmologie, Université de Nantes.

de Berquen R. (1661) *Merveilles des indes orientales et occidentales*, Bibliothèque nationale de France, Paris.

de Vielcastel H. (1855) Commande de bijoux faite par la reine Catherine de Médicis à Dujardin, orfèvre du roi Charles IX, 1571, Paris. In Archives de l'art français, t. III, 1853–1855, pp. 39–46.

Dumersan T.M. (1838) Histoire du cabinet des médailles, antiques et pierres gravées avec une notice sur la Bibliothèque Royale, et une description des objets exposés dans cet établissement, p. 31.
Farges F., Panczer G., Benbalagh N., Riondet G. (2015) The Grand Sapphire of Louis XIV and the Ruspoli sapphire. *G&G*, Vol. 51, No. 4, pp. 392–409, http://dx.doi.org/10.5741/GEMS.51.4.392
Fritsch E., Rondeau B., Hainschwang T., Quellier M.-H. (2007) A contribution to the understanding of pink color in diamond: The unique, historical Grand Condé. *Diamond and Related Materials*, Vol. 16, No. 8, pp. 1471–1474, http://dx.doi.org/10.1016/j.diamond.2006.12.006
Gaillou E., Post J.E. (2007) An examination of the Napoleon diamond necklace. *G&G*, Vol. 43, No. 4, pp. 352–357, http://dx.doi.org/10.5741/GEMS.43.4.352
Giuliani G., Chaussidon M., Schubnel H.-J., Piat D.H., Rollion-Bard C., France-Lanord C., Giard D., de Narvaez D., Rondeau B. (2000) Oxygen isotopes and emerald trade routes since antiquity. *Science*, Vol. 287, No. 5453, pp. 631–633, http://dx.doi.org/10.1126/science.287.5453.631
Gübelin, E. (1982) Gemstones of Pakistan: Emerald, ruby, and spinel. *G&G*, Vol. 18, No. 2, pp. 123–139.
Guo H., Yu X., Zheng Y., Sun Z., Ng M.F.-Y. (2020) Inclusion and trace element characteristics of emeralds from Swat Valley, Pakistan. *G&G*, Vol. 56, No. 3, pp. 336–355, http://dx.doi.org/10.5741/GEMS.56.3.336
Hackenbroch Y. (1966) Catherine de'Medici and her court jeweller François Dujardin. *The Connoisseur*, Vol. 163, pp. 28–33.
Hermant M., Deldicque M. (2022) *Art de l'enluminure*, No. 81, pp. 4 and 14.
Herodotus (440 BCE) *Histories*. Book 4, English translation by A.D. Godley. Harvard University Press, 1920.
Horae ad usum Romanum ("Roman hours for use"), called the *Book of Hours of Catherine de' Medici*, 16th century, Bibliothèque nationale de France, Paris, MS NAL 82B.
Karampelas S., Al-Shaybani B., Mohamed F., Sangsawong S., Al-Alawi A. (2019) Emeralds from the most important occurrences: Chemical and spectroscopic data. *Minerals*, pp. 9, 561, http://dx.doi.org/10.3390/min9090561
Karampelas S., Gaillou E., Herreweghe A., Maouche F., Hennebois U., Leblan S., Beuve B.M.S., Lechartier M., Nectoux D., Delaunay A. (2022) A gemological and spectroscopic study with mobile instruments of "emeralds" from the coronation crown of Napoleon III. *G&G*, Vol. 58, No. 2, pp. 168–183, http://dx.doi.org/10.5741/GEMS.58.2.168
Karampelas S., Gaillou E., Hennebois U., Herreweghe A., Maouche F., Nectoux D., Delaunay A. (2024) Study of an "Egyptian" emerald from the Mineralogy Museum at the Paris School of Mines. *Journal of Gemmology*, Vol. 39, No. 1, pp. 78–83.
Lane K. (2010) *Colour of Paradise: The Emerald in the Age of the Gunpowder Empires*, Yale University Press, New Haven, Chapter 2.
Moroz I., Roth M., Boudeulle M., Panczer G.J. (2000) Raman microspectroscopy and fluorescence of emeralds from various deposits. *Journal of Raman Spectroscopy*, Vol. 31, pp. 485–490, http://dx.doi.org/10.1002/1097-4555(200006)31:6%3C485::AID-JRS561%3E3.0.CO;2-M
Michelou J.-C., Cornuz L., Michelou Z., Pardieu V., Giuliani G. (2022) Les gisements d'émeraude du Pakistan. *Émeraudes, tout un monde*!, pp. 247–258.
Nikopoulou M., Karampelas S., Gaillou E., Hennebois U., Maouche F., Herreweghe A., Papadopoulou L., Melfos V., Kantiranis N., Nectoux D., Delaunay A. (2023) Non-destructive study of Egyptian emeralds preserved in the collection of the museum of the Ecole des Mines. *Minerals*, Vol. 13, pp. 158–172, http://dx.doi.org/10.3390/min13020158
Nikopoulou M., Karampelas S., Hennebois U., Gruss P., Gaillou E., Fritsch E., Herreweghe A., Papadopoulou L., Melfos V., Kantiranis N., Delaunay A. (2025) Microscopic, spectroscopic and chemical analysis of emeralds from Habachtal, Austria. *Minerals*, Vols. 15, 22, http://dx.doi.org/10.3390/min15010022
Pliny the Elder (77 CE) *Natural History*. English translation by Eichholz, 1962.
Pouget Fils (1762) *Traité des pierres précieuses et de la manière de les employer en parure*, Bibliothèque nationale de France, Paris.
Putnam A. (2023) Trade in the Italian Renaissance, 14th to 17th Centuries: Imports, Exports, and Trading Partners during the 1300s – 1600s. *ArcGIS StoryMaps*, HIST 388, https://storymaps.arcgis.com/stories/b6ec094db28c4f4b8fde67949ae178e0
"Recueil de devises grecques, latines ou françaises, en vers et en prose" [recueillies par PASSERAT], MS 894, fol. 75r and 78r, Bibliothèque nationale de France, Paris.
Saeseaw S., Pardieu V., Sangsawong S. (2014) Three-phase inclusions in emerald and their impact on origin determination. *G&G*, Vol. 50, No. 2, pp. 114–132, http://dx.doi.org/10.5741/GEMS.50.2.114
Saeseaw S., Renfro N.D., Palke A.C., Sun Z., McClure S.F. (2019) Geographic origin determination of emerald. *G&G*, Vol. 55, No. 4, pp. 614–646, http://dx.doi.org/10.5741/GEMS.55.4.614
Schmetzer K. (2014) Letters: Analysis of three-phase inclusions in emerald. *G&G*, Vol. 50, No. 4, pp. 316–319.
Schwarz D., Giuliani G. (2002) Emeralds from Asia: Pakistan, Afghanistan and India: Historically significant deposits? In: Giuliani G., Jarnot M., Neumeier G., Ottaway T., Sinkankas J., Staebler G. (eds.). *Emerald: The most valuable beryl: The most precious gemstone*. Lapis International, East Hampton, pp. 60–63.
Schwarz D., Pardieu V. (2009) Emeralds from the silk road countries – A comparison with emeralds from Colombia. Fall/Winter, *InColor*, pp. 2–7.
Scordia L. (2010) Le bijou d'émeraude Renaissance du Cabinet des Médailles. In *Le pouvoir et la foi au Moyen Âge, en Bretagne et dans l'Europe de l'Ouest*. Dir. Sylvain Soleil et Joëlle Quaghebeur, Rennes University Press, pp. 545–557.
Solinus C.J. (third century BCE) *Polyhistor*. Chapter 16, Various curiosities in Scythia, and, in this region, of the canine species, of emerald, of the stone called cyanea, of crystal. English translation by Arthur Golding, 1587.
Theophrastus (310 BCE) *Theophrastus on Stones: A Modern Edition with Greek Text, Translation, Introduction, and Commentary*. E.R. Caley and J.F.C. Richards (eds.), Columbus, Ohio, 1956.
Webster R. (1955) The emerald. *Journal of Gemmology*, Vol. 5, No. 4, pp. 185–221.
Weldon R., Ortiz J.G., Ottaway T. (2016) In Rainier's footsteps: Journey to the Chivor emerald mine. *G&G*, Vol. 52, No. 2, pp. 168–187, http://dx.doi.org/10.5741/GEMS.52.2.168
Wood D.L., Nassau K. (1967) Infrared spectra of foreign molecules in beryl. *Journal of Chemical Physics*, Vol. 47, No. 7, pp. 2220–2228, http://dx.doi.org/10.1063/1.1703295

The *Dr. Edward J. Gübelin* Most Valuable Article AWARD

First Place

Laboratory-Grown Diamonds: An Update on Identification and Products Evaluated at GIA

Summer 2024

Sally Eaton-Magaña, Matthew F. Hardman, and Shoko Odake

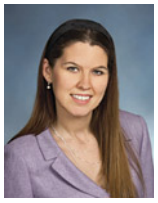
Sally Eaton-Magaña


Matthew F. Hardman


Shoko Odake

Sally Eaton-Magaña is senior manager of diamond identification at GIA in Carlsbad, California, where she investigates the physics of natural, treated, and laboratory-grown diamonds. Dr. Eaton-Magaña received her PhD in chemical engineering from Case Western Reserve University in Cleveland, Ohio. **Matthew Hardman** is a research scientist at GIA in Carlsbad, where he applies machine learning and advanced data analysis techniques to diamonds, colored stones, and pearls. He holds a PhD in geology from the University of Alberta, Canada. **Shoko Odake** is senior manager of diamond identification at GIA in Tokyo. She holds a PhD in chemistry from the University of Tokyo.

Second Place

Observations of Oval-, Pear-, and Marquise-Shaped Diamonds: Implications for Fancy Cut Grading

Fall 2024

Ilene M. Reinitz, Al Gilbertson, Troy Blodgett, Amanda Hawkes, James Conant, and Abhijith Prabhu

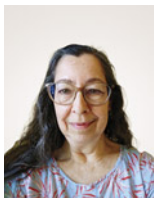
Ilene M. Reinitz


Al Gilbertson


Troy Blodgett

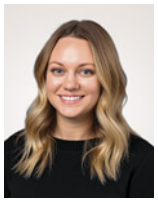
Amanda Hawkes


James Conant


Abhijith Prabhu

Ilene Reinitz, a senior research scientist at GIA in New York, has worked on a variety of projects, from spectroscopy of faceted diamonds and colored stones to using reproducible quantitative measurements of diamond proportions and angles in support of symmetry and cut grading. She holds a PhD in geochemistry from Yale University. **Al Gilbertson** is manager of cut research at GIA in Carlsbad. He is also a cut research historian and was a developer of GIA's Jewelry Forensics classes. **Troy Blodgett** is a senior research scientist at GIA in New York, where he helped develop a machine learning system for evaluating diamond clarity. He received his PhD in geology-remote sensing from Cornell University. **Amanda Hawkes** is manager of research support at GIA in Las Vegas, specializing in the development of fancy cut grade standards. **James Conant** is a senior research mathematician at GIA in Carlsbad, studying the art and science of diamond cut. He earned his PhD in mathematics from the University of California, San Diego. **Abhijith Prabhu** is a research engineer at GIA in Las Vegas, researching and developing standards and tools for cut research.

Third Place

Chemical Analysis in the Gemological Laboratory: XRF and LA-ICP-MS

Winter 2024

Ziyin Sun, Michael Jollands, and Aaron C. Palke


Ziyin Sun


Michael Jollands


Aaron C. Palke

Ziyin Sun is a senior research associate at GIA in Carlsbad. He earned a bachelor's degree in chemistry and a master's degree in analytical chemistry from Nanjing University in China. **Michael Jollands** is a research scientist at GIA in New York. He received his PhD in experimental petrology from Australian National University. **Aaron Palke** is senior manager of research at GIA in Carlsbad. He holds a PhD in geology from Stanford University.

Many thanks to the members of G&G's Editorial Review Board for voting this year.

Lab Notes

Editors

Thomas M. Moses | Shane F. McClure
Sally Eaton-Magaña | Artitaya Homkrajae

Figure 1. This 1.02 ct modified pear portrait-cut natural diamond has a checkered pattern on the flat pavilion, created using a laser. Photo by Gaurav Bera and Tejas Jhaveri; field of view 7.10 mm.

Checkered Pattern on DIAMOND

Recently, the Mumbai laboratory received a modified pear portrait-cut natural diamond weighing 1.02 ct and measuring 6.98 × 5.82 × 2.33 mm. A portrait cut consists of a flat crown and a flat pavilion, creating the appearance of a picture frame. The flat pavilion facet was fashioned with a checkered design using a laser (figure 1). This unique fashioning was done intentionally to enhance the appearance of the diamond. Therefore, it did not impact the diamond's clarity, polish, and symmetry grading.

Standard gemological testing, including microscopic examination, proved that this was a laser-fashioned pattern, and no evidence of clarity or color enhancement was observed. Natural inclusions such as twinning wisps were present, and an SI_1 clarity grade and H color were assigned.

Tejas Jhaveri

Rare GADOLINITE Gemstone

GIA's Tokyo laboratory recently received a 22.33 ct black faceted stone measuring 18.19 × 13.05 × 11.05 mm (figure 2). The stone was nearly opaque, and it was difficult to observe internal inclusions and growth features. Numerous fractures and reflective fingerprints were observed over the entire surface, which showed a very dark green bodycolor with LED fiber-optic lighting under magnification. Metallic minerals with a yellow color were exposed on the surface along fractures (figure 3). The stone had a hydrostatic specific gravity of 4.25. The refractive index ranged from 1.770 to an over-the-limit reading with 1.81 RI liquid, giving a birefringence of at least 0.040.

Figure 2. A 22.33 ct oval mixed-cut gadolinite exhibiting a very dark and almost opaque bodycolor and multiple fractures covering the surface. Photo by Shunsuke Nagai.

Editors' note: All items were written by staff members of GIA laboratories.

Gems & Gemology, Vol. 61, No. 1, pp. 58–71.

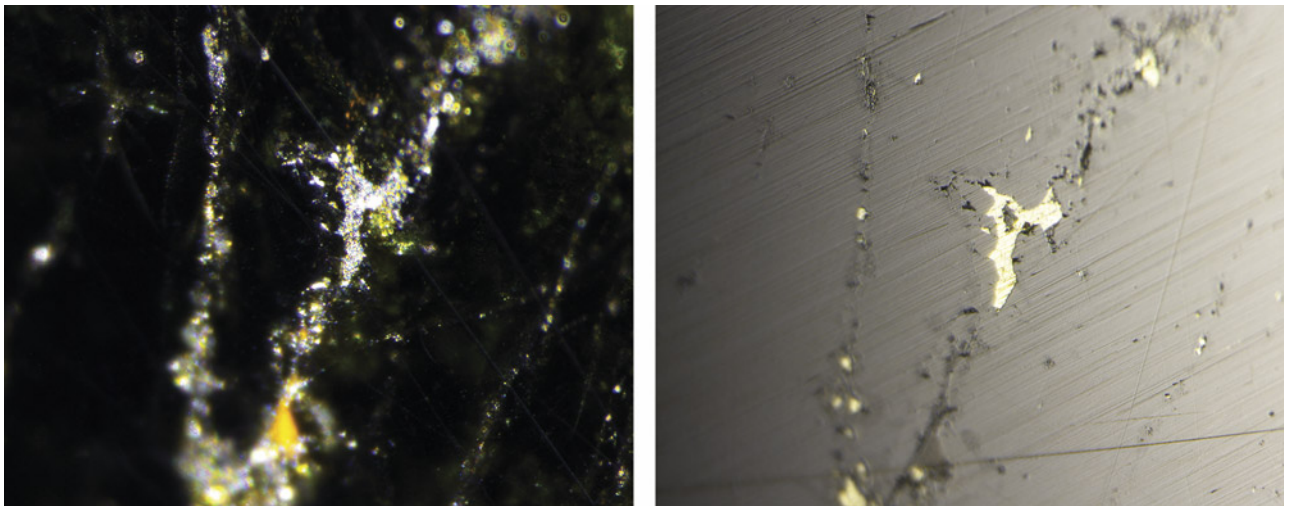

Figure 3. Left: A surface-reaching fracture in gadolinite observed with fiber-optic illumination. The fracture is filled with a reflective material. Right: The same fracture observed under reflective lighting. The yellowish fracture-filling material shows a metallic luster. Photomicrographs by Yusuke Takamura; field of view 1.04 mm.

Raman spectroscopy using 532 nm laser excitation showed a broad band around 900 cm^{-1} and a match to the RRUFF reference spectrum for gadolinite-(Y) (B. Lafuente et al., 2015, https://rruff.info/about/downloads/HMC1-30.pdf). Laser ablation–inductively coupled plasma–mass spectrometry was performed, revealing that the stone contained ytterbium, iron, beryllium, silicon, and rare earth elements (REEs) such as dysprosium and erbium, which is characteristic for gadolinite. The stoichiometric composition of the stone was calculated to be Y = 1.52, the sum of other REEs = 0.42, Fe = 0.80, Be = 1.82, and Si = 2.23, assuming a stoichiometric amount of O = 10. This result closely matched the formula of gadolinite and identified gadolinite-(Y) ($Y_2Fe^{2+}Be_2(Si_2O_{10})$) as the predominant composition. The stone's standard gemological properties, Raman spectroscopic features, and stoichiometry indicated gadolinite-(Y).

Gadolinite-(Y) is a rare mineral species that occurs in metasomatically altered acidic igneous rocks or complex alkaline granite pegmatites (L. Nasdala et al., "Metamict gadolinite-(Y) from Ratnapura, Sri Lanka," *Journal of the Geological Society of Sri Lanka*, Vol. 24, No. 1, 2023, pp. 23–30). Gadolinite can also be obtained from sedimentary deposits along with gem species such as corundum, chrysoberyl, spinel, garnet, tourmaline, topaz, and zircon (C.B. Dissanayake and M.S. Rupasinghe, "Application of geochemistry to exploration for gem deposits, Sri Lanka," *Journal of Gemmology*, Vol. 23, No. 3, 1992, pp. 165–175). Though rarely used as a faceted gemstone, gadolinite is of interest to collectors (E.A. King Jr., "Texas Gemstones," Bureau of Economic Geology, Report of Investigations No. 42, University of Texas at Austin). To our knowledge, this is the first time gadolinite has been submitted to GIA.

Yusuke Takamura and Kazuko Saruwatari

LABORATORY-GROWN DIAMONDS

CVD-Grown Diamond with an Unusual Blue Band

A 1.09 ct D-color diamond grown by chemical vapor deposition (CVD) was recently submitted to the Mumbai laboratory. This submission displayed an interesting blue band, seen through the pavilion facets (figure 4). The blue band could not be observed through the table facet. Infrared spectroscopy showed that it was type IIb with a bulk

Figure 4. A blue growth band can be seen through the pavilion (but not face-up) in this 1.09 ct HPHT-treated CVD-grown diamond. Photo by Gaurav Bera.

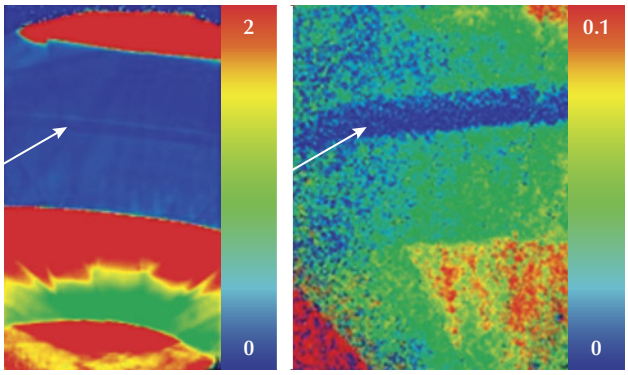

Figure 5. False-color PL maps showing normalized peak intensities (normalized using the diamond Raman line). These were collected using 532 nm excitation to document the SiV^- doublet at 736.6/736.9 nm (left) and 455 nm excitation to document the H3 defect at 503.2 nm (right). The region corresponding to the blue band is indicated by an arrow.

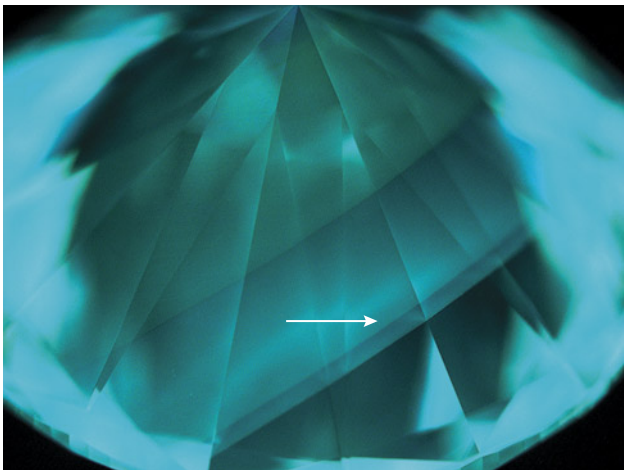

Figure 6. DiamondView imaging of the pavilion of the 1.09 ct diamond. The fluorescence color was consistent with HPHT-treated CVD-grown diamond. The region corresponding to the blue band is indicated by an arrow.

uncompensated boron concentration of ~10 ppb; the observed color was likely due to boron and a higher concentration of uncompensated boron within this blue growth layer.

Boron is present in only about 5% of CVD-grown diamonds, with the 2800 cm^{-1} infrared absorption band indicating the presence of uncompensated boron (S. Eaton-Magaña et al., "Laboratory-grown diamonds: An update on identification and products evaluated at GIA," Summer 2024 *G&G*, pp. 146–167). However, the detected boron concentration is generally <20 ppb, too low to impart blue color. Additionally, thin layers of boron-doped CVD overgrowth on natural diamond have had a high enough concentration to impart a blue color appearance to the combined CVD/natural hybrid stone (e.g., Summer 2017 Lab Notes, pp. 237–239). Nevertheless, boron has not been a common cause of blue color in CVD-grown diamonds, unlike their HPHT-grown counterparts produced through high pressure and high temperature.

Besides boron impurities, the SiV^0 center at 946 nm has been shown to create blue color in CVD diamonds (U.F.S. D'Haenens-Johansson et al., "CVD synthetic gem diamonds with high silicon-vacancy concentrations," *Conference on New Diamond and Nano Carbons*, May 2015, Shizuoka, Japan). However, photoluminescence (PL) mapping indicated this region showed lower silicon (as SiV^- at 737 nm), eliminating silicon as the likely cause of the blue color (figure 5, left).

PL spectroscopy and DiamondView imaging (figure 6) established that this CVD-grown diamond had been subjected to post-growth HPHT annealing. Spectroscopic features supporting this conclusion include several sharp peaks in the 520–580 nm wavelength range (using 514 nm excitation) that develop in CVD-grown diamonds following HPHT treatment (W. Wang et al., "CVD synthetic diamonds from Gemesis Corp.," Summer 2012 *G&G*, pp. 80–97). Pronounced greenish blue phosphorescence was also detected with DiamondView imaging.

No known boron-related features, such as the 648.2 nm peak (attributed to a boron interstitial), were detected by PL mapping using 455 and 532 nm laser excitation within the region corresponding to the blue band (figure 5, left). However, this lack of boron-related PL features is not surprising, as the 648.2 nm peak often does not develop unless the laboratory-grown diamond has been subjected to irradiation and subsequent annealing treatment (B.L. Green, "Optical and magnetic resonance studies of point defects in single crystal diamond," PhD thesis, University of Warwick, 2013). PL mapping with 455 nm excitation (figure 5, right) did indicate that the region with the blue band showed a pronounced decrease in the H3 defect (NVN^0). The thickness of this region with low nitrogen impurities was ~300 μm and corresponded with the blue-colored area.

When boron impurities are present but electrically compensated by other defects such as nitrogen, the 2800 cm^{-1} peak would be undetected or detected at lower concentrations. It is unclear whether this blue layer with a sufficiently high concentration of uncompensated boron to show color was intentionally created by the manufacturer or resulted from an accidental disruption of the standard growth recipe.

Sally Eaton-Magaña, Manisha Bhoir, and Priyanka Kadam

CVD Laboratory-Grown Gem Diamonds from Plasmability

Chemical vapor deposition (CVD) technology has been widely used to grow diamonds for the jewelry market, targeting popular colors and sizes. The majority of these

Figure 7. Three large CVD-grown diamonds submitted by Plasmability to GIA for scientific examination: A matching pair of pear-cut gems weighing 8.88 and 8.89 ct, as well as a 10.13 ct round brilliant. These American-grown diamonds are displayed with a U.S. quarter (24.26 mm diameter) for scale. Photo by Jian Xin (Jae) Liao.

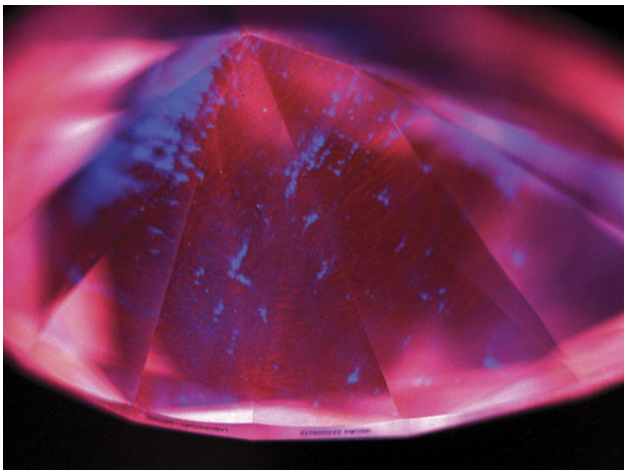

Figure 8. Representative deep-UV fluorescence image of a 2.90 ct CVD diamond from Plasmability, collected using the DiamondView. The image is dominated by red–orange fluorescence from NV^0 centers, a common feature for untreated CVD laboratory-grown diamonds, along with irregular blue fluorescing dislocation bundles. No growth layers were observed, indicating that it was produced through a single uninterrupted growth cycle. Image by Madelyn Dragone.

products are colorless to near-colorless, with a smaller proportion being fancy colored. Producers often rely on post-growth treatment for color improvement, with most colorless and near-colorless CVD diamonds having undergone high-pressure, high-temperature (HPHT) annealing (S. Eaton-Magaña et al., "Laboratory-grown diamond: A gemological laboratory perspective," *Journal of Gems & Gemmology*, Vol. 23, No. 6, 2021, pp. 25–39). Faceted CVD gem diamond sizes span from melee to tens of carats. It is challenging to grow thick samples without crystal quality degradation. Thus, most sizeable gems are produced through multiple CVD growth stages, resulting in layered growth structures. Close to 10 growth steps have been reported in some CVD diamonds tested at GIA (e.g., Summer 2023 Lab Notes, pp. 213–214). Here we report on colorless and near-colorless CVD gem diamonds from the Texas-based company Plasmability, which were produced by single-step growth up to 9 mm in thickness and were not subjected to post-growth treatment.

Recently, GIA tested a few thousand laboratory-grown diamonds manufactured by Plasmability. The sizes ranged from about half a carat to more than 10 carats (figure 7). Approximately 85% were colorless, with the rest being near-colorless. Clarity grades varied from VS to VVS. Deep-UV fluorescence imaging is an effective technology for studying diamond growth history, since different growth sectors or growth interruptions will create discontinuities in fluorescence features. Deep-UV fluorescence images collected using the DiamondView were inspected for several hundreds of samples. They were dominated by red–orange emission from NV^0 centers, with irregular patches of dislocation bundles, associated with blue band-A fluorescence (figures 8 and 9). No growth layers were observed for tested samples, confirming that they were produced by a single growth step. Excluding the dislocation bundles, the fluorescence was homogeneous, evidence that remarkable control was maintained over the various CVD conditions, including temperature, gas composition, pressure, and power throughout the growth period. Any fluctuations in these parameters would otherwise lead to detectable changes in impurity uptake, typically resulting in interfaces parallel to the growth plane. Complementary cathodoluminescence imaging of a selection of the largest diamonds confirmed these observations (figure 9). A review of gem-quality CVD laboratory-grown diamonds submitted to GIA to date weighing 8.00 ct or more has shown that fewer than 1% were grown without interruption, the largest being a 10.13 ct J-color specimen by Plasmability (figures 7 and 9).

Infrared absorption spectroscopy indicated that these were type IIa, typical for gem-quality CVD-grown diamonds. Most stones showed no absorption features from optical defects; however, very weak absorption at 3123 cm^{-1} from NVH^0 was detected for only a few diamonds. Photoluminescence spectroscopy collected at liquid nitrogen temperature using 514 and 633 nm laser excitations revealed weak emissions at 596/597 nm, in addition to moderately strong emissions from NV^0 and NV^- centers at 575 and 637 nm, respectively. A weak emission doublet at 736.6 and 736.9 nm due to SiV^- was recorded in some samples. These observations strongly suggest that no post-growth treatment was applied and that they were as-grown crystals (U.F.S. D'Haenens-Johansson et al., "Synthesis of diamonds and their identification," *Reviews in Mineralogy and Geochemistry*, Vol. 88, 2022, pp. 689–753).

In summary, high-quality CVD-grown gem diamonds are produced by Plasmability using a single-step growth

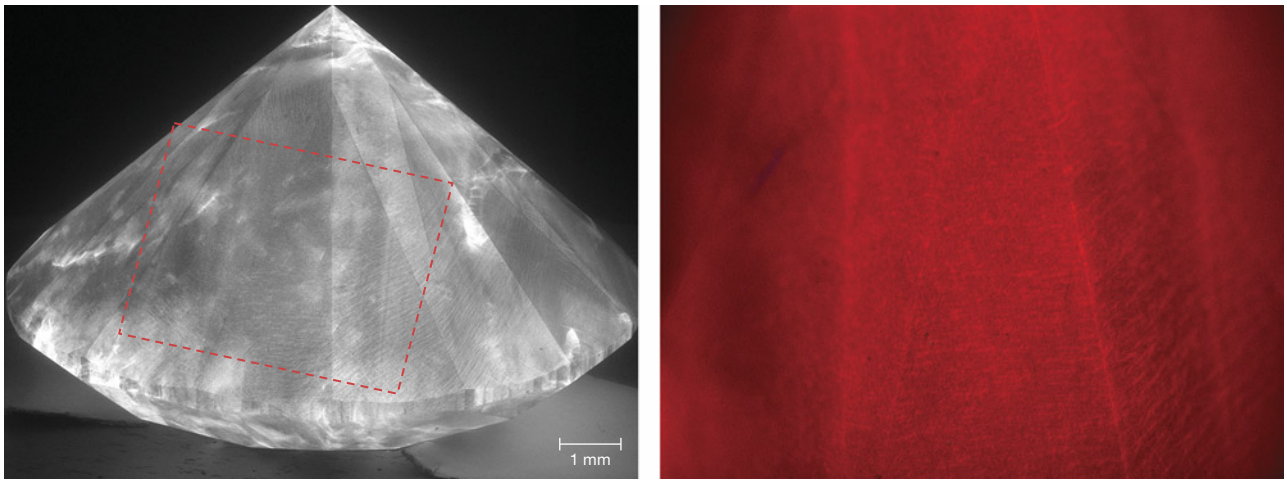

Figure 9. The absence of distinct layers and interfaces in the cathodoluminescence (left) and deep-UV fluorescence (right) images for a 10.13 ct CVD laboratory-grown diamond by Plasmability confirms that it was produced by a single growth event. Fine linear striations can be observed, characteristic of step-flow growth. Images by Elina Myagkaya (left) and Ulrika D'Haenens-Johansson (right).

process. Additionally, their colorless and near-colorless grades were achieved without post-growth treatment. This combination of features is rare in gem-quality CVD-grown diamonds.

Ulrika D'Haenens-Johansson, Tingyen Yeh, Stephanie Persaud, Elina Myagkaya, Wuyi Wang, and Thomas Moses

Fancy Vivid Yellow HPHT-Grown Diamonds

GIA's Hong Kong laboratory recently received 26 yellow laboratory-grown diamonds, ranging from 1.03 ct to 2.32 ct with VVS to VS clarity. They were all color graded as Fancy Vivid yellow except for one that was Fancy Intense yellow. It had a very attractive yellow color with no other color components. As shown in figure 10, the diamonds were cut into different shapes: ovals, cushions, hearts, and a pear. These were undisclosed as laboratory-grown diamonds when submitted for examination. Examination confirmed that all were grown by high-pressure, high-temperature (HPHT).

Diamonds grown by the HPHT process have been commercially available since the mid-1990s (U.F.S. D'Haenens-Johansson et al., "Large colorless HPHT-grown synthetic gem diamonds from New Diamond Technology, Russia," Fall 2015 *G&G*, pp. 260–279). To produce yellow diamonds, isolated nitrogen is incorporated into the crystal. As the growth processes continue to improve, consistent production of larger size and better color diamonds is now possible (Winter 2016 Lab Notes, p. 416). The submission of these 26 laboratory-grown diamonds, which possessed a similar intensity of yellow color, caught our attention.

Fourier-transform infrared spectroscopy confirmed that 25 of the samples were type Ib diamonds, with a sharp peak at 1344 cm^{-1} and a broader absorption at 1130 cm^{-1} and no detectable A-center. The concentration of isolated nitrogen was within 4–16 ppm. Only one sample with Fancy Intense color showed an additional 2800 cm^{-1} boron-related feature (3 ppb in B^0 concentration) in two orientations besides 1344 and 1130 cm^{-1}. This special sample was a mixed-type diamond. Since the concentration of isolated nitrogen

Figure 10. Selection of Fancy Vivid yellow HPHT-grown diamonds, ranging from 1.03 ct to 2.32 ct. Photo by Johnny Leung.

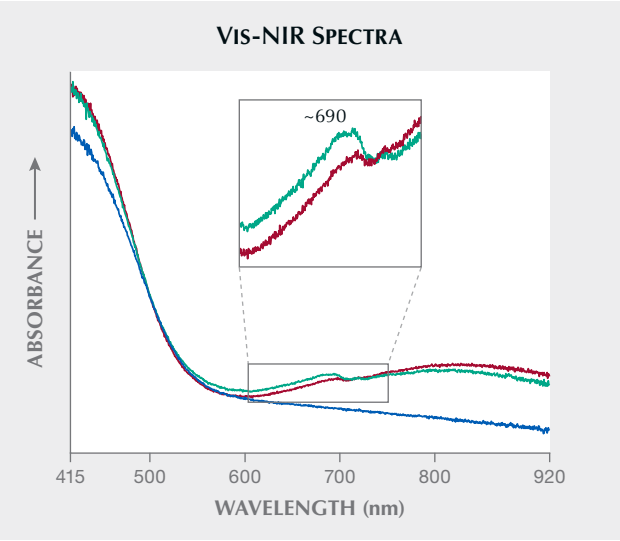

Figure 11. Vis-NIR spectra of 26 samples. The blue line is a representative spectrum for 24 of the samples. The red and green lines are two samples with nickel-related defects. Spectra are offset vertically for clarity.

determined the color of this diamond, it must be well controlled to produce an attractive, vivid yellow color.

Ultraviolet/visible/near-infrared (UV-Vis-NIR) spectroscopy showed a very strong absorption by isolated nitrogen occurring in the ultraviolet range and extending into the visible range, creating a yellow hue. Among the 26 samples, 24 showed very similar Vis-NIR spectra, represented by the blue curve in figure 11. Two showed slightly different Vis-NIR spectra (the red and green curves in figure 11), with the additional absorption at ~690 nm indicating nickel-related defects (W. Wang et al., "Natural type Ia diamond with green-yellow color due to Ni-related defects," Fall 2007 *G&G*, pp. 240–243).

Photoluminescence (PL) spectroscopy was conducted at liquid nitrogen temperature with several laser excitations. PL spectra features for these HPHT-grown diamonds were predominantly nitrogen-related defects. H3 was present in the 457 nm PL spectrum with varying intensities. Around half of the samples had moderate H3 intensity, and ~23% had strong H3. More than half showed H2 in the 830 PL spectrum. All these emission features were exceptionally sharp and consistent with HPHT growth with very low dislocations. Moreover, nitrogen vacancy centers (NV^0, NV^-) were present in the 514 nm spectrum. Approximately 73% of the samples showed an 882.7/884.4 nm doublet in 830 nm PL from the well-known nickel-related defect. (Two samples showed an extremely strong 883/884 nm doublet; these same two showed a 690 nm peak in the Vis-NIR spectrum.)

Fluorescence images collected using the DiamondView revealed a distinctive cuboctahedral growth pattern typical of HPHT-grown diamond (figure 12). The strong green fluorescence color observed was due to the presence of H3. This color is different from the weak green/yellow fluorescence of natural type Ib diamond. Green phosphorescence was also detected.

Microscopic examination with crossed polarizers revealed no strain patterns (anomalous birefringence) except for small strain fields around some metallic flux inclusions. Lack of strain indicates a very low dislocation density, which is also a characteristic of HPHT-grown diamonds. Magnification exposed the presence of color zoning with a banded structure. Also observed were some pinpoints and fractures.

All 26 stones were concluded as HPHT-grown diamonds with similar gemological properties. To consistently produce this attractive Fancy Vivid yellow color, isolated nitrogen concentration, temperature and pressure, and growth environment must be carefully controlled.

Figure 12. DiamondView imaging of two of the diamonds revealed cuboctahedral growth patterns and green fluorescence. Images by Ka Wing Tam and Wing Hin Choi.

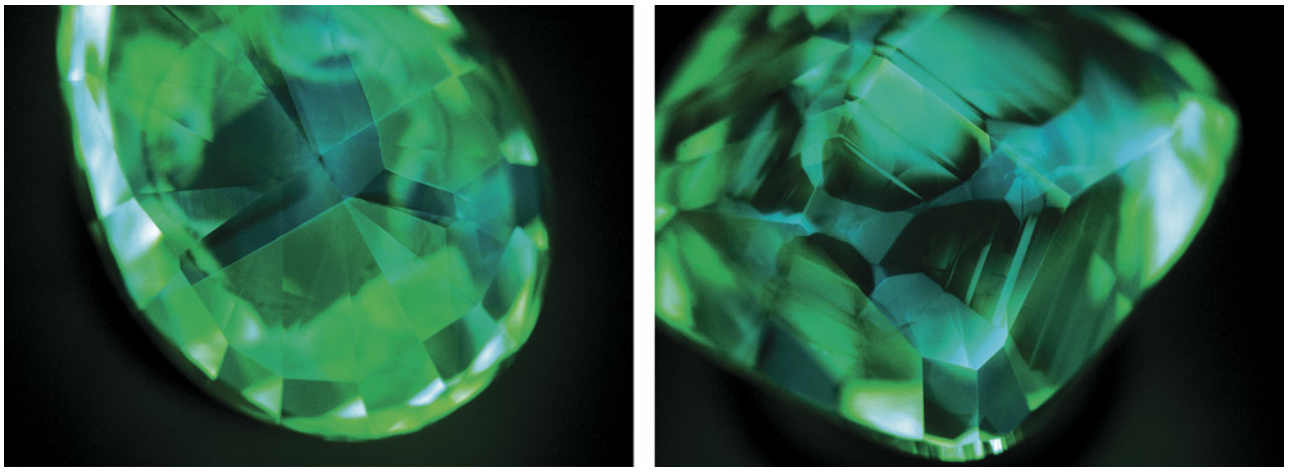

This indicates that the manufacturer knew the growth parameters to produce these attractive yellow diamonds.

Suet Man Yau and Terry "Ping Yu" Poon

Black OPAL with Unique Play-of-Color

The Carlsbad laboratory recently examined a black oval cabochon displaying play-of-color, set in a white metal ring with 24 near-colorless round brilliants (figure 13). The stone measured approximately 19.56 × 14.28 × 3.00 mm. Standard gemological testing revealed a spot refractive index of 1.44, as well as weak blue long-wave fluorescence, very weak blue short-wave fluorescence, and weak green phosphorescence. These gemological properties were consistent with Australian black opal.

The visual impact of this opal was particularly striking, displaying vivid orange play-of-color when viewed face-up and brilliant flashes of green, blue, red, and yellow when gently rocked. The unique play-of-color pattern resembled broad, blocky brush strokes separated by areas of gray potch (figure 14). This array of iridescent colors was caused by light interacting with the silica spheres within the opal. However, the exact process behind the formation of such a distinct pattern is unknown, making this stone one of the more fascinating opals the author has encountered.

Jessa Rizzo

PEARLS

Assembled Bead Cultured Half-Pearl

Recently, the Carlsbad laboratory received for identification a loose, undrilled button-shaped item weighing 9.51 ct and measuring 12.56 × 12.45 × 8.87 mm (figure 15). This item appeared to be a typical mabe, the term for an assembled cultured shell blister, due to its composite nature and distinct seamline between a pinkish orange nacre dome top and a white mother-of-pearl shell base (figure 16, left). This type of assemblage is commonly manufactured from a thin nacre dome of a cultured shell blister cut from the shell surface with the half-dome implanted nucleus removed. Then the nacre dome is cleaned, filled, and sometimes colored with various kinds of artificial materials such as resin and backed with a piece of polished shell for stability.

Upon microscopic observation, the top dome portion appeared to be a thick nacre material due to the opaque-

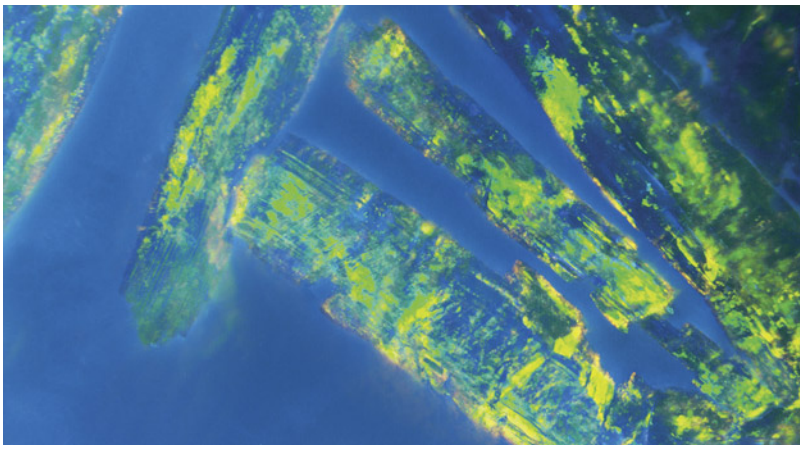

Figure 14. Unique blocky brush strokes of play-of-color in the Australian black opal. Photomicrograph by Jessa Rizzo; field of view 7.19 mm.

Figure 13. A black opal cabochon displaying orange play-of-color when viewed face-up. Photo by Annie Haynes.

Figure 15. Assembled freshwater bead cultured half-pearl on an American freshwater shell. Photo by Rhonda Wilson.

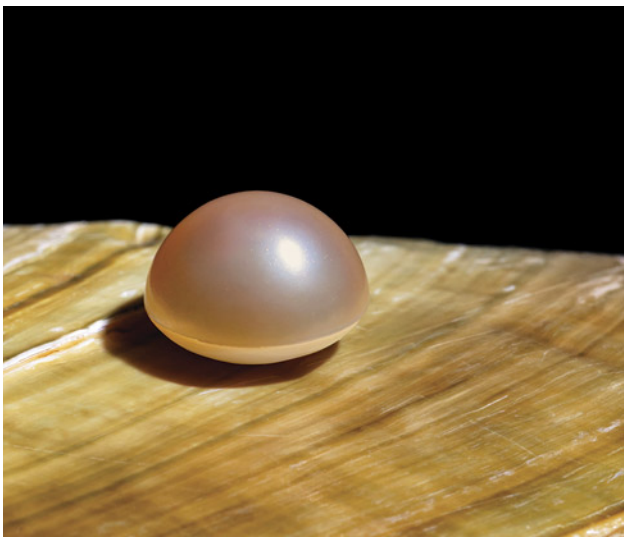

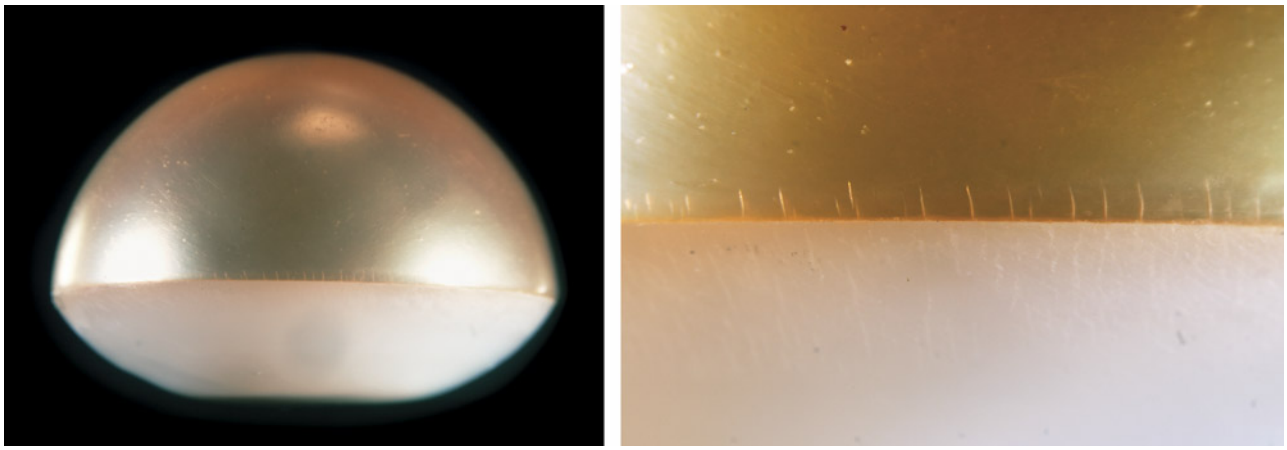

Figure 16. Left: Side view of assembled freshwater bead cultured half-pearl showcasing the nacre dome top and shell backing. Right: Vertical fractures on the pinkish orange half. Photomicrographs by Kendra Carty; fields of view 16.57 mm (left) and 4.47 mm (right).

ness of the nacreous surface, unlike the thin translucent nacre dome typically observed on most mabe materials. The surface contained common pits and scratches. However, many short vertical fractures were present within the surface of the top dome along the boundary (figure 16, right), an uncommon characteristic for mabe. The pinkish orange color appeared uniform, and a lack of unusual color concentrations suggested a natural color origin. This was subsequently confirmed with Raman spectroscopy using a 514 nm laser excitation, revealing two natural polyenic pigments at 1134 and 1526 cm^{-1} along with aragonite peaks.

The boundary between the two sections was clearly visible in the real-time X-ray microradiography (RTX) image, and glue material appeared as bright radiopaque lines. Surprisingly, the top nacre dome had a thick nacre layer containing a few growth arcs within, and a semi-spherical demarcation of a bead nucleus (indicated by arrows in figure 17) was present. The structure resembled a typical bead cultured pearl. Further, the drilled bead nucleus, a common feature in freshwater pearls, suggested the bead cultured pearl was of freshwater origin (Summer 2017 Gem News International, pp. 255–256; A. Abduriyim, "Cultured pearls from Lake Kasumigaura: Production and gemological characteristics," Summer 2018 *G&G*, pp. 166–183). Energy-dispersive X-ray fluorescence chemical analysis of both the nacre dome top and shell base also indicated freshwater origin. The shell base showed a tight structure with very faint banding.

These findings indicated that the item was not a mabe as initially believed but rather an assembled freshwater bead cultured half-pearl. The vertical fractures shown under high magnification were likely caused by the sawing process (see again figure 16, right). This unique discovery was a first for GIA, demonstrating the importance of microradiography imaging in pearl identification.

Amiroh Steen, Kendra Carty, and Artitaya Homkrajae

Enormous South Sea Cultured Pearl with Filled and Partially Hollow Structure

Many unusually large South Sea cultured pearls have been identified at GIA laboratories in the past (e.g., Fall 2013 Lab Notes, pp. 172–173; Summer 2023 Lab Notes, pp. 216–217). However, a recent submission to the New York laboratory particularly piqued the authors' interest. This submission featured a gigantic South Sea bead cultured pearl incorporated into a distinctive lariat necklace (figure 18).

The semi-baroque pearl measured approximately 31.00 × 28.07 × 27.24 mm and exhibited a silvery bodycolor with creamy patches, a common characteristic of pearls harvested from the *Pinctada maxima* oyster. Additionally, energy-dispersive X-ray fluorescence chemical analysis

Figure 17. RTX image showing the half-pearl (top half) with a drilled bead indicated by arrows and shell backing (bottom half).

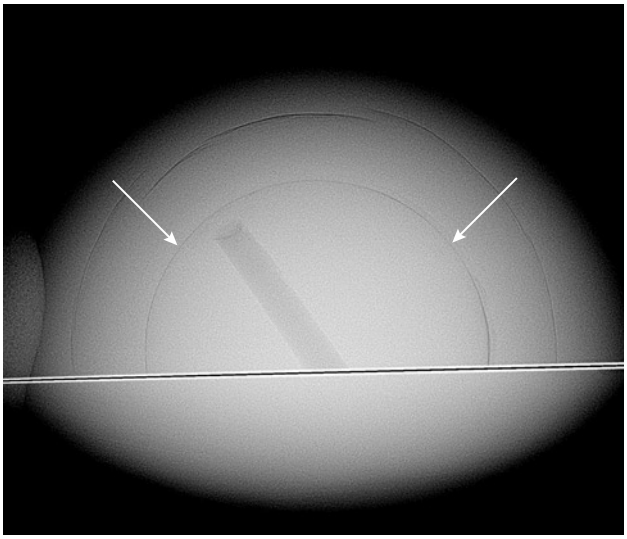

Figure 18. A South Sea bead cultured pearl measuring approximately 31.00 × 28.07 × 27.24 mm set in a lariat necklace, shown alongside a typical 12 mm South Sea cultured pearl (right). Photo by Sood Oil (Judy) Chia.

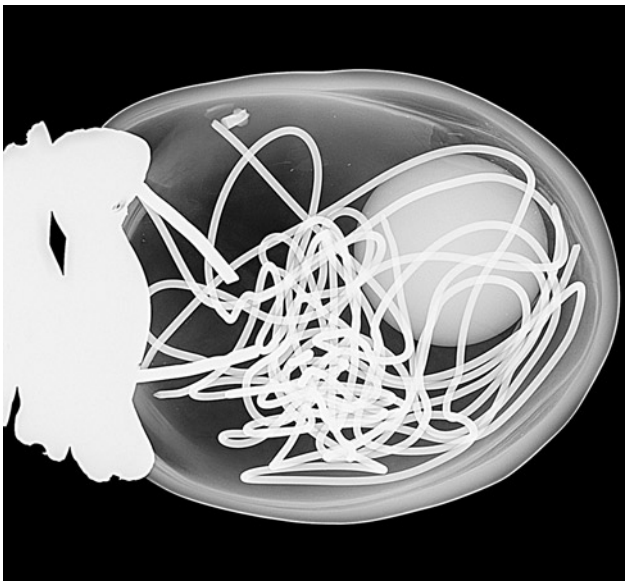

Figure 19. RTX image showing a hollow structure filled with a round bead nucleus and multiple metal wires.

showed low levels of manganese and high strontium content, confirming that the pearl originated from a saltwater environment.

This specimen represents one of the largest cultured pearls tested by GIA from the *Pinctada maxima* mollusk. *Pinctada maxima* is the largest species in the *Pinctada* genus, typically producing pearls ranging from 9 to 14 mm, though it sometimes produces exceptionally large pearls (L. Otter et al., "A look inside a remarkably large beaded South Sea cultured pearl," Spring 2014 *G&G*, pp. 58–62). Due to the pearl's size, it was fascinating to observe the internal growth structure. Real-time X-ray microradiography (RTX) imaging revealed a partially hollow structure containing a round bead nucleus approximately 10.5 mm in diameter, curiously filled with multiple metal wires approximately 0.40 mm in thickness (figure 19). The nacre thickness varied between approximately 0.50 mm to 1.00 mm.

Large pearls of either natural or cultured origin with hollow structures have occasionally been detected in laboratories, often filled with foreign materials such as resin, metals, shells, and even pearls (Fall 2013 Lab Notes, pp. 172–173; Spring 2014 Lab Notes, pp. 66–67; Summer 2019 Lab Notes, pp. 251–254). The observation of this large pearl filled with multiple metal wires was particularly interesting. Hollow pearls can be fragile due to their structural composition; the insertion of wires may serve to enhance durability, helping secure the bead in place, as well as retain weight.

This exquisite item was noteworthy for its size and intriguing internal structure. The lariat necklace featured a partially oxidized white metal set with numerous round brilliants gradually transitioning from near-colorless to gray and black, harmonizing with the beauty of the pearl.

Emiko Yazawa and Joyce Wing Yan Ho

Natural Non-Nacreous Pearls from Various Marine Mollusks

GIA's Bangkok laboratory received for identification a set of 35 loose non-nacreous pearls displaying a wide range of bodycolors including white, orange, pink, brown, purple, and black. The pearls were near-round to round in shape and exhibited surface structure characteristics from various marine mollusk species (figure 20). Arranged in a necklace layout, they weighed from 3.96 ct to 51.63 ct and measured 8.40 × 8.01 mm to 19.20 × 18.93 mm (figure 21).

Observation with a 10× loupe and a microscope showed no evidence of color treatment on any of the pearls. Raman spectroscopy with a 514 nm argon-ion laser, as well as an 830 nm diode laser, was used to confirm color origin and examine the surface composition of all the pearls. The majority of the colored pearls displayed two main natural polyenic pigment peaks at 1120–1135 cm^{-1} and 1505–1530 cm^{-1}, indicating their natural color origin. Real-time X-ray microradiography and energy-dispersive X-ray fluorescence analyses confirmed these were natural saltwater pearls.

Species determination was based mainly on the combination of colors and external appearances, internal growth structures, spectroscopic properties, and surface characteristics under magnification. Most of the pearls were porcelaneous and exhibited various flame structure patterns and high porcelain-like luster. All the white pearls were typical clam pearls produced from the Tridacninae subfamily. Under microscopic examination, many of the clam pearls displayed well-arranged flame patterns radiating from the centers (J-P. Gauthier et al., "Evidence of rotation in flame-structure pearls from bivalves of the Tridacnidae family," Summer 2019 *G&G*, pp. 216–228). The Melo pearls (from *Melo* species) were a yellowish

Figure 20. A set of 35 non-nacreous pearls submitted for examination exhibited a variety of colors and surface structures, indicating they were formed by various mollusk species. Photo by Nuttapol Kitdee.

orange color with visible flames that appeared to have jagged edges (Summer 2021 Lab Notes, pp. 152–153). Cassis pearls (from *Cassis* species) were present in various hues and saturations of light orange, pinkish orange, and

Figure 21. The 35 near-round and round non-nacreous pearls, 482.01 carats total, arranged in a necklace layout. Photo by Nuttapol Kitdee.

Figure 22. Characteristic surface patterns observed on representative pearls produced from Cassis *species in the necklace layout. A: Overlapping long, slender flame structures. B: Iridescent concentric rings observed slightly below the surface. C: Mottled surface structure with irregular streaks and patches. Photomicrographs by Kwanreun Lawanwong; fields of view 4.80 mm (A and C) and 2.88 mm (B).*

orangy brown. They shared characteristic long slender flames, some of which were overlapping (figure 22A). Iridescent concentric rings (Newton's rings) were also observed slightly below the surface of some Cassis pearls (figure 22B), similar to a previously reported feature (Fall 2012 Lab Notes, pp. 211–212). Another orangy brown Cassis pearl had a non-nacreous surface with a mottled appearance containing irregular streaks and patches but lacked any flame pattern (figure 22C; C. Zhou et al. "Disordered dolomite as an unusual biomineralization product found in the center of a natural Cassis pearl," *PLOS One*, Vol. 18, No. 4, 2023, article no. e0284295). Porcelaneous pearls from the Fasciolariinae subfamily (horse conch), *Aliger gigas* (conch; formerly known as *Strombus gigas* and *Lobatus gigas)*, and *Spondylus* species (thorny oyster) mollusk were also identified.

A group of scallop pearls from the Pectinidae family were identified in the collection. These pearls exhibited non-nacreous surfaces in the form of calcite, displaying a segmented patchwork of cells commonly found in scallop pearls and shells (figure 23, left). Some showed brownish purple and purplish brown colors typically produced by *Nodipecten* species, also known as the lion's paw scallop (K. Scarratt and H.A. Hänni, "Pearls from the lion's paw scallop," *Journal of Gemmology*, Vol. 29, No. 4, 2004, pp. 193–203). An additional black calcite pearl was concluded to be a pen pearl from the *Pinna* species. This pearl was semitranslucent and exhibited characteristic cellular surface structure (figure 23, right; N. Sturman et al., "Observations on pearls reportedly from the Pinnidae family (pen pearls)," Fall 2014 *G&G*, pp. 202–215; Winter 2014 Gem News International, pp. 305–306).

Finally, a few pearls in the collection exhibited borderline or unusual characteristics, and thus the producing mollusk species could not be determined. These included an orange pearl with a spiral surface pattern (see Micro-World, pp. 77–78 of this issue).

These pearls were likely produced in oceans and seas around the world, from the South China Sea to the Gulf of California (Sea of Cortez) and the Caribbean Sea. Finding a good-quality saltwater natural non-nacreous pearl is challenging, and the creation of this necklace layout required a great deal of effort and years of perseverance. The authors were grateful for the opportunity to examine this extraordinary set of pearls from a wide range of marine mollusk species.

Areeya Manustrong, Ravenya Atchalak, Kwanreun Lawanwong, and Chunhui Zhou

*Figure 23. Characteristic non-nacreous surface patterns observed on representative pearls produced from different mollusk species in the necklace layout. Left: Segmented patchwork of cells on a lion's paw scallop pearl (*Nodipecten *species). Right: Cellular structure and surface cracks on a pen pearl (Pinnidae family). Photomicrographs by Kwanreun Lawanwong; fields of view 7.20 mm (left) and 1.80 mm (right).*

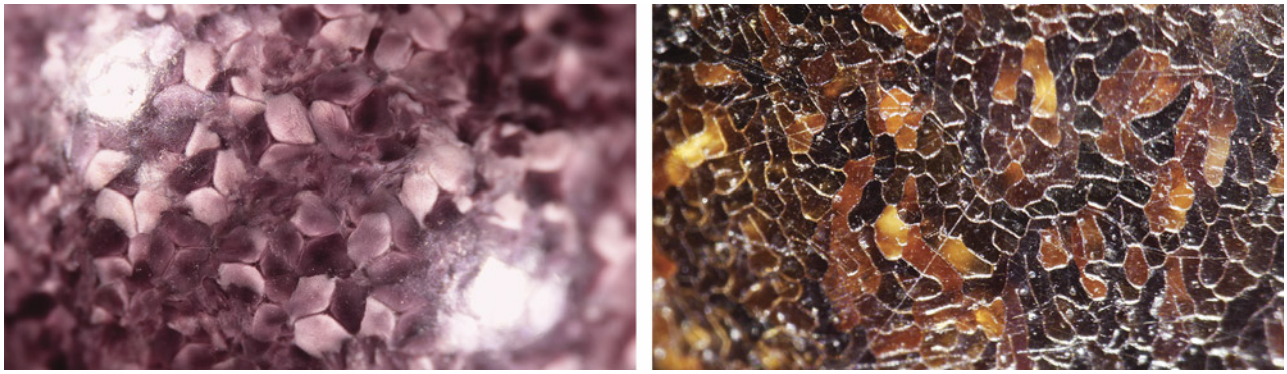

Rock Crystal QUARTZ Skull

Recently, the Carlsbad laboratory received a remarkable sculpture for an identification report. The piece, named "Daath," was composed of two separate carvings: a skull weighing 3898.6 g and measuring 18.90 × 13.77 × 12.81 cm and an interlocking lower jawbone weighing 213.7 g and measuring 11.46 × 8.35 × 7.35 cm (figure 24). Microscopic examination revealed that both the skull and jawbone were doubly refractive and displayed natural fingerprints and fluid inclusions. The inclusion suite, in tandem with Raman spectroscopy, confirmed that both were carved from rock crystal quartz. A highly polished surface added to the brilliance of the sculpture.

Carved by Jarex Schmidt, the sculpture was completed over the course of four years. The carvings began as two pristine quartz crystals that were mined in 2014 from the Zigras mine in Blue Springs, Arkansas (figure 25). Rock crystal quartz is actively mined in the eastern portion of Arkansas, which is globally recognized for producing large, high-quality specimens suitable for carvings (https://www.geology.arkansas.gov/minerals/industrial/Quartz-(Industrial).html).

After more than 1,400 hours of meticulous hand carving and polishing, the quartz pieces were transformed into an extraordinary replica of a human skull. Realistic detail was captured with stunning accuracy and craftsmanship to create this one-of-a-kind carving.

Jessa Rizzo and Nicole Ahline

Figure 25. Left: One of the rock crystal quartz crystals from the Zigras mine in Blue Springs, Arkansas, next to the skull the artist used as a reference for the sculpture. Right: The skull and jawbone components before more details were added. Courtesy of Jarex Schmidt.

Figure 24. "Daath," a 4112.3 g rock crystal quartz sculpture carved by Jarex Schmidt. Photo by Annie Haynes.

Irreversible Photochromism in SYNTHETIC SAPPHIRE

Recently, a 1.70 ct light blue stone was submitted as an alexandrite to the New York laboratory for identification (figure 26, left). Standard gemological testing yielded a refractive index of 1.760–1.768 and a specific gravity of 3.99, values consistent with corundum. Microscopic examination revealed an internally clean stone. It did not display curved color banding under diffused light, and Plato lines were not observed under cross-polarized light. Due to the lack of diagnostic inclusions and growth structures, the authors examined the stone's short-wave ultraviolet fluorescence under a mercury mineral lamp (S. Elen and E. Fritsch, "The separation of natural from synthetic colorless sapphire," Spring 1999 *G&G*, pp. 30–41). The stone displayed a moderately strong yellow "chalky" fluorescence with a banded pattern that is not known to be observed in natural stones. During the exposure time, which was only a few seconds, a photochromic effect occurred in which the bodycolor changed from light blue to yellow (figure 26, right). Photochromism can be defined as the reversible change of color from exposure to electromagnetic radiation, typically due to wavelengths of light from the visible to ultraviolet range.

Laser ablation–inductively coupled plasma–mass spectrometry returned very low concentrations of gallium (0.022–0.025 ppma), supporting a synthetic origin. The unnaturally high levels of nickel (28.3–31.2 ppma) may explain the sudden and drastic color change exhibited by this stone. In the late 1990s, researchers from the joint venture Tairus experimented with varying concentrations of Ni^{2+}, Ni^{3+}, and Cr^{3+} to grow blue gem-quality hydrothermal sapphires with an even color distribution. Interestingly, some of their light greenish blue nickel-doped sapphires displayed a stable color change to yellow when artificially irradiated with gamma radiation (V.G. Thomas et al., "Tairus hydrothermal synthetic sapphires doped with nickel and chromium," Fall 1997 *G&G*, pp. 188–202). However, the sapphire studied here did not share the swirl-like growth observed in Tairus laboratory-grown sapphires.

Yellow and orange photochromism has been a known phenomenon in sapphires for some time (R. Crowningshield, "Developments and highlights at the Gem Trade Lab in New York: X-ray bombarded sapphires," Summer 1969 *G&G*, p. 57; K. Nassau and G.K. Valente, "The seven types of yellow sapphire and their stability to light," Winter 1987 *G&G*, pp. 222–231). Until now, however, changes in color with exposure to UV light have always been found to be reversible with exposure to white light.

The authors tried to revert the stone back to its original color, starting with the standard color stability test performed on all padparadscha sapphires submitted to GIA. This involves exposing the stone to a high-strength incandescent light source. When no change was observed, additional attempts were made, including gentle heating similar to that performed on "chameleon" diamonds, as well as X-ray exposure and long-term illumination under an LED light source containing no UV component. Images were collected before and after each stability test, and the bodycolor remained unchanged after every attempt to revert the stone to its original color. Despite these efforts, the sapphire was returned to the client as yellow.

This stone serves as a cautionary tale. Synthetic sapphire is often observed under short-wave UV or placed in a DiamondView to look for curved banding. Caution should be used when using these tests, at least on some colors of possible synthetic sapphire. To the authors' knowledge, this is the first documented case of corundum with irreversible photochromism encountered in a gemological laboratory. One should avoid exposing these pale blue laboratory-grown sapphires to UV radiation until this phenomenon is better understood.

Axle Estrella and Tyler Smith

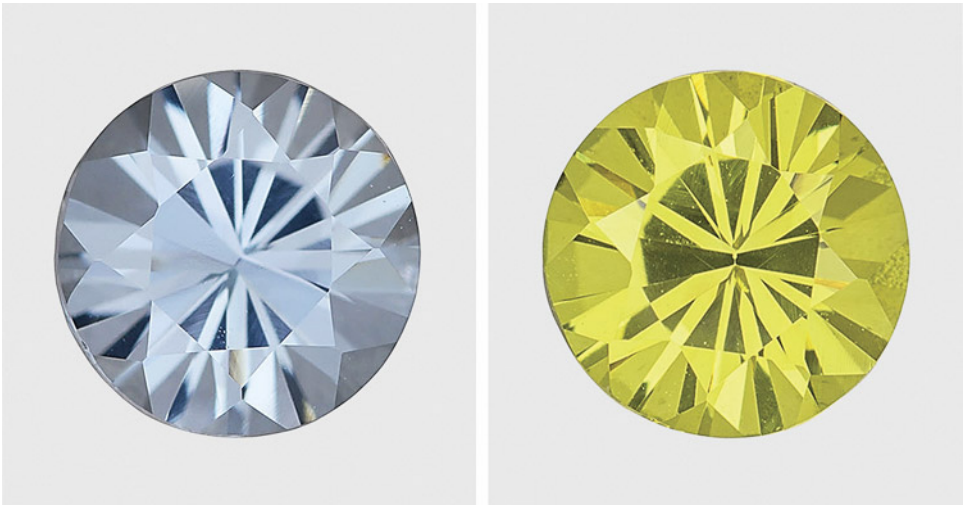

Figure 26. Synthetic sapphire before (left) and after (right) exposure to short-wave ultraviolet radiation. Photos by Jian Xin (Jae) Liao (left) and Annie Haynes (right).

Rare Gem-Quality VIITANIEMIITE

The 4.86 ct near-colorless faceted gemstone measuring 10.56 × 8.63 × 7.31 mm shown in figure 27 was submitted to GIA's Bangkok laboratory for testing. The gemstone exhibited a refractive index ranging from 1.540 to 1.557, a biaxial negative optic nature, and a specific gravity of 3.10. When viewed in ultraviolet light, it displayed weak orange fluorescence under long-wave UV and strong yellow fluorescence under short-wave UV.

Raman spectroscopy confirmed the mineral's identity as the rare phosphate mineral viitaniemiite $Na(Ca,Mn^{2+})Al(PO_4)(F,OH)_3$ (A. Pajunen and S.I. Lahti, "The crystal structure of viitaniemiite," *American Mineralogist*, Vol. 69, 1984, pp. 961–966), with spectra matching the RRUFF viitaniemiite database entry (B. Lafuente et al., 2015, https://rruff.info/about/downloads/HMC1-30.pdf). Energy-dispersive X-ray fluorescence analysis detected high concentrations of phosphorus and calcium, along with aluminum and sodium, consistent with the phosphate composition of viitaniemiite. Microscopic examination revealed several notable internal features, including strong angular growth (figure 28, left), twinning, fingerprint inclusions, two-phase inclusions (figure 28, right), growth tubes, and tiny transparent crystals.

Viitaniemiite is known for its rarity and typically occurs in very small sizes in colorless, light blue, light green, and pale yellow hues within granitic pegmatites. The identification of viitaniemiite in a gemstone of this size was remarkable, given that the mineral is typically found in much smaller forms (S.I. Lahti, "On the granitic pegmatites of the Eräjärvi area in Orivesi, southern Finland," Geological Survey of Finland, Bulletin 34, Vol. 314, 1981, pp. 51–56). This discovery expands the known occurrences of viitaniemiite in gem-quality specimens and contributes valuable data to the gemological community.

Figure 27. A 4.86 ct near-colorless faceted viitaniemiite. Photo by Lhapsin Nillapat.

Vararut Weeramongkhonlert

Figure 28. A rare gem-quality viitaniemiite shows angular growth (left) and a plane of irregular two-phase inclusions (right). Photomicrographs by Suwasan Wongchacree; fields of view 6.51 mm (left) and 2.32 mm (right).

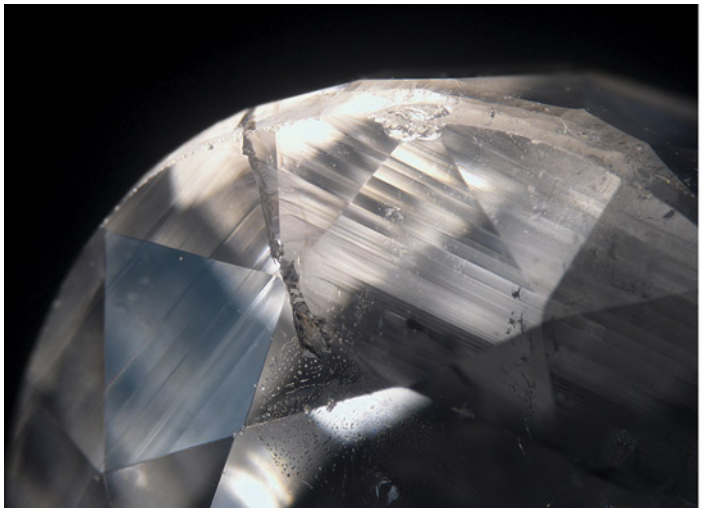

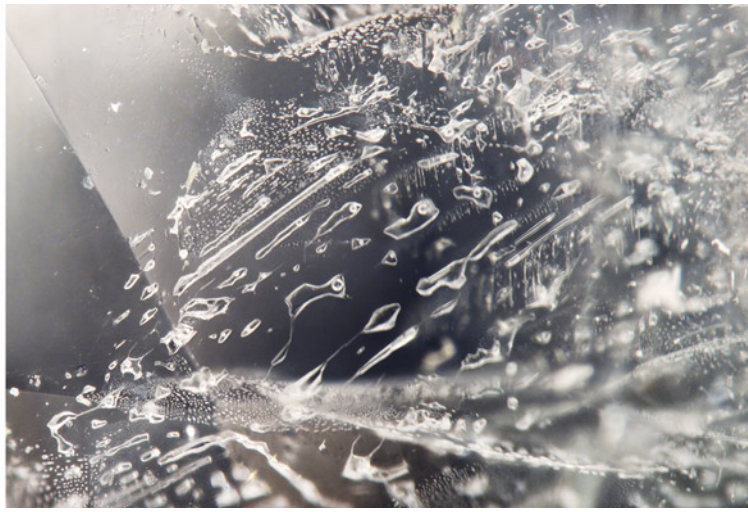

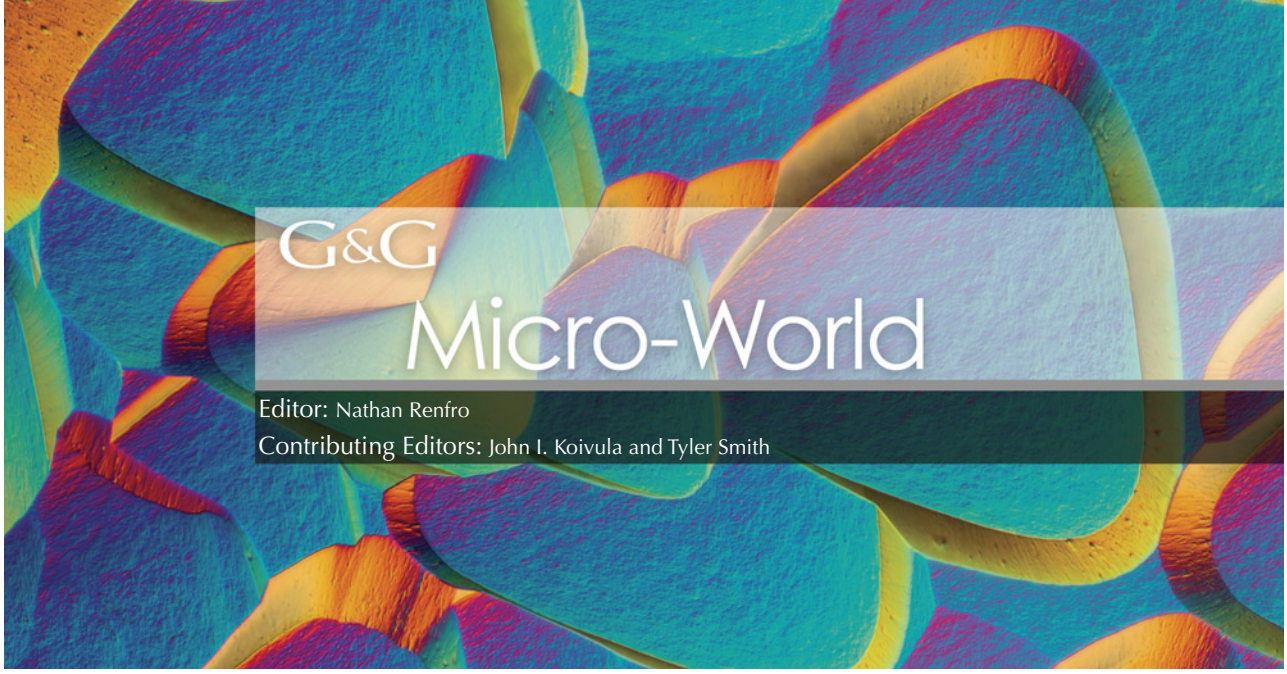

Aquamarine with Fluorite Inclusions

The specimen shown in figure 1, weighing 1418 ct and measuring approximately 77 × 55 × 45 mm, is a sharp, well-formed hexagonal light blue aquamarine crystal with attached muscovite crystals. The sample is from the well-known and highly productive Chumar Bakhoor mines of Pakistan's Hunza Valley in the Nagar district of Gilgit-Baltistan. A dozen white octahedral fluorite inclusions, identified as such based on their shape, hardness, and polarized light response (confirmed isometric), are visible throughout the crystal (figure 2).

Considering the Chumar Bakhoor mines have been in operation for the last four decades, this is a surprisingly one-of-a-kind specimen. A literature search failed to turn up any other examples of fluorite inclusions in aquamarine.

Russell E. Behnke
Meriden, Connecticut

Figure 1. Twelve white octahedral fluorite crystals ranging from 5 to 10 mm across are visible inside this well-formed aquamarine crystal. Photo by Russell E. Behnke.

Figure 2. Close-up of three fluorite crystals in aquamarine. Photomicrograph by Harold Moritz; field of view 15 mm.

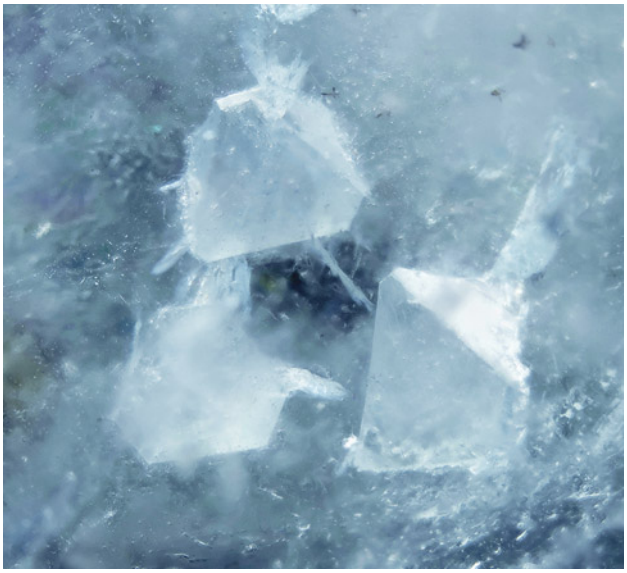

About the banner: This etched surface of a diamond from Wyoming shows modified trigons. Photomicrograph by Nathan Renfro; field of view 1.14 mm.

Gems & Gemology, Vol. 61, No. 1, pp. 72–81.

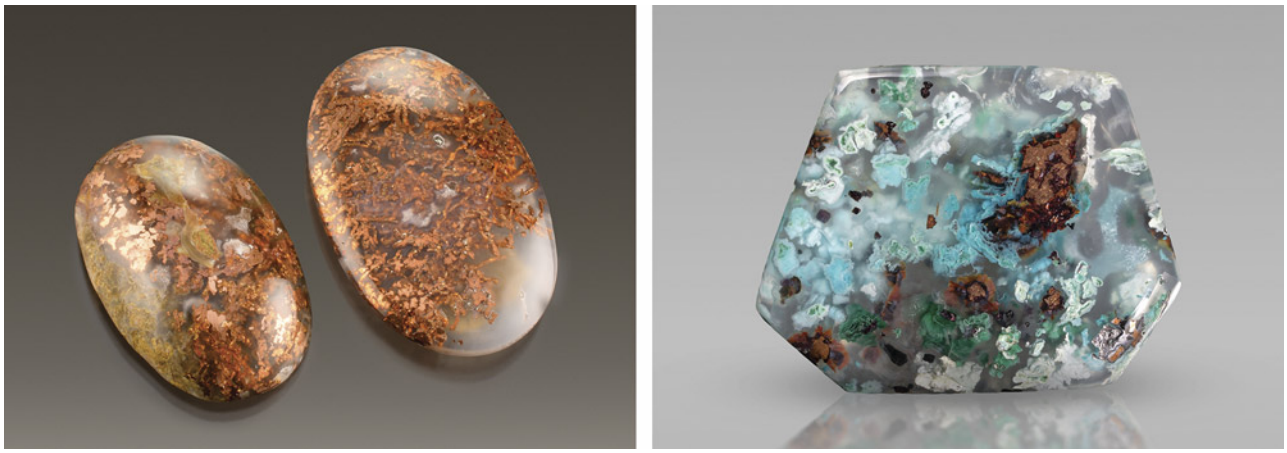

Figure 3. Left: Containing abundant amounts of native copper but no secondary copper minerals, these two chalcedony quartz cabochons, weighing more than 40 ct each, come from Lawang Kori, West Java Province, Indonesia. Right: This 16.91 ct chalcedony cabochon from Obi Island, Indonesia, on the other hand, contains secondary copper minerals including turquoise blue chrysocolla, green malachite, and a small amount of deep red cuprite. Photos by Annie Haynes (left) and Rhonda Wilson (right).

Copper in Indonesian Chalcedony

The authors recently examined two oval double cabochons consisting of chalcedony quartz, each with a multitude of glistening metallic native copper inclusions (figure 3, left). These gems were reportedly from Lawang Kori, Garut Regency, West Java Province, Indonesia, and weighed 43.04 and 46.68 ct, respectively, with corresponding measurements of 30.78 × 20.46 × 7.88 mm and 36.21 × 23.19 × 7.88 mm.

A chalcedony deposit was previously reported on Obi Island, Indonesia (J. Ivey and B.M. Laurs, "Copper minerals in chalcedony from Obi Island, Indonesia," *Journal of Gemmology*, Vol. 38, No. 5, 2023, pp. 512–521), producing material containing an abundance of azurite, chrysocolla, cuprite, malachite, and other secondary copper minerals (figure 3, right). However, these secondary copper minerals are absent in the Lawang Kori material (figure 4).

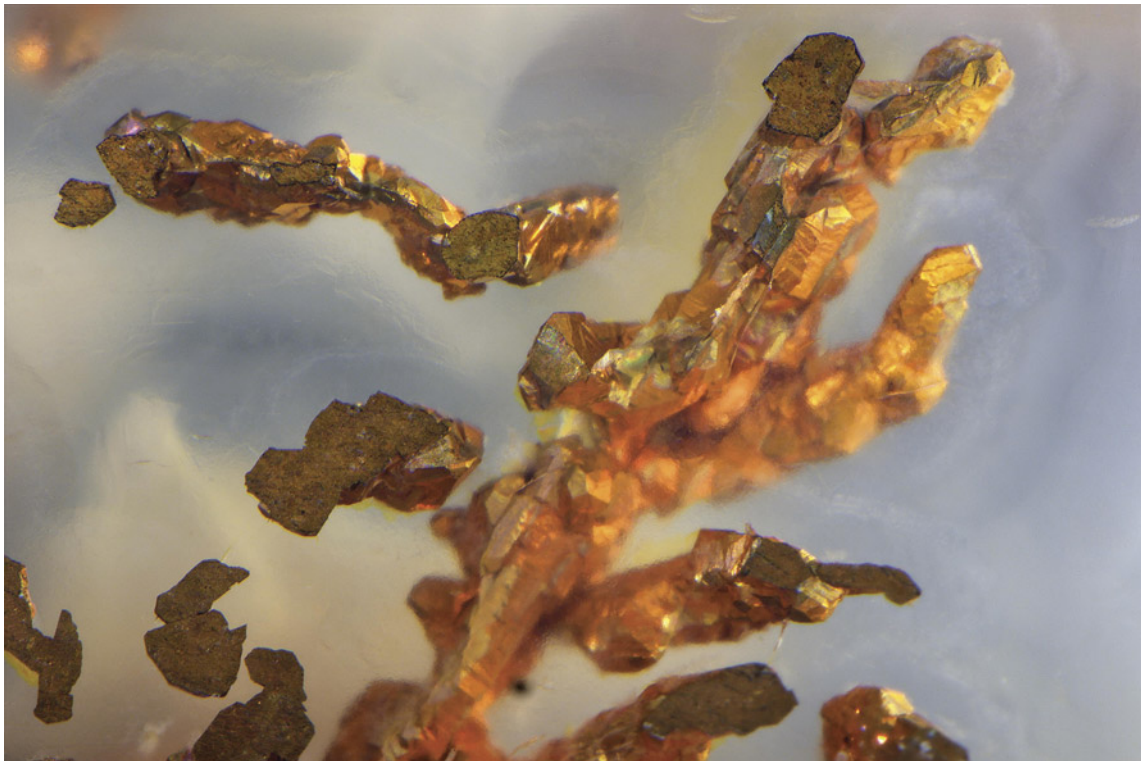

Figure 4. The chalcedony cabochons from Lawang Kori, Indonesia, contain an abundance of elemental copper but lack brightly colored secondary copper minerals. Photomicrograph by Nathan Renfro; field of view 5.63 mm.

Figure 5. Crystal inclusions in a 0.50 ct natural diamond resembling a fly with mirror reflection and human eyes with prism reflection. Photomicrograph by Jignesh Sojitra.

This new material is ideal for cutting and takes an excellent polish, which should make it a marketable variety of chalcedony.

John I. Koivula and Nathan Renfro
GIA, Carlsbad

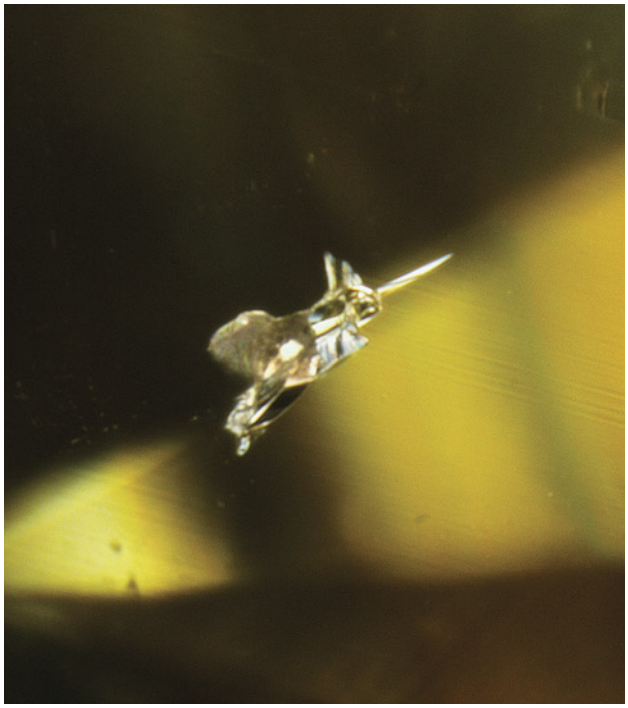

Figure 6. An omphacite inclusion surrounded by fractures in an orangy yellow diamond takes the shape of a hummingbird in flight. Photomicrograph by Mei Yan Lai; vertical field of view 0.99 mm.

Diamond Inclusions "Watching a Fly"

Examination of a 0.50 ct H-color type Ia natural diamond with SI_2 clarity recently revealed intriguing inclusions. Under the microscope, one crystal inclusion seen with a mirror reflection resembled a fly or similar winged insect (figure 5). Nearby, another crystal resembling an eye topped off with an eyebrow was duplicated by a prism image. The serendipitous combination of these features caused the whole scene to evoke a pair of eyes watching an insect. This inclusion scene invites the viewer to look closely at the diamond and appreciate details that might have gone unnoticed.

Jignesh Sojitra and Manohar Chache
GIA, Surat

"Hummingbird" in Orangy Yellow Diamond

The authors recently studied a 1.29 ct natural Fancy Intense orangy yellow diamond containing a pale grayish green mineral inclusion, identified by Raman spectroscopy as omphacite. This inclusion was surrounded by several fractures, which together had the appearance of a hummingbird in flight (figure 6).

Omphacite is a sodium-rich variety of clinopyroxene derived from eclogite, a mantle rock formed through high-

pressure and high-temperature metamorphism of subducted oceanic crust. Consequently, this small hummingbird-shaped inclusion reveals the recycling of crustal material into the deep earth millions or billions of years ago.

Matthew F. Hardman and Mei Yan Lai
GIA, Carlsbad

Rose-Shaped Cloud Inclusion in Diamond

Recently, the authors examined a 0.36 ct diamond with D color and SI_2 clarity. The diamond contained a cluster of cloud inclusions arranged to form an interesting pattern (figure 7). Best observed through the pavilion facets, the inclusion displayed a spiraled, petal-like structure conforming to a triangular outline. Overall, the impurity cloud gave the impression of a delicate rose, a rewarding sight for a gemologist who thoroughly examines their subject.

Satyam Soni and Deepak Raj
GIA, Surat

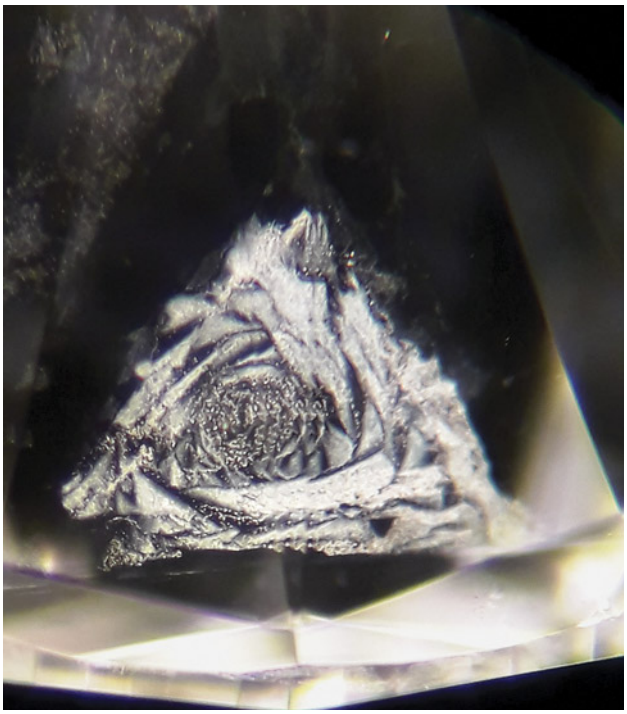

Figure 7. A cloud in a 0.36 ct diamond with SI_2 clarity resembling a rose. Photomicrograph by Deepak Raj.

Dendritic Patterns in Emerald

Dendritic, or tree-like, patterned inclusions are captivating features found in emeralds that significantly enhance their beauty and uniqueness. Typically composed of iron, manganese, or other trace elements, these minerals crystallize into intricate patterns that resemble natural foliage or tree branches. Dendritic patterns form under specific geological conditions, where variations in temperature, pressure, and the presence of different minerals can create such striking formations.

Alternatively, dendritic inclusions can result from clarity-enhancing treatments, where oils or resins are introduced to improve the visual quality of the emerald (figure 8). When these substances dry, they can leave behind patterns that closely resemble some natural inclusions.

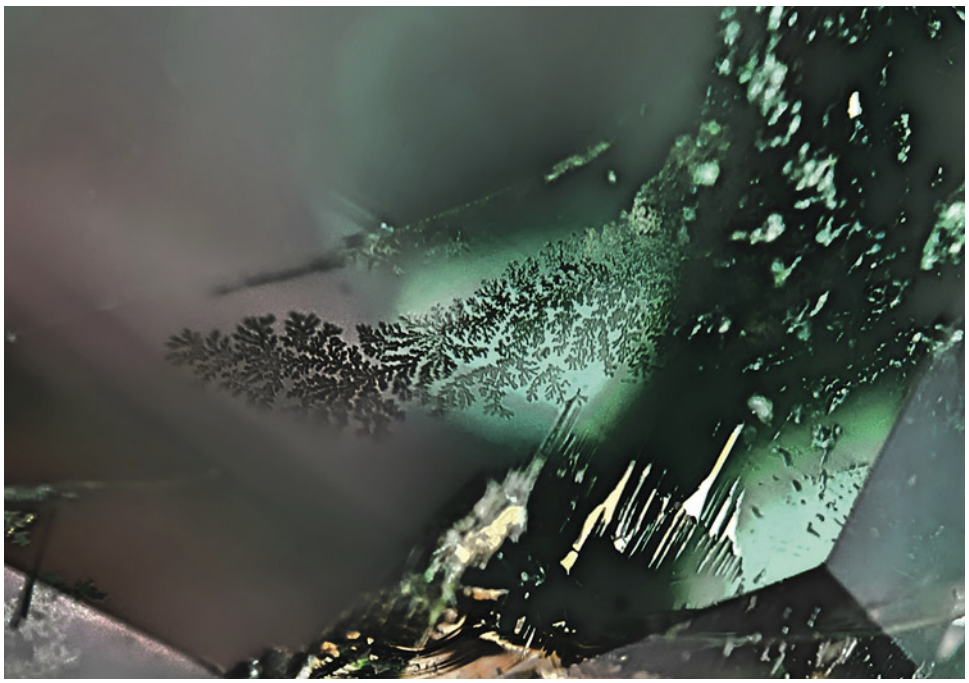

Figure 8. These dendritic patterns in a partially filled fissure in an emerald resemble natural foliage, also known as jardin. *Photomicrograph by Sameer Din Faqir; field of view 2.50 mm.*

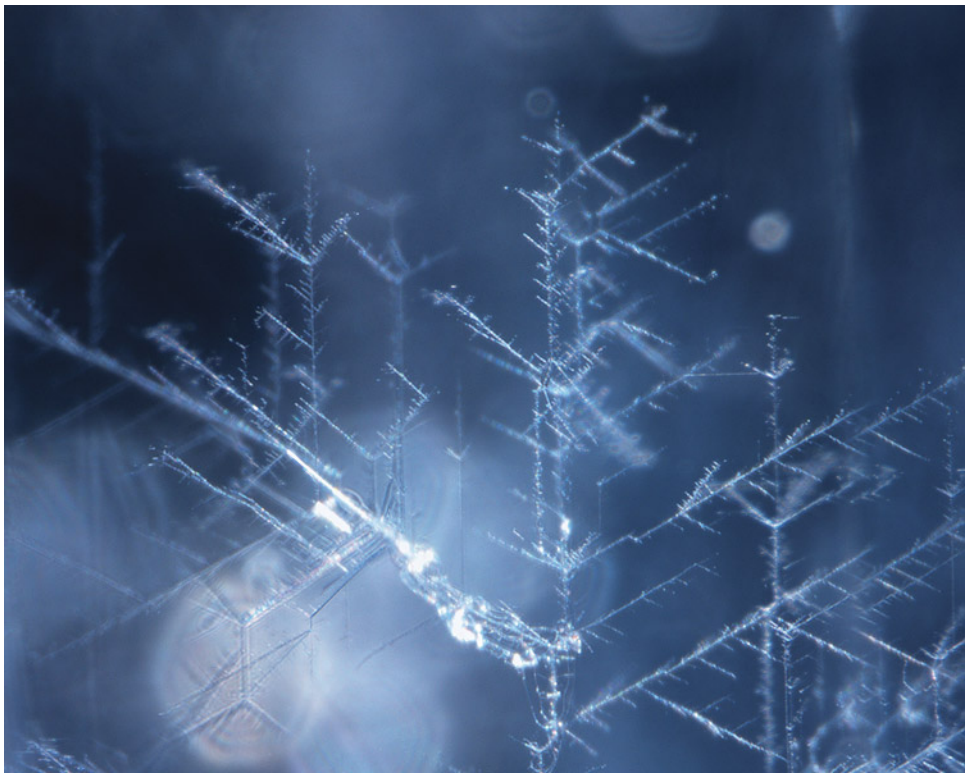

Figure 9. Unique hollow channels resembling rime ice in a 1.78 ct jeremejevite. The vertical direction of this photo corresponds to the c-axis of the stone. Photomicrograph by Makoto Miura; field of view 1.48 mm.

This inclusion suite in emerald is commonly referred to as a *jardin*, which translates to "garden" in French. Each *jardin* tells a unique story, showcasing the complex interplay of geological processes and human intervention that contribute to its allure. As no two gardens are alike, each piece is truly one-of-a-kind.

Sameer Din Faqir
Metal Testing Gemological Laboratories
Jeddah, Saudi Arabia

"Rime Ice" on Trees in Jeremejevite

Jeremejevite is a rare aluminum borate mineral with an ideal chemical formula of $Al_6B_5O_{15}[F,OH]_3$ (K. Scarratt et al., "Jeremejevite: A gemological update," Fall 2001 *G&G*, pp. 206–211). Its crystal system is hexagonal, and this mineral tends to occur in pegmatitic or volcanic deposits as a prismatic crystal. The authors recently examined a violetish blue jeremejevite measuring 10.48 × 4.98 × 4.04 mm and weighing 1.78 ct.

The stone contained unique dendritic inclusions resembling the encasing of a tree in ice, known as rime ice, along the *c*-axis (figure 9). The "trunk" was parallel to the direction of the *c*-axis, and the "branches" extended from the trunk at approximately a 60° angle. On the other side, a lightning-strike pattern was observed (figure 10). Specific Raman spectra were not detected from these inclusions, suggesting they may be a kind of hollow channel within the crystal. Similar internal features have been observed in Namibian materials and were likely formed by the "step" growth of jeremejevite crystals (Scarratt et al., 2001; "Jeremejevite: A description of a 400 crystal collection from Namibia and a preliminary study of five color types," GIA Research News, 2009). Crystal growth can create attractive patterns such as these unique inclusions in jeremejevite.

Makoto Miura and Yusuke Katsurada
GIA, Tokyo

Figure 10. Hollow channels form unique patterns resembling a lightning strike in the 1.78 ct jeremejevite. Photomicrograph by Makoto Miura; field of view 1.06 mm.

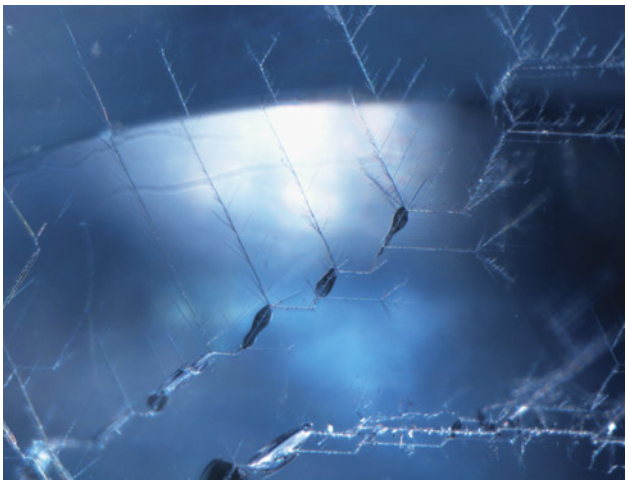

Snowflakes in Opal

Recently, the author examined a 6.85 ct black opal cabochon, likely from Ethiopia due to the digit pattern of its play-of-color (B. Rondeau et al., "Play-of-color opal from Wegel Tena, Wollo Province, Ethiopia," Summer 2010 *G&G*, pp. 90–105; B. Rondeau et al., "On the origin of digit patterns in gem opal," Fall 2013 *G&G*, pp. 138–146). This opal contained several inclusions, such as black spots concentrated along pits and scratches, indicating that it was treated to produce a darker color and enhance the play-of-color phenomenon. Additionally, metallic octahedral crystals were identified as pyrite by Raman analysis. Interestingly, fiber-optic illumination revealed whitish snowflake inclusions (figure 11), which were identified as aragonite through Raman analysis. To the author's knowledge, these are the first documented aragonite snowflake inclusions in opal.

Narint Jaisanit
GIA, Bangkok

Figure 12. The spirals on the pearl display a scale-like pattern with short flames on the rim of each scale. Photomicrograph by Ravenya Atchalak; field of view 4.67 mm.

Spiral Patterns on a Non-Nacreous Pearl

Spiral patterns are frequently observed in nature, such as those in fingerprints, plant stems, shells, or even faraway galaxies. Recently, a collection of 35 pearls arranged in a necklace layout was submitted to GIA's Bangkok laboratory (see Lab Notes, pp. 66–68 of this issue). This submission included a 6.79 ct orange round non-nacreous pearl that possessed an enchanting spiral surface structure. The pearl exhibited a noticeable patchy series of circular features covering the entire surface. Under 30× magnification, the circular features appeared scale-like, with a spiral pattern within each "scale" and short flames on the rims (figure 12). The pearl displayed no evidence of a worked

Figure 11. Group of aragonite snowflake inclusions in opal likely from Ethiopia. Photomicrograph by Narint Jaisanit; field of view 1.80 mm.

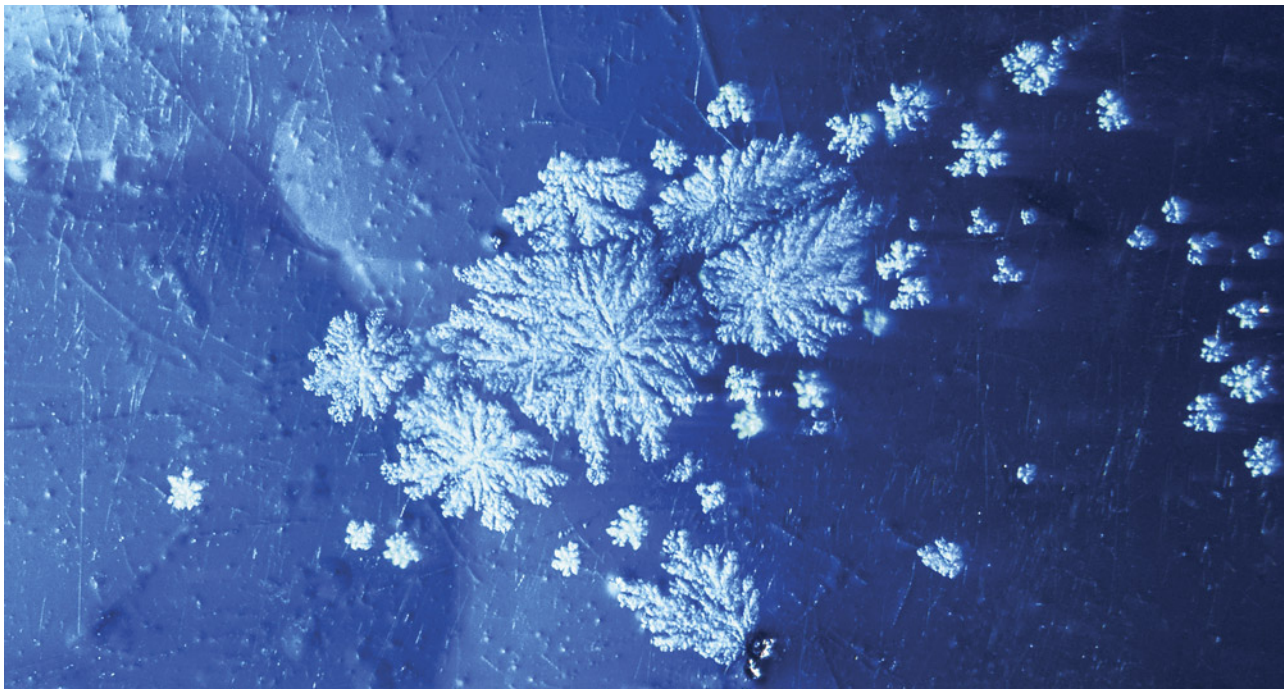

surface, only some fine visible scratches, suggesting the spiral structure was original to the pearl and not caused by any surface treatment.

Real-time X-ray microradiography, energy-dispersive X-ray fluorescence, and Raman spectroscopy indicated the pearl was of saltwater origin and natural color. Its high porcelain-like luster, spiky short flames, and orange body-color resembled some Melo (*Melo* species) and horse conch (Fasciolariinae subfamily) pearls. However, the spiral structure is rarely observed and has only been encountered in a few non-nacreous pearls previously studied by GIA. Therefore, the mollusk species that formed this pearl is currently undeterminable, and further study is required for precise mollusk determination. While the exact species that produced this special pearl remains inconclusive, its fascinating spiral pattern is undoubtedly worthy of note.

Ravenya Atchalak
GIA, Bangkok

Kyanite in Quartz

Although quartz is known to host a diverse assortment of mineral inclusions, well-formed bladed kyanite inclusions in quartz are rarely observed. At first glance, the 7.83 ct blue-colored stone in figure 13 appeared to contain dumortierite, but further inspection revealed distinct bladed blue crystals that deviated from the expected prismatic morphology of dumortierite.

Raman spectroscopy identified several minerals including quartz, kyanite, and some iron sulfides. Kyanite, an aluminum silicate mineral typically associated with metamorphic rocks, provided the stone's light blue color. Opaque metallic hexagonal sulfide crystals were scattered throughout the host. Occasional reddish orange crystals, located too deep within the stone for identification with Raman, were likely mica given the mineral association and structure.

These eye-visible inclusions come together to form a brightly colored quartz with a slight shimmer and unique character.

Jeffrey Hernandez
GIA, Carlsbad

Devitrified Glass "Pom-Poms" in Ruby

The authors recently examined a 13.99 ct red cushion mixed cut, which revealed interesting inclusions upon microscopic examination. Standard gemological testing of the host material proved consistent with ruby but yielded some unusual results. When subjected to short-wave ultraviolet light, the stone displayed a chalky yellow fluorescence concentrated within surface-reaching fractures.

Magnification revealed a collection of fine particles and altered crystals with discoid fractures typical of some natural rubies after heat exposure. Curiously, the stone exhibited partially healed fractures with flux-like textures, with some fractures also containing round and flattened gas bubbles. The authors also observed structures of whitish acicular projections radiating outward that formed spiked spherical crystals resembling pom-poms or sea urchins (figure 14). These formations occurred within filled cavities that displayed visible luster differences from the host corundum. Laser ablation–inductively coupled plasma–mass spectrometry, Raman spectroscopy, and X-ray imaging confirmed the presence of a foreign material, and X-ray fluorescence identified bismuth within the filled cavities. The authors concluded that bismuth glass was present

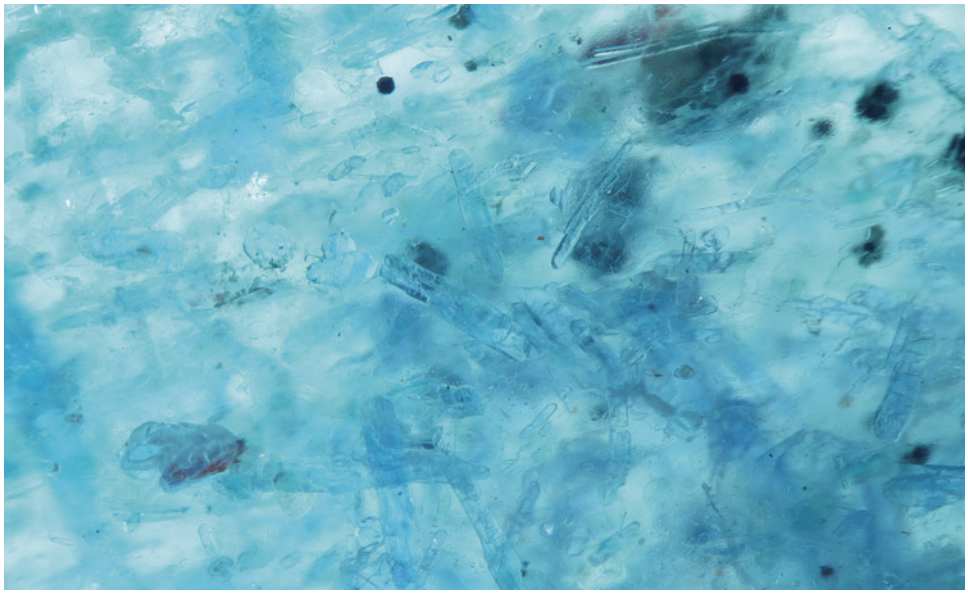

Figure 13. A chaotic assortment of crystal inclusions comprises the busy interior of this quartz. Photomicrograph by Jeffrey Hernandez; field of view 3.57 mm.

Figure 14. Devitrified glass inclusions resembling pom-poms or sea urchins in a clarity-enhanced ruby. Photomicrograph by Kevin Bishop and Joseph Hukins; field of view 1.99 mm.

in the ruby as a clarity enhancement treatment. The acicular pom-pom formations were a result of devitrification of the bismuth glass filler at some stage in the annealing process, a likely unintended and unwelcome byproduct for a treater with the goal of clarity enhancement, but a visually appealing feature for a gemologist nonetheless.

Kevin Bishop and Joseph Hukins
GIA, New York

Evil Eye in a Flux-Healed Mong Hsu Ruby

As mined, Burmese ruby from Mong Hsu can be unattractive due to dense clouds and unusual blue cores, resulting in a low-grade cloudy material. Heat treatment is typically performed to remove the blue color and silk, making the final product a rich, clear red. Because the majority of Mong Hsu rubies are heavily fractured, they are often heated with a flux such as borax to fill voids and allow the fractures to partially heal. The result is a much clearer and more durable product.

The fissures in a recently examined 1.22 ct heat-treated Mong Hsu ruby were also healed with residual flux. In this case, the mirror reflection of the flux-healed fissure from a step pavilion facet resulted in an inclusion resembling an evil eye (figure 15). When this stone is viewed under a microscope, an evil eye appears to be staring back at the observer.

Ungkhana Atikarnsakul
GIA, Bangkok

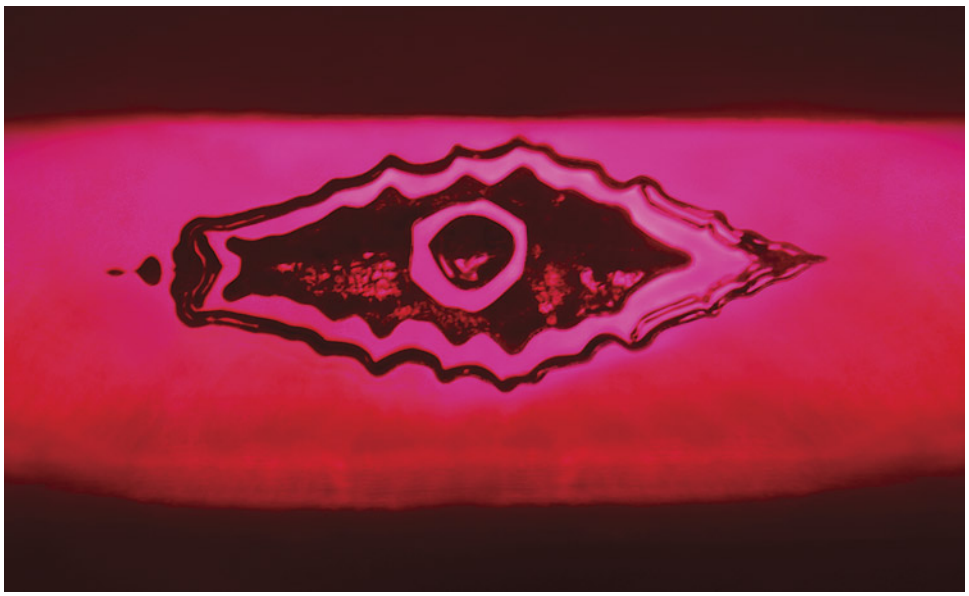

Figure 15. The reflection of a flux-healed fissure from a step pavilion facet in this Mong Hsu ruby resembles an evil eye. Photomicrograph by Ungkhana Atikarnsakul; field of view 1.07 mm.

Prismatic Zircon in Kashmir Sapphire

Recently, the author examined a faceted blue oval sapphire. Standard gemological properties and chemical analysis indicated a geographic origin of Kashmir. Microscopic examination revealed internal graining, fine particle banding, and fingerprint inclusions. Interestingly, elongated zircon inclusions were also observed, displaying attractive birefringent interference colors under cross-polarized filters caused by the splitting of light in the doubly refractive crystals (figure 16). Kashmir sapphire is one of the rarest and most valuable gemstones in the world, renowned for its beauty and quality, and this stone was no exception.

Narint Jaisanit
GIA, Bangkok

Lepidolite in Copper-Bearing Tourmaline

The author recently examined a 0.53 ct copper-bearing tourmaline with a well-formed transparent crystal (figure 17). Raman spectroscopy identified the crystal as lepidolite ($K(Li,Al)_3(Al,Si,Rb)_4O_{10}(F,OH)_2$), a member of the mica group. Lepidolite frequently occurs alongside tourmaline but is usually seen in lower-quality stones or collector specimens. Typical inclusions observed in gem-quality tourmalines include tubules, fine needles, and fluid inclusions. Lepidolite crystals in tourmaline have been observed in stones from multiple localities, so such an inclusion is not an indicator of geographic origin. Due to the preference of less included stones in jewelry, it is rare to encounter a sizeable, well-formed crystal in a faceted gem-quality tourmaline.

Virginia Schneider
GIA, New York

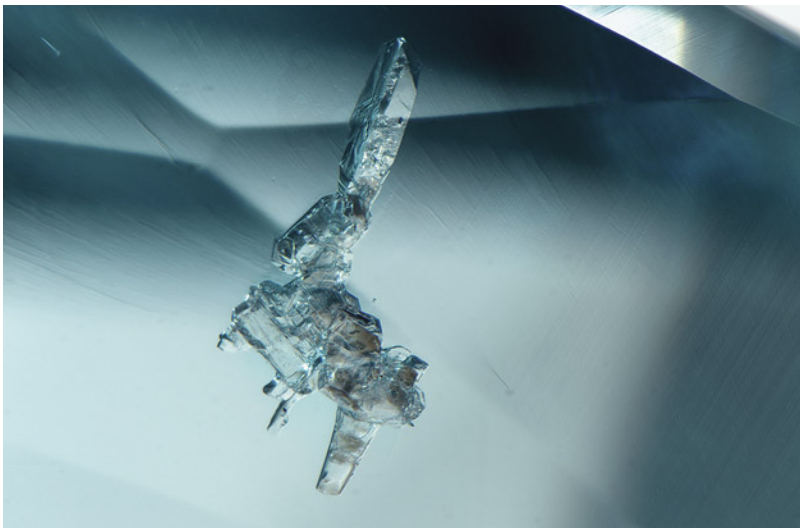

Figure 17. Prismatic colorless lepidolite crystal in a copper-bearing tourmaline. Photomicrograph by Virginia Schneider; field of view 1.58 mm.

Quarterly Crystal: Fluorite in Quartz from China

With its high degree of transparency and relatively good durability, colorless rock crystal quartz is the perfect host for a variety of mineral inclusions. As a common crustal mineral, it often forms as a single transparent crystal, sometimes of significant size.

This issue's Quarterly Crystal, a 3230.50 ct transparent crystal measuring 108.84 × 97.42 × 65.40 mm (figure 18), comes from the Yaogangxian mine in Hunan Province, China. The singly terminated quartz specimen with eye-

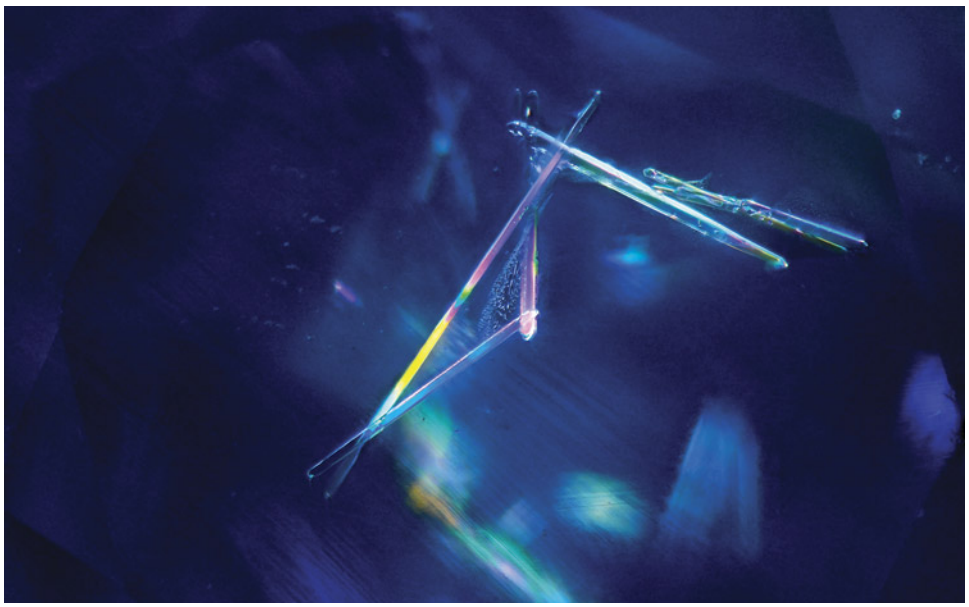

Figure 16. Prismatic elongated zircon in Kashmir sapphire. Photomicrograph by Narint Jaisanit; field of view 2.88 mm.

Figure 18. Transparent, colorless terminated 3230.50 ct single crystal of Chinese quartz with geometric growth features decorating the surface with eye-visible apple green inclusions. Photo by Annie Haynes.

visible apple green inclusions was purchased from Nabeel Ashraf of Poetry In Gems (San Diego, California).

As shown in figure 19, examination of the quartz crystal revealed numerous near-colorless to apple green, transparent to translucent, euhedral inclusions identified by Raman analysis as fluorite. These fluorite crystals showed directional deposition and were all present in a phantom plane, situated only on one side of the quartz specimen. This, together with the sharp-edged condition of the fluorite crystals, suggested that they were syngenetic with the quartz host.

While transparent colorless quartz is relatively common at the Yaogangxian mine, this large quartz crystal made a unique host for the numerous fluorite inclusions.

John I. Koivula, Nathan Renfro, and Maxwell Hain
GIA, Carlsbad

Figure 19. Scattered transparent to translucent, near-colorless to apple green crystals of isometric fluorite, the largest measuring 11.2 mm. The fluorite inclusions fluoresce a strong blue when exposed to UV radiation. Photomicrograph by Nathan Renfro; field of view 32 mm.

The following 25 questions are from the four 2024 issues of *G&G*. Please refer to the articles in those issues to find the single best answer to each question.

Visit gia.edu/gems-gemology to take the Challenge online. Entries must be received no later than **September 1, 2025**. All entries will be acknowledged with an email.

Score 75% or better, and you will receive a certificate of completion (PDF file). Earn a perfect score, and your name also will be listed in the Fall 2025 issue of *Gems & Gemology*.

1. "Ice jade" is
   A. a trade name for white nephrite.
   B. transparent to semitransparent.
   C. always completely colorless.
   D. only found in Guatemala.

2. The earliest gem-quality laboratory-grown diamonds were generally
   A. fancy yellow-orange.
   B. near colorless.
   C. brown.
   D. pink.

3. An oval-shaped diamond with a length-to-width ratio < 1.2 may be called a
   A. "navette."
   B. "moval."
   C. "round."
   D. "roval."

4. Jewelry designs created exclusively using generative AI
   A. are always completely unique.
   B. are always structurally sound.
   C. are not copyright protected.
   D. are never "hallucinations."

5. UV-Vis-NIR spectroscopy demonstrates that ruby's red color comes from
   A. absorption bands in the violet and yellow-green.
   B. strong absorption in the orange to red region.
   C. selective reflectance in the green and blue.
   D. transmission in the ultraviolet.

6. With an increase in crystal symmetry, Raman and XRD plotted data
   A. have more peaks.
   B. reduce in complexity.
   C. reduce in intensity.
   D. have broader peaks.

7. Quartz is found in turquoise deposits
   A. that always contain gypsum.
   B. exclusively in Tianhu East.
   C. only in China.
   D. worldwide.

8. 3D photoluminescent mapping
   A. can only be done at liquid nitrogen temperatures.
   B. is used to detect beryllium diffusion in sapphire.
   C. can reveal the growth history of a gemstone.
   D. is used in phase identification.

9. If an instrument's calibration is off, quantitative data will be skewed, displaying
   A. a lack of random error.
   B. systematic error.
   C. high accuracy.
   D. low precision.

10. Compared to cassiterite from Viloco, Yunling cassiterite
   A. has lower concentrations of iron and antimony.
   B. has less homogenous cobalt concentrations.
   C. does not contain beryl inclusions.
   D. contains tourmaline needles.

11. Amethyst from La Manche
   A. contains fluid inclusions with extremely low salinity.
   B. formed at temperatures below 100°C.
   C. is consistently a deep purple.
   D. contains fluorite inclusions.

12. What advantage does EDXRF have over LA-ICP-MS for a gemologist?
   A. It can accurately quantify beryllium in corundum.
   B. It can target extremely small areas on a gem.
   C. It has much lower limits of detection.
   D. It is completely nondestructive.

13. How does X-ray imaging using digital technology versus photosensitive film differ?
   A. Structures that more strongly absorb X-rays are darker with digital X-ray imaging.
   B. Digital X-ray imaging uses carbon tetrachloride to minimize reflections.
   C. Photosensitive film X-ray imaging relies on scintillators.
   D. Photosensitive film X-ray imaging is more modern.

14. A nanoscale thin film gem coating is more likely to delaminate if it is
   A. the same material as the gem.
   B. lattice mismatched to the gem.
   C. grown with CVD.
   D. too thin.

15. Anorthoclase from Vietnam
   A. is easily identified with standard gemological testing.
   B. is a stable and durable gem material.
   C. is a common alkali feldspar.
   D. is most popular in yellow.

16. Machine learning can aid in gemological identification when
   A. extremely large datasets containing patterns are available.
   B. working with a new mineral never characterized before.
   C. only a few examples of a particular gem are available.
   D. there are no distinct separation characteristics.

17. When performing FTIR, it is important to clean the gemstone to
   A. avoid hindering detection of CO_2.
   B. increase water vapor absorptions.
   C. avoid saturating the detector.
   D. remove oil from handling.

18. Pure sodium pyroxene (jadeite) is
   A. colorless.
   B. purple.
   C. green.
   D. blue.

19. Luminescence can be excited by
   A. photons.
   B. friction.
   C. heat.
   D. all of the above.

20. As CVD diamond growth evolves, which diagnostic feature has become less reliable?
   A. 2800 cm^{-1} peak in IR spectra
   B. SiV^- peaks in PL spectra
   C. Yellow coloration
   D. Type II

21. Portable Raman devices are not substitutes for standard gemological testing because
   A. some gems do not exhibit distinct Raman spectra.
   B. none of them come with custom databases.
   C. they cannot separate ruby from garnet.
   D. they cannot be used with diamonds.

22. For observers evaluating face-up appearance of fancy-shaped diamonds, what feature resulted in the most disagreement?
   A. Length-to-width ratios
   B. Windowing
   C. Crushed ice
   D. Bow ties

23. When working with a customer, generative AI can aid a designer by
   A. creating photorealistic "sketch to render" images from a drawing.
   B. creating designs that are optimized for manufacturing.
   C. intuitively understanding what the customer wants.
   D. acting as a substitute for a trained artist.

24. X-ray computed microtomography is better than X-ray radiography for
   A. separating pearls based upon luminescence to manganese.
   B. seeing internal features in pearls and gems.
   C. separating freshwater and saltwater pearls.
   D. rapid screening of pearls.

25. Machine learning is more efficient than a gemologist when
   A. looking at complex spectroscopic signatures.
   B. determining the refractive index of a gem.
   C. looking for inclusions in a microscope.
   D. determining the value of a gem.

To take the Challenge online, please scan the QR code.

GEM NEWS INTERNATIONAL

Contributing Editors
Gagan Choudhary, *IIGJ-Research & Laboratories Centre, Jaipur, India* (gagan.choudhary@iigjrlc.org)
Guanghai Shi, *School of Gemmology, China University of Geosciences, Beijing* (shigh@cugb.edu.cn)

TUCSON 2025

In general, 2025 was a strong year for Tucson vendors at the various shows. Like last year, foot traffic was generally low with moments of high activity, while buying remained focused. Vendors who offered unique and exceptional items performed very well with established customers. Many buyers were there for just a few days with shopping lists and plans to visit specific vendors. A number of vendors reported that some buyers previewed items online prior to visiting to make purchase decisions. At the shows, one could see buyers using video calling apps to show colleagues prospective purchases during the decision-making process, a noted change in the purchasing dynamics from the past. Some vendors expressed frustration with having great sales the first couple of days, followed by very slow activity—a possible result of the focused buying. Overall, the feedback indicated that sales were fairly unchanged or slightly better compared to last year. Several vendors reported that they had record first-day sales.

AGTA reported upticks in both the number of buyers and the number of hotel rooms rented through their block (J. Heebner, "Gemstone & jewelry sales at 2025 AGTA GemFair Tucson reflect bright spots in business," February 12, 2025, https://agta.org/gemstone-jewelry-sales-at-2025-agta-gemfair-tucson-reflect-bright-spots-in-business/). For 2025, AGTA took each badge recipient's photograph and printed it on both sides of the badge itself. The intent was to eliminate badge-borrowing and to prevent unregistered attendees from using lost or discarded badges. This extra set of security measures was favorably received. Notably, the 2026 AGTA GemFair will eliminate its weekend days and will run for five days instead of seven, aligning with the observation that buyers are attending for shorter, more focused periods. With the ability to view high-quality images and videos from vendors' websites and social media feeds before visiting the shows, today's buyers are armed with a lot more information than in the past, and purchasing seems much more targeted.

Beyond the AGTA GemFair, other wholesale venues in Tucson such as the Gem & Jewelry Exchange (GJX), the Pueblo Gem & Mineral Show, the Gem & Lapidary Wholesalers Holidome and Gem Mall shows, and the JOGS Gem & Jewelry Show also exhibited light foot traffic even though the number of buyers was similar if not slightly

Figure 1. Left: 18K yellow gold "Flames" ring with 25.19 ct Mexican fire opal. Right: This 18K yellow gold "Spice" ring features a rare 6.57 ct fire opal with remarkable play-of-color surrounded by a halo of faceted fire opals (1.96 carats total) and two side fire opals in orange (0.73 carats total). Courtesy of Paula Crevoshay.

Editors' note: Interested contributors should send information and illustrations to gandgeditorial@gia.edu.

Gems & Gemology, Vol. 61, No. 1, pp. 84–108.

Figure 2. Left: "Dance of the Jungle" layout with 316 carats total of mandarin garnet, green tourmaline, and peridot. Courtesy of Constantin Wild. Right: Wild shows a different orange and green "Dance of the Jungle" layout with 37.26 carats total of tsavorite garnet, fire opal, chrome diopside, and Mali garnet. Photo by Jennifer Stone-Sundberg; courtesy of Constantin Wild.

higher than in previous years. In general, sales of higher-end, rare, and unusual goods were brisk early on. Compared to years past, these shows seemed more polished and more solidly focused on gems, minerals, and jewelry with less of an open market feel. For shows open to the public such as the 22nd Street Mineral, Fossil, Gem & Jewelry Show, foot traffic was quite high due to the variety of price points and offerings.

Clearly a lot of higher-end material was moving, as evidenced by GIA's Show Service Laboratory having an all-time record year, with more than a 10% increase in submissions over past years. The lab noted the usual mix of primarily ruby, sapphire, emerald, Paraíba tourmaline, and alexandrite, with some less prominent and more unusual stones submitted as well.

Green stones were very popular once again, particularly pure green to yellowish green. Emerald, especially Colombian, was heavily represented at the shows as well as other green stones including tourmaline, tsavorite, demantoid, chrome diopside, peridot, sphene, unheated sapphire, and even chrysoberyl. Vibrant yellowish orange to orangy red stones were another apparent trend, and mandarin garnet, Mexican fire opal (particularly deep red; figure 1), red Oregon sunstone, and deeply colored citrine were prolific. We found many instances of green and orange together in jewelry and loose gemstone sets, such as in Constantin Wild's Jungle series layouts (figure 2). Unheated sapphire in greens, teals, and steely blues were yet again some of the hottest stones, as were unheated "opalescent" or "sleepy" stones such as an exceptional example of a bright blue sapphire with pink and orange flashes offered by Dudley Blauwet that he likened to the fire from a fine Australian opal (figure 3). Bicolor stones were even more popular this year, and tricolor stones in a wide variety of materials were also prevalent (figure 4). Pantone's Color of the Year for 2025, Mocha Mousse, was represented in many brown

Figure 3. An exceptional 5.02 ct, 9.9 × 9.0 mm opalescent blue sapphire from An Phu, Vietnam, with eye-visible bands of silk in addition to pink and orange flashes reminiscent of play-of-color in opal from Australia. Photo by Anna Merritt; courtesy of Dudley Blauwet Gems.

Figure 4. Rainbow fluorite cabochons measuring 10 × 12 mm. Photo by Kevin Schumacher; courtesy of Jennifer Stone-Sundberg.

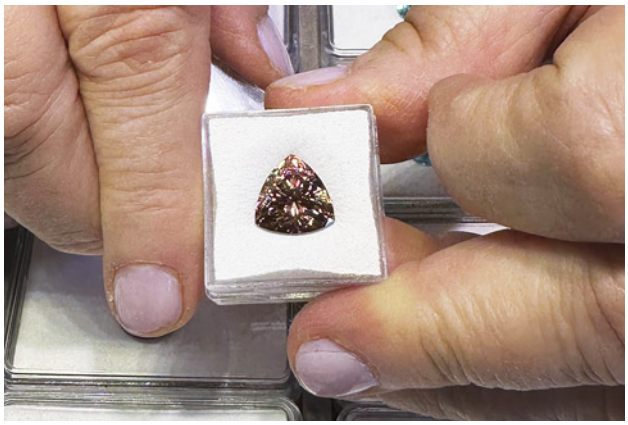

Figure 5. An 11.7 mm, 8.34 ct "mocha" zircon trillion. Photo by Jennifer Stone-Sundberg; courtesy of Mayer & Watt.

Figure 7. Imperial topaz with schiller: 1.51 ct, 7.89 ct, and 2.48 ct from left to right. Photo by Kevin Schumacher; courtesy of Jennifer Stone-Sundberg.

gemstones offered, including a bright "mocha" zircon from Mayer & Watt (figure 5). Other popular brown gems included topaz, tourmaline, diamond, and smoky or a warmer so-called "whiskey" or "brandy" citrine quartz.

Figure 6. This 22-inch "Ethereal Light" necklace contains 35 translucent Ethiopian opal beads totaling 426 carats and is finished with an 18K gold handmade clasp. Courtesy of Paula Crevoshay.

Precious opal, particularly fine Ethiopian opal, was abundant throughout the shows. The demand for Ethiopian opal has not slowed since this material first appeared in Tucson in 2009 and was prominently featured in many high-end jewelry pieces in the AGTA designer showroom (figure 6). In addition to opal, phenomenal gems of many varieties were extremely popular this year, including star sapphire and ruby, schiller sunstone from Oregon and India, and other feldspars such as labradorite, moonstone, and in particular the new "rainbow moonstone" from Madagascar we reported on last year (Spring 2024 GNI, p. 102).

Beyond phenomenal gems, included stones were also trending, such as Imperial topaz with golden and red schiller (figure 7), quartz with golden rutile from Brazil (figure 8), and moss agate. Eric Braunwart of Columbia Gem

Figure 8. Brazilian rutilated quartz bangle (6.5 inches in circumference). Photo by Mimi Travis; courtesy of Tao Hsu.

Figure 9. Moss agate cabochons measuring 12 × 10 mm (left) and 10 × 7 mm (right). Photo by Kevin Schumacher; courtesy of Columbia Gem House.

House reported that moss agate went viral after several Instagram posts promoted the stone's organic patterns and uniqueness for engagement rings (figure 9).

For faceted stones, there was a noticeable uptick in the number of heart-shaped and step-cut hexagonal stones (figure 10) in a range of materials, from Colombian emerald to rainbow moonstone to tourmaline. Marquise brilliant- and step-cut as well as shield step-cut gems were also popular.

A notable trend among jewelry buyers was the desire for something unique and personal. Interestingly, none of the winning entries for the AGTA Spectrum Awards for engagement rings and bridal wear featured a central diamond, focusing on tsavorite garnet, spinel, sapphire, and tourmaline instead. This movement was also evident in the popularity of one-of-a-kind stones, including bicolor, hazy, and phenomenal stones, as well as custom cuts and those with features such as eye-visible inclusions.

Another growing trend, men's bejeweled brooches, was observed throughout Tucson this year. Men's brooches have been evolving over the past couple of years in terms of size, inclusion of stones, and stone colors (G. Trebay, "The bro-brooch sweeps awards season," March 13, 2024, *New York Times*, https://www.nytimes.com/2024/03/13/style/brooches-male-celebrities-oscars.html).

We hope you find our coverage of the shows informative, as we dive deeper into some of the trends highlighted in this overview and feature some of the notable newer materials and unique stories encountered.

Jennifer Stone-Sundberg and Tao Hsu
GIA, Carlsbad

Lisa Kennedy
GIA, New York

COLORED STONES AND ORGANIC MATERIALS

"Enhydro" amethyst from Morocco. Known for its sharp hourglass color zoning and double termination, Moroccan amethyst has been well documented and characterized in the past (Spring 2017 GNI, pp. 126–127). However, it was the precise placement and aqueous nature of the inclusions

Figure 10. A pair of 5 mm hexagonal step-cut grape garnets from the State of Odisha on the Bay of Bengal in eastern India. Courtesy of Eric Braunwart, Columbia Gem House.

Figure 11. Left: "Enhydro" amethysts from Morocco. Right: This 16.60 ct triangular-shaped enhydro amethyst, measuring 17 × 19 mm, contains a large primary fluid inclusion with a free-moving gas bubble prominently oriented in the center of the table. Photos by Lisa Kennedy; courtesy of Gem & Gold Creations.

in the deeply saturated, large faceted amethysts that caught the author's attention at the Pueblo show this year.

The gemstones were exhibited by Gem & Gold Creations (Scottsdale, Arizona) as "enhydro" amethyst (figure 11, left). "Enhydro" comes from the Greek word *enhydros*, which means "water within." In gemology, *enhydro* terminology is typically reserved for a hollow nodule or geode of chalcedony containing water. However, "enhydro quartz" is often used in the trade to describe colorless, transparent crystalline quartz with fluid inclusions or liquid-filled cavities. The most interesting examples have a gas bubble within the fluid inclusion that moves freely when the stone is turned.

The Moroccan amethysts displayed were of similar nature to the more commonly seen colorless enhydro quartz, each containing a large primary fluid inclusion with a free-moving gas bubble prominently oriented in the center of the table facet (figure 11, right). Many of the playful inclusions were so large that magnification was not needed to observe them.

Inclusions such as these aren't only a treat for the eyes—they also serve as a fascinating reminder of a gemstone's natural origin. Fluid inclusions are rare samples of natural fluids that were trapped inside rocks and minerals long ago during their formation. A gas bubble within a fluid inclusion is a result of temperature changes endured during a mineral's journey to the earth's surface. As the mineral and the fluid cool down over time, the fluid shrinks at a faster rate than the mineral, causing a gas bubble to exsolve within the fluid.

These specimens with eye-visible fluid inclusions were a rare find with such a rich and even reddish purple hue—the most prized hue for amethyst. Ai Van Pham, owner of Gem & Gold Creations, noted that out of the 70 kg of rough amethyst he purchased from Morocco, only 10 amethysts were considered enhydro once faceted.

Lisa Kennedy

New Nigerian green beryl find. A unique new find of green beryl was discovered in 2024 in the Nasarawa Eggon mine in Nigeria. A few dealers at the Pueblo and Mineral City shows carried the material, referring to it as vanadium-bearing beryl (figure 12). Most of the stones had concentrated color-zoned bands near the terminations. Energy-dispersive X-ray fluorescence revealed iron and trace amounts of vanadium and chromium in the green zones, with the near-colorless areas primarily containing trace amounts of iron. The concentrated green color bands near the terminations exhibited pinkish orange fluorescence under long-wave (365 nm) UV light. The banding observed in these exciting new beryl samples is similar to that of Torrington emeralds from Australia.

Rhonda Wilson
GIA, Carlsbad

Figure 12. Green beryl crystals weighing 41.90 ct (left) and 4.08 ct (right) from a new source in Nigeria display concentrated color zones. Photo by Rhonda Wilson; courtesy of Rhonda Wilson (left) and Maxwell Hain (right).

Figure 13. This 1800.20 ct "rainbow calcite" collector stone was exhibited at the GJX show. Photo by Annie Haynes; courtesy of Kaufman Enterprises.

Large "rainbow calcite." A remarkable large calcite recently seen at the GJX show displayed a dazzling array of colors resulting from both high dispersion and birefringence (C.S. Hurlbut and C.A. Francis, "An extraordinary calcite gemstone," Winter 1984 *G&G*, pp. 222–225). Exhibited by Kaufman Enterprises (San Diego, California), the collector stone weighed 1800.20 ct (figure 13) and was precision cut by Italian gemstone cutter Luigi Mariani in 2024 over the course of six months. The calcite rough was mined in Brazil in the 1980s and weighed over 6000 ct. Calcite that shows these vibrant colors may be known as "rainbow calcite" in the trade. This extraordinary stone is one of the best calcite examples examined by GIA.

Jessa Rizzo
GIA, Carlsbad

New fluorite deposit in Nigeria. Exploring the various gem and mineral shows in Tucson always has surprises in store, and this year was no exception, with a batch of fluorite specimens from Nigeria exhibited at the Pueblo show by Jigga Collins Mineraux (Sécheras, France). This new find of fluorite ranges in color from gray-blue to gray-green to bluish green under artificial light, shifting to violetish blue in sunlight (figure 14, left). Under natural lighting, most of the crystals show a bicolor effect created by obvious color zoning, with a green core highlighted by blue edges (figure 14, right). All specimens show strong fluorescence when exposed to long-wave (365 nm) UV light, turning to violet-blue or an intense electric blue color (figure 15).

The fluorite comes in clusters of euhedral, often twinned cubes ranging in size from 1 cm to more than 15 cm each, regularly associated with quartz, pyrite, galena, and calcite. Some of the crystals observed contained eye-visible fluid inclusions.

Nigeria is known for its variety of industrial and precious mineral resources, including some important fluorspar deposits. Collection-grade fluorite specimens were previously known from the Jos Plateau area, Benue state, and a few other localities (J.I. Omada et al., "The Kigom peralkaline granite pluton of the Nigerian Younger Granite suite," *Global Journal of Geological Sciences*, Vol. 1, No. 1, 2003, pp. 1–12; S.O. Akande et al., "Minerology, fluid inclusion and genesis of the Arufu and Akwana Pb Zn F mineralization, middle Benue Trough, Nigeria," *Journal of African Earth Sciences (and the Middle East)*, Vol. 7, No. 1, 1988, pp. 167–180).

According to Collins, the exhibited mineral specimens come from a recently discovered deposit related to some areas of the Jalingo mine in the state of Taraba. The fluorite was located in 2022, and operations began in early 2023. Though the material had been introduced at the Sainte-Marie-aux-Mines Mineral & Gem Show (France) and at the Munich Show in 2023 (R. De Ascenção Guedes et al., "Une passion nommée Sainte-Marie-aux-Mines!," *Le Règne Minéral*, No. 172, 2023, pp. 6–16; R. De Ascenção Guedes

Figure 14. Fluorite specimens from the Jalingo mine in northeastern Nigeria shown in sunlight displaying violetish blue color (left) and obvious color zoning (right). Courtesy of Jigga Collins.

Figure 15. A twinned fluorite crystal from Nigeria (approximately 7 inches in diameter) shown under fluorescent light (left) and long-wave UV light (365 nm, right). Courtesy of Jigga Collins.

et al., "Munich 2023!," *Le Règne Minéral*, No. 174, 2023, pp. 7–31), the Pueblo show was its North American debut.

Collins noted that some of the largest mined specimens reached 35–40 kg in weight and about 80 cm in height. While 3 to 5 tons have been mined so far, the use of improper tools and limited mining expertise led to excessive damage of the extracted material during the earliest operations, leaving top-quality specimens scarce. Mining operations have since improved and production remains seasonally active.

Cristiano Brigida
GIA, New York

Green jadeite-omphacite from Guatemala. At the GJX show, Pillar & Stone (San Francisco, California) offered bright green jade from Guatemala, confirmed to range from jadeite to omphacite, that was highly translucent to nearly transparent. This was Pillar & Stone's first year showing these pyroxene-dominant jades, known in the trade as *fei cui*. Nata Heng showed us many individual pieces, matched pairs, and beads in an intense green coupled with high translucency/near transparency similar to that of fine "imperial green" Burmese jadeite-omphacite jade (figure 16). This material was being sold as Guatemalan imperial green jade. Heng also presented an equivalent set of Burmese jade pieces for side-by-side comparison, noting that the Guatemalan material is considerably less expensive than that of the same color and size from Myanmar. S.I.E. Liu et al. recently reported on the similar appearances of this newer source of "imperial green" jade from Guatemala and the material from Myanmar (see figures 1 and 2 in S.I.E. Liu et al., "Geographic origin determination of high-quality green jadeite-omphacite jade (*fei cui*) from Myanmar, Guatemala and Italy using statistical processing coupled with spectroscopic and chemical analyses," *Journal of Gemmology*, Vol. 39, No. 2, 2024, pp. 124–144).

Having visited the Chinese markets processing and selling this Guatemalan material in Jieyang and Guangzhou, Heng reported that one of the largest miners was sending approximately 8 tons of rough each week for processing, with about 20% of the gem-grade material being green. As the green color is concentrated in veins up to 5.5 mm thick, Guatemalan green jade is generally much thinner than material from Myanmar when cut and used in jewelry. As this material can be quite iron-rich, resulting

Figure 16. Nata Heng showing the various shapes and sizes of finished Guatemalan jade processed in China. Photo by Jennifer Stone-Sundberg; courtesy of Pillar & Stone.

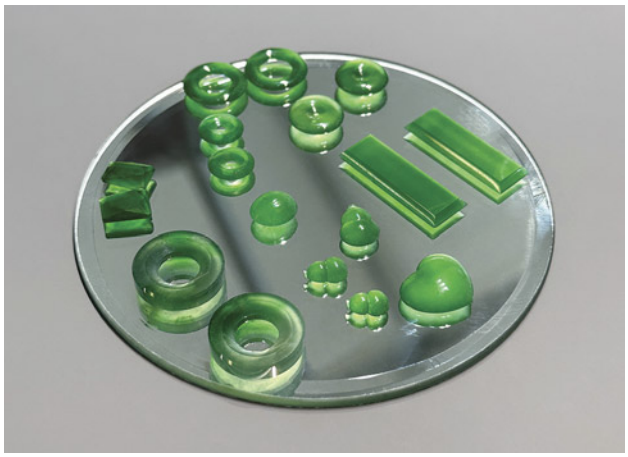

Figure 17. Several Guatemalan jade pieces placed on a mirror to demonstrate the transparency of the material. Photo by Jennifer Stone-Sundberg; courtesy of Pillar & Stone.

Figure 18. Mechanical keyboard with select jade keycaps. Photo by Lisa Kennedy; courtesy of Carter Stay, Keycap Quarry.

in a deep saturated green color, some choose to cut it relatively thin when used in jewelry to keep the color saturation from being too intense. To best demonstrate its incredible translucency/near transparency, Heng placed many of the pieces on a mirror (figure 17). At the AGTA show, Mason-Kay (Centennial, Colorado) was also selling green jade from Guatemala. To our knowledge, this is the first year that this bright green and nearly transparent jade from Guatemala has been offered in Tucson. With the lower price point, Heng predicts a growing trend toward more affordable top-quality green jadeite and omphacite (*fei cui*) jade.

Jennifer Stone-Sundberg and Aaron Palke
GIA, Carlsbad

Wim Vertriest
GIA, Bangkok

Gemstone artisan keycaps. At the 22nd Street show, Carter Stay, owner and artisan behind Keycap Quarry (Salt Lake City, Utah), shared his unique craft with the author, opening up about what led him to pursue an alternative use for one of nature's most beautiful creations—gemstone keycaps for mechanical keyboards (figure 18).

A mechanical keyboard has a physical switch beneath each keycap that transfers keystrokes to a printed circuit board, resulting in a distinct feel compared to other keyboards. Popular among computer gamers, like Stay himself, mechanical keyboards provide a tactile experience. Artisan keycaps are custom-made for these keyboards, designed to stand out from mass-produced options. They are often crafted in small batches from materials such as metal, resin, or clay.

Growing up in Utah and being surrounded by rock hounds and lapidaries fostered Stay's fascination with rocks. Like many eager to seize opportunity amid the challenges of the COVID-19 pandemic, he launched Keycap Quarry at just 16 years old, and it has since grown into a thriving enterprise with more than 34,000 followers on Instagram. Stay offers a wide variety of gemstone keycaps including opal, jade, quartz, and various agates (figure 19). Each keycap is the result of Stay's careful selection of the finest rough materials, followed by his keen attention to detail while cutting and polishing.

Stay highlighted the importance of selecting the right slab, or rough material, and how it influences the shape of

Figure 19. Various gemstone keycaps including rutilated quartz, chrysocolla malachite, amethyst, fossilized red horn coral, charoite, turquoise, opal, wavelite, and more. Courtesy of Carter Stay, Keycap Quarry.

Figure 20. Topaz in matrix keycap with an inlaid base of sterling silver. Courtesy of Carter Stay, Keycap Quarry.

his keycaps. By sourcing slabs with tighter patterns, he's able to more efficiently display the unique designs inherent to the stones within the smaller, face-up area of his keycaps. He typically creates keycaps with a square profile, which allows him to use and show off more of the gem material. However, the finish of the top of the keycap varies depending on the stone—he's created keycaps with faceted, carved, domed, flat, and raw, unaltered tops.

One of Stay's most popular keycap varieties is the amethyst cluster, with the top remaining in its crystal form. Stay enjoys capturing the tactile essence of gems (figure 20). He lightheartedly mentioned that customers request that "he does a backspace key with the 'pokey' ones [raw, unaltered tops], acting like a negative reinforcement if you make a mistake."

Customers enjoy following Stay's entire production story, from mining and digging to cutting and polishing, which he often chronicles on Instagram. He has recorded himself digging for fossils at U-Dig Fossils Quarry in Delta, Utah, followed by cracking open the shale and discovering fossilized trilobites to take home and create into keycaps (figure 21). He has also worked with other fossils that he did not collect, such as ammonite, turritella agate, and mammoth molar.

As a self-taught rock enthusiast and lapidary, Stay expressed the value of coming to the Tucson gems shows—not only for the stones, but for the connections he continues to make each year. These unique connections allow him to deepen his understanding of the gemstones he works with. It's also where he met Luke Miller, owner of Yax Tun Minerals (Denver, Colorado) specializing in Guatemalan jade, who allowed Stay the extraordinary opportunity to exhibit his gemstone keycaps at the Yax Tun booth this year.

Figure 21. Set of one-of-a-kind trilobite fossil keycaps. Courtesy of Carter Stay, Keycap Quarry.

So, what's next for Stay? He's happy with his current business that allows him to combine two niches—rocks and gaming—and that he's been able to put his own spin on these unique materials for the gem industry. "That is the direction the art and lapidary world is going. People want the different and unique stuff, rather than the mass-produced items," he noted. Stay also shared his interest in creating jewelry in the future, having recently acquired a collection of tools from a retiring goldsmith. With his keen attention to detail, passion, and background working with computers, including 3D printing, he's perfectly poised for the new era of jewelry manufacturing.

Lisa Kennedy

"Bubble obsidian" from Armenia. Obsidian is a volcanic glass formed when silica-rich lava cools so fast that crystal formation is only visible with a microscope. The glassy and amorphous nature of obsidian makes it hard and brittle. Due to its highly conchoidal fracture, obsidian has been an ideal material for manufacturing cutting tools since the Neolithic era (ca. 7000–1700 BCE). In addition, obsidian is a popular ornamental gem due to its workability and the occurrence of attractive varieties.

At the 22nd Street show, the author encountered an unusual type of obsidian characterized by an extremely vesicular, or "bubbly," structure featuring large, often oriented degassing cavities (figure 22, left). In the specimens observed, the bubbles reached more than 2 inches in length, varied in size, and were separated by extremely thin and sharp septa (figure 22, right). Some specimens contained several intact bubbles (figure 23).

The specimens were presented by Bojo Jewelry & Minerals (Yerevan, Armenia), an exhibitor offering a wide range of gems and jewelry from Armenia, including obsidian and turquoise. The dealer, Artak Bojikyan, who named the material "bubble obsidian," noted it was an unexpected find last year resulting from road construction on the Arteni Mountain in Armenia's Aragatsotn region, one of the most significant obsidian occurrences in the Caucasus Mountains. Bojikyan noted that a few large boulders have been found so far, and more may be recovered in the upcoming months.

Figure 23. Detail of intact degassing bubbles in one obsidian specimen. Photo by Cristiano Brigida; courtesy of Bojo Jewelry & Minerals.

Armenian obsidian, also known as "mahogany" obsidian in the trade, is a high-quality compact stone, typically displaying distinctive reddish brown streaks against a black bodycolor. According to Bojikyan, this is the first time this type of highly vesicular obsidian from the Arteni Mountain deposit has been offered at a trade show, and it attracted the attention of scientists and collectors.

Cristiano Brigida

Figure 22. Left: Oriented degassing bubbles in obsidian "quenched" during the cooling process. Right: The vesicles varied in size and shape and were separated by extremely thin and sharp septa. Photos by Cristiano Brigida; courtesy of Bojo Jewelry & Minerals.

Figure 24. A faceted pezzottaite, measuring approximately 6 × 4 mm, with a group of rough (largest piece ~25 mm in diameter) exhibiting purplish pink to red color from the Vakinankaratra region of Madagascar. Photo by Nathan Renfro; courtesy of Lamine Kakro and Yianni Melas.

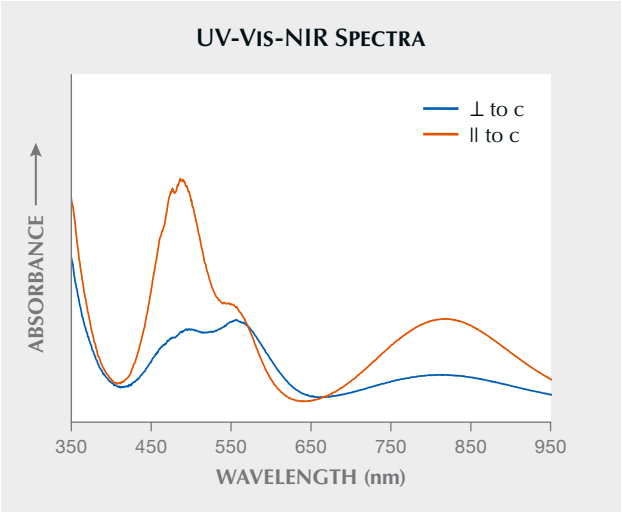

Figure 26. UV-Vis-NIR absorption spectra of pezzottaite from Vakinankaratra, Madagascar. The difference in the spectra based on orientation explains the pleochroism observed in the pezzottaite samples.

New deposit of pezzottaite from Madagascar. Pezzottaite is a rare, purplish pink gemstone and a mineral of the beryl group, characterized by high lithium and cesium contents ($Cs(Be_2Li)Al_2(Si_6O_{18})$). In Tucson, the authors encountered a parcel of highly saturated purplish pink to red pezzottaite (figure 24) from a new deposit in Madagascar with color noticeably more saturated than earlier known production from the Sakavalana granitic pegmatite near Ambatovita (B.M. Laurs et al., "Pezzottaite from Ambatovita, Madagascar: A new gem material," Winter 2003 *G&G*, pp. 284–301). The stones ranged in sizes from as small as 2 mm to tabular crystals approximately 25 mm in diameter and were reportedly from the Sahatany Valley in the Vakinankaratra region of central Madagascar. Rough samples of the material (5.02 carats total) were acquired from Lamine Kakro and Yianni Melas at the AGTA show and later analyzed at GIA (figure 25).

Standard gemological testing indicated refractive indices from n_e = 1.600–1.611 and n_o = 1.610–1.621 and specific gravity from 3.05–3.14. The stones had a pinkish purple hue with medium tone and moderate to strong saturation. All samples demonstrated strong pleochroism, showing purplish pink when viewed perpendicular to the *c*-axis and reddish orange when viewed parallel to the *c*-axis. Crystallographic orientations were determined visually for samples with preserved crystal form. Three of the samples showed uniaxial interference figures in the polariscope, and all samples were inert under short-wave and long-wave fluorescence. These gemological properties were consistent with pezzottaite, although the color was much more intense than that of previously observed stones. Microscopic examination revealed numerous fractures and

Figure 25. Rough samples of pezzottaite (5.02 carats total) acquired at the AGTA show from the parcel shown in figure 24. The difference in appearance is due to the small size of the acquired samples and resultant lower saturation. Photo by Annie Haynes.

small fluid inclusions, though the samples were generally free of foreign mineral inclusions.

Raman spectroscopy confirmed the identity of the material as pezzottaite by an intense peak at ~1100 cm^{-1}, which is not present in beryl. Fourier-transform infrared spectroscopy showed features associated with water in the crystal structure, which confirmed its distinction from red beryl despite having a similar color. Ultraviolet/visible/near-infrared (UV-Vis-NIR) spectra were collected parallel and perpendicular to the crystallographic *c*-axis (figure 26), with differences based on orientation matching observations of moderate to strong pleochroism and no evidence of dyes altering the color. Elemental concentrations were determined by laser ablation–inductively coupled plasma–mass spectrometry (LA-ICP-MS) analysis. Three spots were ablated on each sample, for a total of 18 analyses: Cs_2O ranged from 10.88–16.79 wt.% in the samples, while Li_2O ranged from 1.94–2.51 wt.% (table 1).

Standard gemological testing and advanced testing both confirmed the identity of the samples as pezzottaite. These samples are remarkable due to their vivid saturation which makes them unique compared to the previously available pezzottaite.

Alexander A. Goodsuhm and Nathan Renfro
GIA, Carlsbad

Wim Vertriest
GIA, Bangkok

TABLE 1. Chemical analyses of pezzottaite (determined by LA-ICP-MS) from Vakinankaratra, Madagascar.

Oxide	wt.% range (avg)
Li_2O	1.94–2.51 (2.24)
BeO	7.74–9.59 (8.53)
Na_2O	0.34–1.31 (0.72)
Al_2O_3	14.99–17.51 (16.45)
SiO_2	54.87–59.84 (56.90)
K_2O	0.004–0.074 (0.041)
CaO	0.032–0.78 (0.40)
TiO_2	0.001–0.008 (0.003)
MnO	0.001–0.021 (0.011)
Fe_2O_3	0.004–0.046 (0.016)
Rb_2O	0.025–0.19 (0.13)
Cs_2O	10.88–16.79 (14.58)

Figure 27. Cat's-eye labradorite earrings set in 14K gold. The stones measure 7 × 5 mm. Photo by Kevin Schumacher; courtesy of Ben Kho Gems.

Phenomenal gems. This year, phenomenal gems were very popular and selling well throughout the Tucson shows, illustrating the growing desire for one-of-a-kind stones. Phenomena such as asterism, schiller, play-of-color, and iridescence were on full display at all of the major shows. Vendors reported strong sales of fine asteriated gems such as star ruby and sapphire from Sri Lanka, Vietnam, and Myanmar; moonstone of all varieties, but particularly "rainbow moonstone" with orange flash and blue adularescence from Madagascar; sunstone with reddish gold schiller from Oregon and India; precious opal from all over the world; and a wide variety of labradorite.

These fascinating optical phenomena arise from many different sources, with the common theme being how light interacts with inclusions and/or the host material itself. Parallel needle inclusions aligned with crystallographic directions in crystals can yield attractive cat's-eyes (figure 27) or stars when these stones are properly cut. Precious opal can show a rainbow of colors (play-of-color) when incoming light interacts with the host by being diffracted as it passes through the oriented silica spheres comprising the material. Many gems belonging to the feldspar group of minerals—including moonstone, sunstone, and labradorite—can exhibit iridescence related to light interacting with thin film structures or with platy particulate inclusions (R.J. Strutt, "Studies of iridescent colour, and the structure producing it. III.—The colours of labrador felspar," *Proceedings of the Royal Society London A*, Vol. 103, No. 720, 1923, pp. 34–45).

At the AGTA show, Eric Braunwart of Columbia Gem House (Vancouver, Washington) showed us a remarkable 13.2 ct star ruby from Vietnam in a brilliant purplish red (figure 28). His regard for the stone due to its exceptionally sharp star, rarity, and beauty was apparent. Reports from other vendors such as Dudley Blauwet with booths at multiple shows, indicated that star sapphire and star ruby were selling very well this year.

Figure 28. Exceptional 13.2 ct star ruby from Vietnam measuring 12.3 × 11.0 mm. Photo by Jennifer Stone-Sundberg; courtesy of Columbia Gem House.

Opal has traditionally been one of the most popular phenomenal gems, and this year its presence was exceptionally strong. Remarkable examples with striking play-of-color from Australia, North America, and particularly Ethiopia were in high demand. This material ranges from opaque to transparent; its matrix color is generally white, gray, or black; and its play-of-color can assume many forms including pinprick-sized spots all the way up to large brush strokes (see Lab Notes, p. 64 of this issue). Braunwart shared an exceptional faceted Mexican fire opal with high transparency and brilliant flashes of color spanning the entire rainbow (figure 29).

Labradorite, a relatively inexpensive plagioclase feldspar that has been used extensively as a high-end countertop material, was first recognized in Labrador, Canada, in 1770. It has since been identified in locations all over the world. Its iridescent effect, known as labradorescence, can display a wide range of iridescent colors including blue, green, yellow, orange, and violet (figure 30). Labradorite was offered in a wide range of qualities and price points at the shows this year. Several Idar-Oberstein cutters at GJX exhibited high-end labradorite carvings along with their tourmaline, beryl, peridot, amethyst, and agate carvings.

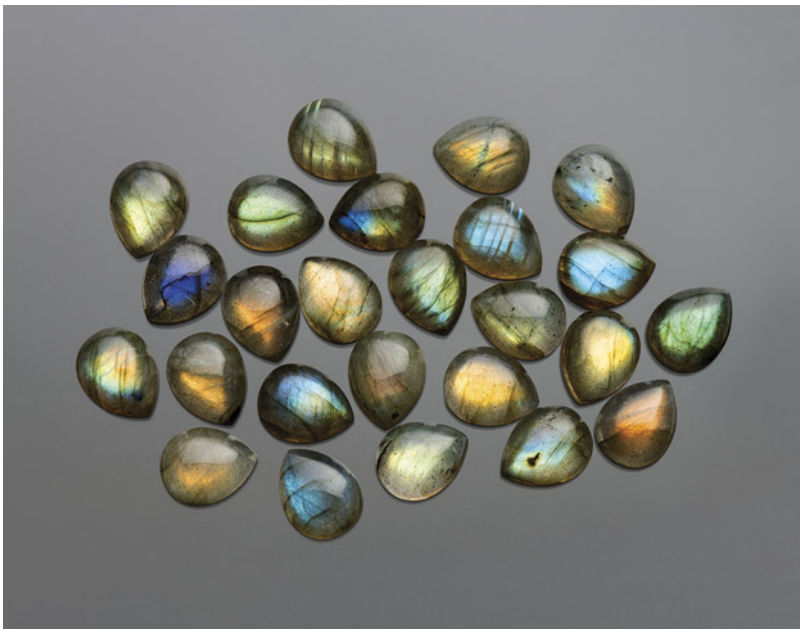

Figure 30. Colorful 8 × 10 mm teardrop labradorite cabochons. Photo by Kevin Schumacher; courtesy of Shanghai Jade Gems Factory.

Figure 29. Highly transparent pear-shaped crystal opal from Mexico showing play-of-color. The opal measures 22.2 × 16.7 mm and weighs 17.82 ct. Photo by Jennifer Stone-Sundberg; courtesy of Columbia Gem House.

Figure 31. A 9.5 mm, 3.25 ct rainbow moonstone with orange flash and blue adularescence from Madagascar. Photo by Jennifer Stone-Sundberg; courtesy of Mayer & Watt.

Figure 32. A 63.0 ct hand-carved Indian sunstone squirrel with a tourmaline leaf measuring 33.5 mm high (left) and a 43.10 ct Oregon sunstone depicting a moon face inspired by Beethoven measuring 11.8 mm high (right). Both carved by Hans-Ulrich "Uli" Pauly of Idar-Oberstein, Germany. Photos by Gaby Pauly; courtesy of Pauly Carvings.

Highly transparent "rainbow moonstone" from Madagascar—a plagioclase feldspar confirmed to be of the labradorite variety, so therefore not a true moonstone—was one of this year's hottest materials after making its debut last year (Spring 2024 GNI, p. 102). Several vendors at AGTA and GJX carried this material both faceted and en cabochon, with the faceted stones being slightly more popular. Many layouts and matched sets were on display in shapes ranging from rounds to hearts to hexagons. At AGTA, Mayer & Watt (Maysville, Kentucky) offered a wide selection of various cuts and sizes with strong yellow to orange flash and blue adularescence (figure 31).

Sunstone, a gem known for its reddish golden metallic schiller, was available through more vendors and shows than in years past. Oregon sunstone, once a curiosity, is now a highly sought gem by many around the world. Oregon sunstone is a plagioclase feldspar colored by copper (S. Jin et al., "Special colors and optical effects of Oregon sunstone: Absorption, scattering, pleochroism, and color zoning," Fall 2023 *G&G*, pp. 298–322). This unique gem has fine copper schiller that can take on many different appearances depending upon copper particle size. Other sunstones exhibit thin plates of reddish hematite schiller, such as those from India. Idar-Oberstein carver Hans-Ulrich "Uli" Pauly carves both Oregon sunstone and Indian sunstone into exquisite *objets d'art*, which were on display at the GJX show in the Idar-Oberstein Pavillion (figure 32). At the Holidome show, Sami Gems & Jewellers (Jaipur, India) offered sunstone from India. This material varied from densely included with high metallic luster and a rich reddish gold color to transparent (figure 33). The faceted transparent stone in figure 33 (top right) showed a faint bluish cast on two ends and a reddish golden cast on the other two, with a light scattering of metallic inclusions throughout. Suwalin Shamsi ("Sami") indicated that the material comes from Madras (Chennai) in Tamil Nadu, a region in southern India known for farming.

Figure 33. Sunstone with schiller from Madras, India, demonstrating the variety available in terms of depth of color and transparency. Note the bicolor nature of the larger faceted gem (13 × 17 mm), which exhibits a blue tinge at the top and bottom. Photo by Jennifer Stone-Sundberg; courtesy of Sami Gems & Jewellers.

Phenomenal gems always carry appeal, as they delight the observer and can inspire a desire to learn more about the science behind them. The availability of so many varieties provides the opportunity to appreciate the complex and diverse optical phenomena responsible for their captivating special effects.

Jennifer Stone-Sundberg

Update on Montana's Rock Creek sapphire. Sapphire, rough and faceted, from the Rock Creek deposit in Montana has become one of the pillar gems of American origin in the global colored gemstone market. Over the past 10 years, Potentate Mining, the company operating the mine and marketing Rock Creek sapphire, has successfully developed a solid clientele base in North America. The rough sapphire

Figure 34. Top: The open pit mining operation in the "meadow" area of the Rock Creek deposit. Bottom: The recently built 10-jig processing plant at the new mining area. Courtesy of Potentate Mining.

Figure 35. An assortment of rough sapphires (5–10 mm in diameter) extracted from the new mining area displaying characteristics typical of stones from the Rock Creek deposit, including many with a yellow "yolk" at the center. Courtesy of Potentate Mining.

business has been robust, including successful sales at this year's AGTA show.

The company has had a mission to bring Montana sapphire to a wider retail market in the United States. To accomplish this goal, steady sizable production of rough sapphire and a more diverse clientele around the globe are some of the prerequisites.

Potentate Mining has secured both the Eureka Gulch and the Rock Creek mining properties over the past 10 years in the Gem Mountain District near the historic town of Philipsburg in Montana. This includes the old alluvial workings and the surrounding hilltops, the largest privately held sapphire mining claim since the late 1800s. The

Figure 36. The inaugural Montana sapphire tender was held in Bangkok at the end of 2024. Left: The auction space featured ample natural light and private cubicles for clients to view the lots. Right: Some of the larger Montana sapphire rough offered at the inaugural tender in Bangkok. Courtesy of Potentate Mining.

newest development at the mine occurs in the "meadow" area that has not been worked on for decades (figure 34, top). To increase the processing capacity, a new washing plant was recently added to the site (figure 34, bottom). The new plant features 10 jigs and a water recycling system. Six out of the 10 jigs work on sapphires of a normal size range. Two other jigs process oversized sapphires, and the last two manage the tiny sapphires and the limited amount of fine gold. The new mining area produces sapphire rough ranging from 2.5 to 12 mm, and the production looks similar to that of older mining areas on the hilltops (figure 35). With this new area in operation, the production of rough sapphire has increased.

In an effort to expand the Montana sapphire market globally, Potentate Mining in collaboration with the Bonas Group, a reputable diamond and gemstone tender company, hosted an inaugural Montana sapphire tender in December of 2024 in Bangkok, Thailand (figure 36). As the global hub of colored gemstone trading, Bangkok attracts buyers from all around the world and is a crucial location for Montana sapphire trading. The tender offered nearly 80 kg of Montana sapphire rough. Most buyers had sapphire cutting and jewelry manufacturing expertise and were mainly from India, Thailand, and other Asian countries. According to Potentate Mining, the heated rough was their best seller, with its risk of heat treatment eliminated. This inaugural tender provided a good learning opportunity for both the buyers and the hosts. Most buyers were not very familiar with Montana sapphire; it will take them time to learn about the potential of these stones and their reaction to heat treatment. The seller will also need time to learn the preferences of these new buyers in order to provide proper goods.

The success of the inaugural tender moved Potentate Mining one step closer to bringing Montana sapphire to more consumers and being a key supplier of sapphire in the global marketplace. More tenders have been planned for the next few years. The increased sapphire production from this deposit will be able to supply both the North American market and the newly developed global clientele base.

Tao Hsu

Figure 37. A Caribbean queen helmet shell carved by Vincenzo Imposimato depicting the COVID-19 pandemic. Courtesy of Massa Gioconda.

World events carved in a shell. A remarkable shell lamp (figure 37), hand carved by Italian artist Vincenzo Imposimato, was exhibited at GJX by the Massa Gioconda company (Naples, Italy). For nearly 40 years, Massa Gioconda has been dedicated to high-quality, handcrafted coral, turquoise, and shell pieces, such as this exquisitely detailed shell lamp.

Carved from a Caribbean queen helmet shell (*Cassis madagascariensis*), Imposimato's lamp was inspired by the global challenges brought on by the COVID-19 pandemic. Through intricate engravings, the artist captured the events and emotions from multiple perspectives. The result is a thoughtful visual representation of the pandemic's widespread impact. Through his craftsmanship, Imposimato not only preserves traditional techniques but also redefines shell carving as a profound form of storytelling.

At the center of the design, the virus takes on the form of a looming demon reaching out to the lone figure who resists its grasp. A clock serves as a reminder of the race against time to develop treatments and solutions. To the left, a doctor cradles a newborn—a symbol of hope

Figure 38. Details of the hand-carved shell lamp. Left: A doctor cradles a newborn as a symbol of hope. Right: World leaders with their eyes closed contemplating the global impact of the virus. Courtesy of Massa Gioconda.

(figure 38, left). To the right, world leaders with closed eyes are portrayed above a world map, capturing the uncertainty during the early days of the pandemic (figure 38, right). The scene at the bottom pays tribute to the many lives lost.

This intricate engraving is a testament to the perseverance of individuals and communities, the determination to overcome adversity, and the unwavering belief that no matter the challenges faced, a brighter and more united future is always within reach.

Edyta Banasiak
GIA, New York

Gem-quality spinel from southern Malawi. At the AGTA show, the author spoke with Brent Smith, owner of Phoenix Gems (Holly, Michigan), who shared a few parcels of rough spinel of different colors recently mined in Malawi. According to Smith, despite identifying spinel occurrences in 2014 (G.W.P. Malunga, *An Analysis of Mineral Resources of Malawi*, 2014), actual mining operations did not begin until 2024 and are actively producing reasonable quantities, though an exact figure is not yet available. The stones ranged in weight from 4 ct to more than 10 ct.

A few parcels contained pink stones, in a range of tones from light to medium-dark and saturations up to moderately strong (figure 39, left). The stones were translucent to transparent and relatively clean, containing minimal inclusions and fractures visible with magnification. Smith noted that the pink stones fluoresce a bright red color under UV light.

Another two lots of spinel ranged in hue from bluish gray to grayish blue to violet-blue, with no reported fluo-

Figure 39. Parcels of rough pink spinel (left) and gray-blue spinel (right) from Malawi, ranging from approximately 4 to 7 ct. Courtesy of Phoenix Gems.

rescence under UV light (figure 39, right). Their tones ranged from medium-light to dark. The gray and blue material observed was highly transparent and lacked eye-visible inclusions. Smith reported that he had encountered some dark purple spinel from Malawi as well.

The spinel exhibited was reportedly mined in Makoko, a village in the southern part of the country. According to Smith, the early findings from this location were small and very poor in quality, until valuable gem-quality crystals were found during recent operations. Based on conversations with some other gem dealers familiar with the area, one of whom lives on site, all agree that no gem-quality spinel has been produced nor is known in the trade from Malawi to date. Phoenix Gems reports to be the only dealer exhibiting this new Malawian material this year.

Malawi is still under development and requires the establishment of ethical practices to allow real beneficiation for the communities. Smith explained that Phoenix Gems cooperates with the Export Development Fund (EDF), a subsidiary of the Reserve Bank of Malawi. These institutions are working with miners and mine owners to establish a safe and official selling channel that guarantees paying local miners a fair market value for the rough. On the international scale, EDF is committed to making the material available and recognized in worldwide marketplaces. The cooperation between local institutions and international dealers to build transparency and value throughout the supply chain is an encouraging sign for a sustainable and fair gem trade for Malawi.

Cristiano Brigida

Figure 40. Unheated Paraíba tourmaline melee from the Mulungu mine in Rio Grande do Norte, Brazil. Photos by Kevin Ferreira.

Paraíba tourmaline melee: An entry-level market perspective. At the GJX show, we discussed the evolving market landscape of Paraíba tourmaline with Kevin Ferreira, coauthor of *Paraiba: The Legacy of a Color*. Known for its unparalleled neon glow and rarity, Paraíba tourmaline has long been associated with the high-end market. However, an entry-level market exists, primarily through melee stones, which offer a more accessible price point for jewelers and collectors.

"In the last two years, the price of Paraíba has risen tremendously and at a steady pace," Ferreira noted. However, he emphasized that melee stones provide an excellent low-cost introduction into the Paraíba space, allowing jewelers to experiment with a non-traditional gemstone that boasts a head-turning color. First appearing in the market in the late 1990s, melee Paraíba tourmaline made this otherwise unattainable gemstone more accessible. Today, melee stones are produced two to three times yearly, with approximately 80% originating from the Mulungu mine in Rio Grande do Norte, Brazil (figure 40). The total annual yield is approximately 5000 carats of gems, including both faceted material and cabochon stones. Yet only 10 to 15% meet the clean neon blue standard in sizes ranging from 1.0 to 1.8 mm. The remaining 85% tends to be greenish or included. Some cuprian tourmaline may initially exhibit colors other than the classic neon blue but can undergo heat treatment to achieve the highly desirable vibrant hue, further expanding the range of available material.

Looking ahead, the market for Paraíba tourmaline is poised for structural shifts. As end consumers increasingly seek direct access to mining sources and bypass traditional wholesale channels, there will be a greater emphasis on price stabilization and transparency. This supply chain evolution presents challenges and opportunities, requiring a stronger focus on ethical trade practices and business integrity to ensure fair distribution and sustained market stability.

Ultimately, color remains the most critical determinant of a Paraíba tourmaline's value. Whether in melee sizes or larger specimens, the vibrancy and saturation of the neon hue drive demand, securing Paraíba tourmaline's place as one of the most coveted gemstones in today's market.

As the market continues to evolve, the demand for Paraíba tourmaline melee will likely grow, offering new and seasoned jewelers and collectors opportunities to engage with this extraordinary gemstone. With increasing transparency and ethical sourcing initiatives, the industry is poised to navigate the challenges ahead while preserving the allure and prestige of Paraíba tourmaline for generations to come.

Edyta Banasiak

Figure 41. One of the largest of the five väyrynenites displayed was this elongated emerald cut weighing 1.21 ct. Photo by Lisa Kennedy; courtesy of FYI Pearl & Gem.

Rare faceted väyrynenite. At the GJX show, a set of uniquely saturated gemstones exhibited by FYI Pearl & Gem (Dallas, Texas) caught the author's eye. Five faceted väyrynenites with weights ranging from 0.74–1.24 ct displayed a vivid, slightly orangy pink color, reminiscent of fine "padparadscha" sapphire (figure 41). Owner Marc Freeman explained that the stones were from Afghanistan. Their appearance aligned with previous observations describing Afghan väyrynenite as being more pink and less orange than the Pakistani material (Summer 2006 GNI, pp. 184–185).

Named after Heikki Allan Väyrynen, a professor of mineralogy from Finland, väyrynenite was recognized as a new mineral in the mid-1950s. The manganese-beryllium-phosphate ($BeMn^{2+}(PO_4)(OH)$) typically displays a light pink to orangy pink color, and is very rarely faceted—especially in weights larger than a carat.

With a hardness of only 5 on the Mohs scale, väyrynenite is not the best choice for jewelry and is better suited for display as a prized collector gem. Still, the vibrant saturation and size of these five stones are a testament to the magical wonders of Mother Nature. Freeman has a few more pieces of rough in reserve to be cut, which will bring even more of these larger, saturated väyrynenite gemstones to the market.

Lisa Kennedy

JEWELRY DESIGN

Innovative bangles. In the jewelry world, innovation continuously drives the industry forward, with jewelry designers often at the forefront of the creative attempt. The author found two bangles exemplifying this astonishing innovation at the AGTA show, exhibited at the Somewhere in the Rainbow collection booth.

The first of the two bangles was designed and constructed by Jeremy May of London, who creates jewelry using pages from books (figure 42, top). May's "literary jewel" design concept was born out of a gift idea for his wife to celebrate their first wedding anniversary, in which he crafted a ring literally made of paper. Debuted to the public in 2009, these reimagined paper jewels attract bookworms and those who value sustainability through repurposing from all over the world.

Figure 42. Top: Bangle by Jeremy May constructed of pages cut out of a book. Bottom: The bangle is placed into the book where it was cut out, serving as a "jewelry box" for the piece. Photos by Tao Hsu; courtesy of the Somewhere in the Rainbow collection.

To make a literary jewelry piece, May begins by selecting a book that serves both as the material and in many cases, its inspiration as well, and then cuts the jewel's shape out of the pages. Depending on the design, sometimes additional colored papers are used to add pops of color. Applying a proprietary laminating process, May turns the thick stack of cut-out paper into a compact solid piece that can be further processed and polished. Layers of

Figure 43. Left: This bangle by Pawel Kaczynski is made of ruffled stainless steel with a magnetic clasp. Right: This top view of the bangle shows its double-tier structure. Photos by Tao Hsu; courtesy of the Somewhere in the Rainbow collection.

varnish are applied to give the item a high gloss. From start to finish, the process often takes at least eight weeks for one piece. In addition to hololith-style jewelry cut directly from the book pages, May also constructs jewelry pieces by assembling various laminated paper components. Each creation comes with the original book to use as a "jewelry box," adding to the significance of owning such a one-of-a-kind and distinctive jewelry piece (figure 42, bottom). To May, each book carries its own unique story, not only related to the content but also through its ownership history. Creating these pieces gives a second life to the words as they're revealed on jewelry.

The second bangle was designed by Polish jewelry artist Pawel Kaczynski, who has been using jewelry as a means of artistic expression since the mid-1990s and is best known for his creative application of steel, silver, and gold. This bangle is a representative piece from his "Structure" collection, constructed with pleated and folded stainless steel mesh in a double-tiered configuration (figure 43). Using patinated stainless steel mesh, Kaczynski's design mimics the appearance of tree bark. While the rigidity and hardness of stainless steel make it challenging to manipulate in jewelry making, the mesh used in this bangle leaves it soft to touch and flexible to wear. The bangle closes with a magnetic stainless steel clasp. The characteristic cream color patina coating adds to the realism of the piece. In addition to this piece, Kaczynski applies other colored patina to his stainless steel jewelry, shaping and folding the mesh to form endless interesting structures and surfaces.

Tao Hsu

Nature-inspired jewelry. We met Boom Chappell (figure 44), jewelry designer and founder of Metal Studio Jewelry, at the Pueblo show, where she shared her unconventional approach to jewelry making. Based in the picturesque town of Chiang Mai in northern Thailand, Chappell transforms her passion for nature and gemstones into exquisite one-of-a-kind creations (figure 45, left).

Her process is entirely organic. Unlike traditional designers who begin with sketches, Chappell prefers to work directly with the materials: "Sketching feels restrictive to me. Instead, I start shaping the piece as I go, allowing creativity to flow naturally." By letting each gemstone guide her, she crafts pieces that are not only visually stunning but deeply meaningful.

Chappell thrives on collaboration, working closely with clients to bring their visions to life. "Sometimes, a customer will request something deeply personal—like incorporating their children's birthstones into a necklace. I take their story and translate it into a piece of art they can cherish forever." Her talent for directly transforming raw stones into wearable works of art sets her apart, ensuring that each piece resonates with its owner.

Selecting a favorite design is nearly impossible for her—she sees each gemstone as an unread book, its story unfolding as she works. "Even though I've set countless stones, no two are ever the same," Chappell reflects. "Each gemstone has its own texture, energy, meaning, and presence, making every creation a unique journey."

One of her most challenging creations features a drusy quartz gemstone. Originally envisioned as a solo centerpiece, Chappell expanded the design, weaving in complementary stones such as labradorite, freshwater pearls, and striking orange and blue kyanite (figure 45, right). "This drusy quartz gem's natural formation is incredibly intricate," she explains. "A single mistake could break a fragile tip, so patience and precision are key."

Figure 44. Boom Chappell at the Pueblo Gem & Mineral Show. Photo by Edyta Banasiak.

Figure 45. Left: "The Ant on the Sugar" ring, symbolizing persistence and determination, consists of drusy quartz measuring 4 × 3 cm. Right: This necklace, one of Boom Chappell's most challenging pieces, features drusy quartz, labradorite, freshwater pearls, and blue and orange kyanite. Photos by Edyta Banasiak; courtesy of Metal Studio Jewelry.

Over time, Chappell has noticed a shift in how people value handcrafted jewelry. At trade shows, visitors often pause to admire her work, sensing the intention woven into each design. These moments of recognition fuel her passion and reaffirm her dedication to her craft. In a world of mass production, her work serves as a powerful reminder of the artistry that only human hands and an inspired mind can achieve.

Edyta Banasiak

RESPONSIBLE PRACTICES

Gems Keep Giving. On February 5 at the Pima County Historic Courthouse in Tucson, Hayley Henning, chairperson of Gems Keep Giving, introduced us to the nonprofit focused on improving the lives of small scale–mining and gem-cutting communities around the world. This 501c3 organization, started by the International Colored Gemstone Association, is now autonomous. Gems Keep Giving works to develop better living conditions, provide safety protections, ensure sustainability of resources, and protect the environment with projects funded via ethical and transparent partnerships.

Henning presented on the progress made in Kamtonga, Kenya, with Gems Keep Giving's first project. This tsavorite mining community has benefited from the contributions of solar energy and clean drinking water. The organization aims to apply this model in other mining regions to provide community members with needed resources, while ensuring that mining profits are shared fairly. A second presentation by Brian Cook summarized his project in Brazil to provide safety equipment and sustainable farming in a community that produces rutilated quartz.

A collaboration between Gems Keep Giving and Italian brands Margherita Burgener and Petramundi has produced a limited-edition set of 10 pins. These titanium and gemstone pins, designed by Emanuela Burgener and handcrafted in Valenza, Italy, symbolize the foundation's mission. Each pin contains a unique gemstone, and all 10 include a central pink titanium heart representing the Gems Keep Giving logo, with five extending branches for the five major gem-sourcing continents. The gemstones were carefully chosen to represent the location of each

Figure 46. Left: Gabriela Farfan (right), Coralyn W. Whitney curator of gems and minerals for the Smithsonian National Museum of Natural History, accepts the original Gems Keep Giving pin from Hayley Henning, chairperson of the organization. Right: The original prototype pin featuring a Montana sapphire. Photos by Jennifer Stone-Sundberg.

project, whether a specific community or country. The original prototype pin, which contains a Montana sapphire and represents North America, was donated to the Smithsonian National Museum of Natural History's gem and mineral collection and presented to curator Gabriela Farfan during the event (figure 46). Over the next three months, Gems Keep Giving will raise money for future projects similar to their first in Kenya, awarding the remaining pins to the top donors.

Jennifer Stone-Sundberg and Tao Hsu

Wearable art jewelry supporting families in Guatemala. At the Colors of the Stone show, the author met exhibitor Pat Pannell, founder of Chick Boss, a handmade wearable art jewelry business launched in 2010 in San Andrés, Guatemala (figure 47). From the beginning, Pannell intended to help local families thrive financially, educationally, and emotionally through her business. Over the past 15 years, Chick Boss has become an inspiring example of how a small jewelry company can make a large impact.

For Pannell, the journey began long before the establishment of Chick Boss. She fell in love with Guatemala in 2001 during her stay with a host family while participating in a Spanish immersion program. Pannell noticed that some of the family's 10 children did not attend school because they could not afford uniforms and tuition. Through her own efforts, Pannell funded all schooling for the children, encouraging them to reach the education levels they aspired to. All 10 finished high school, and a few of them went on to earn their college degrees.

The experience with her host family left Pannell wanting to make a positive impact on others in Guatemala. With no experience in the gem and jewelry trade, Pannell turned to her sister Jeanne Sheridan to establish Chick Boss in 2010. At the time, Sheridan designed and produced one-of-a-kind jewelry using copper, brass, and gemstones in the United States. To support Pannell's vision for a business in Guatemala, Sheridan had to shift her focus to the practicality and reproducibility of the pieces. She began training locals on beading work, primarily stringing, and the traditional cold-connection technique to make jewelry completely by hand (figure 48). Since cold-connection techniques do not require the use of heat, trainees were

Figure 48. Jeanne Sheridan training local Guatemalan women and men to become bead stringers and metalsmiths. Photos by Pat Pannell.

Figure 47. Pat Pannell, founder of Chick Boss, at the Colors of the Stone show. Photo by Loren Kayfetz.

Figure 49. The award-winning Sound Collection featuring repurposed vinyl records, imitation pearls, and aluminum. Photo by Che Velasquez; courtesy of Chick Boss.

able to learn and execute the method more easily. Sheridan also worked with a translator to produce detailed illustrated training materials.

The first group of four women trainees learned beading work and metalsmithing. After four 4-hour training sessions, they were ready to carry out the work from home, benefiting from flexible schedules. Within six months, eight beaders were fully developed. A few teenagers were trained in metalsmithing, some of whom have become experienced craftspeople and are now training new hires on their own.

In 2012, at a Central American artisan craft trade show, Pannell and Sheridan met Marilyn Polanco, a talented jewelry designer from Guatemala with a degree in industrial design. Polanco soon became the primary designer for Chick Boss, bringing a contemporary and bold look to the designs with components and patterns that could be easily reproduced utilizing the employees' existing skills and materials.

The various collections produced at Chick Boss's San Andrés workshop showcase the versatility of designs from these Guatemalan artisans. Among them, the Sound Collection featuring repurposed vinyl records won the 2021 Buyer's Choice Award for Best Jewelry from the Museum Store Association (figure 49). A collaboration with Casa Del Jade in Antigua added Guatemalan jadeite jade stones to jewelry pieces, honoring the most important gem resource in the country (figure 50).

Since its establishment, Chick Boss has consistently donated 1–5% of its gross sales to multiple charity organizations and supported approximately 25 families in the local community. The artisans are compensated well beyond what is required by Fair Trade standards, allowing them to support their families, keep their children in school, and continue to pursue their own dreams. In the near future, Chick Boss plans to hire a local jeweler who can provide additional training for the team. Equipment for silver and gold plating will be purchased to allow for further expansion. Pannell and her partners hope that their story can inspire more business owners to engage in sustainable practices through community support.

Tao Hsu

Figure 50. The "River" necklace (left) and "Flower" cuff (right) from the Sculptural Collection featuring Guatemalan jadeite jade stones. Photos by Marty Kelly; courtesy of Chick Boss.

Figure 51. Left: Two pieces of surfite, a surfboard manufacturing byproduct, shaped like miniature surfboards. Right: The tag on the back of this piece of surfite is visible due to the translucency of the material. Photos by Tao Hsu.

Surfite: A surfboard manufacturing byproduct. The Tucson gem and jewelry shows provide a venue for creative minds continuously pushing the boundaries of materials that can be used in jewelry. Industrial byproducts of unexpected origin sometimes become well-received and even desired products in the gem and jewelry marketplace, including fordite, a byproduct of an automobile painting process (Spring 2016 GNI, pp. 87–88). Over the past decade, fordite has become a popular item at trade shows.

A colorful translucent material called surfite recently caught the author's attention in Tucson. Surfite is produced from the solidified accumulation of surfboard paint. More than two dozen steps are followed to produce a surfboard, including the hot-coat and gloss-coat paint procedures. Much like fordite forms, as paint is poured on a surfboard, it often drips on the floor below, leaving gradually hardened layers that accumulate in random patterns over time. This accumulation process can take several weeks before a workable thickness is reached.

Once treated as waste and thrown into landfills, this material is now exploited by some creative artists for use in jewelry making. Multiple exhibitors at the Colors of the Stone and Pueblo shows carried surfite cabochons of various shapes (figure 51). These cabochons can be mounted in precious metal or drilled to make a pendant. The material can also be shaped into a hololith-style ring or bangle. Unlike the opaque fordite, surfite is often translucent, which might be caused by a difference in paints used or the method of paint application.

As the gem and jewelry trade continues to explore sustainable practices, recycling and repurposing can open new doors to the industry. Many industrial byproducts can take up to 1,000 years to decompose in landfills. Recognizing the beauty of these materials and applying them in jewelry can allow designers to embark on a new creative journey.

Tao Hsu

ANNOUNCEMENTS

Eighth annual Gianmaria Buccellati Foundation Award winner. Eleanor H. Yeh, a graduate of GIA's Jewelry Design program in London, received the eighth annual Gianmaria Buccellati Foundation Award for Excellence in Jewelry Design. The 14 finalists from eight of GIA's worldwide campuses were announced, followed by the winner, at the GIA Alumni Collective's "Night at the Museum" event held during the AGTA GemFair in Tucson. Yeh's winning design, a Renaissance-inspired necklace featuring intricate goldwork, South Sea pearls, and vibrant gems, stood out to the panel of judges for its precision and realism of the floral element (figure 52).

Created in partnership with the Gianmaria Buccellati Foundation in 2018, the award recognizes outstanding talent in design among GIA students worldwide. Larry French, chief officer for North American strategies at the foundation, said, "On behalf of the Gianmaria Buccellati

Figure 52. Eleanor H. Yeh's winning necklace design sketch for the 2024 Gianmaria Buccellati Foundation Award for Excellence in Jewelry Design, featuring intricate goldwork, South Sea pearls, and vibrant gems.

Foundation, I want to congratulate Ms. Eleanor H. Yeh, this year's winner, plus all the other finalists whose work so enriched this competition. I also want to recognize the talented GIA design instructors who helped guide the students on their way to the final judging in Tucson. Our founder, Gianmaria Buccellati, believed that designing jewelry was an art and, like all art, needed to be studied and practiced in order to grow into a master designer."

As part of the award, Yeh will travel to Italy and meet with a representative from the foundation.

The 2025 Gianmaria Buccellati Foundation Award for Excellence in Jewelry Design competition is underway and open to students in GIA's Jewelry Design courses who meet the eligibility requirements. Visit www.gia.edu/buccellati-foundation-award-jewelry-design for more information.

REGULAR FEATURES

IN MEMORIAM

Henry A. Hänni. Renowned Swiss gemologist and educator Henry A. Hänni (figure 1) passed away on January 9, 2025, at the age of 80.

Hänni began his career as a technical assistant at the Mineralogical Institute of the University of Basel in Switzerland. Inspired to pursue more advanced studies in gemology and mineralogy, Hänni ultimately earned a PhD in 1980 from the university with a thesis on beryl from the Swiss Alps.

That year, he joined the Swiss Gemmological Institute (SSEF), later assuming the director position in 1990. In 1996, he became a professor of gemology at the University of Basel. Throughout his career, Hänni authored countless papers in multiple languages, including several for *Gems & Gemology* on colored stones and pearls, and also served on *G&G*'s review board. In 2004, he received the Accredited Gemologists Association's Antonio C. Bonanno Award for Excellence in Gemology.

After his retirement in 2009, Hänni remained active in the gemological community, both in gemstone research and education. In addition to his pioneering work in cultured pearl and gemstone analysis, treatment detection, and origin determination, he will be remembered for inspiring young gemologists with his passion and mentorship. We extend our heartfelt condolences to Hänni's family, friends, and colleagues.

Figure 1. Henry A. Hänni (1945–2025), a groundbreaking researcher and educator in the field of gemology.

ERRATA

1. In the Winter 2024 article "Chemical analysis in the gemological laboratory: XRF and LA-ICP-MS" on p. 546, second column, the sentence "Saltwater pearls typically exhibit higher manganese and lower strontium concentrations, while freshwater pearls show lower manganese and higher strontium" should read "Freshwater pearls typically exhibit higher manganese and lower strontium concentrations, while saltwater pearls show lower manganese and higher strontium."

2. In the Winter 2024 article "Analysis of gemstones at GIA laboratories," several references were omitted from the Reference section on p. 614. A complete reference list is available at https://www.gia.edu/gems-gemology/winter-2024-gemstone-analysis. We thank Robert Kane for pointing out this error.